

Antarctic grounding line migration from satellite laser altimetry

Bryony Isabella Diana Freer

The University of Leeds

School of Earth and Environment

British Antarctic Survey

Ice Dynamics and Palaeoclimate

Submitted in accordance with the requirements for the degree of

Doctor of Philosophy

July 2024



British Antarctic Survey

NATURAL ENVIRONMENT RESEARCH COUNCIL

Declaration

I confirm that the work submitted is my own, except where work which has formed part of jointly authored publications has been included. My contribution and the other authors to this work has been explicitly indicated below. I confirm that appropriate credit has been given within the thesis where reference has been made to the work of others.

The research described in Chapter 2 has been published as: Freer, B. I. D., Marsh, O. J., Hogg, A. E., Fricker, H. A., & Padman, L. (2023). Modes of Antarctic tidal grounding line migration revealed by Ice, Cloud, and land Elevation Satellite-2 (ICESat-2) laser altimetry. *The Cryosphere*, 17(9), 4079–4101. https://doi.org/10.5194/tc-17-4079-2023. B. I. D. Freer led the study, supervised by O. J. Marsh, H. A. Fricker and A. E. Hogg. B. I. D. Freer conducted the data analysis and wrote the manuscript. All authors provided insights regarding the interpretation of data and reviewed and edited the manuscript.

The research described in Chapter 3 has been accepted for publication as: Freer, B. I. D., Marsh, O. J., Hogg, A. E., Fricker, H. A., Siegfried, M. R., Floricioiu, D., Sauthoff, W., Rigby, R., and Wilson, S. F. (2024, in review) Coincident lake drainage and grounding line retreat at Engelhardt Subglacial Lake, West Antarctica. *Journal of Geophysical Research: Earth Surface.* B. I. D. Freer led the study, supervised by O. J. Marsh, H. A. Fricker and A. E. Hogg. B. I. D. Freer conducted the data analysis and wrote the manuscript. O. J. Marsh, D. Floricioiu, R. Rigby, S. F. Wilson and W. Sauthoff contributed some datasets. All authors provided insights regarding the interpretation of data and reviewed and edited the manuscript.

The research described in Chapter 4 has been prepared as a manuscript to be submitted as: Freer, B. I. D., Marsh, O. J., Bradley, A. T., Fricker, H. A. and Hogg, A. E. (2024, *in prep*) Surface impression of the basal stress transition at the grounding line of the Ross Ice Shelf, Antarctica. *Journal of Glaciology.* B. I. D. Freer led the study, supervised by O. J. Marsh, H. A. Fricker and A. E. Hogg. B. I. D. Freer conducted the satellite data analysis and wrote the manuscript. O. J. Marsh and A. T. Bradley helped with the modelling work. All authors provided insights regarding the interpretation of data and reviewed and edited the manuscript.

This copy has been supplied on the understanding that it is copyright material and that no quotation from the thesis may be published without proper acknowledgement. The right of Bryony Isabella Diana Freer to be identified as the Author of this work has been asserted by Bryony Isabella Diana Freer in accordance with the Copyright, Designs and Patents Act 1988.

Acknowledgements

Thank you to my supervisors Oliver Marsh, Anna Hogg and Helen Fricker for your unwavering support, advice, and encouragement over the past four years. It has been a privilege to work together, and this thesis has been greatly improved by your contributions. I look forward to continued collaboration in the future. I would also like to thank Laurie Padman, Matt Siegfried and Alex Bradley for your invaluable guidance and mentorship during the co-authorship of the three papers in this thesis.

A special thank you to the SENSE CDT directors, managers, and students for providing such an enriching training environment. Starting a PhD during the Covid-19 pandemic was tough, but I am grateful for our community and collective resilience to get through that time still smiling! I extend particular thanks to Emily Dowd, Calum Hoad and Morag Fotheringham, with whom I share the immense pride of co-founding SatSchool.

Thank you to the whole team at isardSAT for a wonderful three-month CASE industry placement in 2023.

I am very grateful for the many friends I have met at BAS along the way, especially my office mates in Room 39 who have made coming into work so fun: Millie, Max, Zelna, Roseanne, Evelyn, Andy, James, Dorothea, Rachel, Lizzie, and Qinggang. Alongside Jo, Jon, Paul, Holly, Chris, Tom and Ennis, our collective West Hub writing days, puzzles, Dulcedo breaks, cycle adventures, pub quizzes and lido swims have helped me stay sane! And a huge thank you to Team SID in Leeds: Heather, Ben, Bean, Trys, Sally, Ross, Katie, and Mae.

My PhD experience in Cambridge has been greatly enriched by my communities outside of work. I am extremely grateful to my lovely housemates Lucy, Hannah, Ben, and Charlotte; to all of St John's Voices for providing such musical nourishment; and to all the girls at Cottenham Jaguars for all the fun week-in week-out on the netball court.

Finally, to my family – Mum, Dad and Annabel – thank you for everything. I could not have achieved this without you.

Abstract

In this thesis I present new methods and observations to improve our understanding of the patterns and drivers of Antarctic grounding line (GL) migration over various time-scales, using satellite laser altimetry and other satellite datasets.

First, I develop a new method to measure short-term, tidal GL migration using ICESat-2 repeat-track laser altimetry (RTLA), locating the GL position at multiple individual tidal states along the same satellite track. Applied to the grounding zone (GZ) of the Bungenstockrücken ice plain, this technique identifies a 1,300 km^2 area of ephemeral grounding over which the GL migrates by up to 15 km between low and high tide, and reveals four distinct modes of tidal migration: "linear", "asymmetric", "threshold" and "hysteresis". I also combine this technique with differential synthetic aperture radar interferometry (DInSAR) to reveal the ungrounding of an ice plain on the Ross Ice Shelf over 15 years.

Next, I present a 21-year time series of subglacial lake activity at Engelhardt Subglacial Lake (SLE) in West Antarctica, compiled from ICESat, ICESat-2 and CryoSat-2 altimetry. I document, for the first time, the second drainage of this lake on record, beginning in July 2021, and detect up to 13 km of GL retreat downstream of the lake over the same period with a combination of ICESat-2, DInSAR and high-resolution digital elevation model (DEM) data. Using these observations, I evaluate the mechanism triggering SLE drainage, the cause of the observed GL retreat, and the interplay between subglacial hydrology and GL dynamics.

Finally, I map the spatial distribution and shape of wave-like surface features (WSFs) associated with the basal stress transition around the Ross Ice Shelf GZ, using DEM and ICESat-2 data. I demonstrate that satellite observations of WSFs, combined with viscous beam theory, can improve estimates of GL location, basal properties, and ice thickness in Antarctic GZs.

Abbreviations

AIS	Antarctic Ice Sheet
ATLAS	Advanced Topographic Laser Altimeter System
CATS2008	Circum-Antarctic Tidal Simulation 2008
COSMO-SkyMed (CSK)	Constellation of Small Satellites for Mediterranean basin Observation
DEM	Digital elevation model
DInSAR	Differential Synthetic Aperture Radar Interferometry
ESA	European Space Agency
FRIS	Filchner-Ronne Ice Shelf
GL	Grounding line
GLAS	Geoscience Laser Altimeter System
GT	Ground track
GZ	Grounding zone
ICESat-2	Ice, Cloud, and land Elevation Satellite-2
InSAR	Synthetic Aperture Radar interferometry
MCoRDS	Multichannel Coherent Radar Depth Sounder
MEaSUREs	Making Earth System Data Records for Used in Research Environments programme (NASA)
NASA	National Aeronautics and Space Administration
Point F	Inland limit of ice shelf flexure
Point G	True grounding line
Point H	Hydrostatic limit (inland limit of ice in complete hydrostatic equilibrium with full tidal range)
Point I_b	Break-in-slope
REMA	Reference Elevation Model of Antarctica
RGT	Reference Ground Track
RIS	Ross Ice Shelf
RPT	Reference Pair Track
RTLA	Repeat-Track Laser Altimetry
SAR	Synthetic Aperture Radar
SLE	Engelhardt Subglacial Lake
WSF	Wave-like surface feature

Table of Contents

List of Figures ..... **x**

List of Tables ..... **xxiii**

Chapter 1: Introduction and Background 1

1.1. The Antarctic Ice Sheet and role of grounding line migration 1

1.1.1. The Antarctic Ice Sheet 1

1.1.2. The grounding line 3

1.1.3. Grounding line migration 4

1.2. Observing the grounding line 5

1.2.1. Hydrostatic methods 7

1.2.2. Surface slope methods 7

1.2.3. Differential Interferometric Synthetic Aperture Radar (DInSAR) 8

1.2.4. Pseudo-crossover radar altimetry (PCRA) 10

1.2.5. Repeat-track laser altimetry (RTLA) 10

1.2.6. Observing grounding line migration with ICESat 12

1.2.7. Observing grounding line migration with ICESat-2 13

1.3. Key grounding zone processes and knowledge gaps 15

1.3.1. The spatial extent of tidal grounding line migration around Antarctica 16

1.3.2. The mechanisms of tidal grounding line migration 17

1.3.3. The impact of tidal grounding line migration on basal melt rates 17

1.3.4. The impact of tidal grounding line migration on basal drag and ice flow 18

1.3.5. Impact of subglacial hydrology on basal melt rates and tidal grounding line migration 18

1.3.6. Impact of upstream subglacial lake drainage on grounding zone dynamics 19

1.3.7. Challenge of locating the basal stress transition 19

1.3.8. Uncertain ice thickness estimates in the grounding zone 20

1.4. Knowledge gaps lead to uncertainty in future ice sheet and sea level projections 20

1.5. Aims and Objectives 22

1.6. Thesis structure 23

References 24

Chapter 2: Modes of Antarctic tidal grounding line migration revealed by Ice, Cloud, and land Elevation Satellite-2 (ICESat-2) laser altimetry 38

Abstract 39

2.1. Introduction 39

2.2. Grounding lines and their detection 42

2.2.1. Features of the grounding zone 42

2.2.2. Methods for detecting the grounding zone 44

2.3. Data and Methods 46

2.3.1. Datasets 46

2.3.2. Repeat-track laser altimetry 48

2.3.3. Study region 55

2.4. Results 56

2.4.1. Extent of tidal grounding line migration at Bungenstockrücken 56

2.4.2. Long-term grounding zone change at Bungenstockrücken 58

2.4.3. Modes of tidal grounding line migration 60

2.5. Discussion 66

2.5.1. Advantages of our ICESat-2 RTLA method for monitoring tidal grounding line behaviour 66

2.5.2. Implications for grounding line monitoring 67

2.5.3. Implications for modelling tidal ice shelf flexure and grounding line migration 69

2.5.4. Insights into tidal processes in the ice shelf-ocean-subglacial system 73

2.6. Summary and outlook 76

References 78

Chapter 3: Coincident lake drainage and grounding line retreat at Engelhardt Subglacial Lake, West Antarctica 89

Abstract 90

Plain Language Summary 91

3.1. Introduction 91

3.2. Study Region 93
3.3. Data 94
3.4. Methods 97
3.4.1. Surface elevation change 97
3.4.2. Subglacial hydrological flow pathways 99
3.4.3. Grounding line change 99
3.4.4. Engelhardt Ice Ridge retreat 100
3.5. Results 100
3.5.1. Surface elevation change at SLE 100
3.5.2. Grounding line retreat 105
3.6. Discussion 113
3.6.1. Engelhardt Subglacial Lake (SLE) drainage 113
3.6.2. Revisiting the relationship between SLE drainage and grounding line retreat 114
3.6.3. Implications of grounding line retreat 118
3.7. Summary 119
Acknowledgments 120
Open Research 121
Supplementary Material 123
References 123
Chapter 4: Surface impression of the basal stress transition at the grounding line of Ross Ice Shelf, Antarctica 134
Abstract 135
4.1. Introduction 135
4.1.1. Background 135
4.1.2. Motivation for studying WSFs 137
4.1.3. Study Area 139
4.2. Data 140
4.2.1. REMA Digital Elevation Model 140
4.2.2. ICESat-2 satellite laser altimetry 141
4.2.3. MCoRDS airborne radar-depth sounder 141
4.2.4. Ice thickness, velocity and DInSAR GL 142

4.3. Methods 142
4.3.1. Measuring WSF geometry 142
4.3.2. Integrating satellite observations with a viscous beam model 145
4.3.3. Examine the impact of WSFs on ice thickness estimates in the GZ 148
4.4. Results 150
4.4.1. Spatial variability of WSFs 150
4.4.2. Inferring ice viscosity and basal drag 154
4.4.3. Locating the GL 155
4.4.4. Impact of WSF on GZ ice thickness estimates 156
4.4.5. Temporal evolution of WSFs 161
4.5. Discussion 162
4.5.1. Spatial variability of WSFs 162
4.5.2. Improving estimates of GL location and ice thickness using a viscous beam model 165
4.5.3. Temporal evolution of WSFs 168
4.5.4. Limitations of our approach 170
4.6. Summary 171
Acknowledgements 172
Appendix A 173
Appendix B 175
Supplementary Material 177
S4.1 Adjustment of the Firn Correction 177
S4.2. Amplitude vs. Wavelength of Ross Ice Shelf WSFs 180
References 181
Chapter 5: Synthesis and Conclusions 191
5.1. Summary and synthesis of principle findings 192
5.1.1. A new method to detect tidal GL migration with ICESat-2 (Chapter 2) 192
5.1.2. The GL migrates by up to 15 km with the tide at two Antarctic ice plains (Chapters 2 & 3) 195

5.1.3. Four modes of tidal GL migration revealed with ICESat-2 (Chapter 2) 197
5.1.4. A 21-year record of subglacial lake activity at Engelhardt Subglacial Lake (Chapter 3) 198
5.1.5. 13 km of GL retreat and the ungrounding of an ice plain downstream of Engelhardt Subglacial Lake (Chapter 3) 199
5.1.6. Revisiting the interaction between subglacial lake drainage and GL migration (Chapters 3 & 4) 203
5.1.7. Evidence of subglacial bed form detected from satellite imagery (Chapter 3) 204
5.1.8. First large-scale study of wave-like surface features at Antarctic GZs (Chapter 4) 205
5.1.9. Inferring basal drag and ice viscosity from the geometry of wave-like surface features in Antarctic GZs (Chapter 4) 206
5.1.10. An independent method to locate the GL that best represents the basal stress transition (Chapter 4) 206
5.1.11. Improving ice thickness estimates in Antarctic GZs (Chapter 4) 207
5.2. Uncertainty Evaluation 208
5.2.1. ICESat-2 Datasets and Methods 208
5.2.2. Deriving DInSAR Grounding Lines 212
5.2.3. Measuring Grounding Line Retreat and WSF Dimensions with the REMA Digital Elevation Model 213
5.3. Recommendations for future work 215
5.3.1. Antarctic-wide assessment of the spatial extent of tidal GL migration 215
5.3.2. Antarctic-wide assessment of tidal GL migration modes 216
5.3.3. Antarctic-wide assessment of wave-like surface features in GZs 217
5.3.4. Deriving further basal information from observations of wave-like surface features 218
5.3.5. In situ measurements to validate and complement satellite datasets 220
5.3.6. Looking forward to upcoming satellite missions 222
5.4. Concluding Remarks 224
References 225

List of Figures

1.1 Cumulative ice sheet mass change (left axis) and resulting sea level contribution (right axis) between 1992 and 2020 for Greenland and Antarctica, as well as each of the Antarctic sub-regions: West Antarctica, East Antarctica, Antarctic Peninsula. Shaded regions represent the associated uncertainties (detailed in Otosaka et al., 2023). Dashed lines show the results from the latest IMBIE-2 assessment. Figure reproduced from Otosaka et al. (2023). **2**

1.2 Schematic of a simplified Antarctic ice sheet grounding zone. **4**

1.3 Schematic representation of the margin of an idealised ice sheet. Point G marks the location of the true grounding line (GL) at the limit of flotation. The GL proxies detectable by satellites are: Point F, the landward limit of tidal ice flexure; Point J, the first point of hydrostatic equilibrium; Point I_b, the break in slope; Point I_m, the local elevation minimum; Point H, the landward limit of the hydrostatic zone of free-floating ice shelf. The flexure zone is defined as the region between Points F and H. The grounding zone refers only to the distance over which Point F migrates across the tide cycle. Black dashed dotted line: hydrostatic ice surface. Red dotted line: dimensionless amplitude of tidal flexure. The distances between the individual GL proxies depend on local ice and bedrock properties. Figure adapted from Friedl et al. (2020). **6**

1.4 Example of TerraSAR-X DInSAR image over the GL of the Kamb Ice Stream, West Antarctica. The flexure zone is visible as the band of dense fringes, with each fringe representing a modulo 2π difference of the phase difference between the two input interferograms (due to vertical tidal flexure). The landward fringe indicates the landward limit of tidal flexure, Point F, and the seaward fringe (slightly more ambiguous) indicates Point H (Friedl et al., 2020). **9**

1.5 First example of the RTLA method, as presented in Fricker & Padman (2006): (a) ICESat 'retided' elevation profiles for the seven repeats along Track 218. (b) Elevation anomaly profiles for the four high-quality filtered repeats differenced against the mean elevation profile **11**

from (a), with horizontal coloured lines showing the tide predictions from CATS02.01 (Padman et al., 2002). Vertical dashed lines mark the derived locations of GL proxies: Point F, Point I_b and Point H. Figure reproduced from Fricker & Padman (2006).

1.6 Schematic illustrating the six-beam pattern of ATLAS (Smith et al., 2019). The central Reference Pair Tracks (RPTs) follow the Reference Ground Track (RGT) that matches the nadir track of the predicted orbit. The instrument is shown here in the forward direction with "strong" beams on the right side of be beam pair (green) tracking ~2.5 km behind the "weak" beams (blue). Note the relative positions of weak and strong beams reverse when ATLAS is oriented in the backwards direction. Figure reproduced from Smith et al. (2019). **14**

1.7 Schematic depicting the key grounding zone processes and satellite missions used in this thesis. **15**

1.8 Observed and projected future global mean sea level change relative to 1900, for a range of greenhouse gas emissions scenarios. Dashed red lines: low-likelihood, high impact storyline, including ice sheet instability processes. Figure reproduced from IPCC AR6 synthesis report (IPCC, 2023). **21**

2.1 (a) Idealised cross section of an ice plain GZ, showing the location of typical satellite-derived GZ proxies: Point Ib, the first break-in-slope; Point F, the inland limit of tidal flexure (represented here as approximately equal to Point G, the true GL); Point H, the inshore limit of hydrostatic equilibrium. (b) Idealised cross section of an ice plain GZ experiencing tidal GL migration, showing the difference in position of the ice shelf and migration of Point F between high tide (F_{max}) and low tide (F_{min}), across 24 hours of a simplified ~12 h semidiurnal tide cycle. **43**

2.2 Method used to define three types of reference profile for elevation anomaly calculations along ICESat-2 ground tracks, as illustrated for RGT 559 GT3L at the Bungenstockrücken ice plain. (a) Location of Bungenstockrücken on the Ronne Ice Shelf. Red diamonds show the locations used to calculate annual tide distributions. (b) ICESat-2 ground tracks crossing the MEaSUREs and ASAID GLs in the study area (Rignot et al., 2016; Bindschadler and Choi, 2011). (c-e) Repeat surface elevation profiles and anomalies of RGT 559 GT3L, each using **47**

a different reference profile: (c) mean profile calculated using cycles 4, 6, 8, 9, 11, 12, 13; (d) neutral profile of cycle 13; (e) lowest-sampled tide profile of cycle 9. The reference profile at zero-elevation anomaly is shown as a black dashed line, and the latitude of the derived Point F positions for each cycle along-track as coloured circles along the *x*-axis. Dashed coloured lines show the modelled tide height at the time of each cycle at the most seaward point along-track (in (e) these are differenced from the tide of cycle 9). (f) Histogram of CATS2008 modelled tide heights experienced over a single year, centred on 01/01/2020 (Howard et al., 2019), with vertical coloured dashed lines showing the tide height at each repeat cycle. (g) Tidal time series showing tide height, velocity and phase during the 24 hour period before and after the ICESat-2 overpass for each repeat cycle at RGT 559 GT3L.

2.3 Method used to locate Point F per repeat cycle from ICESat-2 elevation anomalies, as illustrated for RGT 559 GT3L. (a) Elevation anomalies for repeat cycles 4, 6, 8, 11, 12 and 13, each calculated against the lowest-sampled tide reference profile of cycle 9. Dashed coloured lines indicate the CATS2008 modelled tide height per cycle, differenced from the tide of cycle 9 (Howard et al., 2019). (b-g) Individual elevation anomalies for each repeat cycle, with the low-pass-filtered anomalies in black and the second derivative of the filtered anomalies in green. Vertical dashed lines show the along-track latitude where Point F has been located from the peak(s) of the second derivative. (h) Map showing the derived position of Point F per repeat cycle along RGT 559 GT3L. (i) Along-track migration distance of Point F per cycle for RGT 559 GT3L as a function of coincident tide height, overlain on the histogram of tide heights experienced over a single year (centred on 1 January 2020). **54**

2.4 Tidal GL migration at Bungenstockrücken, measured by ICESat-2 RTLA. (a) The location of Point F at every sampled repeat cycle per ICESat-2 ground track is coloured by percent of maximum tide height, overlain on the Reference Elevation Model of Antarctica (REMA) 8 m DEM (Howat et al., 2018), MEaSUREs GL (Rignot et al., 2016), ASAID break in slope GL (Bindschadler and Choi, 2011) and the most recent ICESat-2 derived break in slope (Point I_b) along each ground track (Li et al., 2022b). The two areas with the largest observed GL migration are highlighted as Areas A and B, and the locations for RGT 559 GT3L, 537 GT3L and 574 GT3L are shown. (b-c) The repeat elevation profiles **57**

and anomalies of RGT 559 GT3L, with repeat cycles coloured by tide (as percent of maximum tide height) and labelled in (c). The location of ICESat-2 Point Ib is marked with a vertical dashed line (Li et al., 2022b). (d-e) The equivalent repeat elevation profiles and anomalies for RGT 574 GT3L.

2.5 (a) Comparison of the ICESat-2 derived Point F positions at Bungenstockrücken to the following: (i) the ICESat-derived Point F (Brunt et al., 2010a), (ii) the ICESat-derived maximum inland Point F2 (Brunt et al., 2011), and (iii) the MEaSUREs GL (Rignot et al., 2016), derived from 2009 RADARSAT-2 data. (b) Comparison of the ICESat-2-derived Point F positions per repeat cycle from this study to the ICESat-2-derived Point F dataset from Li et al. (2022b) that locates a single Point F per ground track. (c) Comparison between the Point I_b from ASAID (Bindschadler and Choi (2011); derived from Landsat-7 and ICESat), ICESat (Brunt et al., 2010a) and ICESat-2 (Li et al., 2022b). **59**

2.6 Four modes of tidal grounding line migration observed along ICESat-2 ground tracks at Bungenstockrücken. Three examples are shown per mode, which are classified from top to bottom as the following: (a–c) linear, with a linear relationship between tide height and GL migration distance; (d–f) asymmetric, with higher tides causing an increased rate of GL migration; (g–i) threshold, with a sharp tide threshold above which there is significant GL migration; and (j–l) hysteresis, with a difference in the impact of tidal variability on GL migration during the rising- vs. falling-tide phase. In each example we show the along-track migration distance between each Point F and Point F measured at the lowest-sampled tide as a function of coincident tide height from CATS2008 (Howard et al., 2019). Note the variable *y*-axis scale between ground tracks. The orientation of the triangle indicates whether the repeat cycle was sampled during a rising- or falling-tide phase. Histograms show the distribution of tide heights experienced across a single year, centred on 1 January 2020. (m) Map of Bungenstockrücken showing ICESat-2 ground tracks coloured by migration mode (excluding tracks with < 1 km tidal migration or < 2 m tide range sampled). **61**

2.7 (a) The spatial pattern of tidal GL migration observed in Area B, Bungenstockrücken. Point F identified for every repeat cycle of each ICESat-2 ground track is coloured by percent of maximum tide height. (b–c) Schematics depicting the flow of water in between the seaward **65**

and landward GL positions inferred from ICESat-2 RTLA results in Area B, during the rising- and falling-tide phase. (d–e) The repeat elevation profiles and anomalies of RGT 537 GT3L, calculated using the lowest-sampled tide reference profile from cycle 4. Repeat cycles are coloured by tide (as percent of maximum tide height), and the cycle numbers are labelled in (e) alongside the CATS2008 modelled tide heights, differenced from the tide at cycle 4. (f–g) The individual elevation anomalies for cycles 9 and 12 against the lowest-sampled tide profile of cycle 4. Inset panels show the time series of tide heights for the 24 h before and after the time of ICESat-2 overpass at each cycle, showing the coincident tide phase and velocity.

2.8 Schematic summarising impacts of tidal flexure and GL migration on the ice shelf-ocean-subglacial system. These include impacts on the following: ice velocity (Gudmundsson, 2007; Thompson et al., 2014; Robel et al., 2017, 2022; Mosbeux et al., 2023); GZ surface profile (e.g., Schoof, 2011); inland seawater incursion (Warburton et al., 2020; Robel et al., 2022); variations in subglacial water pressure (Rosier et al., 2015; Begeman et al., 2020); the formation of estuarine features in the GZ (Horgan et al., 2013a); enhanced basal melt (Makinson et al., 2011; Mueller et al., 2012); basal shear stress (Anandakrishnan et al., 2003); till compaction, leading to changes in basal lubrication (Walker et al., 2013; Christianson et al., 2013; Sayag and Worster, 2013); the formation of tidal seabed ridges (Dowdeswell et al., 2020; Graham et al., 2022); and ocean circulation through tidal mixing. The landward and seaward tidal GL positions are labelled as F_{max} and F_{min}. **73**

3.1 Location of Engelhardt Subglacial Lake (SLE) near the Ross Ice Shelf grounding line on the Gould Coast. (a) MEaSUREs ice velocity (Rignot et al., 2017) overlain with the location of known active subglacial lakes (Siegfried & Fricker, 2018), modelled hydrological pathways and the 2009 MEaSUREs GL (Rignot et al., 2016). (b) Zoom of SLE area in (a) showing the estimated subglacial lake boundary on the Reference Elevation Model of Antarctica (REMA) DEM mosaic (Howat et al., 2019). The location of the east and west embayments and GL promontory are labelled, alongside the estimated ice plain area (Brunt et al., 2010). **94**

3.2 Combining satellite laser and radar altimetry elevations. Flowchart of methods used to derive a time-series of mean ice sheet surface **98**

elevation values within each crossover zone (CZ1–4) at SLE, using elevation data from ICESat (2003–09) and ICESat-2 (2018–2024) laser altimetry and CryoSat-2 radar altimetry (2010–2021). Note that all elevation values are illustrative.

3.3 Satellite laser and radar altimetry measurements of surface elevation change at SLE, 2003–2024. (a) Location of the four crossover zones (CZ1–4) used to calculate mean elevation change at SLE, and ICESat (red) and ICESat-2 (white) RGTs. (b) Repeat surface elevation profiles along ICESat-2 RGT 343 ground track 1R (GT1R), April 2019 – April 2024; location in (a). (c) 21-year time-series of mean surface elevation at SLE, measured within CZ1–4 by ICESat (2003–09), CryoSat-2 (2010–20) and ICESat-2 (2019–24). Error bars represent one standard deviation of along-track surface elevation measurements within each CZ (note error bars are too small to be visible for some ICESat and ICESat-2 data points). Grey shading shows the ICESat-2 ATL15 coverage period (used in Fig. 3.4). **102**

3.4 Temporal evolution of surface elevation change at SLE, April 2019 – January 2024. (a–s) ATL15 gridded surface elevation change at SLE and its upstream feeder lake between consecutive quarter-year intervals (Smith et al., 2024). Lake boundaries (dashed black lines) were manually delineated based on the observed surface subsidence area, and circles in (a) mark the location of crossover zones 1–4. (q) Mean and median cumulative elevation change within the SLE boundary from the onset of SLE drainage (July 2021 – January 2024). **103**

3.5 SAR imagery showing surface damage and crevassing at SLE and the GZ. (a) Time-series of TerraSAR-X multi-look backscatter images 2012–23 along the SW margin of SLE, showing the development of crevasses caused by drainage-induced surface subsidence (c.f. Fried et al., 2014). (c) Extensive region of crevassing downstream of SLE and at the upstream end of the GZ promontory. (d) Large surface undulations and more complex surface crevassing around the GZ promontory. (e) Tide-induced strand cracks parallel to the newly retreated GL of the west embayment. **104**

3.6 GL migration and surface elevation change downstream of SLE, 2009–24. (a) February 2009 RADARSAT-2 DInSAR and derived GL (black line), showing the east and west embayment and central grounded promontory. White hashed area shows the approx. location of the grounded ice plain identified in Brunt et al. (2010). (b) TerraSAR-X **105**

DInSAR and derived GLs from July and October 2023 (white dashed and solid lines, respectively). (c) ICESat-2 ATL15 gridded surface elevation change across the wider Gould Coast, 2019–24 (Smith et al., 2024). (d) Zoom of (c) over the same region as (a–b) showing the 2023 GL positions.

3.7 Engelhardt Ice Ridge retreat, 2003–24. (a–b) REMA DEM strips from 30 October 2012 and 12 February 2022 (Howat et al., 2019), showing the closest available DInSAR GL positions. Coloured circles mark the location of the ridge at the 40-m elevation contour along ICESat track 172 (red) and ICESat-2 RGT 343 ground track 1R (GT1R) (black) for each of the sampled time stamps in (c–d). (c) Repeat surface elevation profiles along ICESat RGT 172, combining elevations from ICESat November 2003 – March 2009 (circles) and elevations sampled along the same ground track from REMA DEM strips October 2012 – February 2022 (triangles). (d) Repeat surface elevation profiles along ICESat-2 RGT 343 GT1R, combining elevations from ICESat-2 April 2019 – April 2024 (circles) and elevations sampled along the same ground track from REMA DEM strips October 2012 – February 2022 (triangles). (e–f) Ridge retreat distance at the 40-m elevation contour along: (e) ICESat RGT 172, November 2003 – February 2022; and (f) ICESat-2 RGT 343 GT1R, October 2012 – April 2024. **107**

3.8 Timeline of GL retreat and ice plain ungrounding in the west embayment from a combination of RADARSAT-2 and TerraSAR-X DInSAR and ICESat-2 RTLA. (a) February 2009; (b) September 2012; (c) April 2016 (weak signal of GL retreat marked with dashed white line); (d) May 2019, ICESat-2 repeat elevation and elevation anomalies along RGT 526 GT3L showing tidal flexure (i.e. ungrounding) over the section of the track crossing the ice plain on 2 May 2019; (e) July 2023; (f) October 2023. Black line shows the 2009 GL for comparison between images. The white hashed area in (a) shows the approx. location of the grounded ice plain identified in Brunt et al. (2010). The total expected vertical height difference for each DInSAR image are provided in Table 3.1. **109**

3.9 ICESat-2 RTLA measurements of tidal flexure and tidal GL migration within the newly ungrounded ice plain at the west embayment. (a) Repeat ATL06 surface elevation profiles along ICESat-2 RGT 23 GT2L from 26 March (gold), 25 June (blue), 24 September (purple) and 23 December (green) 2021 across the newly ungrounded ice plain **111**

(location in (f)). (b–d) ATL06 elevation anomalies from 26 March (gold), 25 June (blue) and and 23 December (green) 2021, each calculated against the low tide reference profile of 24 September 2021 (purple). Derived location of Point F (inland limit of tidal flexure) for either side of the channel are shown by the coloured dots along the x-axis. (e) Modelled tides 24 h before and after each sampled ICESat-2 overpass, extracted from the Circum-Antarctic Tidal Simulation 2008 (CATS2008_v2023; Howard et al., 2019) using the pyTMD software package (version 2.1.0., Sutterley et al., 2017). (f) Location of derived Point F positions for each date (coloured dots) along ICESat-2 RGT 23 GT2L (solid black) overlain on the October 2023 TerraSAR-X DInSAR. (g) Point F positions along the western (blue) and eastern (red) edge of the newly ungrounded ice plain from all intersecting ICESat-2 RGTs, overlain on the TerraSAR-X multi-look backscatter image from 14 October 2023.

3.10 DInSAR time-series showing the change in the shape and length of the grounded promontory separating the east and west GL embayments. DInSAR fringes and delineated GL for four epochs: (a) February 2009 (RADARSAT-2); (b) April 2016 (TerraSAR-X); (c) July 2023 (TerraSAR-X); (d) October 2023 (TerraSAR-X). (e) All delineated GL positions overlain on the October 2023 (TerraSAR-X) DInSAR for comparison. **112**

S3.1 ATL15 surface elevation change and elevation change uncertainty across the Gould Coast, 2019 – 2024. (a) ATL15 total elevation change between April 2019 and January 2024. (b) ATL15 elevation change uncertainty over the same time period as in (a). (c) Histogram showing the distribution of elevation change uncertainty values across the entire Gould Coast study area. **123**

4.1 Schematic of the wave-like surface feature (WSF) observed at some Antarctic grounding zones. **137**

4.2 Location map of the Ross Ice Shelf ice streams and outlet glaciers examined in this study. We show catchment boundaries of the major Siple Coast ice streams and Trans-Antarctic glaciers (Mouginot et al., 2017). Clockwise from bottom left these include, EC: Echelmeyer, MA: MacAyeal, BI: Bindschadler, KA: Kamb, WH: Whillans, ME: Mercer, SC: Scott, AM: Amundsen, LI: Liv, SH: Shackleton, BE: Beardmore, LK: Lennox-King, NI: Nimrod, BY: Byrd, MU: Mulock. **140**

4.3 Flowchart of the algorithm used to locate the WSF depression and bump, and calculate its amplitude and wavelength, from a single surface height profile across the GZ. This used the SciPy library (Virtanen et al., 2020) and the Savitzky-Golay smoothing filter (Savitzky & Golay, 1964). **144**

4.4 The dimensionless, analytical profiles of (a) vertical velocity, (b) ice surface and (c) ice bottom height immediately downstream of the GL (dashed line), from the viscous beam model of Schoof (2011). Predictions of real-world WSF characteristics are recovered by reversing the vertical and horizontal scaling appropriate to the dimensions of each observed WSF. **146**

4.5 Grounding zone schematic, showing the different measurements of ice thickness (h = *measured;* h_f = *flotation; hi = hydrostatic;* h_{firn} = *firn*), ice surface height (z = measured; z_f = flotation) and ice bottom height (R = *measured,* R_i = *hydrostatic*), referenced to mean sea level. Point G marks the true GL, and Point G_f marks the floatation GL, located where the h_f first exceeds h. The inset panel shows the geometry of the firn correction, F_c, calculated as the difference between the actual thickness of the firn, h_{firn}, and the thickness if the firn was at the density of meteoric ice, $h_{firn\_\rho i}$. The densities of water, ice and firn are denoted by ρ_{water}, ρ_{ice} and ρ_{firn}. **149**

4.6 Location, amplitude and wavelength of WSFs around Ross Ice Shelf, observed from the REMA DEM. The central panel shows the location of glaciers and ice streams included in this study, marked in bold where WSFs have been identified (clockwise from bottom left, EC: Echelmeyer, MA: MacAyeal, BI: Bindschadler, KA: Kamb, WH: Whillans, ME: Mercer, SC: Scott, AM: Amundsen, LI: Liv, SH: Shackleton, BE: Beardmore, LK: Lennox-King, NI: Nimrod, BY: Byrd, MU: Mulock). Outer panels show the location of WSFs at each GZ, with the WSF depression (circles) coloured by amplitude. Black lines depict the distance between the WSF depression and bump (i.e., half the WSF wavelength). **152**

4.7 Boxplot showing the amplitude and wavelength of the WSFs on the Trans-Antarctic glaciers and Siple Coast ice streams. **153**

4.8 The ratio between the basal drag and ice viscosity (Equation 4.1, Appendix B) as a function of WSF wavelength, λ, GL ice velocity, u_{gl}, and GL ice thickness, h_{gl}. Also shown are locations of individual Ross **154**

Ice Shelf glaciers and ice streams determined from satellite-derived values along their representative profiles. Grey lines show contours of consistent drag-to-viscosity ratio.

4.9 Observed and modelled WSF surface profiles and GL positions for each Ross Ice Shelf glacier. Each panel shows the observed surface height along each representative profile (orange) and the fitted surface profile from the viscous beam model (dashed black line; Schoof, 2011). Vertical lines show the GL position predicted by the viscous beam model (black), always at $x=0$ at the basal stress transition point, and the DInSAR GL (red), which marks the inland limit of tidal flexure (Rignot et al., 2016). **156**

4.10 Modelled and hydrostatic ice surface, thickness and bottom height across the GZ for a modelled WSF surface profile. (a) The modelled WSF surface profile (Schoof, 2011), scaled to the dimensions of the Kamb WSF. (b) Modelled (pink) and hydrostatic (green) ice thickness along the same profile. (c) Modelled and hydrostatic ice bottom height along the same profile. Pink hashed areas indicate where the use of hydrostatic equilibrium overestimates ice thickness and ice bottom depth, and green hashed areas indicate where it underestimates ice thickness and ice bottom depth. **157**

4.11 Measured, hydrostatic and modelled ice surface height, ice thickness and ice bottom height across the Mulock WSF (location in Fig. 4.6). (a) Ice surface height measured by MCoRDS, z (black; Paden et al., 2010), and derived from the viscous beam model, zm (pink). (b) Ice thickness measured by MCoRDS, h (black), calculated from the MCoRDS surface using the hydrostatic assumption, h_i (green), and derived from the viscous beam model, h_m (pink). (c) Ice bottom height measured by MCoRDS, R (black); calculated using the hydrostatic assumption, R_i (green); and derived from the viscous beam model, R_m (pink). **159**

4.12 Measured, hydrostatic and modelled ice surface height, ice thickness and ice bottom height across the Kamb WSF (location in Fig. 4.6). (a) Ice surface height measured by MCoRDS, z (black; Wang et al., 2016) and derived from the viscous beam model, z_m (pink). (b) Ice thickness measured by MCoRDS, h (black), calculated using the hydrostatic assumption, h_i (green), and derived from the viscous beam model, h_m (pink). (c) Ice bottom height measured by MCoRDS, R (black); calculated using the hydrostatic assumption, R_i (green); and derived from the viscous beam model, R_m (pink). (d) TerraSAR-X InSAR **160**

fringes show the location of MCoRDS profile (thick black line) across the Kamb GZ (same distance along-track as in panels a-c), and the location of the modelled and DInSAR GLs and the WSF depression and bump. Individual TerraSAR-X scenes were acquired at: (i) 2017-02-27 T14:38:59; (ii) 2017-03-10 T14:38:59; and (iii) 2017-03-21 T14:38:59.

4.13 Change in surface height over the WSF at Engelhardt Ice Ridge between 2019 and 2023 from repeat ICESat-2 measurements along RGT 343 GT1R (location in Fig. 4.6). Coloured circles mark the location of the WSF depression minima at each ICESat-2 repeat (between two stable positions D1 and D2) and coloured triangles mark the WSF bump maxima. Vertical lines show the DInSAR GL positions from 2009 (Rignot et al., 2016) and July 2023 (Chapter 3; Freer et al., 2024) and the GL position predicted by the viscous beam model using the July 2023 ICESat-2 surface profile. (b) Time series of the WSF amplitude between 2019 and 2023. (c) Time series of the WSF wavelength between 2019 and 2023. **162**

S4.1 Ice surface, thickness and base elevation profiles across the Mulock Glacier WSF from MCoRDS (Paden et al., 2010), BedMachine (Morlighem, 2022) and calculated using the hydrostatic assumption, using different firn corrections. (a) No firn correction; (b) BedMachine firn correction; (e) adjusted firn correction (BedMachine firn correction +16 m). **178**

S4.2 Relationship between amplitude and wavelength of the WSFs of the representative profile from each glacier and the ice thickness, velocity, and velocity gradient at the intersection with their respective grounding line. Square markers are used for Siple Coast ice streams, circles for Trans-Antarctic glaciers. **180**

5.1 (copy of Figure 1.7). Schematic depicting the key grounding zone processes and satellite missions used in this thesis. Pink numbers indicate which Chapter(s) each process has been addressed in throughout the thesis. **191**

5.2 Schematic of the four modes of tidal GL migration identified from ICESat-2 RTLA measurements at the Bungenstockrücken ice plain (Chapter 2; Freer et al., 2023). **197**

5.3 Evidence from the ICESat-2 record of tidal flexure (i.e., ungrounding) across the ice plain downstream of SLE from at least May 2019 onwards. (a) ICESat-2 ATL06 repeat elevation profiles along RGT 526 GT3L for cycles 3, 4, 5, 7 and 8. Cycle 4 was sampled at the lowest tide, so is used as the reference elevation profile for calculating anomalies in (c–f). Inset plot shows the CATS2008 modelled tide height during the period 24 h before and after cycle 4 was sampled (Howard et al., 2019). (b) Location of ICESat-2 RGT 526 GT3L across the newly ungrounded section of the West Embayment, downstream of Engelhardt Subglacial Lake, with the TerraSAR-X derived GLs from July and October 2023 (dashed and solid white lines) and the ICESat-2-derived Point F positions (coloured circles). (c–f) ICESat-2 ATL06 elevation anomalies along RGT 526 GT3L for cycles 3, 5, 7 and 8, calculated against the reference profile from the low tide surface elevation profile (cycle 4). Derived Point F positions are shown with coloured circles along the *x*-axis. **200**

5.4 The schematic life cycle of an ice plain at low and high (dashed line) tide (reproduced from Brunt et al., 2011) compared to DInSAR observation showing a similar evolution of the ice plain downstream of Engelhardt Subglacial Lake. (a) An ice plain where the regions between Points F and C (the coupling line/first break-in-slope, I_b) is 'lightly grounded; (b) an ice plain experiencing 'ephemeral grounding', where Point F migrates between positions F1 and F2 depending on the tide; (c) a 'relict' ice plain, where the ice downstream of Point F has recently become fully floating but the surface has not yet fully conformed to flotation. (d) RADARSAT-2 DInSAR from February 2009 (solid black line = Point F shown by solid black line); (e) TerraSAR-X DInSAR from April 2016 showing signals of ephemeral grounding (solid white line = Point F1; dashed line = Point F2); (f) TerraSAR-X DInSAR from October 2023 (solid white line = Point F). Information about DInSAR processing is given in Table 3.1. **202**

5.5 Airborne radar-depth sounding profile across the Engelhardt Ice Ridge (CReSIS, 2024), showing possible evidence of a subglacial bed ridge at the location of the grounded promontory observed in the DInSAR record. Pink and red dashed lines mark the automatic picks of the surface and bed elevations from the radar profiles. **204**

5.6 REMA elevation error, obtained from the root mean square of the differences in elevation between the DEM and altimetry data **214**

following registration, or the differences among co-registered DEMs in the case of alignment. Note the logarithmic colour scale. Figure reproduced from Howat et al., (2019).

5.7 Effect of basal sliding law on vertical velocity near the GL and WSF surface profile (re-run of MISMIP experiment 1a4; Pattyn et al., 2012). (a–c) Vertical velocity across the GL using: (a) Weertman sliding law with exponent 1 (Equation 5.1); (b) Weertman sliding law with exponent 3 (Equation 5.1); (c) Coulomb sliding law with exponent 3 (Equation 5.2). (d) Surface elevation profiles showing the WSF profile for each sliding law in (a–c). Figure produced by Carlos Martín (2024; personal communication). **219**

5.8 Suggested observations of ice-shelf cavities required to understand ice melt in Antarctica. Figure reproduced from Rignot (2023). **222**

List of Tables

2.1 Existing grounding line datasets used in this study to compare to our ICESat-2 RTLA results. **56**

3.1 Image processing information and acquisition time for all RADARSAT-2 and TerraSAR-X DInSAR scenes used in this study. The tidal heights for each individual pass were calculated at the location shown in Figure 3.1 [83.161°S, 160.5°W] using the CATS2008 model (Howard et al., 2019), corrected for the inverse barometer effect (IBE) using the daily air pressure values from the National Center for Environmental Prediction and the National Center for Atmospheric Research Reanalysis (NCEP/NCA). The expected vertical height difference for each DInSAR is calculated using the tides from individual passes: *[t2-t1] + [t3-t2]*. **96**

4.1 Amplitude and wavelength (mean and standard deviation, SD) of the observed WSFs at each Ross Ice Shelf GZ in this study. **153**

5.1 Advantages and limitations of ICESat-2 RTLA and DInSAR (and specifically short-repeat DInSAR) for monitoring tidal grounding zone processes. **193**

Chapter 1

Introduction and Background

In this introductory chapter, I first provide an overview of the Antarctic Ice Sheet and the importance of continued monitoring to understand its present and future dynamics and impact on global sea-level rise. Then, I introduce the grounding line (GL) as a critical boundary at the margin of the ice sheet and review the main methods used to measure its location, including a more focussed description of satellite laser altimetry missions and techniques. Following this, I highlight the current gaps in our understanding and observations of grounding zone (GZ) processes that motivate much of this work. Finally, I outline the primary aim, objectives, and structure of the thesis.

1.1. The Antarctic Ice Sheet and role of grounding line migration

1.1.1. The Antarctic Ice Sheet

The Antarctic Ice Sheet (AIS) is a vital indicator of climatic change and a primary driver of sea level rise. Satellite observations showed that the AIS lost 2671 ± 530 Gt of ice between 1992 and 2020, raising global mean sea level by 7.4 ± 1.5 mm (Otosaka et al., 2023; Figure 1.1). There is widespread evidence that this ice mass loss is caused by anthropogenic climate change; with warming ocean temperatures in particular driving outlet glacier and ice shelf melt around Antarctica (Slater et al., 2021). However, the complexity of numerical simulations required to predict the ice sheet's dynamic response to climate forcing leads to considerable uncertainty in the projected AIS contribution to future sea level rise, and it has been identified as the most uncertain component of the 21st century sea level budget (Pattyn & Morlighem, 2020; IPCC, 2023a). In coupled Earth system models, these simulations rely on accurate representation of the ice sheet, which in turn requires knowledge of ice-sheet processes and boundary conditions. Constraining these model inputs to improve confidence in projections of future ice sheet evolution and sea level rise requires widespread and accurate

observations of these processes at the relevant spatial and temporal scales (Edwards et al., 2021; Aschwanden et al., 2021).

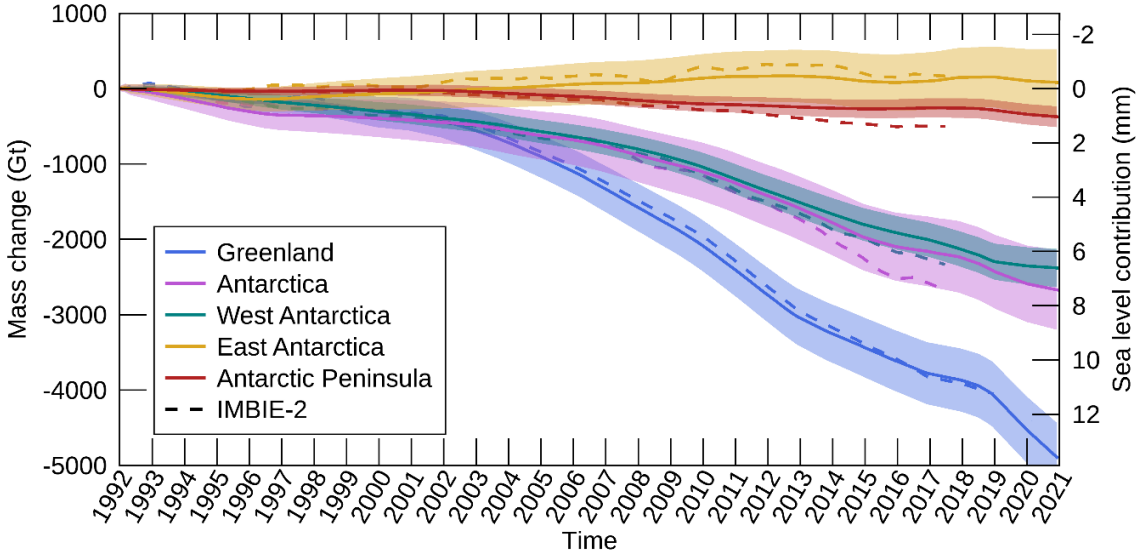


Figure 1.1. Cumulative ice sheet mass change (left axis) and resulting sea level contribution (right axis) between 1992 and 2020 for Greenland and Antarctica, as well as each of the Antarctic sub-regions: West Antarctica, East Antarctica, Antarctic Peninsula. Shaded regions represent the associated uncertainties (detailed in Otosaka et al., 2023). Dashed lines show the results from the latest IMBIE-2 assessment. Figure reproduced from Otosaka et al. (2023).

Recent mass loss from the AIS has been shown to be strongly linked to changes in the floating ice shelves that fringe 74% of its coastline (Joughin et al., 2012), yet observations of these regions are particularly lacking (Rignot, 2023). Ice shelves play an important role in ice sheet dynamics due to both their location directly at the ice-ocean interface (Dinniman et al., 2016), and the buttressing force they exert on upstream ice flow from outlet glaciers and ice streams (Gudmundsson et al., 2019). It is therefore vital that we improve our ability to monitor ice shelf change and represent them accurately in numerical ice sheet models (Edwards et al., 2021). This includes their current continent-wide configuration, as well as their behaviour on both short and long timescales.

1.1.2. The grounding line

Most of the mass loss from the AIS has been attributed to an acceleration in ice flow across the grounding line (GL) (e.g., Khazendar et al., 2016, Mouginot et al., 2014; Rignot et al., 2014; Scheuchl et al., 2016), which marks the boundary between the grounded ice sheet (in contact with the bed) and the adjoining floating ice shelf (in hydrostatic equilibrium with the ocean) (Fig. 1.2; Thomas, 1979). At the GL, the ice detaches from the underlying bed and ice flow transitions from a regime dominated by vertical shear and basal drag, to primarily buoyancy-driven flow dominated by longitudinal stretching and lateral shear with no basal drag (Schoof, 2007). There can be high rates of basal melt here as ocean water comes into contact with the base of the ice shelf (Jenkins et al., 2006; Depoorter et al., 2013) and can directly melt grounded ice at the GL (Ciracì et al., 2023). Accurate knowledge of the location and thickness of ice at the GL is critical for estimates of ice sheet mass balance, as it marks the optimal location for computing ice discharge (Hogg et al., 2018). Numerical ice sheet models are also particularly sensitive to the amount of basal melt at the GL (Arthern & Williams, 2017; Goldberg et al., 2019). These are therefore important boundary conditions for models that predict future ice sheet evolution and its impact on global sea level change (Pattyn, 2018).

The GL has been classed as an Essential Climate Variable, a variable that "critically contributes to the characterisation of Earth's climate" to be monitored on a regular scale (Bojinski et al., 2014). However, the GL is challenging to *precisely* locate, since it is both a subglacial and transitory feature that migrates over short and long timescales in response to a range of upstream and downstream forcings (e.g., Adhikari et al., 2014; Friedl et al., 2020; Park et al., 2013; Thomas, 1979).

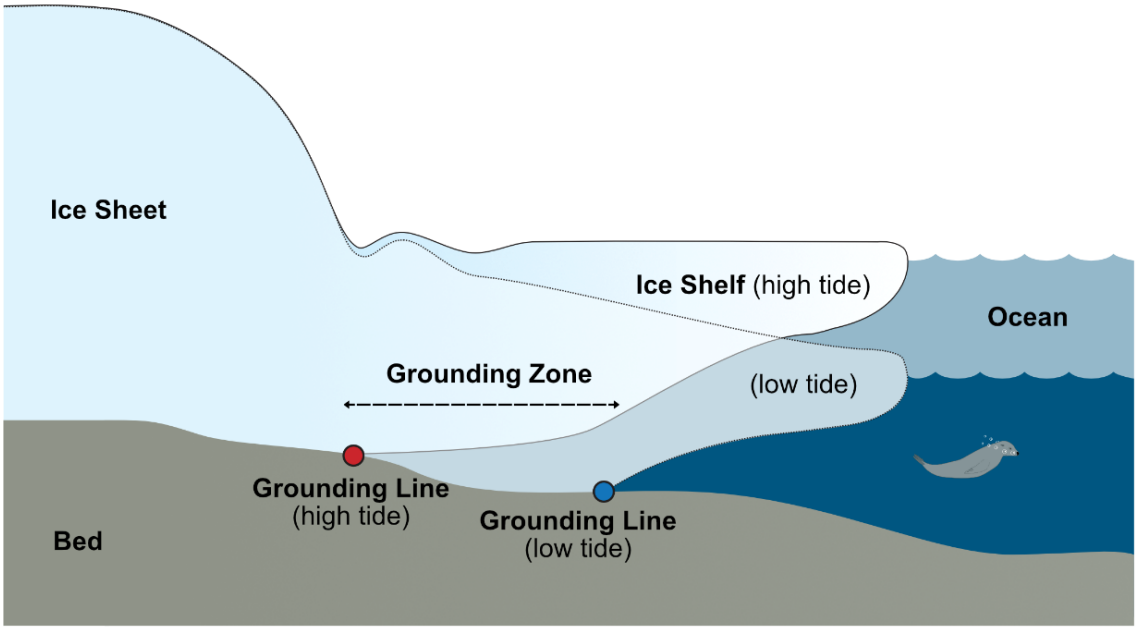


Figure 1.2. Schematic of a simplified Antarctic ice sheet grounding zone.

1.1.3. Grounding line migration

Over long timescales (annual-decadal), GLs are a sensitive indicator of ice sheet stability and so GL migration can indicate changes in local environmental forcing (Dutrieux et al., 2014; Joughin et al., 2010, 2012; Konrad et al., 2018). Sustained ice thickening can cause the GL to advance, whereas sustained thinning can cause retreat. Thinning can be caused by surface melt (e.g., Luckman et al., 2014; Trusel et al., 2015) or by subglacial melt in response to incursion of warm ocean water into the subglacial cavity (the predominant mechanism in Antarctica; Adusumilli et al., 2020; Cook et al., 2016; Rignot et al., 2013).

Ice shelf thinning reduces the buttressing force exerted on upstream ice, and GL retreat reduces basal friction, both of which can cause acceleration and dynamic thinning of upstream ice masses and increased contribution to global sea level (Friedl et al., 2018; Park et al., 2013; Wouters et al., 2015). Where such thinning occurs over a retrograde bed, this can trigger a positive feedback whereby an initial thinning causes the GL to retreat into deeper water, where a higher strain rate increases mass loss from the ice sheet,

leading to further retreat. This mechanism, termed "Marine Ice Sheet Instability" (MISI), is based on the understanding that since ice flux increases with ice thickness, GLs located on retrograde slopes are inherently unstable (Durand et al., 2009; Favier et al., 2014; Weertman, 1974). This effect is of particular concern in West Antarctica, where a large proportion of the ice sheet is grounded below sea level. Given that MISI is mostly controlled by the dynamics of the GL, continuous monitoring and improved process understanding could help to identify potential regions of instability (Hogg et al., 2018).

Over shorter timescales (hourly–daily), the location of the GL is also complicated by oscillations in sea level driven by ocean tides, the inverse barometer effect (IBE) and ocean circulation variability, that induce dynamic flexure of the ice shelves (Vaughan, 1995). Over the course of a single tidal cycle the GL can be expected to migrate landward as a rising tide lifts more of the ice shelf from its bed, and to return to its most advanced position at low tide (Fig. 1.2; Brancato et al., 2020). The region between the landward and seaward limits of tidally-induced GL migration is considered the grounding *zone* (GZ), which can be up to several kilometers wide (Fricker & Padman, 2006; Brunt et al., 2010b, Chen et al., 2023; Milillo et al., 2017, 2019; Rignot et al., 2024).

1.2. Observing the grounding line

The location of the true GL, i.e., the point at which the ice starts to float and the location of the basal stress transition, is the variable required for most glaciological and oceanographic applications. However, since it is a subglacial feature it can only be directly measured through in-situ geophysical surveys (e.g., MacGregor et al., 2011; Catania et al., 2010) or the use of remotely operated vehicles deployed from the shelf edge or through boreholes (Schmidt et al., 2023), which are impractical over large areas.

In lieu of direct observations of the GL, several surface expression features detectable in satellite data are used as proxies for GL location (Fig. 1.3; Friedl et al., 2020). These are typically defined using either hydrostatic methods (using the hydrostatic assumption), dynamic methods (measuring the ocean tide-induced changes in surface elevations across the GZ) or static methods (identifying topographic features on the ice

surface). The choice of GL proxy usually depends on the nature of the scientific question being posed, but these methods often produce differing estimates for the true GL location. Several techniques have been developed to detect different combinations of these GL proxies using a range of satellite sensors, which I summarise below.

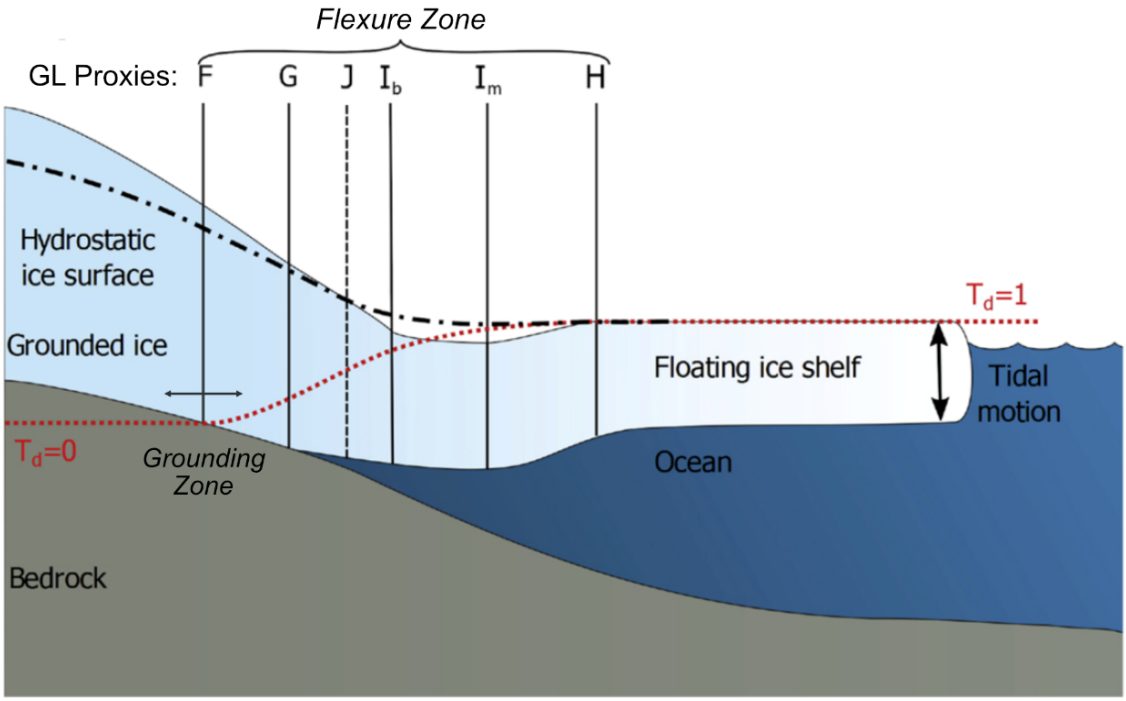


Figure 1.3. Schematic representation of the margin of an idealised ice sheet. Point G marks the location of the true grounding line (GL) at the limit of flotation. The GL proxies detectable by satellites are: Point F, the landward limit of tidal ice flexure; Point J, the first point of hydrostatic equilibrium; Point I_b, the break in slope; Point I_m, the local elevation minimum; Point H, the landward limit of the hydrostatic zone of free-floating ice shelf. The flexure zone is defined as the region between Points F and H. The grounding zone refers only to the distance over which Point F migrates across the tide cycle. Black dashed dotted line: hydrostatic ice surface. Red dotted line: dimensionless amplitude of tidal flexure. The distances between the individual GL proxies depend on local ice and bedrock properties. Figure adapted from Friedl et al. (2020).

1.2.1. Hydrostatic methods

Typically, large-scale ice sheet models locate the position of the GL using a hydrostatic assumption based on a flotation criterion that determines whether ice is floating or grounded (Docquier et al., 2011; Goldberg et al., 2009):

$$\rho_i h + \rho_w R(x,y) \begin{cases} < 0 & \text{for floating ice,} \\ = 0 & \text{at the GL,} \\ > 0 & \text{for grounded ice,} \end{cases} \tag{1.1}$$

where h is ice thickness, ρ_w is the density of seawater (assumed to be 1027 kg m^{-3}), ρ_i is the ice density (typically assumed to be 917 kg m^{-3} for meteoric ice), and R is the bed elevation relative to mean sea level. In simple terms, this says that ice will float when the ocean pressure is sufficient to support the weight of the overlying ice column, otherwise it will be in contact with the bed. This assumes that the ocean at hydrostatic pressure is always available to support the weight of the ice column when it can do so. While the hydrostatic assumption is useful and computationally efficient method to approximate the GL location for use in large-scale models, it is limited by uncertainties in compiled or modelled datasets of ice thickness and bed elevation that are used for these calculations, such as Bedmap2 (Fretwell et al., 2013) and BedMachine Antarctica (Morlighem et al., 2020). These uncertainties are highest within GZs (Chuter & Bamber, 2015; Griggs & Bamber, 2011), where the assumption of hydrostatic equilibrium breaks down as the shelf is partially supported by buoyancy and partly by transmitted beam stresses from the inland grounded ice (Chartrand & Howat, 2023).

1.2.2. Surface slope methods

Static methods typically locate the break-in-surface-slope, Point I_b (Fig. 1.3), which arises due to the abrupt change in basal shear stress as ice transitions from the grounded ice sheet to the floating ice shelf. This is most commonly identified directly from laser and radar altimetry data (e.g., Brunt et al., 2010; Hogg et al., 2018; Li et al., 2022) and digital elevation models (DEMs; e.g., Horgan & Anandakrishnan, 2006), or indirectly from surface shading in optical imagery (e.g., Scambos et al., 2007; Christie et al., 2016). A combination of these methods was used to derive the ASAID (Antarctic Surface Accumulation and Ice Discharge) Antarctic-wide GL map (Bindschadler et al.,

2011). The main limitation of using Point I_b as a GL proxy is the inconsistency in the distance between Point I_b and Point G across different regions, which is influenced by variations in ice thickness, basal traction, ice speed and rheology (Bamber and Bentley, 1994; Brunt et al., 2010b; Dawson and Bamber, 2017; Depoorter et al., 2013; Fricker and Padman, 2006; Rignot et al., 2011). It is particularly prone to errors in the presence of ice plains (Fricker et al., 2009), where low surface slopes, multiple break-in-slopes and significant decoupling of the break-in-slope from the true GL position can make it difficult to accurately locate Point I_b (Corr et al., 2001; Fricker and Padman, 2006; Fricker et al., 2009; Brunt et al., 2011; Li et al., 2022).

1.2.3. Differential Interferometric Synthetic Aperture Radar (DInSAR)

Interferometric synthetic aperture radar (InSAR) measures surface displacement between two coherent SAR images within centimetre accuracy and can be used in the GZ to identify horizontal ice flow and vertical tidal deflection (Minchew et al., 2017; Wild et al., 2018). By differencing InSAR image pairs from different epochs it is possible to remove the phase contribution of steady horizontal ice flow, leaving a signal of vertical tidal flexure that enables GL identification (Rignot, 1996; Fig. 1.4). This technique, known as differential synthetic aperture radar interferometry (DInSAR), has been used with data from a range of satellite missions including Sentinel-1, TerraSAR-X, RADARSAT-2 and COSMO-SkyMed to produce high-resolution quasi-continuous maps of Points F and H around Antarctica (e.g., Milillo et al., 2017, 2019, 2022; Mohajerani et al., 2021; Rignot et al., 2016).

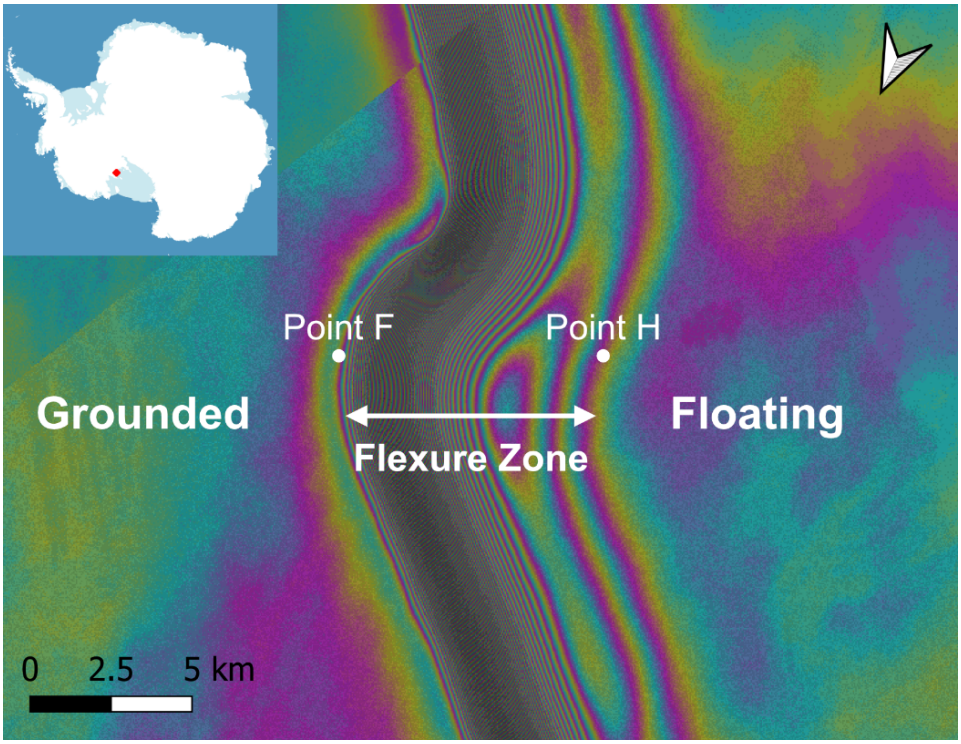


Figure 1.4. Example of TerraSAR-X DInSAR image over the GL of the Kamb Ice Stream, West Antarctica. The flexure zone is visible as the band of dense fringes, with each fringe representing a modulo 2π difference of the phase difference between the two input interferograms (due to vertical tidal flexure). The landward fringe indicates the landward limit of tidal flexure, Point F, and the seaward fringe (slightly more ambiguous) indicates Point H (Friedl et al., 2020). SAR image dates: (i) 21/02/2017 T14:47:26; (ii) 04/03/2017 T14:47:26; (iii) 15/03/2017 T14:47:26.

The GL identified using this technique can be ambiguous because it is determined from a composite of images captured at three or four tidal states. The quadruple tide level of the resulting GL is the difference of the four individual tide levels at each of the constituent SAR scenes composing the differential interferogram, i.e. *[t2-t1] - [t4-t3]*. This can be achieved with three consecutive images, using the central image (*t2*) in both InSAR pairs, i.e. *[t2-t1] + [t2-t3]*. Rabus & Lang (2002) suggest that if the quadruple tide level is less than ~10% of the total tidal range in the region, it is possible to misplace the GL by up to several kilometres using this technique. It also means that it

is difficult to attribute a certain GL position derived using this method to a specific tidal state, as it is associated with three or four different tidal states.

A key limitation with DInSAR is also the requirement for a sufficiently short temporal baseline between images to maintain interferometric coherence, particularly over fast-flowing regions like the glaciers of the Amundsen Sea embayment. Additionally, large polar gaps in coverage at the southernmost ice shelves have limited coverage across large parts of the Filchner-Ronne and Ross Ice Shelves. Recent advances in higher-temporal resolution InSAR satellites, such as COSMO-SkyMed and ICEYE, which can provide repeat-pass acquisitions with as short as a 1-day temporal baseline, have enabled GL mapping in these regions and enabled some monitoring of short-term GL migrations (Brancato et al., 2020; Chen et al., 2023; Ciracì et al., 2023; Kim et al., 2024; Milillo et al., 2017, 2019, 2022; Zhong et al., 2023). However, access to imagery from these satellites is charged and can only be acquired on request, which limits its more widespread usage across Antarctica (Friedl et al., 2020).

1.2.4. Pseudo-crossover radar altimetry (PCRA)

CryoSat-2 radar altimetry has been used to map Points F and H by applying a pseudo-crossover method to detect tidal flexure (Dawson and Bamber, 2017, 2020). This provides good spatial coverage by utilising large data volumes over a multi-year record but cannot be used to detect short-term GL migration between specific tides due to its long repeat cycle (369 d). Additionally, since the method requires stacking data from multiple tracks, it is not possible to derive GL information for single time stamps using this method (Friedl et al., 2020). It is, however, more computationally efficient than DInSAR methods.

1.2.5. Repeat-track laser altimetry (RTLA)

Repeat-track laser altimetry (RTLA) is a technique that can be used to identify Points F and H along discrete satellite laser altimetry ground tracks that cross the grounding zone. The method was first presented by Fricker & Padman (2006) using data from NASA's Ice, Cloud, and Land Elevation Satellite (ICESat), which was in orbit from 2003–2009. It is based on the principle that by comparing repeat measurements of ice

shelf elevation profiles taken across the GZ sampled at different phases of the ocean tide, and differencing them against a mean elevation profile, it is possible to identify elevation anomalies that relate to the landward and seaward limits of ice flexure, Points F and H (Fig. 1.5). This technique has subsequently been applied to data from ICESat-2 and provides an alternative view of GZ structure that is complementary to other techniques including DInSAR (Fricker et al., 2009). It is particularly effective at identifying the GL in the presence of ice plains, which are challenging to detect in other types of satellite imagery.

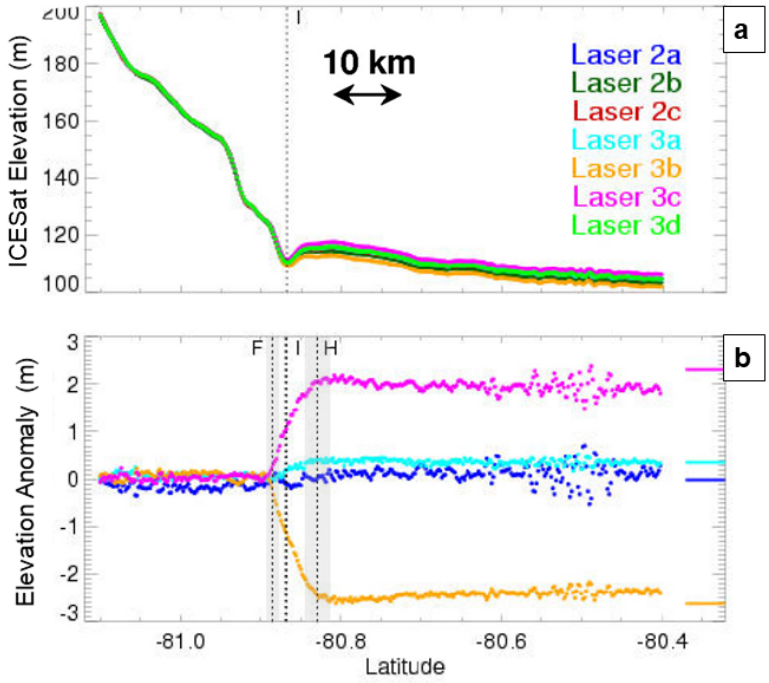


Figure 1.5. First example of the RTLA method, as presented in Fricker & Padman (2006): (a) ICESat 'retided' elevation profiles for the seven repeats along Track 218. (b) Elevation anomaly profiles for the four high-quality filtered repeats differenced against the mean elevation profile from (a), with horizontal coloured lines showing the tide predictions from CATS02.01 (Padman et al., 2002). Vertical dashed lines mark the derived locations of GL proxies: Point F, Point I_b and Point H. Figure reproduced from Fricker & Padman (2006).

In this thesis I focus on the use of satellite laser altimetry to examine Antarctic GL migration. In the history of spaceborne Earth observation, there have been just two satellite laser altimeters designed with the capability to measure the cryosphere – ICESat and ICESat-2 (Magruder et al., 2024). In sections 1.2.5 and 1.2.6 I provide a more detailed overview of both missions and summarise the research that has been conducted using this data to examine Antarctic grounding zones. More detailed information about other specific satellite missions used in this thesis (such as TerraSAR-X and CryoSat-2) are provided within the relevant chapters.

1.2.6. Observing grounding line migration with ICESat

NASA first pursued spaceborne laser altimetry in the mid-1990s with the development of the Ice, Cloud, and Land Elevation Satellite (ICESat) mission (Magruder et al., 2023). ICESat operated from February 2003 to October 2009 with the primary objective to detect changes in ice sheet elevation with sufficient accuracy to assess their impact on global sea level (Zwally et al., 2002). It carried the Geoscience Laser Altimeter System (GLAS) instrument, a 1064 nm laser altimeter optimised for operation over ice sheets due to its smaller footprint (~70 m) that provided high precision (<0.1 m) repeat surface elevation retrievals every ~170 m along-track (Schutz et al., 2005). Technical issues forced the operational plan to be modified so that ICESat operated in a 'campaign mode', limiting acquisitions of repeat-track data to the 33-day sub-repeat of the satellite's 91-day repeat orbit. This reduced the number of ground tracks and meant that there were just two or three campaigns per year (Schenk & Csatho, 2012).

Despite these adjustments, the ICESat mission was able to measure surface elevations under optimal conditions (flat, reflective surfaces) with a vertical precision of 3 cm (Fricker et al., 2005) and geolocation accuracy < 4.5 m (Magruder et al., 2005). Of particular relevance to this thesis, the data from ICESat led to significant advances in the study of Antarctic grounding zones. Fricker & Padman (2006) first developed the RTLA methodology using data from the ICESat mission to identify the landward and seaward limits of tidal ice shelf flexure at the Institute Ice Stream, providing GZ location and width information along each ground track (Fig. 1.5). This technique was subsequently

used to map the grounding zones (Points F, H and I_b) of the Amery Ice Shelf (Fricker et al., 2009), Ross Ice Shelf (Brunt et al., 2010b) and eventually all Antarctic ice shelves (Brunt et al., 2010a). It was shown to be particularly effective at identifying ice plains and measuring tidal GL migration (Brunt et al., 2010b, 2011). A key limitation of ICESat was that its ground tracks did not repeat exactly, but with across-track separations up to 100 m. This track offset could lead to significant differences in elevations measured between repeat cycles, especially in areas of steep topography, and there was no built-in capability to correct this using measurements of cross-track slope (Fricker & Padman, 2006). This issue limited the effectiveness of the RTLA approach in certain GZ regions and became a key consideration when designing the follow-on ICESat-2 mission.

1.2.7. Observing grounding line migration with ICESat-2

NASA launched the Ice, Cloud, and land Elevation Satellite-2 (ICESat-2) in 2018, carrying the world's first spaceborne photon counting laser altimeter: ATLAS (Advanced Topographic Laser Altimeter System). The system builds upon the success of the original ICESat mission (2003–09), aiming to measure the height of the Earth's surface in unprecedented detail, with a primary focus on the cryosphere (Markus et al., 2017).

ICESat-2 makes repeat measurements over a pre-determined set of 1387 reference ground tracks (RGTs) with a repeat cycle of 91 days (i.e., ~ four cycles per year over each track). The ATLAS instrument works by transmitting laser pulses to the Earth's surface and measuring individual photon returns, to determine along-track surface elevations (Smith et al., 2019). The transmitted laser pulse has a wavelength of 532 nm and is split into six beams configured in a 2 x 3 array, with each of the three beam pairs separated by 3.3 km – as shown in Figure 1.6. These three beam pairs collect observations in the along-track direction, and each comprise one "strong" and one "weak" beam separated by 90 m; the former containing 4x greater pulse energy (Martino et al., 2019). These six beams follow six ground tracks: GT1L, GT1R, GT2L, GT2R, GT3L and GT3R (Fig. 1.6). Each beam has a spatial footprint diameter of ~11 m and measurements are taken every 0.7 m along-track (Magruder et al., 2024). This

configuration significantly improves the repeat-track capabilities of ICESat-2, allowing for the calculation of across-track slopes, addressing a key issue of the ICESat mission (Fricker & Padman, 2006).

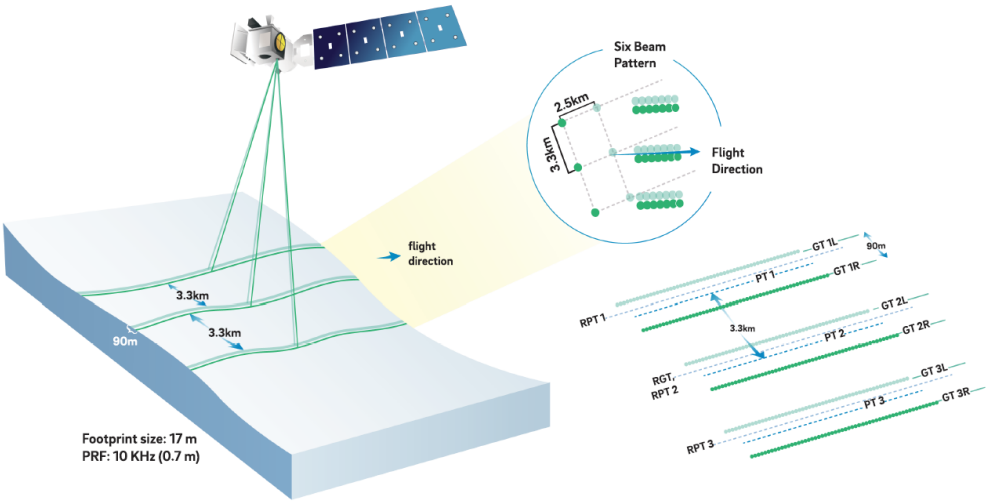


Figure 1.6. Schematic illustrating the six-beam pattern of ATLAS (Smith et al., 2019). The central Reference Pair Tracks (RPTs) follow the Reference Ground Track (RGT) that matches the nadir track of the predicted orbit. The instrument is shown here in the forward direction with "strong" beams on the right side of be beam pair (green) tracking ~2.5 km behind the "weak" beams (blue). Note the relative positions of weak and strong beams reverse when ATLAS is oriented in the backwards direction. Figure reproduced from Smith et al. (2019).

Prior to the work presented in this thesis, the only studies that have specifically used ICESat-2 data to study Antarctic grounding zones have been led by Tian Li (Li et al., 2020, 2022a, 2022b, 2023). They were the first to apply the RTLA methodology to ICESat-2 ATL06 land ice elevation data to locate GZ Points F, H and I_b. They first applied this method to all ICESat-2 ground tracks crossing the Larsen C GL (Li et al., 2020) and then expanded across Antarctica (Li et al., 2022a) to produce a continent-wide dataset of GZ Points F, H and I_b (Li et al., 2022b). This is a highly valuable and comprehensive dataset of GL location, particularly in regions where other methods provided unreliable GL estimates, and can also be used in conjunction with other datasets to identify regions of long-term GL retreat, such as at Totten and Moscow University glaciers (Li et al., 2023). However, their method is limited for studying tidal GL migration, as it identifies only a single Point F per ICESat-2 ground track.

1.3. Key grounding zone processes and knowledge gaps

Observations of grounding zones have recently been described as *"the missing key to understand ice melt in Antarctica"* (Rignot, 2023). In order to understand past, present, and future ice loss, it is vital that we understand how ice in the grounding zone and the position of the GL respond to a range of upstream and downstream forcings. Here, I introduce the current gaps in our knowledge and observational record of three particular GZ forcings, which motivate much of the work presented in this thesis: the impact of ocean tides, subglacial hydrology and the basal stress transition. These are illustrated in Figure 1.7, alongside all the satellite and airborne datasets that I use in this thesis to examine them. I will return to this schematic throughout the thesis to emphasise the connections between the research presented in each chapter.

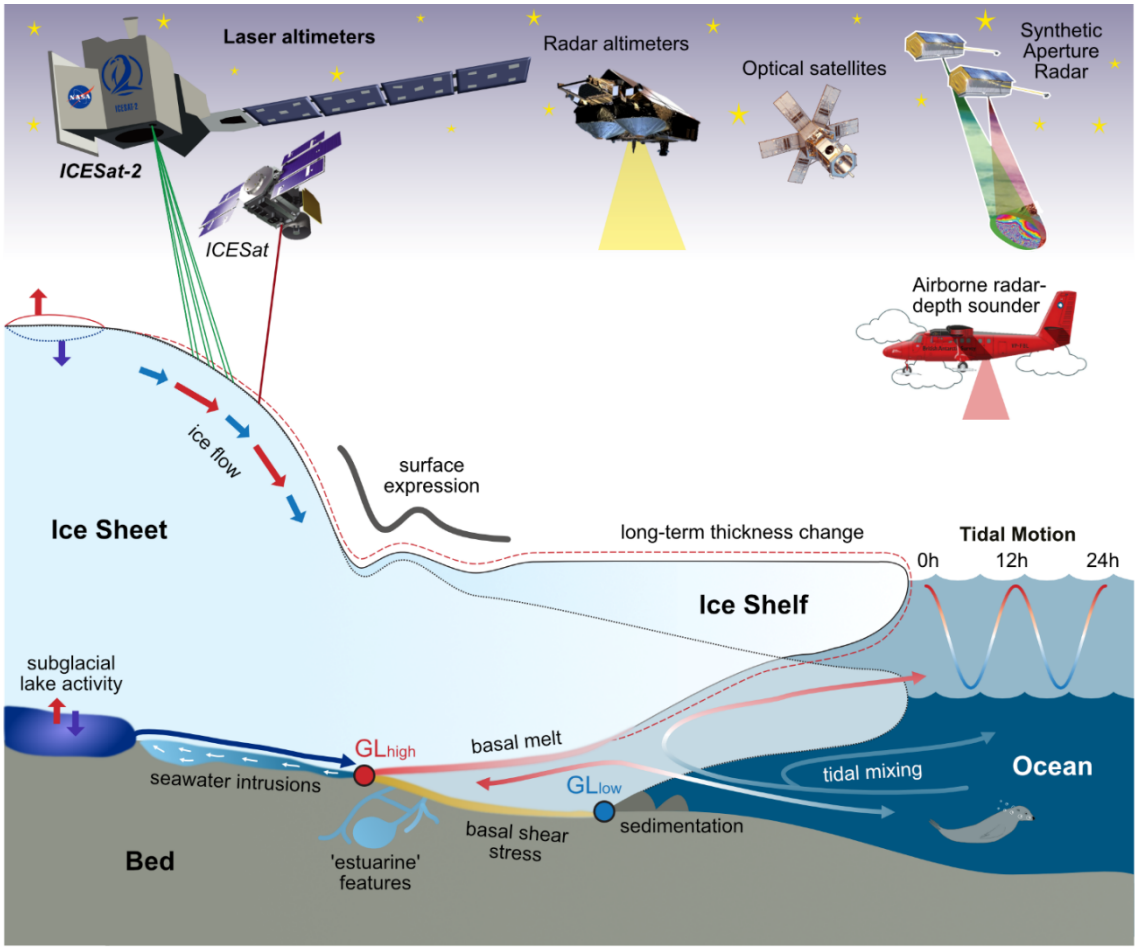


Figure 1.7. Schematic depicting the key grounding zone processes and satellite missions used in this thesis.

1.3.1. The spatial extent of tidal grounding line migration around Antarctica

Recent satellite observations, particularly from short-repeat interferometric synthetic aperture radar missions (e.g., COSMO-SkyMed-2G, Sentinel-1 and ICEYE), have revealed that GLs can migrate by several kilometres over the tidal cycle, much further than expected from hydrostatic equilibrium (Brancato et al., 2020; Chen et al., 2023; Ciracì et al., 2023; Kim et al., 2024; Milillo et al., 2017, 2019, 2022; Rignot et al., 2024; Zhong et al., 2023). However, these studies are typically limited to individual glaciers, and there is currently no comprehensive, pan-Antarctic assessment of the extent and variability of tidal GL migration. This has implications for our confidence in measurements of long-term GL advance of retreat – key indicators of broader ice dynamic changes – because it shows that these could be incorrect where obscured or superimposed with signals of tidal GL migration (Rignot et al., 2014).

This further motivates the need to quantify short-term GL variability around the entire margin of the AIS, but achieving this is currently hindered by the lack of suitable satellite data with sufficient spatial coverage and temporal resolution. Many satellites, such as Sentinel-1, do not cover the southernmost ice shelves, including large parts of the Filchner-Ronne and Ross ice shelves. Access restrictions to COSMO-SkyMed and ICEYE data further complicate this effort (Friedl et al., 2020). Additionally, maintaining interferometric coherence requires short satellite repeat times, which is challenging in rapidly changing regions like Thwaites Glacier (Milillo et al., 2019). Sampling the full tidal range, including the highest spring tides and lowest neap tides, is arguably the most crucial factor required to measure the full extent of tidal GL migration (Freer et al., 2023). This presents a significant challenge due to the limited window each month to capture these most extreme tidal states and the lack of control over the precise timing of satellite overpasses. The likelihood of sampling the full tide range increases over time as we collect more data and integrate measurements from different missions.

1.3.2. The mechanisms of tidal grounding line migration

We currently have limited understanding of the mechanisms by which tidal ice shelf flexure causes short-term migration of the GL. Various representations of tidal flexure have been modelled using elastic and viscoelastic frameworks (Holdsworth, 1969; Vaughan, 1995; Schmeltz et al., 2002; Walker et al., 2013), but only some allow for tidal GL migration. These models produce varying results, with some predicting a linear GL response to tidal forcing (e.g., Sayag & Worster, 2013) and others predicting asymmetric migration, where upstream GL migration during high tide is greater than the downstream migration during low tide (e.g., Tsai & Gudmundsson et al., 2015; Rosier & Gudmundsson, 2020; Warburton et al., 2020; Zhong et al., 2023). The chosen representation of tidal flexure and GL migration can impact the results of larger-scale modelling studies (e.g., Mosbeux et al., 2023). Although some localised in situ measurements of tidal flexure have been made to examine these mechanisms (Smith, 1991; Vaughan, 1995), there are relatively few satellite observations that adequately sample the full tide range to test and validate the models. Motivated by this, I propose using repeat track laser altimetry with ICESat-2 to test the validity of these theoretical models and improve our characterisation of tidal GL behaviour.

1.3.3. The impact of tidal grounding line migration on basal melt rates

Tides enhance basal melt of ice shelves (Padman et al., 2018) and account for ~4% of the total basal ice loss from the AIS (Richter et al., 2022). Tidal currents energise the flow and ocean mixing in the sub-ice shelf cavity, enhancing the turbulent exchange of heat and salt in the ice-ocean boundary layer (Mueller et al., 2012). As the GL migrates over the tidal cycle, it allows pressurised seawater to flush back and forth within the grounding zone at high entrainment speeds, directly melting the grounded ice (Ciracì et al., 2023; Warburton et al., 2020; Horgan et al., 2013; Milillo et al., 2017). These kinds of seawater intrusions could have significant, yet currently overlooked, implications on ice sheet dynamics (Bradley & Hewitt, 2024; Robel et al., 2022). Evidence from the palaeo record at Thwaites Glacier indicates that past rates of GL retreat were twice as high during spring tide phases compared to neap tide phases, attributed to the enhanced tidal mixing and basal melt within the GZ during spring tides when the GL migrated further

upstream (Graham et al., 2022). This underscores the importance of better constraining the present location and extent of tidal GL migration around Antarctica, as it may identify regions vulnerable to future retreat.

1.3.4. The impact of tidal grounding line migration on basal drag and ice flow

In areas experiencing tidal GL migration, basal drag should decrease at high tide as more of the ice shelf area lifts from the bed. This can modulate buttressing stresses exerted on the upstream grounded ice (Robel et al., 2017) and lead to ice flow acceleration on tidal timescales, as has been observed at several locations in Antarctica (e.g., Anandakrishnan et al., 2003; Bindschadler et al., 2003; Brancato et al., 2020; Marsh et al., 2013; Rack et al., 2017). As a specific example, the presence of tides was found to enhance ice flow across the entire Filchner-Ronne Ice Shelf by 21% (Rosier & Gudmundsson, 2020). Again, the extent to which ice dynamics are impacted by tidal grounding zones processes around the AIS margins remains insufficiently constrained for accurate representation in large-scale ice sheet models.

1.3.5. Impact of subglacial hydrology on basal melt rates and tidal grounding line migration

The routing of subglacial water across the grounding zone contributes to the fluxes of freshwater entering the ice shelf cavity, which has been shown to increase localised basal melt rates (Marsh et al., 2016; Pelle et al., 2023) leading to ice shelf thinning and reduced grounding zone stability (e.g., Fricker et al., 2007). Additionally, the permeability of the subglacial hydrological network has been proposed as a key influence on the dynamics of tidal GL migration (Warburton et al., 2020): low permeability can lead to seawater at high tide becoming trapped and draining more slowly on a falling tide, leading to an asymmetric pattern of tidal GL migration. However, these properties are almost impossible to observe – either in-situ or using remote sensing techniques – due to the difficulty of access beneath multiple kilometres of ice (Priscu et al., 2021; Siegfried & Fricker, 2021; Siegfried et al., 2023).

1.3.6. Impact of upstream subglacial lake drainage on grounding zone dynamics

The volume of water flowing across the grounding zone, and therefore the capacity for basal melt, increases significantly in the event that a subglacial lake upstream begins to drain (Le Brocq et al., 2013; Marsh et al., 2016). Recent advances in satellite altimetry have provided direct observations of active subglacial lake fill-and-drain cycles by identifying the associated patterns of surface uplift and subsidence (e.g., Fricker et al., 2007, 2014, 2016; Malczyk et al., 2020; Siegfried & Fricker, 2021; Stubblefield et al., 2023). Despite this, active subglacial lakes remain one of the major physical uncertainties on projections of future ice sheet dynamics and sea-level rise (Siegfried & Fricker, 2021; S. Sun et al., 2020). In particular, key questions remain regarding the triggers and mechanisms of subglacial lake drainage (Siegfried et al., 2023) and the influence of drainage on grounding zone dynamics – specifically how it may affect basal friction, GL retreat, localised ice shelf melt rates and sediment transport (Carter et al., 2017; Fricker & Scambos, 2009; Simkins et al., 2017).

1.3.7. Challenge of locating the basal stress transition

The location of the sharp change in basal shear stress at the GL is an important boundary condition for large-scale ice sheet models (Schoof, 2007), but is challenging to precisely locate. The discontinuity in vertical velocity across this basal transition can cause surface undulations – termed "wave-like surface features" by Schoof (2011) – to develop across the GZ, as have been observed in several settings (e.g., Anandakrishnan et al., 2007; Chartrand & Howat, 2023; Hulbe et al., 2016; Swithinbank, 1955; Vaughan, 1994). Various process models have attempted to resolve this surface profile across the GZ using a range of viscoelastic frameworks (e.g., Barcilon & MacAyeal, 1993; Chugunov & Wilchinsky, 1996; Durand et al., 2009; Nowicki & Wingham, 2008; Sayag & Worster, 2011, 2013; Schoof, 2007, 2011; Weertman, 1974). Where successful, the theory should directly relate the location of the "wave-like surface feature" to the location of the basal stress transition – the boundary condition we want to know – which could be used to improve its representation in large-scale ice sheet models. However, the distribution and geometry of these features around Antarctica is currently unknown.

1.3.8. Uncertain ice thickness estimates in the grounding zone

Satellite-derived estimates of ice thickness and basal melt rate within GZs are subject to large uncertainties due to the breakdown of the hydrostatic assumption (Chuter & Bamber, 2015; Griggs & Bamber, 2011; Kim et al., 2024), which often leads to these regions being masked out (e.g., Griggs & Bamber, 2011; Paolo et al., 2015; Wilson et al., 2017) or interpolated across (e.g., Fretwell et al., 2013; Morlighem et al., 2020). These uncertainties are increased where this wave-like surface feature associated with the basal stress transition appears, causing ice to deviate further from hydrostatic equilibrium (Chartrand & Howat, 2023; Chuter & Bamber, 2015; Griggs & Bamber, 2011; Jenkins et al., 2006; Milillo et al., 2019). Ice sheet models projecting future ice sheet dynamics and sea level rise are very sensitive to these parameters (Arthern & Williams, 2017; Goldberg et al., 2019), therefore it is critical that we improve our ability to resolve ice thickness gradients across Antarctic grounding zones.

1.4. Knowledge gaps lead to uncertainty in future ice sheet and sea level projections

Very few of the GZ processes outlined above are accounted for in numerical ice sheet models, which typically use a fixed GL position determined by flotation conditions alone (eq. 1), assume zero melt at the GL, and lack any representation of subglacial hydrology (Favier et al., 2014; Milillo et al., 2017; Dow, 2022). Given that ice sheet models are particularly sensitive to any changes in the grounding zone, these limitations may compromise the accuracy of projections of future ice sheet evolution and sea-level rise (Fig. 1.8). However, representing these processes in models is an ongoing challenge that necessitates improvements in both our process understanding – currently hindered by the scarcity of observations within grounding zones (Rignot, 2023) – and the capability of models to represent these processes numerically at appropriate spatial and temporal scales (Burgard et al., 2022).

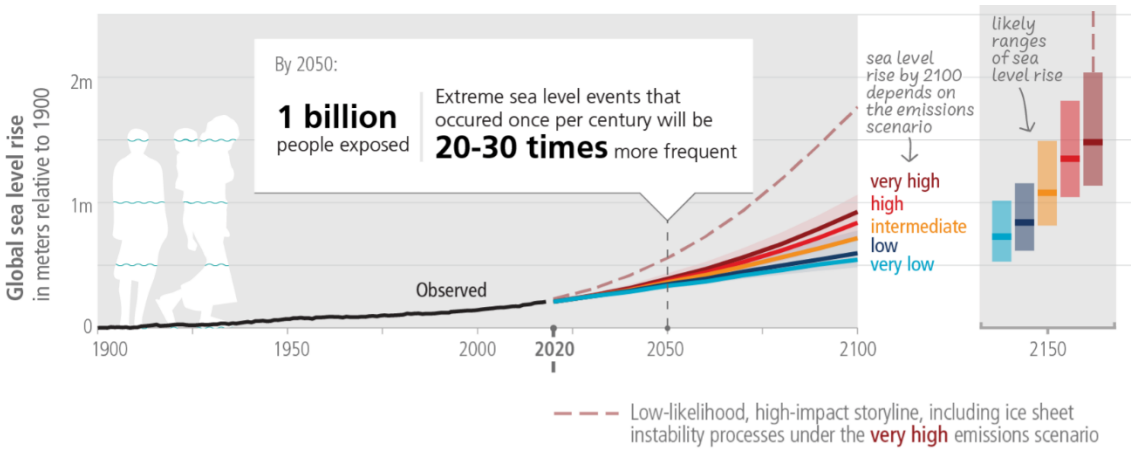


Figure 1.8. Observed and projected future global mean sea level change relative to 1900, for a range of greenhouse gas emissions scenarios. Dashed red lines: low-likelihood, high impact storyline, including ice sheet instability processes. Figure reproduced from Intergovernmental Panel on Climate Change AR6 synthesis report (IPCC, 2023b).

1.5. Aims and Objectives

This thesis aims to use satellite laser altimetry in combination with other satellite datasets to improve understanding of the patterns and drivers of GL migration in Antarctica, over a range of time-scales.

This will be achieved through the following objectives:

1. Develop a new method using high-resolution repeat-track data from the ICESat-2 mission to improve observations of horizontal GL location on tidal timescales.
2. Apply this technique to grounding zones in Antarctica to measure the extent of tidal GL migration and examine different patterns of short-term tidal GZ behaviour.
3. Use a combination of satellite laser altimetry, radar altimetry, synthetic aperture radar and high-resolution digital elevation models to examine the interactions between subglacial hydrology and GL migration during a subglacial lake drainage event.
4. Use high-resolution digital elevation model and ICESat-2 data in combination with viscous beam theory to examine the long-term surface expression of the basal stress transition at Antarctic grounding zones, and better constrain the estimated GL location and ice thickness within these regions.

1.6. Thesis structure

The remainder of the thesis seeks to fulfil these objectives and is structured as follows: in Chapter 2, I present a novel method that uses repeat-track laser altimetry with ICESat-2 alongside a regional tide model to increase the tidal sampling of GL migration, which allows us to locate the GL at individual tidal states. Using this method, I measure the total extent of tidal GL migration at an ice plain on the Ronne Ice Shelf, and identify four distinct modes of tidal GL migration. In Chapter 3, I present a 21-year time series of subglacial lake activity at Engelhardt Subglacial Lake in West Antarctica, compiled using ICESat, ICESat-2 and CryoSat-2 altimetry. I document, for the first time, the second drainage of this lake on record, which began in July 2021. Additionally, I detect up to 13 km of GL retreat downstream of the lake over the same period, using a combination of ICESat-2, DInSAR and high-resolution DEM data, and explore the relationship between the GL retreat and the lake drainage. In Chapter 4, I map the spatial distribution of the wave-like surface feature associated with the basal stress transition around the entire Ross Ice Shelf grounding zone, utilising surface elevation profiles from a high-resolution DEM and ICESat-2. I examine how satellite observations of these features, combined with viscous beam theory, can improve estimates of GL location, basal properties and ice thickness in Antarctic grounding zones. In Chapter 5, I synthesise the thesis findings, put them in a wider context and discuss potential avenues for future research.

References

Adhikari, S., Ivins, E. R., Larour, E., Seroussi, H., Morlighem, M., & Nowicki, S. (2014). Future Antarctic bed topography and its implications for ice sheet dynamics. *Solid Earth*, *5*(1), 569–584. https://doi.org/10.5194/se-5-569-2014

Adusumilli, S., Fricker, H. A., Medley, B., Padman, L., & Siegfried, M. R. (2020). Interannual variations in meltwater input to the Southern Ocean from Antarctic ice shelves. *Nature Geoscience, 13(*9), 616–620. https://doi.org/10.1038/s41561-020-0616-z

Anandakrishnan, S., Voigt, D. E., Alley, R. B., & King, M. A. (2003). Ice stream D flow speed is strongly modulated by the tide beneath the Ross Ice Shelf. *Geophysical Research Letters, 30*(7). https://doi.org/10.1029/2002GL016329

Anandakrishnan, S., Catania, G. A., Alley, R. B., & Horgan, H. J. (2007). Discovery of Till Deposition at the Grounding Line of Whillans Ice Stream. *Science, 315*(5820), 1835–1838. https://doi.org/10.1126/science.1138393

Arthern, R. J., & Williams, C. R. (2017). The sensitivity of West Antarctica to the submarine melting feedback. *Geophysical Research Letters, 44*(5), 2352–2359. https://doi.org/10.1002/2017GL072514

Aschwanden, A., Bartholomaus, T. C., Brinkerhoff, D. J., & Truffer, M. (2021). Brief communication: A roadmap towards credible projections of ice sheet contribution to sea level. *The Cryosphere, 15*(12), 5705–5715. https://doi.org/10.5194/tc-15-5705-2021

Bamber, J., & Bentley, C. (1994). A comparison of satellite-altimetry and ice-thickness measurements of the Ross Ice Shelf, Antarctica. *Annals of Glaciology, 20*, 357–364. https://doi.org/10.3189/1994AoG20-1-357-364

Barcilon, V., & MacAyeal, D. R. (1993). Steady flow of a viscous ice stream across a no-slip/free-slip transition at the bed. *Journal of Glaciology, 39*(131), 167–185. https://doi.org/10.3189/S0022143000015811

Bindschadler, R., Choi, H., Wichlacz, A., Bingham, R., Bohlander, J., Brunt, K., et al. (2011). Getting around Antarctica: new high-resolution mappings of the grounded and freely-floating boundaries of the Antarctic ice sheet created for the International Polar Year. *The Cryosphere, 5*(3), 569–588. https://doi.org/10.5194/tc-5-569-2011

Bindschadler, R. (1993). Siple Coast Project research of Crary Ice Rise and the mouths of Ice Streams B and C, West Antarctica: review and new perspectives. *Journal of Glaciology, 39*(133), 538–552. https://doi.org/10.3189/S0022143000016439

Bojinski, S., Verstraete, M., Peterson, T. C., Richter, C., Simmons, A., & Zemp, M. (2014). The Concept of Essential Climate Variables in Support of Climate Research, Applications, and Policy. *Bulletin of the American Meteorological Society, 95*(9), 1431–1443. https://doi.org/10.1175/BAMS-D-13-00047.1

Bradley, A. T. & Hewitt, I. J. (2024) Tipping point in ice-sheet grounding-zone melting due to ocean water intrusion. *Nature Geoscience*. https://doi.org/10.1038/s41561-024-01465-7

Brancato, V., Rignot, E., Milillo, P., Morlighem, M., Mouginot, J., An, L., et al. (2020). Grounding Line Retreat of Denman Glacier, East Antarctica, Measured With COSMO-SkyMed Radar Interferometry Data. *Geophysical Research Letters, 47*(7). https://doi.org/10.1029/2019GL086291

Brunt, K., Fricker, H. A., O'Neel, S., & Padman, L. (2010) ICESat-Derived Grounding Zone for Antarctic Ice Shelves (Version 1) [Dataset]. U.S. Antarctic Program (USAP) Data Center. https://doi.org/10.7265/N5CF9N19.

Brunt, K. M., Fricker, H. A., Padman, L., Scambos, T. A., & O'Neel, S. (2010). Mapping the grounding zone of the Ross Ice Shelf, Antarctica, using ICESat laser altimetry. *Annals of Glaciology, 51*(55), 71–79. https://doi.org/10.3189/172756410791392790

Brunt, K. M., Fricker, H. A., & Padman, L. (2011). Analysis of ice plains of the Filchner–Ronne Ice Shelf, Antarctica, using ICESat laser altimetry. *Journal of Glaciology, 57*(205), 965–975. https://doi.org/10.3189/002214311798043753

Burgard, C., Jourdain, N. C., Reese, R., Jenkins, A., & Mathiot, P. (2022). An assessment of basal melt parameterisations for Antarctic ice shelves. *The Cryosphere, 16*(12), 4931–4975. https://doi.org/10.5194/tc-16-4931-2022

Carter, S. P., Fricker, H. A., & Siegfried, M. R. (2017). Antarctic subglacial lakes drain through sediment-floored canals: theory and model testing on real and idealized domains. *The Cryosphere, 11*(1), 381–405. https://doi.org/10.5194/tc-11-381-2017

Catania, G., Hulbe, C., & Conway, H. (2010). Grounding-line basal melt rates determined using radar-derived internal stratigraphy. *Journal of Glaciology, 56*(197), 545–554. https://doi.org/10.3189/002214310792447842

Chartrand, A. M., & Howat, I. M. (2023). A comparison of contemporaneous airborne altimetry and ice-thickness measurements of Antarctic ice shelves. *Journal of Glaciology*, 1–14. https://doi.org/10.1017/jog.2023.49

Chen, H., Rignot, E., Scheuchl, B., & Ehrenfeucht, S. (2023). Grounding Zone of Amery Ice Shelf, Antarctica, From Differential Synthetic-Aperture Radar Interferometry.

Geophysical Research Letters, 50(6), e2022GL102430. https://doi.org/10.1029/2022GL102430

Christie, F. D. W., Bingham, R. G., Gourmelen, N., Tett, S. F. B., & Muto, A. (2016). Four-decade record of pervasive grounding line retreat along the Bellingshausen margin of West Antarctica. *Geophysical Research Letters, 43*(11), 5741–5749. https://doi.org/10.1002/2016GL068972

Chugunov, V. A., & Wilchinsky, A. V. (1996). Modelling of a marine glacier and ice-sheet-ice-shelf transition zone based on asymptotic analysis. *Annals of Glaciology, 23*, 59–67. https://doi.org/10.3189/S0260305500013264

Chuter, S. J., & Bamber, J. L. (2015). Antarctic ice shelf thickness from CryoSat-2 radar altimetry. *Geophysical Research Letters, 42*(24), 10,721-10,729. https://doi.org/10.1002/2015GL066515

Ciracì, E., Rignot, E., Scheuchl, B., Tolpekin, V., Wollersheim, M., An, L., et al. (2023). Melt rates in the kilometer-size grounding zone of Petermann Glacier, Greenland, before and during a retreat. *Proceedings of the National Academy of Sciences, 120*(20), e2220924120. https://doi.org/10.1073/pnas.2220924120

Cook, A. J., Holland, P. R., Meredith, M. P., Murray, T., Luckman, A., & Vaughan, D. G. (2016). Ocean forcing of glacier retreat in the western Antarctic Peninsula. *Science, 353*(6296), 283–286. https://doi.org/10.1126/science.aae0017

Corr, H. F. J., Doake, C. S. M., Jenkins, A., & Vaughan, D. G. (2001). Investigations of an "ice plain" in the mouth of Pine Island Glacier, Antarctica. *Journal of Glaciology, 47*(156), 51–57. https://doi.org/10.3189/172756501781832395

Dawson, G. J., & Bamber, J. L. (2017). Antarctic Grounding Line Mapping From CryoSat-2 Radar Altimetry. *Geophysical Research Letters, 44*(23), 11,886-11,893. https://doi.org/10.1002/2017GL075589

Dawson, G. J., & Bamber, J. L. (2020). Measuring the location and width of the Antarctic grounding zone using CryoSat-2. *The Cryosphere, 14*(6), 2071–2086. https://doi.org/10.5194/tc-14-2071-2020

Depoorter, M. A., Bamber, J. L., Griggs, J. A., Lenaerts, J. T. M., Ligtenberg, S. R. M., van den Broeke, M. R., & Moholdt, G. (2013). Calving fluxes and basal melt rates of Antarctic ice shelves. *Nature, 502*(7469), 89–92. https://doi.org/10.1038/nature12567

Dinniman, M., Asay-Davis, X., Galton-Fenzi, B., Holland, P., Jenkins, A., & Timmermann, R. (2016). Modeling Ice Shelf/Ocean Interaction in Antarctica: A Review. *Oceanography, 29*(4), 144–153. https://doi.org/10.5670/oceanog.2016.106

Docquier, D., Perichon, L., & Pattyn, F. (2011). Representing Grounding Line Dynamics in Numerical Ice Sheet Models: Recent Advances and Outlook. *Surveys in Geophysics, 32*(4–5), 417–435. https://doi.org/10.1007/s10712-011-9133-3

Dow, C. F. (2022). The role of subglacial hydrology in Antarctic ice sheet dynamics and stability: a modelling perspective. *Annals of Glaciology, 63*(87–89), 49–54. https://doi.org/10.1017/aog.2023.9

Durand, G., Gagliardini, O., de Fleurian, B., Zwinger, T., & Le Meur, E. (2009). Marine ice sheet dynamics: Hysteresis and neutral equilibrium. *Journal of Geophysical Research, 114*(F3), F03009. https://doi.org/10.1029/2008JF001170

Dutrieux, P., De Rydt, J., Jenkins, A., Holland, P. R., Ha, H. K., Lee, S. H., et al. (2014). Strong Sensitivity of Pine Island Ice-Shelf Melting to Climatic Variability. *Science, 343*(6167), 174–178. https://doi.org/10.1126/science.1244341

Edwards, T. L., Nowicki, S., Marzeion, B., Hock, R., Goelzer, H., Seroussi, H., et al. (2021). Projected land ice contributions to twenty-first-century sea level rise. *Nature, 593*(7857), 74–82. https://doi.org/10.1038/s41586-021-03302-y

Favier, L., Durand, G., Cornford, S. L., Gudmundsson, G. H., Gagliardini, O., Gillet-Chaulet, F., et al. (2014). Retreat of Pine Island Glacier controlled by marine ice-sheet instability. *Nature Climate Change, 4*(2), 117–121. https://doi.org/10.1038/nclimate2094

Fretwell, P., Pritchard, H. D., Vaughan, D. G., Bamber, J. L., Barrand, N. E., Bell, R., et al. (2013). Bedmap2: improved ice bed, surface and thickness datasets for Antarctica. *The Cryosphere, 7*(1), 375–393. https://doi.org/10.5194/tc-7-375-2013

Fricker, H. A., Siegfried, M. R., Carter, S. P., & Scambos, T. A. (2016). A decade of progress in observing and modelling Antarctic subglacial water systems. *Philosophical Transactions of the Royal Society A: Mathematical, Physical and Engineering Sciences, 374*(2059), 20140294. https://doi.org/10.1098/rsta.2014.0294

Fricker, H. A., & Padman, L. (2006). Ice shelf grounding zone structure from ICESat laser altimetry. *Geophysical Research Letters, 33*(15), L15502. https://doi.org/10.1029/2006GL026907

Fricker, H. A., & Scambos, T. (2009). Connected subglacial lake activity on lower Mercer and Whillans Ice Streams, West Antarctica, 2003–2008. *Journal of Glaciology, 55*(190), 303–315. https://doi.org/10.3189/002214309788608813

Fricker, H. A., Scambos, T., Bindschadler, R., & Padman, L. (2007). An Active Subglacial Water System in West Antarctica Mapped from Space. *Science, 315*(5818), 1544–1548. https://doi.org/10.1126/science.1136897

Fricker, H. A., Coleman, R., Padman, L., Scambos, T. A., Bohlander, J., & Brunt, K. M. (2009). Mapping the grounding zone of the Amery Ice Shelf, East Antarctica using InSAR, MODIS and ICESat. *Antarctic Science, 21*(5), 515–532. https://doi.org/10.1017/S095410200999023X

Fricker, H. A., Carter, S. P., Bell, R. E., & Scambos, T. (2014). Active lakes of Recovery Ice Stream, East Antarctica: a bedrock-controlled subglacial hydrological system. *Journal of Glaciology, 60*(223), 1015–1030. https://doi.org/10.3189/2014JoG14J063

Friedl, P., Seehaus, T. C., Wendt, A., Braun, M. H., & Höppner, K. (2018). Recent dynamic changes on Fleming Glacier after the disintegration of Wordie Ice Shelf, Antarctic Peninsula. *The Cryosphere, 12*(4), 1347–1365. https://doi.org/10.5194/tc-12-1347-2018

Friedl, P., Weiser, F., Fluhrer, A., & Braun, M. H. (2020). Remote sensing of glacier and ice sheet grounding lines: A review. *Earth-Science Reviews, 201*, 102948. https://doi.org/10.1016/j.earscirev.2019.102948

Goldberg, D., Holland, D. M., & Schoof, C. (2009). Grounding line movement and ice shelf buttressing in marine ice sheets. *Journal of Geophysical Research: Earth Surface, 114*(F4), 2008JF001227. https://doi.org/10.1029/2008JF001227

Goldberg, D. N., Gourmelen, N., Kimura, S., Millan, R., & Snow, K. (2019). How Accurately Should We Model Ice Shelf Melt Rates? *Geophysical Research Letters, 46*(1), 189–199. https://doi.org/10.1029/2018GL080383

Graham, A. G. C., Wåhlin, A., Hogan, K. A., Nitsche, F. O., Heywood, K. J., Totten, R. L., et al. (2022). Rapid retreat of Thwaites Glacier in the pre-satellite era. *Nature Geoscience, 15*, 706–713. https://doi.org/10.1038/s41561-022-01019-9

Griggs, J. A., & Bamber, J. L. (2011). Antarctic ice-shelf thickness from satellite radar altimetry. *Journal of Glaciology, 57*(203), 485–498. https://doi.org/10.3189/002214311796905659

Gudmundsson, G. H., Paolo, F. S., Adusumilli, S., & Fricker, H. A. (2019). Instantaneous Antarctic ice sheet mass loss driven by thinning ice shelves. *Geophysical Research Letters, 46*(23), 13903–13909. https://doi.org/10.1029/2019GL085027

Hogg, A. E., Shepherd, A., Gilbert, L., Muir, A., & Drinkwater, M. R. (2018). Mapping ice sheet grounding lines with CryoSat-2. *Advances in Space Research, 62*(6), 1191–1202. https://doi.org/10.1016/j.asr.2017.03.008

Holdsworth, G. (1969). Flexure of a Floating Ice Tongue. *Journal of Glaciology, 8*(54), 385–397. https://doi.org/10.3189/S0022143000026976

Horgan, H. J., & Anandakrishnan, S. (2006). Static grounding lines and dynamic ice streams: Evidence from the Siple Coast, West Antarctica. *Geophysical Research Letters, 33*(18). https://doi.org/10.1029/2006GL027091

Horgan, H. J., Alley, R. B., Christianson, K., Jacobel, R. W., Anandakrishnan, S., Muto, A., et al. (2013). Estuaries beneath ice sheets. *Geology, 41*(11), 1159–1162. https://doi.org/10.1130/G34654.1

Hulbe, C. L., Klinger, M., Masterson, M., Catania, G., Cruikshank, K., & Bugni, A. (2016). Tidal bending and strand cracks at the Kamb Ice Stream grounding line, West Antarctica. *Journal of Glaciology, 62*(235), 816–824. https://doi.org/10.1017/jog.2016.74

Intergovernmental Panel on Climate Change (IPCC) (2023a). Ocean, Cryosphere and Sea Level Change. In *Climate Change 2021 – The Physical Science Basis: Working Group I Contribution to the Sixth Assessment Report of the Intergovernmental Panel on Climate Change* (pp. 1211–1362). Cambridge: Cambridge University Press. https://doi.org/10.1017/9781009157896.011

Intergovernmental Panel on Climate Change (IPCC) (2023b) Sections. In Core Writing Team, H. Lee and J. Romero (Eds.) *Climate Change 2023: Synthesis Report. Contribution of Working Groups I, II and III to the Sixth Assessment Report of the Intergovernmental Panel on Climate Change* (pp. 35–115). IPCC, Geneva, Switzerland. doi: 10.59327/IPCC/AR6-9789291691647.

Jenkins, A., Corr, H. F. J., Nicholls, K. W., Stewart, C. L., & Doake, C. S. M. (2006). Interactions between ice and ocean observed with phase-sensitive radar near an Antarctic ice-shelf grounding line. *Journal of Glaciology, 52*(178), 325–346. https://doi.org/10.3189/172756506781828502

Joughin, I., Alley, R. B., & Holland, D. M. (2012). Ice-Sheet Response to Oceanic Forcing. *Science, 338*(6111), 1172–1176. https://doi.org/10.1126/science.1226481

Joughin, I., Smith, B. E., & Holland, D. M. (2010). Sensitivity of 21st century sea level to ocean-induced thinning of Pine Island Glacier, Antarctica. *Geophysical Research Letters, 37*(20). https://doi.org/10.1029/2010GL044819

Khazendar, A., Rignot, E., Schroeder, D. M., Seroussi, H., Schodlok, M. P., Scheuchl, B., et al. (2016). Rapid submarine ice melting in the grounding zones of ice shelves in West Antarctica. *Nature Communications, 7*(1), 13243. https://doi.org/10.1038/ncomms13243

Kim, J. H., Rignot, E., Holland, D., & Holland, D. (2024). Seawater Intrusion at the Grounding Line of Jakobshavn Isbræ, Greenland, From Terrestrial Radar

Interferometry. *Geophysical Research Letters, 51*(6), e2023GL106181. https://doi.org/10.1029/2023GL106181

Konrad, H., Shepherd, A., Gilbert, L., Hogg, A. E., McMillan, M., Muir, A., & Slater, T. (2018). Net retreat of Antarctic glacier grounding lines. *Nature Geoscience, 11*(4), 258–262. https://doi.org/10.1038/s41561-018-0082-z

Le Brocq, A. M., Ross, N., Griggs, J. A., Bingham, R. G., Corr, H. F. J., Ferraccioli, F., et al. (2013). Evidence from ice shelves for channelized meltwater flow beneath the Antarctic Ice Sheet. *Nature Geoscience, 6*(11), 945–948. https://doi.org/10.1038/ngeo1977

Li, T., Dawson, G. J., Chuter, S. J., & Bamber, J. L. (2020). Mapping the grounding zone of Larsen C Ice Shelf, Antarctica, from ICESat-2 laser altimetry. *The Cryosphere, 14*(11), 3629–3643. https://doi.org/10.5194/tc-14-3629-2020

Li, T., Dawson, G. J., Chuter, S. J., & Bamber, J. L. (2022). A high-resolution Antarctic grounding zone product from ICESat-2 laser altimetry. *Earth System Science Data, 14*(2), 535–557. https://doi.org/10.5194/essd-14-535-2022

Li, T., Dawson, G. J., Chuter, S. J., & Bamber, J. L. (2022). ICESat-2 L3 Grounding Zone for Antarctic Ice Shelves (Version 1) [Dataset]. NASA National Snow and Ice Data Center Distributed Active Archive Center. https://doi.org/10.5067/RI67B92708M9

Li, T., Dawson, G. J., Chuter, S. J., & Bamber, J. L. (2023). Grounding line retreat and tide-modulated ocean channels at Moscow University and Totten Glacier ice shelves, East Antarctica. *The Cryosphere, 17*(2), 1003–1022. https://doi.org/10.5194/tc-17-1003-2023

Luckman, A., Elvidge, A., Jansen, D., Kulessa, B., Munneke, P. K., King, J., & Barrand, N. E. (2014). Surface melt and ponding on Larsen C Ice Shelf and the impact of föhn winds. *Antarctic Science, 26*(6), 625–635. https://doi.org/10.1017/S0954102014000339

MacGregor, J. A., Anandakrishnan, S., Catania, G. A., & Winebrenner, D. P. (2011). The grounding zone of the Ross Ice Shelf, West Antarctica, from ice-penetrating radar. *Journal of Glaciology, 57*(205), 917–928. https://doi.org/10.3189/002214311798043780

Magruder, L. A., Farrell, S. L., Neuenschwander, A., Duncanson, L., Csatho, B., Kacimi, S., & Fricker, H. A. (2024). Monitoring Earth's climate variables with satellite laser altimetry. *Nature Reviews Earth & Environment, 5*(2), 120–136. https://doi.org/10.1038/s43017-023-00508-8

Malczyk, G., Gourmelen, N., Goldberg, D., Wuite, J., & Nagler, T. (2020). Repeat Subglacial Lake Drainage and Filling Beneath Thwaites Glacier. *Geophysical Research Letters, 47*(23), e2020GL089658. https://doi.org/10.1029/2020GL089658

Markus, T., Neumann, T., Martino, A., Abdalati, W., Brunt, K., Csatho, B., et al. (2017). The Ice, Cloud, and land Elevation Satellite-2 (ICESat-2): Science requirements, concept, and implementation. *Remote Sensing of Environment, 190*, 260–273. https://doi.org/10.1016/j.rse.2016.12.029

Marsh, O. J., Rack, W., Floricioiu, D., Golledge, N. R., & Lawson, W. (2013). Tidally induced velocity variations of the Beardmore Glacier, Antarctica, and their representation in satellite measurements of ice velocity. *The Cryosphere, 7*(5), 1375–1384. https://doi.org/10.5194/tc-7-1375-2013

Marsh, O. J., Fricker, H. A., Siegfried, M. R., Christianson, K., Nicholls, K. W., Corr, H. F. J., & Catania, G. (2016). High basal melting forming a channel at the grounding line of Ross Ice Shelf, Antarctica. *Geophysical Research Letters, 43*(1), 250–255. https://doi.org/10.1002/2015GL066612

Martino, A. J., Neumann, T. A., Kurtz, N. T., & McLennan, D. (2019). ICESat-2 mission overview and early performance. *Proceedings of the SPIE, 11151*, 111510C. https://doi.org/10.1117/12.2534938

Milillo, P., Rignot, E., Rizzoli, P., Scheuchl, B., Mouginot, J., Bueso-Bello, J., & Prats-Iraola, P. (2019). Heterogeneous retreat and ice melt of Thwaites Glacier, West Antarctica. *Science Advances, 5*(1), eaau3433. https://doi.org/10.1126/sciadv.aau3433

Milillo, P., Rignot, E., Rizzoli, P., Scheuchl, B., Mouginot, J., Bueso-Bello, J. L., et al. (2022). Rapid glacier retreat rates observed in West Antarctica. *Nature Geoscience, 15*(1), 48–53. https://doi.org/10.1038/s41561-021-00877-z

Milillo, P., Rignot, E., Mouginot, J., Scheuchl, B., Morlighem, M., Li, X., & Salzer, J. T. (2017). On the Short-term Grounding Zone Dynamics of Pine Island Glacier, West Antarctica, Observed With COSMO-SkyMed Interferometric Data. *Geophysical Research Letters, 44*(20), 10,436-10,444. https://doi.org/10.1002/2017GL074320

Minchew, B. M., Simons, M., Riel, B., & Milillo, P. (2017). Tidally induced variations in vertical and horizontal motion on Rutford Ice Stream, West Antarctica, inferred from remotely sensed observations. *Journal of Geophysical Research: Earth Surface, 122*(1), 167–190. https://doi.org/10.1002/2016JF003971

Mohajerani, Y., Jeong, S., Scheuchl, B., Velicogna, I., Rignot, E., & Milillo, P. (2021). Automatic delineation of glacier grounding lines in differential interferometric synthetic-aperture radar data using deep learning. *Scientific Reports, 11*(1), 4992. https://doi.org/10.1038/s41598-021-84309-3

Morlighem, M., Rignot, E., Binder, T., Blankenship, D., Drews, R., Eagles, G., et al. (2020). Deep glacial troughs and stabilizing ridges unveiled beneath the margins of the Antarctic ice sheet. *Nature Geoscience, 13*(2), 132–137. https://doi.org/10.1038/s41561-019-0510-8

Mosbeux, C., Padman, L., Klein, E., Bromirski, P. D., & Fricker, H. A. (2023). Seasonal variability in Antarctic ice shelf velocities forced by sea surface height variations. *The Cryosphere, 17*(7), 2585–2606. https://doi.org/10.5194/tc-17-2585-2023

Mouginot, J., Rignot, E., & Scheuchl, B. (2014). Sustained increase in ice discharge from the Amundsen Sea Embayment, West Antarctica, from 1973 to 2013. *Geophysical Research Letters, 41*(5), 1576–1584. https://doi.org/10.1002/2013GL059069

Mueller, R. D., Padman, L., Dinniman, M. S., Erofeeva, S. Y., Fricker, H. A., & King, M. A. (2012). Impact of tide-topography interactions on basal melting of Larsen C Ice Shelf, Antarctica. *Journal of Geophysical Research: Oceans, 117*(C5). https://doi.org/10.1029/2011JC007263

Nowicki, S. M. J., & Wingham, D. J. (2008). Conditions for a steady ice sheet–ice shelf junction. *Earth and Planetary Science Letters, 265*(1), 246–255. https://doi.org/10.1016/j.epsl.2007.10.018

Otosaka, I. N., Shepherd, A., Ivins, E. R., Schlegel, N.-J., Amory, C., van den Broeke, M. R., et al. (2023). Mass balance of the Greenland and Antarctic ice sheets from 1992 to 2020. *Earth System Science Data, 15*(4), 1597–1616. https://doi.org/10.5194/essd-15-1597-2023

Padman, L., Siegfried, M. R., & Fricker, H. A. (2018). Ocean Tide Influences on the Antarctic and Greenland Ice Sheets. *Reviews of Geophysics, 56*(1), 142–184. https://doi.org/10.1002/2016RG000546

Paolo, F. S., Fricker, H. A., & Padman, L. (2015). Volume loss from Antarctic ice shelves is accelerating. *Science, 348*(6232), 327–331. https://doi.org/10.1126/science.aaa0940

Park, J. W., Gourmelen, N., Shepherd, A., Kim, S. W., Vaughan, D. G., & Wingham, D. J. (2013). Sustained retreat of the Pine Island Glacier. *Geophysical Research Letters, 40*(10), 2137–2142. https://doi.org/10.1002/grl.50379

Pattyn, F. (2018). The paradigm shift in Antarctic ice sheet modelling. *Nature Communications, 9*(1), 2728. https://doi.org/10.1038/s41467-018-05003-z

Pattyn, F., & Morlighem, M. (2020). The uncertain future of the Antarctic Ice Sheet. *Science, 367*(6484), 1331–1335. https://doi.org/10.1126/science.aaz5487

Pelle, T., Greenbaum, J. S., Dow, C. F., Jenkins, A., & Morlighem, M. (2023). Subglacial discharge accelerates future retreat of Denman and Scott Glaciers, East Antarctica. *Science Advances, 9*(43), eadi9014. https://doi.org/10.1126/sciadv.adi9014

Priscu, J. C., Kalin, J., Winans, J., Campbell, T., Siegfried, M. R., Skidmore, M., et al. (2021). Scientific access into Mercer Subglacial Lake: scientific objectives, drilling operations and initial observations. *Annals of Glaciology, 62*(85–86), 340–352. https://doi.org/10.1017/aog.2021.10

Rabus, B. T., & Lang, O. (2002). On the representation of ice-shelf grounding zones in SAR interferograms. *Journal of Glaciology, 48*(162), 345–356. https://doi.org/10.3189/172756502781831197

Rack, W., King, M. A., Marsh, O. J., Wild, C. T., & Floricioiu, D. (2017). Analysis of ice shelf flexure and its InSAR representation in the grounding zone of the southern McMurdo Ice Shelf. *The Cryosphere, 11*(6), 2481–2490. https://doi.org/10.5194/tc-11-2481-2017

Rignot, E., Mouginot, J., & Scheuchl, B. (2011). Antarctic grounding line mapping from differential satellite radar interferometry. *Geophysical Research Letters, 38*(10). https://doi.org/10.1029/2011GL047109

Rignot, E., Jacobs, S., Mouginot, J., & Scheuchl, B. (2013). Ice-Shelf Melting Around Antarctica. *Science, 341*(6143), 266–270. https://doi.org/10.1126/science.1235798

Rignot, E., Mouginot, J., Morlighem, M., Seroussi, H., & Scheuchl, B. (2014). Widespread, rapid grounding line retreat of Pine Island, Thwaites, Smith, and Kohler glaciers, West Antarctica, from 1992 to 2011. *Geophysical Research Letters, 41*(10), 3502–3509. https://doi.org/10.1002/2014GL060140

Rignot, E.. (1996). Tidal motion, ice velocity and melt rate of Petermann Gletscher, Greenland, measured from radar interferometry. *Journal of Glaciology, 42*(142), 476–485. https://doi.org/10.3189/S0022143000003464

Rignot, E. (2023). Observations of grounding zones are the missing key to understand ice melt in Antarctica. *Nature Climate Change, 13*(10), 1010–1013. https://doi.org/10.1038/s41558-023-01819-w

Rignot, E., Mouginot, Jeremie, & Scheuchl, B. (2016). MEaSUREs Antarctic Grounding Line from Differential Satellite Radar Interferometry (Version 2) [Dataset]. NASA National Snow and Ice Data Center Distributed Active Archive Center. https://doi.org/10.5067/IKBWW4RYHF1Q

Rignot, E., Ciracì, E., Scheuchl, B., Tolpekin, V., Wollersheim, M., & Dow, C. (2024). Widespread seawater intrusions beneath the grounded ice of Thwaites Glacier, West Antarctica. *Proceedings of the National Academy of Sciences, 121*(22), e2404766121. https://doi.org/10.1073/pnas.2404766121

Robel, A. A., Tsai, V. C., Minchew, B., & Simons, M. (2017). Tidal modulation of ice shelf buttressing stresses. *Annals of Glaciology, 58*(74), 12–20. https://doi.org/10.1017/aog.2017.22

Robel, A. A., Wilson, E., & Seroussi, H. (2022). Layered seawater intrusion and melt under grounded ice. *The Cryosphere, 16*(2), 451–469. https://doi.org/10.5194/tc-16-451-2022

Rosier, S. H. R., & Gudmundsson, G. H. (2020). Exploring mechanisms responsible for tidal modulation in flow of the Filchner–Ronne Ice Shelf. *The Cryosphere, 14*(1), 17–37. https://doi.org/10.5194/tc-14-17-2020

Sayag, R., & Worster, M. G. (2013). Elastic dynamics and tidal migration of grounding lines modify subglacial lubrication and melting. *Geophysical Research Letters, 40*(22), 5877–5881. https://doi.org/10.1002/2013GL057942

Sayag, Roiy, & Worster, M. G. (2011). Elastic response of a grounded ice sheet coupled to a floating ice shelf. *Physical Review E, 84*(3), 036111. https://doi.org/10.1103/PhysRevE.84.036111

Scambos, T. A., Haran, T. M., Fahnestock, M. A., Painter, T. H., & Bohlander, J. (2007). MODIS-based Mosaic of Antarctica (MOA) data sets: Continent-wide surface morphology and snow grain size. *Remote Sensing of Environment, 111*(2–3), 242–257. https://doi.org/10.1016/j.rse.2006.12.020

Schenk, T., & Csatho, B. (2012). A New Methodology for Detecting Ice Sheet Surface Elevation Changes From Laser Altimetry Data. *IEEE Transactions on Geoscience and Remote Sensing, 50*(9), 3302–3316. https://doi.org/10.1109/TGRS.2011.2182357

Scheuchl, B., Mouginot, J., Rignot, E., Morlighem, M., & Khazendar, A. (2016). Grounding line retreat of Pope, Smith, and Kohler Glaciers, West Antarctica, measured with Sentinel-1a radar interferometry data. *Geophysical Research Letters, 43*(16), 8572–8579. https://doi.org/10.1002/2016GL069287

Schmeltz, M., Rignot, E., & MacAyeal, D. (2002). Tidal flexure along ice-sheet margins: comparison of InSAR with an elastic-plate model. *Annals of Glaciology, 34*, 202–208. https://doi.org/10.3189/172756402781818049

Schmidt, B. E., Washam, P., Davis, P. E. D., Nicholls, K. W., Holland, D. M., Lawrence, J. D., et al. (2023). Heterogeneous melting near the Thwaites Glacier grounding line. *Nature, 614*(7948), 471–478. https://doi.org/10.1038/s41586-022-05691-0

Schoof, C. (2007a). Ice sheet grounding line dynamics: Steady states, stability, and hysteresis. *Journal of Geophysical Research, 112*(F3), F03S28. https://doi.org/10.1029/2006JF000664

Schoof, C. (2007b). Marine ice-sheet dynamics. Part 1. The case of rapid sliding. *Journal of Fluid Mechanics, 573*, 27–55. https://doi.org/10.1017/S0022112006003570

Schoof, C. (2011). Marine ice sheet dynamics. Part 2. A Stokes flow contact problem. *Journal of Fluid Mechanics, 679*, 122–155. https://doi.org/10.1017/jfm.2011.129

Schutz, B. E., Zwally, H. J., Shuman, C. A., Hancock, D., & DiMarzio, J. P. (2005). Overview of the ICESat Mission. *Geophysical Research Letters, 32*(21), L21S01. https://doi.org/10.1029/2005GL024009

Siegfried, M. R., & Fricker, H. A. (2021). Illuminating Active Subglacial Lake Processes With ICESat-2 Laser Altimetry. *Geophysical Research Letters, 48*(14). https://doi.org/10.1029/2020GL091089

Siegfried, M. R., Venturelli, R. A., Patterson, M. O., Arnuk, W., Campbell, T. D., Gustafson, C. D., et al. (2023). The life and death of a subglacial lake in West Antarctica. *Geology, 51*(5), 434–438. https://doi.org/10.1130/G50995.1

Simkins, L. M., Anderson, J. B., Greenwood, S. L., Gonnermann, H. M., Prothro, L. O., Halberstadt, A. R. W., et al. (2017). Anatomy of a meltwater drainage system beneath the ancestral East Antarctic ice sheet. *Nature Geoscience, 10*(9), 691–697. https://doi.org/10.1038/ngeo3012

Slater, T., Lawrence, I. R., Otosaka, I. N., Shepherd, A., Gourmelen, N., Jakob, L., et al. (2021). Review article: Earth's ice imbalance. *The Cryosphere, 15*(1), 233–246. https://doi.org/10.5194/tc-15-233-2021

Smith, A. M. (1991). The use of tiltmeters to study the dynamics of Antarctic ice-shelf grounding lines. *Journal of Glaciology, 37*(125), 51–58. https://doi.org/10.3189/S0022143000042799

Smith, B., Fricker, H. A., Holschuh, N., Gardner, A. S., Adusumilli, S., Brunt, K. M., et al. (2019). Land ice height-retrieval algorithm for NASA's ICESat-2 photon-counting laser altimeter. *Remote Sensing of Environment, 233*, 111352. https://doi.org/10.1016/j.rse.2019.111352

Stubblefield, A. G., Meyer, C. R., Siegfried, M. R., Sauthoff, W., & Spiegelman, M. (2023). Reconstructing subglacial lake activity with an altimetry-based inverse method. *Journal of Glaciology*, 1–15. https://doi.org/10.1017/jog.2023.90

Sun, S., Pattyn, F., Simon, E. G., Albrecht, T., Cornford, S., Calov, R., et al. (2020). Antarctic ice sheet response to sudden and sustained ice-shelf collapse (ABUMIP). *Journal of Glaciology, 66*(260), 891–904. https://doi.org/10.1017/jog.2020.67

Swithinbank, C. (1955). Ice Shelves. *The Geographical Journal, 121*(1), 64–76. https://doi.org/10.2307/1791807

Thomas, R. H. (1979). The Dynamics of Marine Ice Sheets. *Journal of Glaciology, 24*(90), 167–177. https://doi.org/10.1017/S0022143000014726

Trusel, L. D., Frey, K. E., Das, S. B., Karnauskas, K. B., Kuipers Munneke, P., Meijgaard, E., & Broeke, M. R. (2015). Divergent trajectories of Antarctic surface melt under two twenty-first-century climate scenarios. *Nature Geoscience, 8*, 927–932. https://doi.org/10.1038/ngeo2563

Tsai, V. C., & Gudmundsson, G. H. (2015). An improved model for tidally modulated grounding-line migration. *Journal of Glaciology, 61*(226), 216–222. https://doi.org/10.3189/2015JoG14J152

Vaughan, D. G. (1994). Investigating tidal flexure on an ice shelf using kinematic GPS. *Annals of Glaciology, 20*, 372–376. https://doi.org/10.3189/1994AoG20-1-372-376

Vaughan, D. G. (1995). Tidal flexure at ice shelf margins. *Journal of Geophysical Research: Solid Earth, 100*(B4), 6213–6224. https://doi.org/10.1029/94JB02467

Walker, R. T., Parizek, B. R., Alley, R. B., Anandakrishnan, S., Riverman, K. L., & Christianson, K. (2013). Ice-shelf tidal flexure and subglacial pressure variations. *Earth and Planetary Science Letters, 361*, 422–428. https://doi.org/10.1016/j.epsl.2012.11.008

Warburton, K. L. P., Hewitt, D. R., & Neufeld, J. A. (2020). Tidal Grounding-Line Migration Modulated by Subglacial Hydrology. *Geophysical Research Letters, 47*(17). https://doi.org/10.1029/2020GL089088

Weertman, J. (1974). Stability of the Junction of an Ice Sheet and an Ice Shelf. *Journal of Glaciology, 13*(67), 3–11. https://doi.org/10.1017/S0022143000023327

Wild, C. T., Marsh, O. J., & Rack, W. (2018). Unraveling InSAR Observed Antarctic Ice-Shelf Flexure Using 2-D Elastic and Viscoelastic Modeling. *Frontiers in Earth Science, 6*, 28. https://doi.org/10.3389/feart.2018.00028

Wilson, N., Straneo, F., & Heimbach, P. (2017). Satellite-derived submarine melt rates and mass balance (2011–2015) for Greenland's largest remaining ice tongues. *The Cryosphere, 11*(6), 2773–2782. https://doi.org/10.5194/tc-11-2773-2017

Wouters, B., Martin-Espanol, A., Helm, V., Flament, T., van Wessem, J. M., Ligtenberg, S. R. M., et al. (2015). Dynamic thinning of glaciers on the Southern Antarctic Peninsula. *Science, 348*(6237), 899–903. https://doi.org/10.1126/science.aaa5727

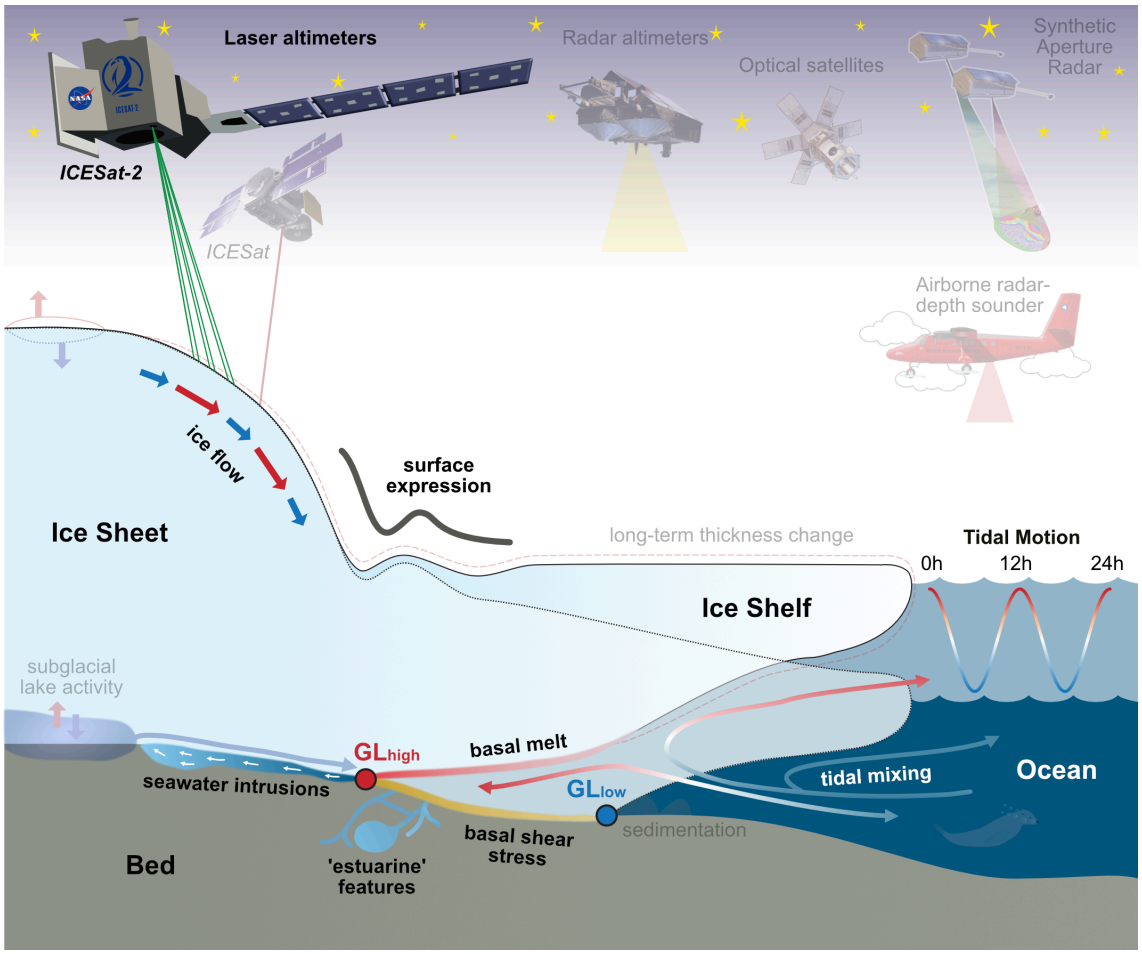
Zhong, M., Simons, M., Minchew, B., & Zhu, L. (2023). Inferring Tide-Induced Ephemeral Grounding in an Ice-Shelf-Stream System: Rutford Ice Stream, West Antarctica. *Journal of Geophysical Research: Earth Surface, 128*(2), e2022JF006789. https://doi.org/10.1029/2022JF006789

Zwally, H. J., Abdalati, W., Herring, T., Larson, K., Saba, J., & Steffen, K. (2002). Surface Melt-Induced Acceleration of Greenland Ice-Sheet Flow. *Science, 297*, 218–222. https://doi.org/10.1126/science.1072708

Chapter 2

Modes of Antarctic tidal grounding line migration revealed by Ice, Cloud, and land Elevation Satellite-2 (ICESat-2) laser altimetry

In this chapter I develop a novel method to measure short-term, tidal grounding line migration using ICESat-2 laser altimetry. I use this method to map the time-varying grounding zone structure of an ice plain on the Ronne Ice Shelf, revealing up to 15 km of grounding line migration across the tide cycle and identifying four distinct tidal migration modes.



The research described in Chapter 2 has been published as:

Freer, B. I. D., Marsh, O. J., Hogg, A. E., Fricker, H. A., & Padman, L. (2023). Modes of Antarctic tidal grounding line migration revealed by Ice, Cloud, and land Elevation Satellite-2 (ICESat-2) laser altimetry. *The Cryosphere*, 17(9), 4079–4101. https://doi.org/10.5194/tc-17-4079-2023

Abstract

Tide-forced short-term tidal migration of the grounding line (GL) of Antarctic ice shelves can impact ice dynamics at the ice sheet margins and obscures assessments of long-term GL advance or retreat. However, the magnitude of tidally-induced GL migration is poorly known, and the spatial pattern and modes of variability are not well characterised. Here we develop and apply a technique that uses ICESat-2 repeat-track laser altimetry to locate the inland limit of tidal ice shelf flexure for each sampled tide, enabling the magnitude and temporal variability of tidal GL migration to be resolved. We demonstrate its application at an ice plain north of Bungenstockrücken, in a region of the southern Ronne Ice Shelf subject to large ocean tides. We observe a 1,300 km^2 area of ephemeral grounding over which the GL migrates by up to 15 km between low and high tide, and identify four distinct modes of migration: "linear", "asymmetric", "threshold" and "hysteresis". The short-term movement of the GL dominates any long-term migration signal in this location, and the distribution of GL positions and modes contains information about spatial variability in the ice-bed interface. We discuss the impact of extreme tidal GL migration on ice shelf-ocean-subglacial systems in Antarctica and make recommendations for how GLs should be more precisely defined and documented in future by the community.

2.1. Introduction

Recent mass loss from the Antarctic Ice Sheet has been attributed to changes in the floating ice shelves that fringe 74% of its margins (Gudmundsson et al., 2019; Joughin et al., 2012) and buttress upstream grounded ice (Dupont & Alley, 2005). Accurate representation of the ice sheet in coupled Earth system models is essential to predict its evolution and the magnitude and rate of its future contribution to sea level rise. This

requires knowledge of ice sheet processes and boundary conditions, including the configuration and behaviour of ice shelves. One important parameter for ice sheet monitoring and modelling is the location of the grounding line (GL), which marks the boundary between the grounded ice sheet and floating ice shelf (Thomas, 1979). As the ice detaches from the underlying bed, ice flow across the wider grounding zone (GZ) transitions from a regime dominated by vertical shear and basal drag to that of primarily buoyancy-driven flow dominated by longitudinal stretching and lateral shear with no basal drag (Schoof, 2007). There are high rates of basal melt at the GL as ocean water comes into contact with the base of the ice shelf (Jenkins et al., 2006; Depoorter et al., 2013). The location of the GL and change in its position over time is, therefore, a sensitive indicator of ice sheet stability and local environmental forcing, with sustained ice thinning causing GL retreat, and thickening causing GL advance (Joughin et al., 2010, 2012; Dutrieux et al., 2014), and it has been identified as an Essential Climate Variable (Bojinski et al., 2014)

Several satellite-based techniques have been used to map features in the GZ, with the primary goal of monitoring long-term change in GL position (Sect. 2.2). The GL is typically located by identifying the inland limit of ice shelf flexure, but this is complicated by the effect of short-term sea level variations, primarily driven by ocean tides, which can cause GL migration on hourly to daily timescales. During a rising tide, increased buoyancy causes more of the ice shelf to lift off the bed and the GL temporarily migrates inland, returning to its most seaward position at low tide (Brancato et al., 2020), with some slight time lag due to the viscoelastic effects of the ice (Reeh et al., 2003). Prior satellite observations have shown that the extent of this short-term tidal GL migration can range from a few hundred metres to several kilometres (Hogg et al., 2016; Brunt et al., 2011; Milillo et al., 2017, 2019, 2022), with the magnitude of this migration controlled by the tide amplitude, local bed topography and the thickness and strength of the ice. The signal of short-term tidal GL migration is superimposed on the long-term signal of GL migration associated with ice dynamic change, which is traditionally calculated by comparing sparsely sampled, individual measurements of GL position through time (e.g., Rignot et al., 2014). Therefore, in order to increase confidence in measurements of

long-term GL migration rates, we must improve our knowledge of the spatially variable pattern of short-term tidal GL migration.

Despite the importance of understanding tidal GL migration, there is currently no pan-Antarctic assessment of its extent or variability. This is mostly because there is a lack of acquired or suitable satellite data in the historical archive with sufficient spatial coverage and temporal resolution. We currently also have a limited understanding of the *mechanisms* of tidal ice shelf flexure and GL migration. Various representations of tidal flexure have been modelled using elastic and viscoelastic frameworks (Holdsworth, 1969; Vaughan, 1995; Schmeltz et al., 2002; Walker et al., 2013), some of which allow for tidal GL migration (Sayag & Worster, 2013; Tsai & Gudmundsson, 2015; Stubblefield et al., 2021) but results vary considerably and the choice of representation of these processes can have a large impact on results of modelling studies (e.g., Mosbeux et al., 2023). Whilst some localised in situ measurements of tidal flexure have been made to examine these processes (Smith, 1991; Vaughan, 1995), there are very few satellite observations with high enough tidal sampling to test and validate these models. Furthermore, modelled projections of future mass loss from West Antarctica are very sensitive to the amount of basal melt and ice flux at the GL (Arthern & Williams, 2017; Goldberg et al., 2019), yet most numerical ice sheet models typically assume a fixed or slowly moving GL determined by flotation conditions alone with zero basal melt (Milillo et al., 2017; Favier et al., 2014). This is an over-simplification in areas subject to extreme tidal variability, where short-term GL migration is likely to impact both ice dynamics through rapid variations in basal shear stress and basal melt rate through changes in cavity geometry, enhancing tidal mixing (Chen et al., 2023; Ciracì et al., 2023; Milillo et al., 2019). Quantifying the extent and influence of tidal GL migration around the margin of Antarctica is valuable for these processes to be more accurately parameterised in ice sheet models.

In this study we present a new approach to observe tidal GL migration that takes advantage of the high along-track resolution and repeat-track configuration of the Ice, Cloud, and land Elevation Satellite-2 laser altimeter mission (ICESat-2) to improve temporal sampling of tidal ice flexure and GL migration. We apply the method to the ice

plain north of the Bungenstockrücken ice rise, on the southern Ronne Ice Shelf. An ice plain is defined as an area of low surface slope close to the GZ where the ice is close to flotation (Alley et al., 1989) and which can sometimes experience "ephemeral grounding" between high and low tide (Schmeltz et al., 2001; Brunt et al., 2011). We show that with ICESat-2 repeat-track laser altimetry (RTLA) it is possible to monitor the time-varying GZ structure at the Bungenstockrücken ice plain in unprecedented detail, and we identify four distinct modes of tidal GL migration. We discuss the implications both for long-term GL monitoring and how these findings inform our process understanding of tidal flexure and GL migration mechanisms in Antarctica.

2.2. Grounding lines and their detection

2.2.1. Features of the grounding zone

The GZ is the region over which the ice transitions from being in constant contact with the bed to floating in hydrostatic equilibrium with the ocean (see Fig. 1). Ice in the GZ is supported by both the hydrostatic pressure from the underlying ocean and internal stresses, and it undergoes tidal flexure (Vaughan, 1995). The true GL location, Point G, refers to the point at which the ice base first detaches from the bed as it flows from the ice sheet. As a subglacial feature within the GZ, Point G can only be directly observed using ground-based radar (MacGregor et al., 2011; Catania et al., 2010) or using remotely-operated vehicles deployed from the shelf edge or through boreholes (Schmidt et al., 2023). However, there are a number of observable surface features in the GZ that relate to the location of Point G, which can be more readily detected in situ or in satellite data and used as GL proxies (Fig. 1). Point F is the landward limit of tidal flexure, and is often located slightly inland of Point G (on the order of hundreds of metres) due to the elastic properties of the ice (Padman et al., 2018; Rignot et al., 2011). Point H is the seaward limit of tidal flexure and inland limit of hydrostatic equilibrium. The break-in-slope, Point I_b, marks the sharp reduction in surface slope that occurs due to the abrupt change in basal shear stress across the GL, and in typical GZs it is located slightly seaward of Point G (Schoof, 2011). However, where a GZ has an ice plain, Point I_b has been observed several kilometres inland of Point G (Corr et al., 2001). We show the locations of the key GZ surface proxies as they relate to Point G for an idealised ice plain

in Fig. 2.1(a), and in Fig. 2.1(b) we depict how Point F can migrate by several kilometres across the tide cycle at an ice plain experiencing ephemeral grounding.

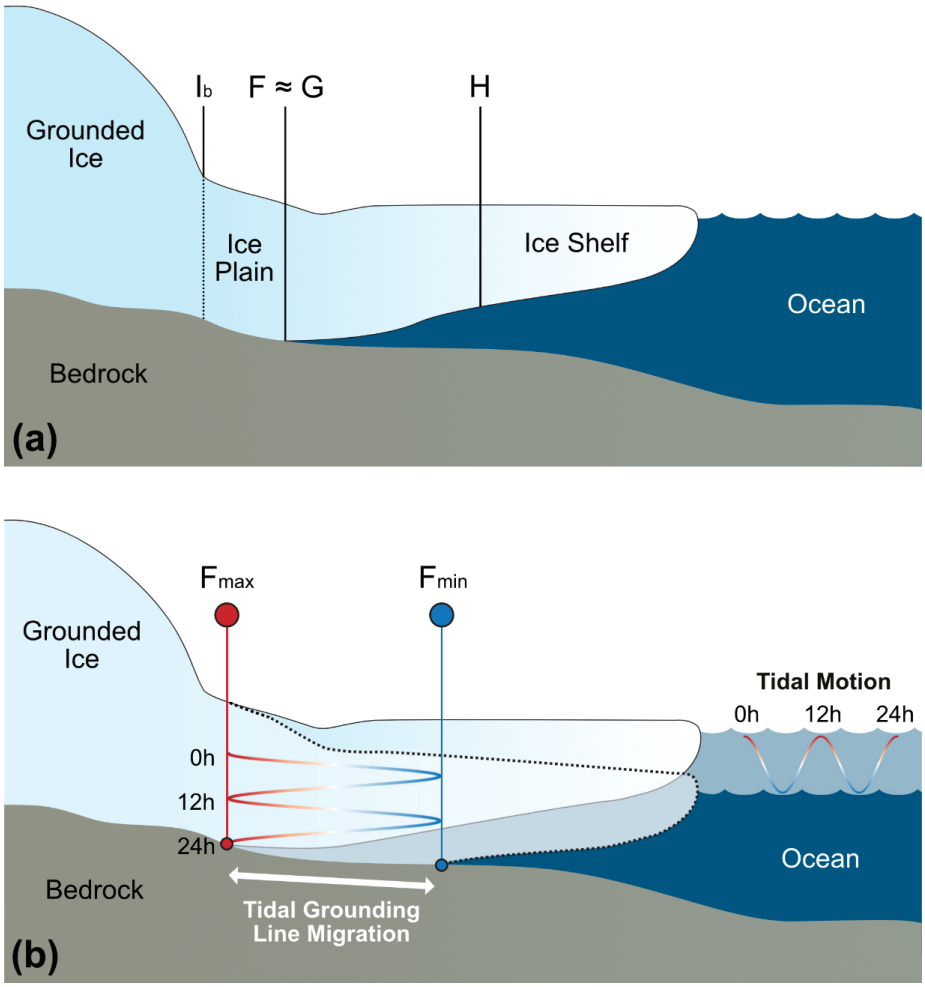


Figure 2.1. (a) Idealised cross section of an ice plain GZ, showing the location of typical satellite-derived GZ proxies: Point I_b, the first break-in-slope; Point F, the inland limit of tidal flexure (represented here as approximately equal to Point G, the true GL); Point H, the inshore limit of hydrostatic equilibrium. (b) Idealised cross section of an ice plain GZ experiencing tidal GL migration, showing the difference in position of the ice shelf and migration of Point F between high tide (F_{max}) and low tide (F_{min}), across 24 hours of a simplified ~12 h semidiurnal tide cycle.

2.2.2. *Methods for detecting the grounding zone*

GZ surface proxies can be measured in situ using instruments such as tiltmeters and GNSS (global navigation satellite system) (Stephenson et al., 1979; Smith, 1991; Vaughan, 1995) or using satellite techniques to obtain more widespread measurements (Rignot, 1996; Friedl et al., 2020). Static satellite methods identify the break-in-slope, Point I_b, either from shadows in a single-epoch optical satellite image (Scambos et al., 2007; Bindschadler et al., 2011) or single-epoch elevation profiles from radar and laser satellite altimetry (Hogg et al., 2018; Brunt et al., 2010a; Li et al., 2022a). Dynamic satellite methods use data acquired at two or more distinct phases of the tidal cycle to locate the limits of tidal flexure, Points F and H. CryoSat-2 radar altimetry has been used to map Point F and H by applying a pseudo-crossover method to detect tidal flexure (Dawson & Bamber, 2017, 2020). This provides good spatial coverage by assimilating large data volumes over a multi-year record, but cannot be used to detect short-term GL migration between specific tides due to its long repeat cycle (369 days). Differential interferometric synthetic aperture radar (DInSAR) is one of the most commonly used dynamic satellite methods and can produce quasi-continuous maps of Points F and H from double-differenced interferograms produced from three or four SAR images acquired at different times in the tidal cycle (Rignot, 1996). However, the temporal sampling and spatial coverage of DInSAR in Antarctica is limited, in part due to its reliance on a short repeat-time between acquisitions to retain interferometric coherence. Sentinel-1 DInSAR has been used to detect tidal GL migration (Mohajerani et al., 2021; Chen et al., 2023), but the coverage only extends to ~77 °S, which excludes the majority of the Ross and Filchner-Ronne GLs. Recent studies using data from the COSMO-SkyMed (CSK) constellation, with a short repeat-period of 1, 3, 4 or 8 d and up to 3 m spatial resolution, have improved DInSAR sampling of tidal GL migration in specific locations (Milillo et al., 2017; Minchew et al., 2017; Brancato et al., 2020), but are still complicated by the fact that interferograms are produced from oblique imagery from at least three different tide times. Moreover, while the relatively short repeat period of CSK enables interferometric coherence to be maintained on faster floating ice streams, the spatial coverage of

coherent SAR image pairs is still limited, constraining the period where continent-wide studies can be performed.

An alternative dynamic satellite technique is repeat-track satellite laser altimetry (RTLA), which was first introduced for GZ detection by Fricker & Padman (2006). For this method, comparison of repeat tracks of ice shelf elevation profiles sampled at different tidal states identifies elevation anomalies that relate to Points F and H along discrete ground tracks. RTLA was pioneered using data from the Geoscience Laser Altimeter System instrument on board the Ice, Cloud and Land Elevation Satellite (ICESat) that was in orbit from 2003 to 2009. However, ICESat only had a single ground track that only repeated to about ±100 m, which led to unrecoverable topographic biases across GZs due to the typically large across-track slopes (Fricker et al., 2009). In contrast, the Advanced Topographic Laser Altimeter System (ATLAS) that launched on board ICESat-2 in 2018 has a six-beam design with more accurate pointing, which reduces across-track deviation from each reference pair track (RPT) to within 4.4 ± 6.0 m (Luthcke et al., 2021), providing better spatial sampling of the GZ. Only two repeat measurements are required to locate Point F using RTLA, providing an advantage over DInSAR which requires at least three repeats, and allows us to attribute the migration of Point F to individual tidal states. Li et al. (2022b) has used these data to locate a single Point F, H and I_b (Fig. 2.1a) along most ICESat-2 ground tracks around Antarctica. This is a highly valuable and comprehensive dataset for the identification of long-term grounding line change, but as only a single Point F has been located per ICESat-2 ground track, it is limited in use for studying tidal GZ processes. Therefore, here we extend the Li et al. (2022b) record at Bungenstockrücken to locate *multiple* positions of Point F along each ICESat-2 ground track as it migrates over the tide cycle (Fig. 2.1b), providing novel observations of tidal GZ behaviour.

2.3. Data and Methods

2.3.1. Datasets

The ATLAS instrument on board ICESat-2 is the first spaceborne photon-counting laser altimeter (Markus et al., 2017). It samples 11 m diameter footprints (Magruder et al., 2021) estimating surface heights every 0.7 m along its 1387 reference ground tracks (RGTs). ATLAS transmits a single beam of 532 nm (green) laser light pulsing at 10 kHz along each RGT, which is split into six beams organised into three pairs, each separated by 3.3 km. The beams in each pair, one "weak" and one "strong", are separated by 90 m across-track, and each beam follows its own ground track (*GT1L, GT1R, GT2R…to GT3L*). The system operates in a 91 d exact-repeat orbit, providing repeat surface height measurements along each ground track about four times per year (Neumann et al., 2019). We obtained data from version 5 of the Land Ice Height (ATL06) product along all ground tracks crossing the Bungenstockrücken GL (Fig. 2.2b). This included data from repeat cycles 3 to 15 (April 2019 to May 2022; Smith et al., 2021), with cycles 1 and 2 omitted due to instrument off-pointing at the start of the mission. ATL06 provides surface height measurements every 20 m along-track, calculated by averaging the level-2 geolocated photon data over 40 m segments (Smith et al., 2019).

We obtained coincident tide amplitudes at the most seaward point of each ICESat-2 ground track per cycle from the circum-Antarctic inverse tide model CATS2008 (Howard et al., 2019) using the pyTMD software (Sutterley et al., 2019). CATS2008 is an update of the model described by Padman et al. (2002) that is widely considered the best performing tidal model in the region, in part due to its assimilation of ICESat altimetry data over large ice shelves (King et al., 2011). We note that this tide information was just used for reference and not directly in the calculation of locations of Point F. We also selected three locations 35–40 km seaward of Bungenstockrücken (Fig. 2.2a) to extract a time series of tide heights over a single year (centred on 1 January 2020). These are used to calculate annual tide distributions across the width of the region, which is important to give context to the range of tides (and therefore locations of Point F) that have been sampled by ICESat-2 along each RGT over the study period. All modelled tides were extracted from locations seaward of the Making Earth System Data Records for Use in

Research Environments (MEaSUREs) Point H to ensure that they represented the ice shelf in hydrostatic equilibrium.

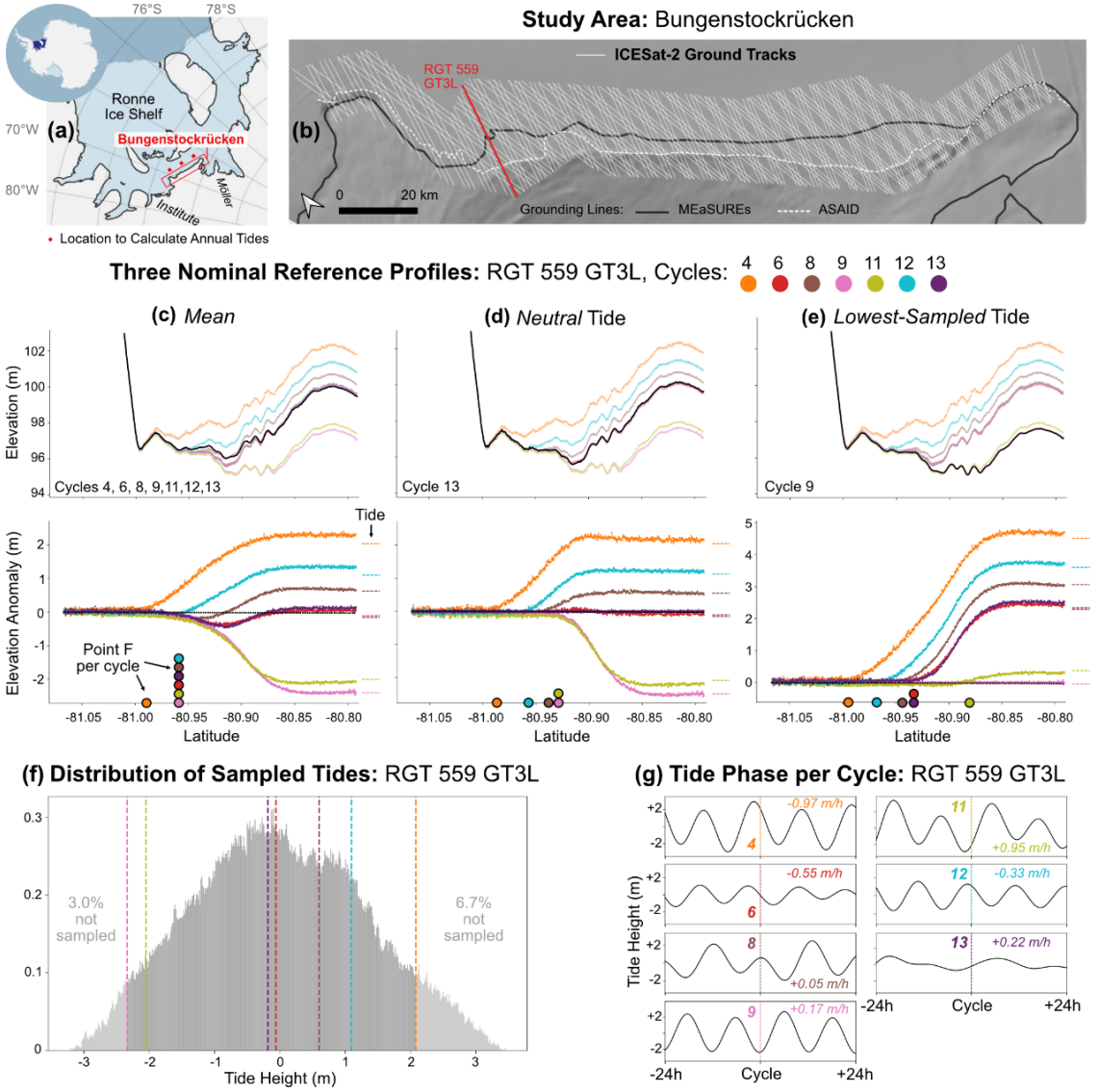


Figure 2.2. Method used to define three types of reference profile for elevation anomaly calculations along ICESat-2 ground tracks, as illustrated for RGT 559 GT3L at the Bungenstockrücken ice plain. (a) Location of Bungenstockrücken on the Ronne Ice Shelf. Red diamonds show the locations used to calculate annual tide distributions. (b) ICESat-2 ground tracks crossing the MEaSUREs and ASAID GLs in the study area (Rignot et al., 2016; Bindschadler & Choi, 2011). (c-e) Repeat surface elevation profiles and anomalies of RGT 559 GT3L, each using a different reference profile: (c) *mean* profile calculated using cycles 4, 6, 8, 9, 11, 12, 13; (d) *neutral* profile of cycle 13; (e) *lowest-sampled* tide profile of cycle 9. The reference profile at zero-elevation anomaly is shown as a

black dashed line, and the latitude of the derived Point F positions for each cycle along-track as coloured circles along the *x*-axis. Dashed coloured lines show the modelled tide height at the time of each cycle at the most seaward point along-track (in (e) these are differenced from the tide of cycle 9). (f) Histogram of CATS2008 modelled tide heights experienced over a single year, centred on 01/01/2020 (Howard et al., 2019), with vertical coloured dashed lines showing the tide height at each repeat cycle. (g) Tidal time series showing tide height, velocity and phase during the 24 hour period before and after the ICESat-2 overpass for each repeat cycle at RGT 559 GT3L.

2.3.2. Repeat-track laser altimetry

RTLA is a dynamic method for GL estimation that uses repeat measurements made at different phases of the tidal cycle to estimate the temporal change in the surface elevation of the ice shelf caused by ocean tides to identify the limits of tidal flexure (Points F and H) as proxies for GL location (Fricker & Padman, 2006). This method typically involves three steps:

i. preparing data,
ii. defining the reference elevation profile,
iii. locating the limits of tidal flexure by calculating elevation anomalies relative to the reference profile.

In this study we present updates to steps ii and iii that allow us to improve the temporal sampling of short-term tidal GL migration. We describe each of these steps below.

2.3.2.1. Preparing data

We obtained ATL06 surface height data along all ICESat-2 ground tracks in the study area (Smith et al., 2021) using the icepyx software library (Scheick et al., 2023, version 0.3.3) . We removed low-quality measurements caused by cloud cover, blowing snow or background photon clustering using the *ATL06_quality_summary* parameter. We rejected all values either without a valid associated across-track-slope measurement and/or where the minimum segment difference exceeds 1 m, which is calculated as the minimum absolute difference between each segment's endpoints and those of its two neighbours (Arendt et al., 2020). Following the method described in Li et al. (2020), we

applied a cross-track slope correction to minimise the effects of rough terrain (Smith et al., 2019), and for each ground track we omitted repeat cycles with fewer than 50% valid measurements along-track, as they are deemed unreliable for GZ calculation. We then performed RTLA analysis along each ground track using the remaining high quality repeat cycles, as described in Sects. 2.3.2.2 and 2.3.2.3.

2.3.2.2. Defining the reference elevation profile

The reference profile is important for identifying the limits of tidal flexure, as it is used as a baseline from which to calculate elevation anomalies for each ICESat-2 repeat sampled at different tidal states. The *mean* elevation profile from all sampled repeats has been used as the reference profile in all previous RTLA studies to locate one or two Point F positions per ground track (Fricker & Padman, 2006; Fricker et al., 2009; Brunt et al., 2010b, 2011; Li et al., 2020, 2022a, b). This allows us to derive one Point F per ground track, which is useful for measuring long-term change but does not make sense for mapping short-term tidal GL migration (for the reasons discussed below). Here we propose two alternative approaches: using a reference profile sampled at a *neutral* tide or at the *lowest-sampled tide*. These are illustrated for RGT 559 GT3L in Fig. 2.2. Before selecting one of these approaches for our study, we first evaluated the results from each and considered the situations for which each would be appropriate. To test each approach, we fitted a cubic B-spline approximation to the valid repeat surface elevation profiles per ground track, using a smoothing parameter of 0.7. The use of an interpolated profile rather than the raw data points is more robust, providing a method for handling small along-track data gaps in individual profiles, which can be consistently applied across all repeat tracks.

(i) ***Mean elevation profile*** (Fig. 2.2c): The mean elevation profile in all prior studies has been calculated as the mean of the interpolated profiles of all sampled repeat cycles along each ground track. However, this reference profile does not represent the true mean ice shelf surface corresponding to zero (neutral) tide. Instead, it gives us the along-track mean of the ice shelf surfaces at the tide phases sampled by ICESat-2. This can introduce an observation bias; for example, the mean reference elevation profile would be biased high if most sampled repeats

of a single RGT are acquired at positive tides, or during one or two extreme high tides. This particularly affects areas experiencing large tidal GL migration, as can be seen clearly in Fig. 2.2c, where the anomalies for cycles 6 and 13 fall below zero between -80.96° S and -80.88° S. This might incorrectly suggest that tidal flexure extends this far inland, when in fact it reflects the skew of the mean reference profile caused by GL migration further inland at higher tides (cycles 4 and 12). Given that we locate Point F along-track where the anomaly gradient for each cycle first deviates from 0 m, this would lead us to incorrectly locate just two Point F positions along this ground track: one for cycle 4 at ~80.99° S and one for all other cycles together at ~81.96° S (Fig. 2.2c). As a result, we see a systematic inland bias in the derived GL position when using the mean reference profile, leading to a large underestimation of the total extent of tidal GL migration along this ground track. We note that this ambiguity could be minimised by reducing the number of repeats used to calculate the mean reference profile to two; however this would require the mean profile to be recalculated several times per track with different pairs of repeat cycles, which would both increase the processing time and prevent a direct comparison of anomaly profiles between cycles.

(ii) ***Neutral tide profile*** (Fig. 2.2d): To more closely represent the true mean ice shelf surface, we can use the elevation profile from a single cycle sampled at a neutral tide as the reference profile. Ideally, this would use the profile sampled close to a 0 m tide during the neap phase, such as cycle 13 on Bungenstockrücken RGT 559 GT3L (Fig. 2.2g). Using the neutral tide profile removes the effect of the skewed mean in the inner regions of the GZ and improves our interpretation of flexure between tides, as we are now directly comparing the surface profiles between two individual tidal states for each cycle. However, it still raises the same issue that for all cycles with a negative elevation anomaly (i.e. here with tides below neutral), we would locate Point F too far inland, where anomalies first deviate from 0 (e.g., cycles 9 and 11 in Fig. 2.2d). We are also unable to locate Point F for cycles sampled close to the neutral tide as there is no deviation in elevation from the reference profile (cycle 6 and 13 in Fig. 2.2d). Again, this

would mean we would underestimate the total extent of tidal GL migration, by overlooking migration that occurs at tides below a neutral level. Moreover, many ICESat-2 RGTs have not been sampled close to a neutral tide, which itself is also difficult to accurately define, because at deep grounding zones the ice surface may not response adequately in phase with the ocean tide. This means it would not be possible to apply this approach consistently across multiple ground tracks.

(iii) ***Lowest-sampled tide profile*** (Fig. 2.2e): Alternatively, we propose that the elevation profile of the repeat cycle sampled at the lowest coincident tide can be used as the reference profile, identified as the cycle with the lowest elevation anomaly at the most seaward sampled point. Again, by using an elevation profile from a single cycle as the reference, we are calculating anomalies against a "real" ice shelf surface profile, giving a more realistic representation of the impact of tidal forcing on ice shelf flexure. This overcomes the issue of the mean reference profile (calculated from multiple cycles of data) being skewed by inland flexure at higher tides, but, unlike the method using the neutral tide profile, it has the additional advantage that it can be applied consistently across RGTs, enabling automation. Most importantly, it allows us to locate Point F for cycles sampled at lower tides that are missed when using both the mean and neutral reference profiles. For RGT 559 GT3L we identify five individual Point F positions using the lowest-sampled reference profile (Fig. 2.2e) as opposed to two with the traditional mean approach (Fig. 2.2c) or four using the neutral tide profile (Fig. 2.2d). Locating the most seaward Point F (from cycle 11 in Fig. 2.2e) gives us a more realistic baseline for the low-tide GL position against which to quantify the extent of migration at each higher sampled tide. Note that we cannot locate Point F for the lowest-sampled tide itself (i.e. cycle 9 in Fig. 2.2e) as there is no lower profile to compare to, but this is a common problem across all methods.

The type of reference profile (*mean* / *neutral* / *lowest-sampled tide*) chosen to calculate elevation anomalies ultimately depends on the scientific question being posed and the tidal sampling by the ICESat-2 RGTs. We must also consider the impact of signals in the repeat elevation profiles that are not associated with tidal displacement,

which can be especially prominent where there are large time gaps between repeat cycles. For example, in regions of fast flowing ice, elevation gradients will advect through the GZ between repeat passes, or alternatively surface mass balance or long-term ice dynamic thickness change could alter the repeat track elevation profiles and obscure the tidal signal. These issues could be addressed by using shorter subsections of the whole time series to define the choice of reference profile. For this study we chose to apply the *lowest-sampled* tide reference track for RTLA analysis across the whole 3-year time series as we found it to be the most effective for assessing *tidal* GL migration. Regardless of the chosen reference profile, the results will be limited by the range of the tidal amplitudes that have been sampled by ICESat-2 along each RGT. The CATS2008 tide model can provide context for this; for example Fig. 2.2f shows that along RGT 559 the lowest 3% and highest 7% of tides have not been sampled, meaning we are unable to locate the full extent of the migration of Point F at these most extreme tides. The tide phase and velocity at each repeat cycle can also affect the observed flexure profile; therefore we also extract this information from CATS2008 to aid our interpretations (Fig. 2.2g).

2.3.2.3. Locating the limits of flexure in regions of ephemeral grounding

Most previous GZ studies using RTLA located a single Point F per track (Fricker and Padman, 2006; Fricker et al., 2009; Brunt et al., 2010b; Li et al., 2020, 2022a, b). However, with our method using the *lowest-sampled* tide as the reference profile, it is possible to locate multiple Point F positions along each ICESat-2 ground track, each sampled at a different tidal state. To achieve this, we calculated the elevation anomalies per repeat cycle against the reference profile for each ground track, as is shown for RGT 559 GT3L in Fig. 2.3. The region where the elevation anomaly is close to 0 m is interpreted as fully grounded ice, and where it is close to the modelled tide prediction with zero gradient as freely floating ice in hydrostatic equilibrium. We compared this with modelled tide predictions from CATS2008 to distinguish the tidal signal from other causes of elevation change, including surface mass balance and ice dynamics. We then located Point F for each repeat cycle using an automated technique adapted from Li et al. (2022a). First, we applied a low-pass Butterworth filter to the elevation anomalies per

cycle, using a normalised cut-off frequency of 0.016 and an order 5, to remove the high-frequency noise whilst retaining the shape of each anomaly curve. From this, we located Point F where the anomaly gradient first deviates from zero and the second derivative of the anomaly peaks (Fig. 2.3b-g). To ensure the correct estimation of Point F, we restricted the choice of peak to where anomaly values < 0.25 m. In certain cases, the chosen peak of the second derivative was visibly incorrect; i.e. the peak related to Point F was not selected, but instead a peak related to another cause of elevation change (e.g., crevasse migration). Since this only affected a small minority of tracks in this study area, it was dealt with by manually adjusting the choice of peak to ensure the peak relating to Point F was selected consistently. We note that more advanced filtering could be applied to address this problem in a more automated way if scaled up to a larger area, but it would likely cause some loss of useful data. For each Point F we then extracted the latitude and longitude as well as the coincident tide height and phase at the time of ICESat-2 overpass from CATS2008, which allows us to map the migration of Point F across the tide cycle (Fig. 2.3h). Finally, to investigate modes of tidal GL migration along each ground track we plotted the distance between Point F and the location of the furthest seaward Point F against the coincident tide height for each repeat cycle, distinguishing between those sampled during rising vs. falling tides (Fig. 2.3i).

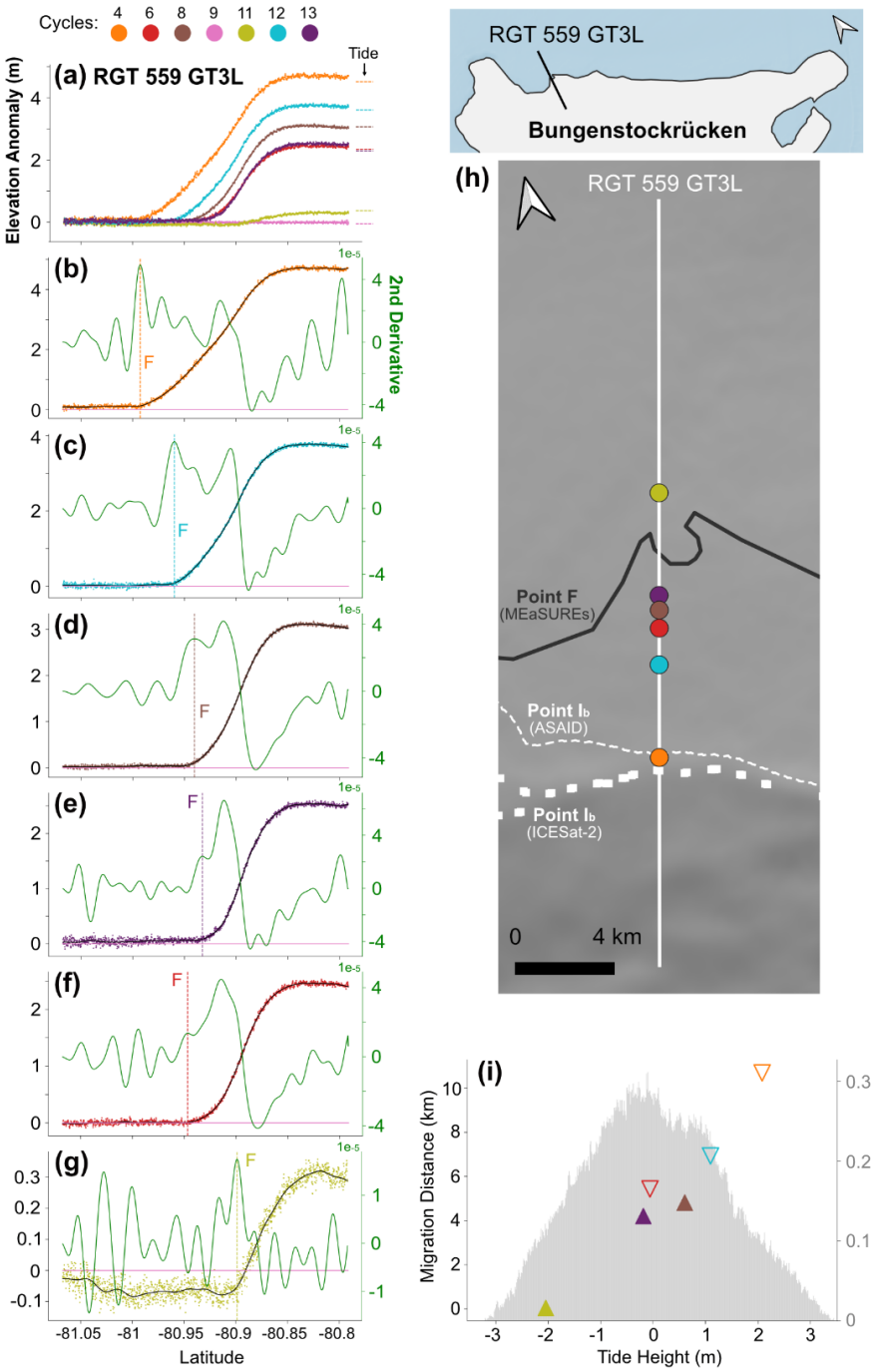


Figure 2.3. Method used to locate Point F per repeat cycle from ICESat-2 elevation anomalies, as illustrated for RGT 559 GT3L. (a) Elevation anomalies for repeat cycles 4, 6, 8, 11, 12 and 13, each calculated against the lowest-sampled tide reference profile of cycle 9. Dashed coloured lines indicate the CATS2008 modelled tide height per cycle, differenced from the tide of cycle 9 (Howard et al., 2019). (b-g) Individual elevation anomalies for each repeat cycle, with the low-pass-filtered anomalies in black and the second derivative of the filtered anomalies in green. Vertical dashed lines show the along-track latitude where Point F has been located from the peak(s) of the second

derivative. (h) Map showing the derived position of Point F per repeat cycle along RGT 559 GT3L. (i) Along-track migration distance of Point F per cycle for RGT 559 GT3L as a function of coincident tide height, overlain on the histogram of tide heights experienced over a single year (centred on 1 January 2020).

2.3.3. Study region

We tested our updated RTLA methodology along all ICESat-2 ground tracks crossing a 220 km section of GL at the ice plain north of Bungenstockrücken, located on the southern Ronne Ice Shelf in between the Institute and Möller ice streams (Fig. 2.2). This is an ideal location to study tidal GL migration for the following four reasons.

1. **Large tidal range with ephemeral grounding.** The southern Ronne Ice Shelf experiences predominantly semidiurnal tides with a 7–8 m total tidal range, one of the largest in Antarctica (Padman et al., 2018). Ephemeral grounding has already been identified over this ice plain in earlier ICESat studies (Brunt et al., 2011).
2. **ICESat-2 sampling.** The high-latitude location, GZ orientation and low cloud cover leads to a high density of unobstructed ICESat-2 tracks crossing normally to the GL (67 RGTs, each with six separate ground tracks).
3. **Low ice velocity.** Ice flows across the GL at ~5 m a^{-1} (Rignot et al., 2017), resulting in little advection of surface features between repeat profiles over the 3-year study period, which could otherwise affect the success of RTLA.
4. **Evidence for past change.** There is evidence that this region has undergone significant GL retreat in the past, and as the upstream ice sheet is currently grounded over a >1.5 km deep basin with a retrograde slope it is potentially susceptible to future ice loss (Ross et al., 2012; Siegert et al., 2013). In general, ice plains are a good location to monitor early signs of change as they are highly sensitive to small perturbations in ice dynamics, sea level, surface mass balance, basal melt and sediment deposition (Brunt et al., 2011; Horgan et al., 2013b).

We compared our results at Bungenstockrücken against five existing GL datasets (Table 2.1).

Table 2.1. Existing grounding line datasets used in this study to compare to our ICESat-2 RTLA results.

Grounding line dataset	Continuous line /discrete points	Satellite(s)	Method	Acquisition date	Reference
MEaSUREs Point F	Line	RADARSAT-2	DInSAR	2009	Rignot et al. (2016)
ICESat Point F	Points	ICESat	RTLA	2003-2009	Brunt et al., (2010a)
ICESat Point F_2 (the maximum inland flexure limit at high tide along eight individual ICESat ground tracks at Bungenstockrücken)	Points	ICESat	RTLA	2003-2009	Brunt et al. (2011)
ICESat-2 Point F	Points	ICESat-2	RTLA	March 2019 – September 2020	Li et al. (2022b)
ASAID Point I_b (Antarctic Surface Accumulation and Ice Discharge Project)	Line	Landsat-7 ICESat	Photo-clinometry and laser altimetry	Landsat-7: 1999-2003 ICESat: 2003-2009	Bindschadler and Choi (2011)
ICESat-2 Point I_b	Points	ICESat-2	Laser altimetry	March 2019 – September 2020	Li et al. (2022b)

2.4. Results

2.4.1. Extent of tidal grounding line migration at Bungenstockrücken

Our results reveal the spatial pattern of tidal GL migration at Bungenstockrücken across a ~1,300 km^2 zone of ephemeral grounding (Fig. 2.4). Across the central part of the study area (between Areas A and B), we observe the inland limit of tide flexure (Point F) to migrate by 5 to 15 km across the GZ, although the total migration distance may be greater in regions where the full tide range has not yet been sampled by ICESat-2. In this central region, Point F measured at the highest tides consistently reaches several

kilometres further inland than the MEaSUREs GL, and as far inland as the ICESat-2 break in slope. The spatial pattern of short-term tidal GL migration is not consistent across the region, with the most migration observed in Areas A and B (Fig. 2.4a).

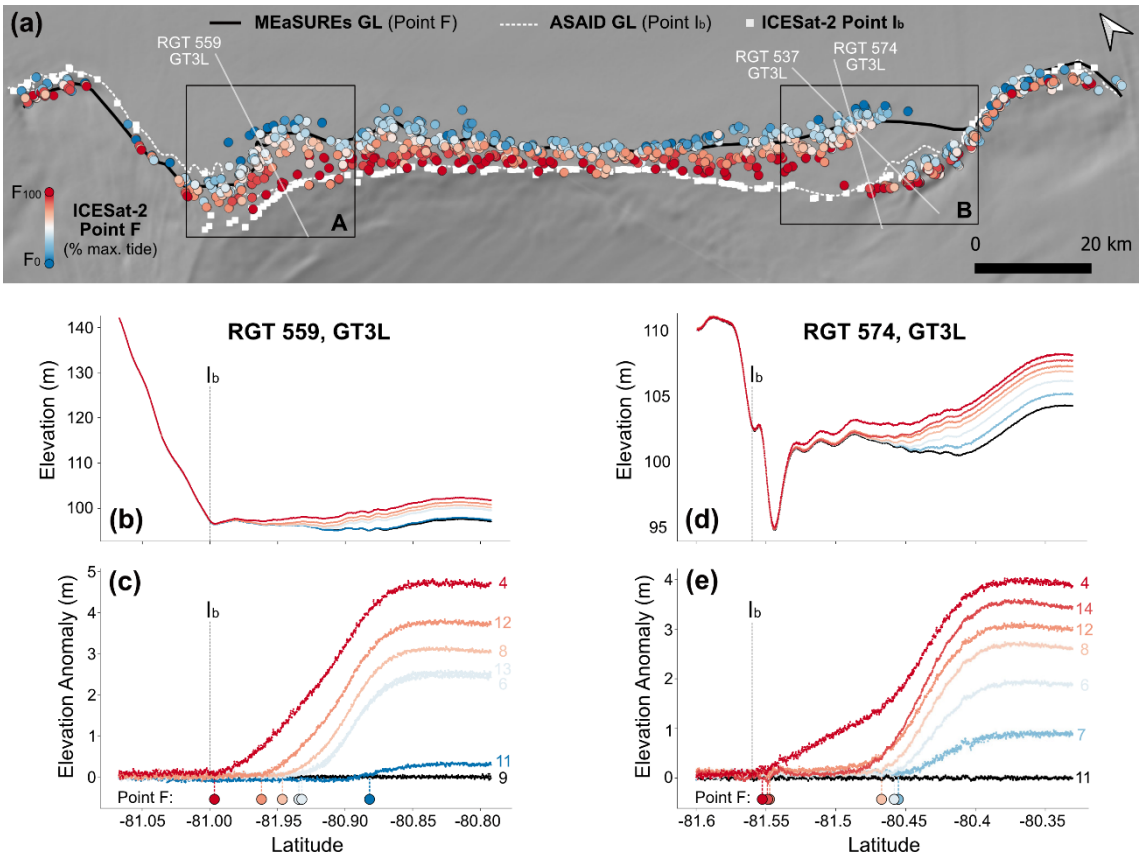


Figure 2.4. Tidal GL migration at Bungenstockrücken, measured by ICESat-2 RTLA. (a) The location of Point F at every sampled repeat cycle per ICESat-2 ground track is coloured by percent of maximum tide height, overlain on the Reference Elevation Model of Antarctica (REMA) 8 m DEM (Howat et al., 2018), MEaSUREs GL (Rignot et al., 2016), ASAID break in slope GL (Bindschadler & Choi, 2011) and the most recent ICESat-2 derived break in slope (Point I_b) along each ground track (Li et al., 2022b). The two areas with the largest observed GL migration are highlighted as Areas A and B, and the locations for RGT 559 GT3L, 537 GT3L and 574 GT3L are shown. (b-c) The repeat elevation profiles and anomalies of RGT 559 GT3L, with repeat cycles coloured by tide (as percent of maximum tide height) and labelled in (c). The location of ICESat-2 Point I_b is marked with a vertical dashed line (Li et al., 2022b). (d-e) The equivalent repeat elevation profiles and anomalies for RGT 574 GT3L.

In Area A and across the central section we observe a fairly consistent migration of Point F with the tide. This is exemplified by the pattern of RGT 559 GT3L (Fig. 2.4b,c), where we observe Point F migrating progressively further inland as tides increase, totalling 10.4 km of GL migration across the ~4.5 m sampled tide range (90.3% of total tide range). At the highest sampled tide of +2.08 m (cycle 4), Point F reaches as far inland as Point I_b, but since 7% of tides experienced in the region exceed +2.08 m, it is possible that flexure extends even further inland at these higher tides. In Area B, we observe two main clusters of Point F, possibly indicating the presence of two stable GL locations (one landward and one seaward) depending on the tide. This pattern can be seen in the surface and anomaly profiles of RGT 574 GT3L (Fig. 2.4d, e), which show ~11.5 km of separation between the seaward GL position near -81.45° S and the landward GL position near 81.55° S. Similarly to RGT 559 GT3L, the landward GL position at the highest sampled tide for RGT 574 GT3L coincides with the ICESat-2 Point I_b, just inland of the large surface undulation visible in the elevation profile (Fig. 2.4d). We note that in parts of Area B the landward GL position extends up to 5 km further inland than the ASAID Point I_b, up to 3 km beyond the ICESat-2 Point I_b, and is positioned around the prominent surface undulations visible in the ice surface topography.

In the areas west of Area A and east of Area B, Point F is consistently located just inland (< 2 km) of the ASAID and ICESat-2 break in slope with little tidal migration. This is consistent with the surface features of a typical GZ (i.e. non-ice plain) (Schoof, 2011), indicating that these regions are beyond the edges of the ice plain.

2.4.2. Long-term grounding zone change at Bungenstockrücken

To assess if there has been any long-term GZ change in our study region, we compared our results to previous GL datasets (Fig. 2.5). By locating multiple Point F positions along each ground track between high and low tide, we have been able to assess almost the entire width of the zone of ephemeral grounding at Bungenstockrücken for the first time. It is difficult to make a direct comparison to other GL products (Fig. 2.5a, b), which only locate a single position of Point F (Rignot et al., 2016; Brunt et al., 2010a; Li et al., 2022b). Nonetheless, we see that across the central

section of Bungenstockrücken, the ICESat-2 derived Point F positions for the highest ~60% of tides are located consistently inland of the MEaSUREs GL, by ~2–10 km (Fig. 2.5a). The ICESat-derived Point F positions are mostly located towards the middle of the band of our ICESat-2-derived Point F positions (Fig. 2.5a), although the maximum inland Point "F_2" positions (Brunt et al., 2011) match more closely our ICESat-2-derived Point F positions at high tide. There has been little long-term change in the position of Point I_b between ICESat, ASAID and ICESat-2, apart from a few locations in Areas A and B where we observe several kilometres of landward migration (Fig. 2.5c).

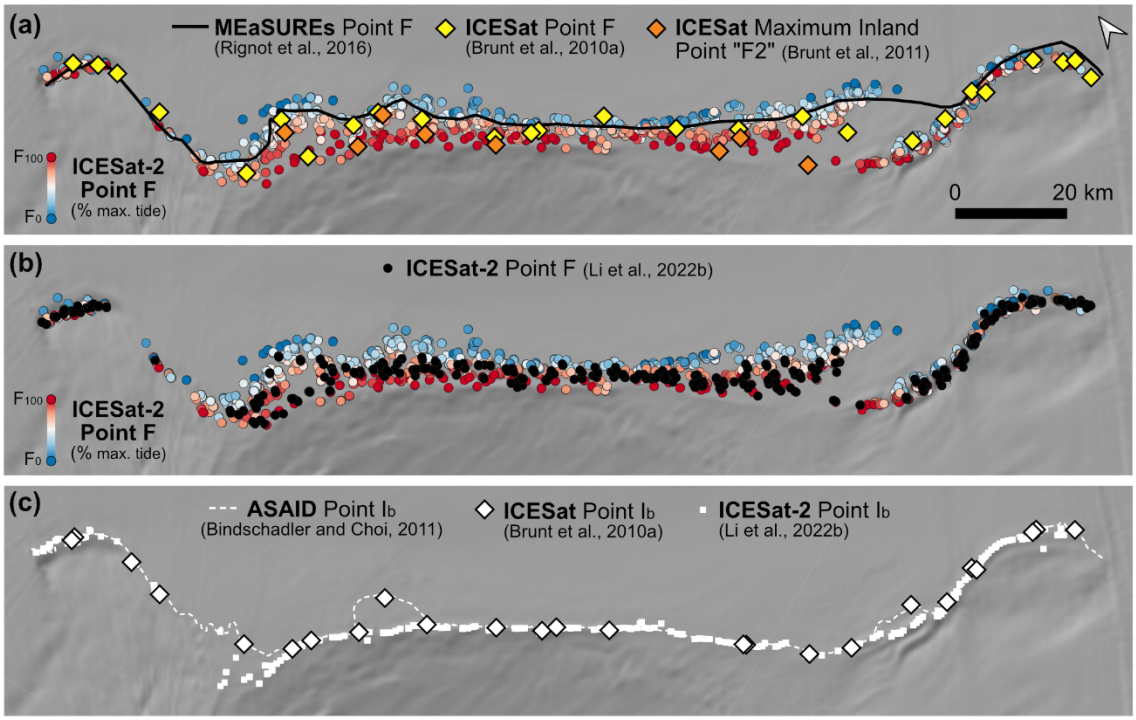


Figure 2.5. (a) Comparison of the ICESat-2 derived Point F positions at Bungenstockrücken to the following: (i) the ICESat-derived Point F (Brunt et al., 2010a), (ii) the ICESat-derived maximum inland Point F_2 (Brunt et al., 2011), and (iii) the MEaSUREs GL (Rignot et al., 2016), derived from 2009 RADARSAT-2 data. (b) Comparison of the ICESat-2-derived Point F positions per repeat cycle from this study to the ICESat-2-derived Point F dataset from Li et al. (2022b) that locates a single Point F per ground track. (c) Comparison between the Point I_b from ASAID (Bindschadler & Choi (2011); derived from Landsat-7 and ICESat), ICESat (Brunt et al., 2010a) and ICESat-2 (Li et al., 2022b).

2.4.3. Modes of tidal grounding line migration

We investigated the relationship between modelled tide height, tide phase and GL migration distance for the ICESat-2 ground tracks at Bungenstockrücken, and identified four distinct modes of tidal GL migration (Fig. 2.6). We manually classified these modes based on visual assessment of the most dominant behaviour. To increase confidence in the classification, we included only tracks where > 2 m of the tide range was sampled and with a total tidal GL migration distance > 1 km. This removes tracks where small uncertainties in GL position associated with tide phase, basal properties and long-term surface change are sufficient to obscure the detail in the patterns of GL migration required for this type of classification.

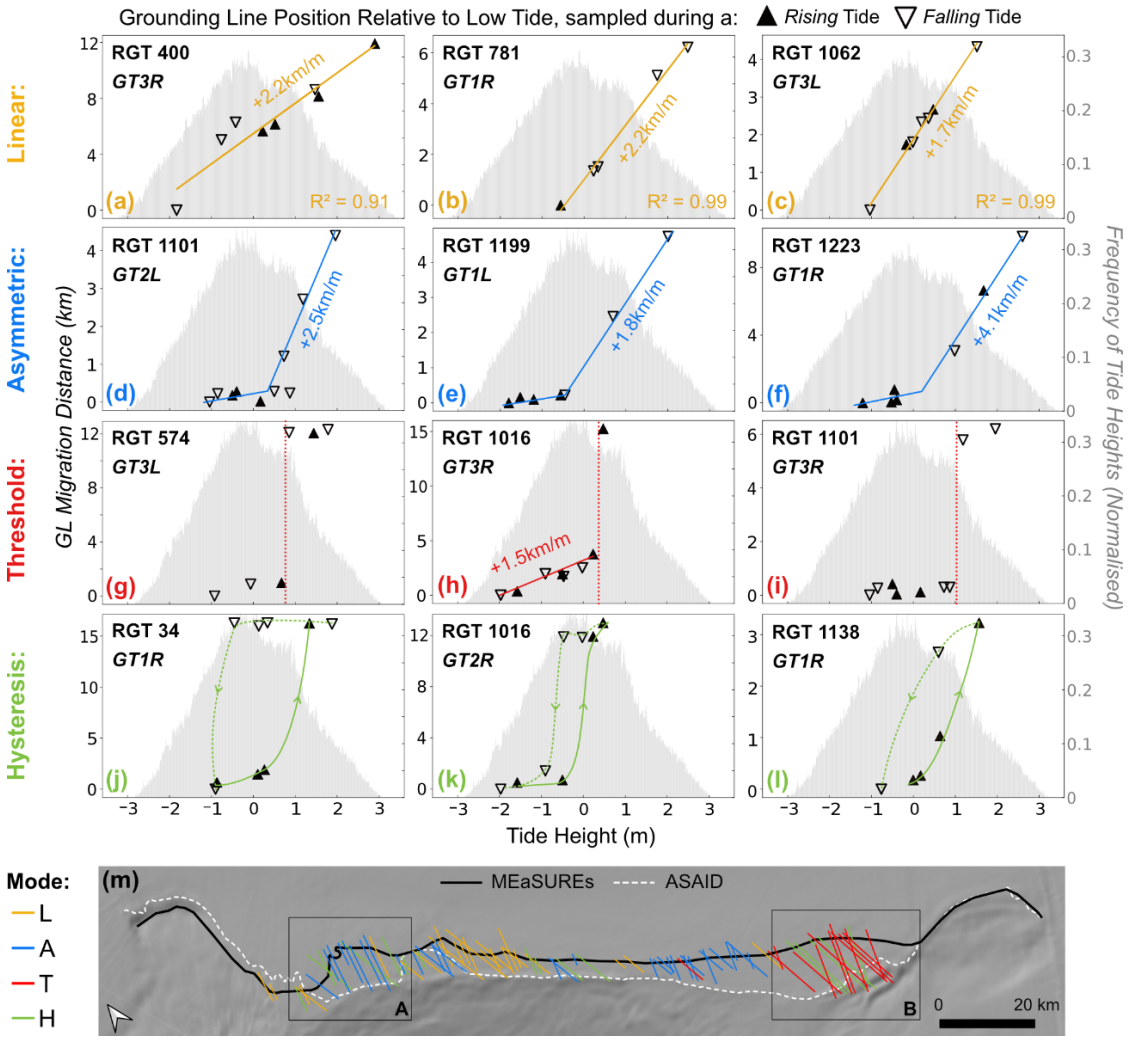


Figure 2.6. Four modes of tidal grounding line migration observed along ICESat-2 ground tracks at Bungenstockrücken. Three examples are shown per mode, which are classified from top to bottom as the following: (a–c) linear, with a linear relationship between tide height and GL migration distance; (d–f) asymmetric, with higher tides causing an increased rate of GL migration; (g–i) threshold, with a sharp tide threshold above which there is significant GL migration; and (j–l) hysteresis, with a difference in the impact of tidal variability on GL migration during the rising- vs. falling-tide phase. In each example we show the along-track migration distance between each Point F and Point F measured at the lowest-sampled tide as a function of coincident tide height from CATS2008 (Howard et al., 2019). Note the variable *y*-axis scale between ground tracks. The orientation of the triangle indicates whether the repeat cycle was sampled during a rising- or falling-tide phase. Histograms show the distribution of tide heights experienced across a single year, centred on 1 January 2020. (m) Map of Bungenstockrücken showing ICESat-2 ground tracks coloured by migration mode (excluding tracks with < 1 km tidal migration or < 2 m tide range sampled).

(1) **Linear** (Fig. 2.6a–c): In this mode we observe a *linear* relationship between tide height and GL migration distance. Within the sampled tide range, the GL migrates by 2.2 km with every metre of tidal change in Fig. 2.6a–b, and by 1.7 km m^{-1} in Fig. 2.6c. Considering a simplified semidiurnal spring tide regime where the tide rises from minimum (-3 m) to maximum (+3 m) within 6 h, this could translate to an average GL retreat rate of about 2 km h^{-1}. We observe little difference between GL positions sampled at rising vs. falling tides. However, we note that, for RGT 781 GT1R (Fig. 2.6b) there is only one Point F measured during falling tide, and for all ground tracks we cannot determine whether the linear response extends out to the most extreme tides. The linear mode of tidal GL migration is seen on ground tracks across the study area, but particularly clustered east of Area A (Fig. 2.6m).

(2) **Asymmetric** (Fig. 2.6d–f): In this mode there is an *asymmetric* relationship between tide height and GL migration, with a large increase in the GL migration rate observed at higher tides. For tides below about +0.5 m in Fig. 2.6d and below 0 m in Fig. 2.6e–f, Point F positions are clustered close together, indicating that there is little tidal GL migration within the lower tidal range. However, as the tide increases beyond this point the rates of GL migration increase sharply to linear rates of +2.5 km m^{-1} in Fig. 2.6d, +1.8 km m^{-1} in Fig. 2.6e and +4.1 km m^{-1} in Fig. 2.6f. Again, outside of the sampled tide range the magnitudes and modes of GL migration are unknown. Ground tracks with an asymmetric mode of tidal GL migration are mainly clustered in Area A and just west of Area B (Fig. 2.6m).

(3) **Threshold** (Fig. 2.6g–i): In this mode there is little GL migration up to a certain tide *threshold*, beyond which the GL migrates significantly with just a small increase in tide. The tide threshold in Fig. 2.6g is at ~+0.7 m and at ~+0.4 m in Fig. 2.6h, and in both examples a < 0.3 m rise of the tide across the threshold causes the GL to migrate inland by over 10 km. At peak spring tide (across the full 6 m tide range) this could feasibly occur within 18 min, translating to a possible maximum GL migration rate exceeding 30 km h^{-1}. On either side of the threshold in Fig. 2.6g and i, further tide change does not cause much more GL migration. This supports the

interpretation that in some locations two fairly stable GL positions (landward and seaward) can exist, as observed in Area B (Fig. 2.4). Considering the histogram of tide distributions, we can infer from this that the GL is at the landward position ~26% of the time in Fig. 2.6g, ~38% in Fig. 2.6h and ~22% in Fig. 2.6i. The majority of ground tracks with threshold tidal GL migration mode are located in Area B (Fig. 2.6m).

(4) **Hysteresis** (Fig. 2.6j–l): In this mode there is a *hysteresis* between tidal forcing and GL migration, related to the *phase* of the sampled tide at each measurement of Point F. This means we observe a different GL migration behaviour between rising and falling tides. For example, along RGT 34 GT1R (Fig. 2.6j) we note a landward and seaward cluster of Point F positions separated by about 15 km, similar to the threshold pattern seen in Fig. 2.6g–i. However, instead of a single tidal threshold that defines if the GL is in the landward or seaward position, in Fig. 2.6j we observe two different thresholds for the rising- and falling-tide phases. From this we infer that at the lowest tides the GL is located in the seaward position, but as the tide rises and crosses some threshold between +0.5 m and +1.2 m there is enough buoyant uplift force to unground the ice. This then causes ocean water to intrude into the GZ cavity and, due to the likely very flat bed, allows the GL to migrate by up to 15 km to its landward position. As the tide rises beyond +1.2 m, the GL does not migrate any further within the sampled tide range. However, as the tide turns and falls below +0.5 m there is not an immediate re-advance of the GL to its seaward position. Instead, the GL is observed to remain at its landward position until the tide has fallen beneath some secondary threshold at about -0.8 m. A similar, if less pronounced, hysteresis mode is observed in Fig. 2.6k–l. Hysteresis is observed on ground tracks across the study area but particularly in Areas A and B and close to ground tracks with asymmetric and threshold modes (Fig. 2.6m).

The spatial pattern of tidal GL migration at Area B confirms the presence of a landward and seaward GL, with the location at any given epoch varying between these depending on the tide (Fig. 2.7a–c). The repeat elevation profiles and anomalies of RGT

537 GT3L reveal more detail about the hysteresis mechanism observed in this region (Fig. 2.7d–g). Along this ground track, cycles 9 and 12 are sampled at a very similar absolute tide height (~0.25 m higher at cycle 9 vs. 12), but their elevation anomaly profiles look very different (Fig. 2.7f–g). This can be explained by comparing the coincident tide phases, which shows that cycle 9 was sampled during a rising tide, whereas cycle 12 was sampled during a falling tide. The extra bump further inland in the anomalies for cycle 12 (between -81.5° S and -81.57° S; Fig. 2.7g) indicates that the ice shelf surface between the seaward and landward GLs has not yet fully recovered from its high tide position. We discuss the potential causes and implications of this in Sect. 2.5.

We note that the four modes of tidal GL migration described here are not necessarily discrete categories. This is highlighted in Fig. 2.6h, which shows that along RGT 1016 GT3R we observe both linear and threshold behaviours in different parts of the tidal cycle. Hysteresis may also be superimposed on top of the other modes, as is arguably visible in Fig. 2.6a, but will become much more clearly identifiable as more repeats are acquired by ICESat-2. We emphasise that there is greater uncertainty in the categorisation of these modes where there are gaps in the sampling of certain tidal ranges, for example above +0.5 m in Fig. 2.6h and k, and there is subjectivity introduced by the manual classification of modes. This could explain the overlap between tracks with different modes in Fig. 2.6m, and particularly those with hysteresis. Our ability to understand and identify these different tidal behaviours will greatly improve as ICESat-2 collects an increasing volume of repeat measurements over the GZ, which should sample more of the tide range. This will improve our confidence in the classification of different modes of tidal GL migration.

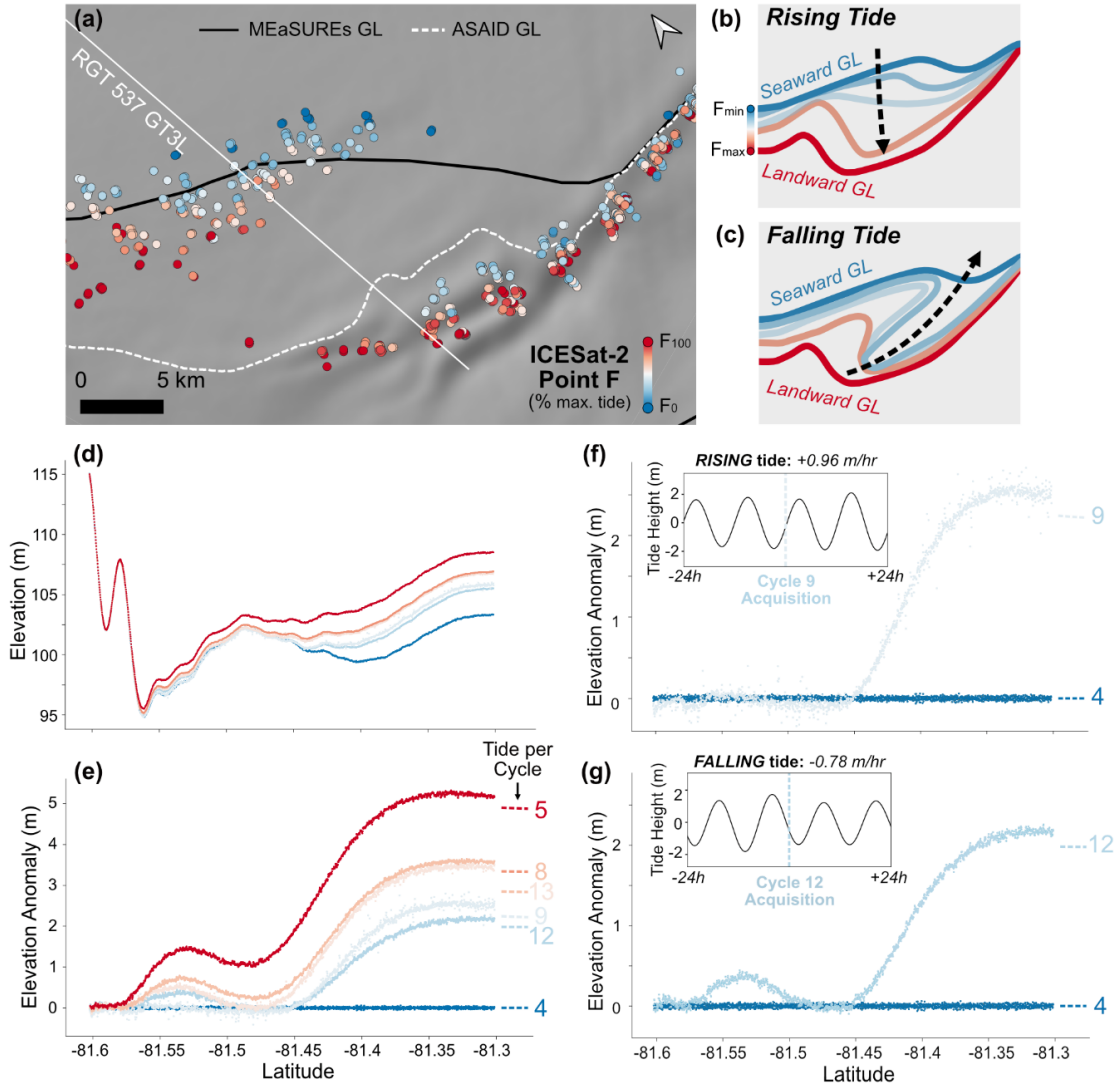


Figure 2.7. (a) The spatial pattern of tidal GL migration observed in Area B, Bungenstockrücken. Point F identified for every repeat cycle of each ICESat-2 ground track is coloured by percent of maximum tide height. (b–c) Schematics depicting the flow of water in between the seaward and landward GL positions inferred from ICESat-2 RTLA results in Area B, during the rising- and falling-tide phase. (d–e) The repeat elevation profiles and anomalies of RGT 537 GT3L, calculated using the *lowest-sampled tide* reference profile from cycle 4. Repeat cycles are coloured by tide (as percent of maximum tide height), and the cycle numbers are labelled in (e) alongside the CATS2008 modelled tide heights, differenced from the tide at cycle 4. (f–g) The individual elevation anomalies for cycles 9 and 12 against the lowest-sampled tide profile of cycle 4. Inset panels show the time series of tide heights for the 24 h before and after the time of ICESat-2 overpass at each cycle, showing the coincident tide phase and velocity.

2.5. Discussion

The improved repeat-track sampling capabilities of ICESat-2 together with our updated RTLA methodology offers several advantages over other satellite-based techniques for monitoring tidal GZ behaviour. Using this approach, our observation of widespread short-term tidal GL migration at Bungenstockrücken has implications for how long-term change is assessed and interpreted and for how the GL is represented in models. Furthermore, monitoring the dynamic movement of the GL provides an independent satellite method to illuminate bed characteristics and processes that can influence stability in the GZ region. We expand on each of these implications below.

2.5.1. Advantages of our ICESat-2 RTLA method for monitoring tidal grounding line behaviour

First, the use of ICESat-2 itself offers several advantages that improve the spatial sampling of tidal GL behaviour compared to other satellites. Its track spacing and six-beam pattern greatly increases the density of measurements compared to ICESat, with 402 separate ground tracks crossing the Bungenstockrücken GZ (using the six beams from 67 ICESat-2 RGTs), compared to 23 ICESat tracks. There is also an improvement in along-track sampling, with ATL06 surface height measurements calculated every 20 m along-track (averaged from 40 m overlapping segments), compared to a spacing of 172 m with ICESat (Schutz et al., 2005). This allows us to better resolve finer-scale details of the shape and configuration of the GL and observe how these may be affected by the tide. Furthermore, ICESat-2's repeat-track configuration and sensitivity to low-amplitude tidal variations allow us to attribute GL migration to specific tidal states, which is not possible with CryoSat-2 radar altimetry (Dawson & Bamber, 2017). ICESat-2 coverage also extends to 88° S, enabling observations in GLs located further south than the limit of most DInSAR coverage.

Second, the use of our updated RTLA technique improves the temporal sampling of tidal GL behaviour. All previous RTLA approaches with both ICESat and ICESat-2 used a mean reference profile calculated from all sampled cycles to derive a single Point F per track (Fricker & Padman, 2006; Fricker et al., 2009; Brunt et al., 2010b; Li et al., 2020,

2022a, b). Our method, by using the lowest-sampled tide as the reference profile, allows us to locate multiple positions of Point F along each ground track as it migrates with the tide. This produces GL measurements at fine temporal resolution, which enables a closer investigation of tidal GZ processes that occur over hourly to daily timescales. Within the time period of this study, we locate up to 11 Point F positions per ground track, each sampled at a different tide, totalling 2402 measurements across the 402 ground tracks. The number of valid measurements per ground track (of a maximum possible 13) largely depends on the number of repeats obscured by cloud cover. As more cycles of ICESat-2 data are acquired in the future, the temporal sampling of tidal GZ behaviour will continue to increase.

2.5.2. Implications for grounding line monitoring

Our observation of up to 15 km of tidal GL migration across the Bungenstockrücken ice plain is one of the largest migration values reported in Antarctica, comparable to the ~15 km found at the Amery GL in DInSAR by Chen et al. (2023). The signal is an order of magnitude higher than the fastest annual average GL retreat of 1.8 km yr^{-1} observed at Pine Island Glacier between 1992 and 2011 (Park et al., 2013) and several orders of magnitude higher than average long-term Antarctic GL migration rates (Konrad et al., 2018). For comparison, the highest estimated deglaciation retreat rates from palaeo-records are > 2.1 and > 10 km yr^{-1} for Thwaites and Larsen A, respectively (Dowdeswell et al., 2020; Graham et al., 2022). Therefore, to accurately measure long-term GZ change it is necessary to isolate the spatially variable pattern of tidal GL migration. At Bungenstockrücken, the observed difference between the MEaSUREs GL and the ICESat-2 derived Point F positions (Fig. 2.5a) could suggest that there has been either up to 10 km of GL retreat since 2009, or no change, depending on whether the MEaSUREs GL was produced from data sampled at high or low tides. This shows the value of providing a precise time stamp in addition to the acquisition date when producing a GL data product, as the tide amplitude at the time of measurement will inform our interpretation about whether a short-term, temporary tidal fluctuation or a longer-term dynamic change has occurred. Similarly, in this particular location, it is also difficult to quantify any long-term GL migration between the ICESat and ICESat-2

records (Fig. 2.5a) because the signal is dominated by tidal variability and different methods have been used to derive Point F. The fact that the small number of ICESat-derived maximum inland Point F_2 positions from Brunt et al. (2011) are broadly consistent with our highest tide ICESat-2 Point F positions, suggests that there has not been significant retreat of the maximum inland flexure limit over the past 10 to 15 years.

Bungenstockrücken provides a reasonable upper bound for rates of tidal GL migration around the ice sheet, as it is located in an ice plain region with low bed slopes and one of the highest tide ranges in Antarctica. Although tidal migration is likely to be much smaller at most Antarctic GLs (depending on tide range and bed properties, including slope and friction coefficient), even an order of magnitude less may still be sufficient to obscure early signs of long-term retreat in response to ice shelf thinning (Milillo et al., 2017; Li et al., 2023) and to impact ice dynamics. Therefore, when assessing long-term GL migration rates from sparse observations of GL location through time, we must consider the tidal state associated with each measurement epoch. Ideally, long-term GL location estimates should be made at the same tidal state or tide difference; however, given the scarcity of GL measurements in most locations, this has historically not been feasible. In lieu of this, our updated ICESat-2 RTLA methodology could be applied around the ice sheet margin to provide a constraint on the expected tidal range and mechanisms of GL movement. This will enable better evaluation of the impact of tides on previously-derived estimates of GL position, and ultimately improve the confidence with which we can assess long-term GL change.

The identification of different modes of tidal GL migration using ICESat-2 RTLA (Fig. 2.6) could be used to identify regions that are particularly sensitive to ice thickness changes, similar to Schmeltz et al. (2001) who showed that areas of ephemeral grounding can reveal subtle changes in ice thickness. In regions with a threshold or hysteresis mode of tidal GL migration, an observed decrease in the tide threshold that defines whether the GL is located in the landward or seaward position could indicate a retreat of the GL and signal dynamic ice thinning. Conversely, if the tide threshold rises it could signal GL advance and ice thickening. We suggest that Area B at Bungenstockrücken (Fig. 2.7) would be an ideal place to monitor this, with its wide zone of ephemeral grounding (up

to 15 km) and numerous ICESat-2 tracks exhibiting either threshold or hysteresis GL migration modes. Monitoring ephemeral grounding in this way could enable us to discriminate between inferred thickness changes due to changing firn-air content, and true ice thickness change (Moholdt et al., 2014). This is useful for detecting early signs of ice sheet change, particularly as the accuracy with which altimeters can measure long-term ice thickness change at the GL is limited by our lack of knowledge about the flotation state of the ice across the GZ (further complicated by tidal GL migration).

2.5.3. Implications for modelling tidal ice shelf flexure and grounding line migration

The representation of GZ processes in ice sheet models strongly impacts projections of future ice sheet mass balance (Arthern & Williams, 2017). The 15 km observed tidal GL migration at Bungenstockrücken is much larger than standard model grid spacing at the GL, which is typically less than 2 km, and down to 250 m where mesh refinement is applied (Cornford et al., 2020) . Similarly, the time step of an ice sheet model is generally much longer than 1 d; therefore, prescribing a sub-daily change in GL position is not generally possible. It is beyond the scope of this study to parameterise tidal GL effects in ice sheet models at dissimilar scales, but any "short-term fixed" GL derived from observations must be applied in a consistent manner, whether this is using the highest, lowest or mean tide position. This choice of a consistent GL is complicated by the fact that different satellite-derived GL products use different surface proxies (i.e. Points F vs. I_b), each of which relate differently to the sharp basal stress boundary, which is the parameter that we generally want to represent in models. Moreover, the extent to which tidal GL migration can blur the basal stress boundary in areas of ephemeral grounding is largely unknown.

Our results at Bungenstockrücken show that the use of ICESat-2 RTLA to map Point F across the tide cycle can improve our understanding of the relationship between short-term GL migration and the long-term ice sheet surface profile. We observe that Point F is located seaward of Point I_b for most of the tidal cycle, but see that at the highest tides it consistently migrates as far inland as Point I_b (Fig. 2.4). As the break-in-slope (I_b) is one of the key surface signatures of the change in basal shear stress at the GL (Schoof,

2011), these observations imply that from a stress-balance perspective the ice sheet geometry is controlled by the furthest inland position that Point F reaches at the highest tides. Although the ice shelf re-grounds seaward of the break-in-slope at low tides, the variable stresses over the ice plain area do not appear to substantially affect the surface profile. There are substantial deviations between flexure-derived GLs and those derived from break-in-slope, which may therefore be partly explained by sampling of GL positions at either mean or non-maximum tides. We propose that the information derived from ICESat-2 RTLA, by better constraining the extent and pattern of tidal GL migration, could be used to better inform the choice of GL in models where observations are used.

Our results provide observational validations for different numerical models of tidal ice flexure and GL migration. The existence of different modes of tidal GL migration within a region experiencing similar tidal forcing indicates that there is a spatial heterogeneity in local bed properties. Therefore, in regions like Bungenstockrücken that experience large tidal GL migration, models of tide flexure that do not allow for movement of the GL (Holdsworth, 1969; Schmeltz et al., 2002; Walker et al., 2013) cannot produce realistic representations of the basal stress or GL velocity change. Sayag and Worster (2013) developed an elastic beam model coupled to an elastically deforming bed that allows the GL to migrate proportionally with tidal forcing. We observe a similar linear mode of GL migration within the sampled tide range along numerous ICESat-2 ground tracks at Bungenstockrücken (Fig. 2.6a–c), as has also recently been observed in parts of West Antarctica using CSK DInSAR (Milillo et al., 2022). In contrast, Tsai & Gudmundsson (2015) modelled the GL as an elastic fracture problem forced by the tidally induced increase in ocean water pressure, concluding that tidally induced GL migration in areas with prograde bed slopes is asymmetric, with the GL migrating up to 9 times further inland at high tide than it migrates seaward at low tide. Along several ICESat-2 ground tracks at Bungenstockrücken we observe a similar kind of asymmetry in the mode of tidal GL migration (Fig. 2.6d–f). It is likely that the shape and stiffness of the bed exert strong controls over the mode of GL migration (Sayag & Worster, 2013), but independent bed information is generally not high enough resolution to further

inform our interpretation of the flexure patterns observed by our ICESat-2 RTLA method.

Our ICESat-2 observations can also inform the representation of elastic and viscous stresses in these models of tidal flexure and GL migration. Both the Sayag & Worster (2013) and Tsai & Gudmundsson (2015) models use purely elastic frameworks, justified due to the short timescales (< 12 h) over which the forcing acts. In reality, ice deforms viscoelastically (Reeh et al., 2003) and so these models overlook any time-dependent viscoelastic deformation that follows the initial elastic response to tides. The hysteresis mode of tidal GL migration observed at Bungenstockrücken (Figs. 2.5j–l and 6) reveals a time delay between the response of the ice shelf surface (and perhaps also the subglacial till) to tidal forcing. Similar observations in Greenland have shown a difference in the surface deflection profile between rising and falling tides, and have been well described by viscoelastic beam models that capture this lag between the change in the tide and the ice shelf response (Reeh et al., 2000, 2003; Wild et al., 2017). Currently no models of tidal flexure exist that use both a viscoelastic framework and allow for migration of the GL, but this may be necessary to better represent these kinds of processes in GZs subject to high tidal variability and could account for the discrepancies between model predictions and observations.

Modes of tidal GL migration and why they differ spatially can also provide insights into the underlying bed topography. As a specific example, we expect that the threshold mode of GL migration (Fig. 2.6g–i) is likely to only exist in regions with a very flat bed where the ice is very close to flotation, whereby a small increase in tide across this threshold can provide enough buoyant force to unground the ice and cause large GL migration. Area B at Bungenstockrücken is likely grounded over a very flat bed, as we observe a cluster of ground tracks with a threshold mode of tidal GL migration (Fig. 2.6m). While Brunt et al. (2011) presented a method to calculate bed slopes from tidal GL migration along ICESat tracks based on a hydrostatic assumption, this assumed a linear relationship between migration distance and tide height, which, as our findings indicate, is not necessarily valid in the GZ. Therefore, our results support the conclusion of Tsai & Gudmundsson (2015) of urging caution when quantitatively inferring bed slopes from

measurements of tidal GL migration. We note that changes in tidal GL behaviour on longer timescales can also provide insight into bed slopes, as was observed at Thwaites where the total width of the zone of ephemeral grounding increased from 0.5 km in 1996 to 2.5 km in 2016–17 as the GL retreated into a region of flatter bed topography (Milillo et al., 2019). There is therefore potential for gaining further information about the bed by identifying any changes in tidal migration modes over time.

The distribution of *modes* of tidal GL migration as well as the *width* and *rate* of tidal GL migration around Antarctic GZs is valuable for informing the choice of parameterisation of tidal flexure mechanisms, basal shear stress and/or basal melt in larger-scale ice sheet models. For example, Mosbeux et al. (2023) considered two different GL migration parameterisations to assess the impact of seasonal sea surface height variability on ice velocities over the Ross Ice Shelf. The first considered an asymmetric treatment of GL migration with elastic fracture mechanics introduced by Tsai & Gudmundsson (2015) and a constant bed slope, and the second defined migration using hydrostatic equilibrium of the GL with BedMap2 bed slopes. They found that the asymmetric treatment led to larger modelled ice shelf velocity variability that more closely matched GNSS observations. Given that the mechanism of migration varies spatially, even across relatively small distances (as we have demonstrated), obtaining reliable observations of the spatial distribution of these GL migration modes around Antarctica is needed to inform the parameterisation of GL processes in larger ice sheet modelling studies. Our study at Bungenstockrücken has successfully demonstrated how ICESat-2 RTLA can be used as a first step towards this.

2.5.4. *Insights into tidal processes in the ice shelf-ocean-subglacial system*

The cyclical, twice-daily ungrounding and tidal flushing of ocean water up to 15 km into the GZ has implications for several processes contributing to the net dynamics of this system (Fig. 2.8). Many of these processes are poorly understood with few observations, and so the use of ICESat-2 RTLA to study tidal GL behaviour in settings like Bungenstockrücken could provide important new insights and constraints.

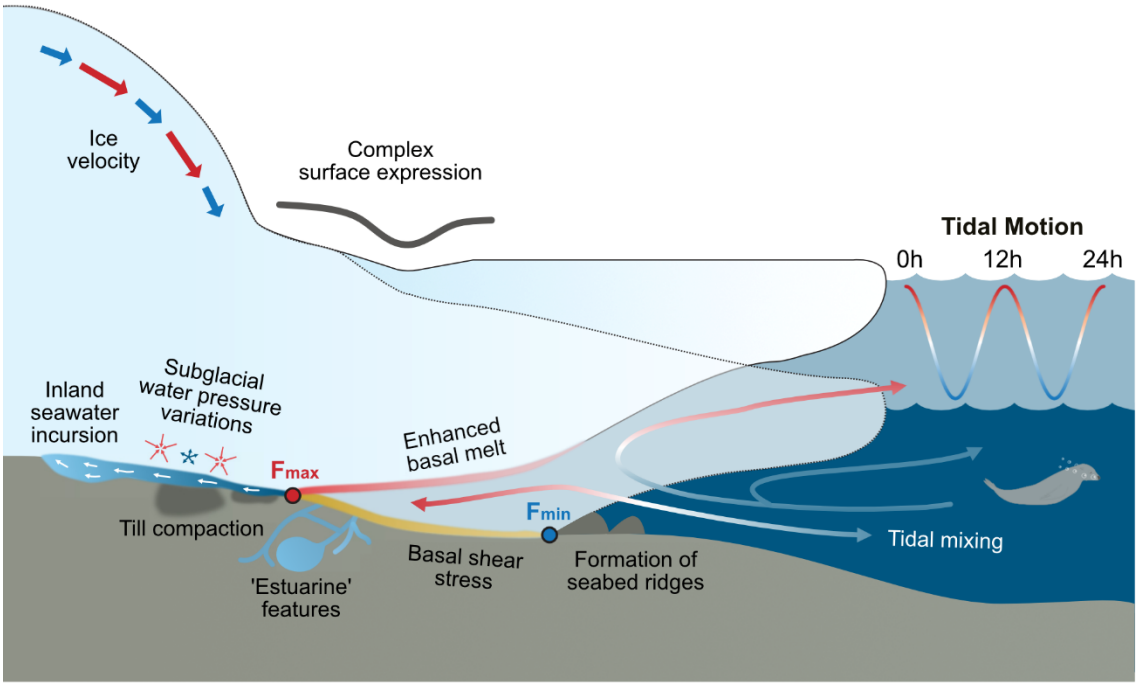


Figure 2.8. Schematic summarising impacts of tidal flexure and GL migration on the ice shelf-ocean-subglacial system. These include impacts on the following: ice velocity (Gudmundsson, 2007; Thompson et al., 2014; Robel et al., 2017, 2022; Mosbeux et al., 2023); GZ surface profile (e.g., Schoof, 2011); inland seawater incursion (Warburton et al., 2020; Robel et al., 2022); variations in subglacial water pressure (Rosier et al., 2015; Begeman et al., 2020); the formation of estuarine features in the GZ (Horgan et al., 2013a); enhanced basal melt (Makinson et al., 2011; Mueller et al., 2012); basal shear stress (Anandakrishnan et al., 2003); till compaction, leading to changes in basal lubrication (Walker et al., 2013; Christianson et al., 2013; Sayag & Worster, 2013); the formation of tidal seabed ridges (Dowdeswell et al., 2020; Graham et al., 2022); and ocean circulation through tidal mixing. The landward and seaward tidal GL positions are labelled as F_{max} and F_{min}.

Little is known about the oceanography close to most of the Antarctic GZ, but the ability to observe the tidal variability of cavity geometry with ICESat-2 RTLA will allow us to model the potential melt rates in these anomalous regions. At Bungenstockrücken, our results indicate that an additional ~1,300 km^2 of ice ungrounds twice-daily between low and high tide (Fig. 2.4), allowing the relatively warm ocean water to reach deeper into the GZ cavity and exposing this additional area to basal melt. The cold High Salinity Shelf Water (HSSW) beneath the Ronne Ice Shelf causes relatively low basal melt rates (compared to warmer regions like the Amundsen Sea that are affected by Circumpolar Deep Water), but depression of the seawater freezing point under pressure means it still has the capacity to melt ice at the GL (Nicholls & Østerhus, 2004; Makinson et al., 2011; Naughten et al., 2021). The very shallow water column (< 100 m) immediately seaward of Bungenstockrücken (Johnson & Smith, 1997) suggests that tidal mixing would be strong here and is likely to be enhanced as water is "pumped" in and out of the cavity as the GL migrates with the tides. Milillo et al. (2019) report significant basal melt over the entire zone of tidal GL migration at Thwaites, and such short-term tidal fluctuations in melt rate and tidal mixing have been shown to impact long-term GL retreat in less stable regions (Graham et al., 2022). Given that projections of future ice sheet mass loss are highly sensitive to basal melt at the GL (Arthern & Williams, 2017; Goldberg et al., 2019; Adusumilli et al., 2020), this once again calls into question the use of fixed GLs with zero melt in ice sheet models. The type of information about tidal GZ behaviour that we can derive from ICESat-2 RTLA will therefore be valuable to improve parameterisations of melt at the GL.

Variation in basal stresses in the GZ caused by tidal flexure and GL migration can also impact the flow of upstream and downstream ice. Grounding and ungrounding of the ice shelf throughout the tidal cycle has several effects: it changes the area affected by basal drag, modifies the driving stress through changes in surface slope (e.g., Makinson et al., 2012; Mosbeux et al., 2023), modulates hydrostatic and flexural stresses (e.g., Rosier & Gudmundsson, 2016), and impacts buttressing (e.g., Robel et al., 2017). Rosier & Gudmundsson (2020) concluded that the presence of tides enhances ice flow across the entire Filchner-Ronne Ice Shelf by 21%. Since ice velocities across the

Bungenstockrücken GL do not exceed ~5 m a^{-1} (Rignot et al., 2017), the impact of tidal GL migration on absolute flow speed here is likely to be low, but it may be more significant in faster flowing regions, such as the Rutford Ice Stream (Minchew et al., 2017).

Our results have implications for testing models and hypotheses in subglacial hydrology. It has been suggested that tidal ice shelf flexure acts to pump ocean water upstream of the GL into the subglacial hydrological system, with implications for basal lubrication, basal melt and till compaction (Christianson et al., 2013; Horgan et al., 2013a; Sayag & Worster, 2013; Walker et al., 2013; Drews et al., 2017; Robel et al., 2022). Airborne radar data indicate the possible presence of brackish water several kilometres inland of the Bungenstockrücken GL (Corr, 2021), which may provide evidence for upstream seawater incursion driven by tidal GL migration. Modelling of this process by Warburton et al. (2020) indicated that water is pumped upstream into the subglacial environment much faster during a rising tide than it drains as the tide falls. Similarly, Stubblefield et al. (2021) model the formation of an extended grounding zone during the falling tide phase, comprising a thin layer of water that drains more slowly than the seaward GL migration due to the flexural response of the ice. The hysteresis mode of GL migration observed at Bungenstockrücken (Figs. 2.6j–l and 7) suggests there is a similar lag in the response of the ice shelf surface to tidal forcing between rising- and falling-tide phases, which could provide observational support for this theory. For example, the pattern observed in Area B (Fig. 2.7) is likely to indicate that a subglacial channel or cavity exists in between the seaward and landward GL positions that fills with water at high tide (above a certain threshold). As the tide falls, the water drains away more slowly and the ice around the seaward GL position (a possible topographic high) regrounds before the landward cavity has fully emptied, forcing the water to be flushed out from this channel to the east (Fig. 2.7b, c). This could be a similar pattern to tidal beach drainage, and supports the idea of "estuary" type features at the ice sheet margins (Horgan et al., 2013a). Knowledge of the modes of tidal GL migration around the coast derived from ICESat-2 RTLA will be useful for constraining such regional models.

2.6. Summary and outlook

We have presented an updated method for determining Antarctic ice shelf grounding line (GL) location from ICESat-2 repeat track laser altimetry (RTLA). We show that, by using the elevation profile at the lowest-sampled tide as the reference profile for calculating anomalies, it is possible to locate the inland limit of tidal flexure at different stages of the tidal cycle. This temporal resolution provides insights into grounding zone (GZ) processes on tidal timescales that are difficult to observe with other methods. We have applied the technique to the GZ of an ice plain north of Bungenstockrücken on the southern Ronne Ice Shelf, where we observe > 15 km of tidal GL migration. This is the largest reported distance of ephemeral grounding anywhere in Antarctica and demonstrates the necessity of accounting for short-term tidal GL migration to accurately measure long-term migration. It also calls into question the use of a fixed or slowly moving GL boundary in ice sheet models, which does not represent the full range of GL migration behaviour. Our updated ICESat-2 RTLA technique also allows us to observe different modes of tidal GL migration, and we classify four modes at the Bungenstockrücken ice plain: linear, asymmetric, threshold and hysteresis. This can provide observational validation for models of tidal ice shelf flexure, GL migration and subglacial hydrology at the GZ, and offers a tool for future explorations of bed characteristics, basal melt and basal shear stress in these sensitive parts of the ice sheet. We suggest that monitoring the change in extent and modes of tidal GL migration around Antarctica could provide vital early indications of wider ice sheet change.

Based on the findings of this study, we make four recommendations for future work:

(1) Any future satellite-derived measurement of GL position should be accompanied with a timestamp (at least to the closest hour), ideally also with coincident tide height and phase. For DInSAR this information should be provided per image, and for RTLA for both the reference and repeat cycle tides. This will allow a more robust assessment of the impact of tidal processes on individual measurements of the GL position.

(2) Future studies should scale this analysis up across Antarctica to derive a continent-wide dataset of the extent and mode of tidal GL migration. This could be used to improve confidence in long-term records of GL migration.

(3) Targeted ground-based surveys in regions subject to extreme tidal variability would be valuable to better understand the link between these surface observations and the processes taking place within and beneath the ice in GZs on tidal timescales. We suggest that Bungenstockrücken would be a suitable location, due to its high tidal signal, low ice velocity and crevassing, and current long-term stability which isolates the tidal signal from long-term change.

(4) The observations presented here have only been possible to obtain using ICESat-2. Therefore, it is crucial that we extend our satellite-based *repeat-track* sampling of ice sheet surface elevation beyond this satellite mission to continue this valuable record as ice sheets continue to respond to the changing climate.

Code Availability. The code developed for this study can be found at https://doi.org/10.5281/zenodo.8037209.

Data Availability. The ICESat-2 ATL06 data, ICESat-2 grounding zone products and the MEaSUREs grounding line product used in this study are available from the National Snow and Ice Data Center (NSIDC). The ASAID grounding line and ICESat-derived grounding zone products are available from the U.S. Antarctic Program Data Center.

Author Contribution. BF and OM planned the research; BF conducted the data analysis and wrote the manuscript. All authors provided insights in the interpretation of data, and reviewed and edited the manuscript.

Competing interests. The authors declare that they have no conflict of interest.

Acknowledgements. This work was led by BF at British Antarctic Survey (BAS) and the School of Earth and Environment at the University of Leeds. BF was supported by the Natural Environment Research Council (NERC) SENSE Centre for Doctoral Training (NE/T00939X/1). AEH was supported by the NERC DeCAdeS project (NE/T012757/1)

and the ESA Polar+ Ice Shelves project (ESA-IPL-POE-EF-cb-LE-2019-834). HAF was supported by NASA grant 80NSSC20K0977. LP was supported by the ESR ICESat-2 grant 80NSSC21K0911. The authors gratefully acknowledge the National Aeronautics and Space Administration for acquiring the ICESat-2 satellite data.

References

Adusumilli, S., Fricker, H. A., Medley, B., Padman, L., & Siegfried, M. R. (2020). Interannual variations in meltwater input to the Southern Ocean from Antarctic ice shelves. *Nature Geoscience, 13*(9), 616–620. https://doi.org/10.1038/s41561-020-0616-z

Alley, R. B., Blankenship, D. D., Rooney, S. T., & Bentley, C. R. (1989). Sedimentation beneath ice shelves — the view from ice stream B. *Marine Geology, 85*(2–4), 101–120. https://doi.org/10.1016/0025-3227(89)90150-3

Anandakrishnan, S., Voigt, D. E., Alley, R. B., & King, M. A. (2003). Ice stream D flow speed is strongly modulated by the tide beneath the Ross Ice Shelf. *Geophysical Research Letters, 30*(7). https://doi.org/10.1029/2002GL016329

Arendt, A., Scheick, J., Shean, D., Buckley, E., Grigsby, S., Haley, C., et al. (2020) 2020 ICESat-2 Hackweek Tutorials (Version 1.0.0) [Software]. Zenodo. https://doi.org/10.5281/zenodo.3966463

Arthern, R. J., & Williams, C. R. (2017). The sensitivity of West Antarctica to the submarine melting feedback. *Geophysical Research Letters, 44*(5), 2352–2359. https://doi.org/10.1002/2017GL072514

Begeman, C. B., Tulaczyk, S., Padman, L., King, M., Siegfried, M. R., Hodson, T. O., & Fricker, H. A. (2020). Tidal Pressurization of the Ocean Cavity Near an Antarctic Ice Shelf Grounding Line. *Journal of Geophysical Research: Oceans, 125*(4). https://doi.org/10.1029/2019JC015562

Bindschadler, R., & Choi, H. (2011). High-resolution Image-derived Grounding and Hydrostatic Lines for the Antarctic Ice Sheet (Version 1) [Dataset]. U.S. Antarctic Program (USAP) Data Center. https://doi.org/10.7265/N56T0JK2

Bindschadler, R., Choi, H., Wichlacz, A., Bingham, R., Bohlander, J., Brunt, K., et al. (2011). Getting around Antarctica: new high-resolution mappings of the grounded and freely-floating boundaries of the Antarctic ice sheet created for the International Polar Year. *The Cryosphere, 5*(3), 569–588. https://doi.org/10.5194/tc-5-569-2011

Bojinski, S., Verstraete, M., Peterson, T. C., Richter, C., Simmons, A., & Zemp, M. (2014). The Concept of Essential Climate Variables in Support of Climate Research,

Applications, and Policy. *Bulletin of the American Meteorological Society, 95*(9), 1431–1443. https://doi.org/10.1175/BAMS-D-13-00047.1

Brancato, V., Rignot, E., Milillo, P., Morlighem, M., Mouginot, J., An, L., et al. (2020). Grounding Line Retreat of Denman Glacier, East Antarctica, Measured With COSMO-SkyMed Radar Interferometry Data. *Geophysical Research Letters, 47*(7). https://doi.org/10.1029/2019GL086291

Brunt, K., Fricker, H. A., O'Neel, S., & Padman, L. (2010) ICESat-Derived Grounding Zone for Antarctic Ice Shelves (Version 1) [Dataset]. U.S. Antarctic Program (USAP) Data Center. https://doi.org/10.7265/N5CF9N19.

Brunt, K. M., Fricker, H. A., Padman, L., Scambos, T. A., & O'Neel, S. (2010). Mapping the grounding zone of the Ross Ice Shelf, Antarctica, using ICESat laser altimetry. *Annals of Glaciology, 51*(55), 71–79. https://doi.org/10.3189/172756410791392790

Brunt, K. M., Fricker, H. A., & Padman, L. (2011). Analysis of ice plains of the Filchner–Ronne Ice Shelf, Antarctica, using ICESat laser altimetry. *Journal of Glaciology, 57*(205), 965–975. https://doi.org/10.3189/002214311798043753

Catania, G., Hulbe, C., & Conway, H. (2010). Grounding-line basal melt rates determined using radar-derived internal stratigraphy. *Journal of Glaciology, 56*(197), 545–554. https://doi.org/10.3189/002214310792447842

Chen, H., Rignot, E., Scheuchl, B., & Ehrenfeucht, S. (2023). Grounding Zone of Amery Ice Shelf, Antarctica, From Differential Synthetic-Aperture Radar Interferometry. *Geophysical Research Letters, 50*(6), e2022GL102430. https://doi.org/10.1029/2022GL102430

Christianson, K., Parizek, B. R., Alley, R. B., Horgan, H. J., Jacobel, R. W., Anandakrishnan, S., et al. (2013). Ice sheet grounding zone stabilization due to till compaction. *Geophysical Research Letters, 40*(20), 5406–5411. https://doi.org/10.1002/2013GL057447

Ciracì, E., Rignot, E., Scheuchl, B., Tolpekin, V., Wollersheim, M., An, L., et al. (2023). Melt rates in the kilometer-size grounding zone of Petermann Glacier, Greenland, before and during a retreat. *Proceedings of the National Academy of Sciences, 120*(20), e2220924120. https://doi.org/10.1073/pnas.2220924120

Cornford, S. L., Seroussi, H., Asay-Davis, X. S., Gudmundsson, G. H., Arthern, R., Borstad, C., et al. (2020). Results of the third Marine Ice Sheet Model Intercomparison Project (MISMIP+). *The Cryosphere, 14*(7), 2283–2301. https://doi.org/10.5194/tc-14-2283-2020

Corr, H. (2021). Processed airborne radio-echo sounding data from the GRADES-IMAGE survey covering the Evans and Rutford Ice Streams, and ice rises in the Ronne Ice Shelf, West Antarctica (2006/2007) (Version 1.0) [Dataset] NERC EDS UK Polar Data Centre. https://doi.org/10.5285/C7EA5697-87E3-4529-A0DD-089A2ED638FB

Corr, H. F. J., Doake, C. S. M., Jenkins, A., & Vaughan, D. G. (2001). Investigations of an "ice plain" in the mouth of Pine Island Glacier, Antarctica. *Journal of Glaciology, 47*(156), 51–57. https://doi.org/10.3189/172756501781832395

Dawson, G. J., & Bamber, J. L. (2017). Antarctic Grounding Line Mapping From CryoSat-2 Radar Altimetry. *Geophysical Research Letters, 44*(23), 11,886-11,893. https://doi.org/10.1002/2017GL075589

Dawson, G. J., & Bamber, J. L. (2020). Measuring the location and width of the Antarctic grounding zone using CryoSat-2. *The Cryosphere, 14*(6), 2071–2086. https://doi.org/10.5194/tc-14-2071-2020

Depoorter, M. A., Bamber, J. L., Griggs, J. A., Lenaerts, J. T. M., Ligtenberg, S. R. M., van den Broeke, M. R., & Moholdt, G. (2013). Calving fluxes and basal melt rates of Antarctic ice shelves. *Nature, 502*(7469), 89–92. https://doi.org/10.1038/nature12567

Dowdeswell, J. A., Batchelor, C. L., Montelli, A., Ottesen, D., Christie, F. D. W., Dowdeswell, E. K., & Evans, J. (2020). Delicate seafloor landforms reveal past Antarctic grounding-line retreat of kilometers per year. *Science, 368*(6494), 1020–1024. https://doi.org/10.1126/science.aaz3059

Drews, R., Pattyn, F., Hewitt, I. J., Ng, F. S. L., Berger, S., Matsuoka, K., et al. (2017). Actively evolving subglacial conduits and eskers initiate ice shelf channels at an Antarctic grounding line. *Nature Communications, 8*(1), 15228. https://doi.org/10.1038/ncomms15228

Dupont, T. K., & Alley, R. B. (2005). Assessment of the importance of ice-shelf buttressing to ice-sheet flow. *Geophysical Research Letters, 32*(4). https://doi.org/10.1029/2004GL022024

Dutrieux, P., De Rydt, J., Jenkins, A., Holland, P. R., Ha, H. K., Lee, S. H., et al. (2014). Strong Sensitivity of Pine Island Ice-Shelf Melting to Climatic Variability. *Science, 343*(6167), 174–178. https://doi.org/10.1126/science.1244341

Favier, L., Durand, G., Cornford, S. L., Gudmundsson, G. H., Gagliardini, O., Gillet-Chaulet, F., et al. (2014). Retreat of Pine Island Glacier controlled by marine ice-sheet instability. *Nature Climate Change, 4*(2), 117–121. https://doi.org/10.1038/nclimate2094

Fricker, H. A., & Padman, L. (2006). Ice shelf grounding zone structure from ICESat laser altimetry. *Geophysical Research Letters, 33*(15), L15502. https://doi.org/10.1029/2006GL026907

Fricker, H. A., Coleman, R., Padman, L., Scambos, T. A., Bohlander, J., & Brunt, K. M. (2009). Mapping the grounding zone of the Amery Ice Shelf, East Antarctica using InSAR, MODIS and ICESat. *Antarctic Science, 21*(5), 515–532. https://doi.org/10.1017/S095410200999023X

Friedl, P., Weiser, F., Fluhrer, A., & Braun, M. H. (2020). Remote sensing of glacier and ice sheet grounding lines: A review. *Earth-Science Reviews, 201*, 102948. https://doi.org/10.1016/j.earscirev.2019.102948

Goldberg, D. N., Gourmelen, N., Kimura, S., Millan, R., & Snow, K. (2019). How Accurately Should We Model Ice Shelf Melt Rates? *Geophysical Research Letters, 46*(1), 189–199. https://doi.org/10.1029/2018GL080383

Graham, A. G. C., Wåhlin, A., Hogan, K. A., Nitsche, F. O., Heywood, K. J., Totten, R. L., et al. (2022). Rapid retreat of Thwaites Glacier in the pre-satellite era. *Nature Geoscience, 15,* 706–713. https://doi.org/10.1038/s41561-022-01019-9

Gudmundsson, G. H. (2007). Tides and the flow of Rutford Ice Stream, West Antarctica. *Journal of Geophysical Research, 112*(F4), F04007. https://doi.org/10.1029/2006JF000731

Gudmundsson, G. H., Paolo, F. S., Adusumilli, S., & Fricker, H. A. (2019). Instantaneous Antarctic ice sheet mass loss driven by thinning ice shelves. *Geophysical Research Letters, 46*(23), 13903–13909. https://doi.org/10.1029/2019GL085027

Hogg, A. E., Shepherd, A., Gourmelen, N., & Engdahl, M. (2016). Grounding line migration from 1992 to 2011 on Petermann Glacier, North-West Greenland. *Journal of Glaciology, 62*(236), 1104–1114. https://doi.org/10.1017/jog.2016.83

Hogg, A. E., Shepherd, A., Gilbert, L., Muir, A., & Drinkwater, M. R. (2018). Mapping ice sheet grounding lines with CryoSat-2. *Advances in Space Research, 62*(6), 1191–1202. https://doi.org/10.1016/j.asr.2017.03.008

Holdsworth, G. (1969). Flexure of a Floating Ice Tongue. *Journal of Glaciology, 8*(54), 385–397. https://doi.org/10.3189/S0022143000026976

Horgan, H. J., Alley, R. B., Christianson, K., Jacobel, R. W., Anandakrishnan, S., Muto, A., et al. (2013). Estuaries beneath ice sheets. *Geology, 41*(11), 1159–1162. https://doi.org/10.1130/G34654.1

Horgan, H. J., Christianson, K., Jacobel, R. W., Anandakrishnan, S., & Alley, R. B. (2013). Sediment deposition at the modern grounding zone of Whillans Ice Stream, West Antarctica. *Geophysical Research Letters, 40*(15), 3934–3939. https://doi.org/10.1002/grl.50712

Howard, S. L., Padman, L., & Erofeeva, S. Y. (2019). CATS2008: Circum-Antarctic Tidal Simulation version 2008 (Version 1) [Dataset]. U.S. Antarctic Program (USAP) Data Center. https://doi.org/10.15784/601235

Howat, I., Morin, P., Porter, C., & Noh, M.-J. (2018). The Reference Elevation Model of Antarctica (Version 1) [Dataset]. Harvard Dataverse. https://doi.org/10.7910/DVN/SAIK8B

Jenkins, A., Corr, H. F. J., Nicholls, K. W., Stewart, C. L., & Doake, C. S. M. (2006). Interactions between ice and ocean observed with phase-sensitive radar near an Antarctic ice-shelf grounding line. *Journal of Glaciology, 52*(178), 325–346. https://doi.org/10.3189/172756506781828502

Johnson, M. R., & Smith, A. M. (1997). Seabed topography under the southern and western Ronne Ice Shelf, derived from seismic surveys. *Antarctic Science, 9*(2), 201–208. https://doi.org/10.1017/S0954102097000254

Joughin, I., Alley, R. B., & Holland, D. M. (2012). Ice-Sheet Response to Oceanic Forcing. *Science, 338*(6111), 1172–1176. https://doi.org/10.1126/science.1226481

Joughin, I., Smith, B. E., & Holland, D. M. (2010). Sensitivity of 21st century sea level to ocean-induced thinning of Pine Island Glacier, Antarctica. *Geophysical Research Letters, 37*(20). https://doi.org/10.1029/2010GL044819

King, M. A., Padman, L., Nicholls, K., Clarke, P. J., Gudmundsson, G. H., Kulessa, B., & Shepherd, A. (2011). Ocean tides in the Weddell Sea: New observations on the Filchner-Ronne and Larsen C ice shelves and model validation. *Journal of Geophysical Research: Oceans, 116*(C6). https://doi.org/10.1029/2011JC006949

Konrad, H., Shepherd, A., Gilbert, L., Hogg, A. E., McMillan, M., Muir, A., & Slater, T. (2018). Net retreat of Antarctic glacier grounding lines. *Nature Geoscience, 11*(4), 258–262. https://doi.org/10.1038/s41561-018-0082-z

Li, T., Dawson, G. J., Chuter, S. J., & Bamber, J. L. (2020). Mapping the grounding zone of Larsen C Ice Shelf, Antarctica, from ICESat-2 laser altimetry. *The Cryosphere, 14*(11), 3629–3643. https://doi.org/10.5194/tc-14-3629-2020

Li, T., Dawson, G. J., Chuter, S. J., & Bamber, J. L. (2022). A high-resolution Antarctic grounding zone product from ICESat-2 laser altimetry. *Earth System Science Data, 14*(2), 535–557. https://doi.org/10.5194/essd-14-535-2022

Li, T., Dawson, G. J., Chuter, S. J., & Bamber, J. L. (2022). ICESat-2 L3 Grounding Zone for Antarctic Ice Shelves (Version 1) [Dataset]. NASA National Snow and Ice Data Center Distributed Active Archive Center. https://doi.org/10.5067/RI67B92708M9

Li, T., Dawson, G. J., Chuter, S. J., & Bamber, J. L. (2023). Grounding line retreat and tide-modulated ocean channels at Moscow University and Totten Glacier ice shelves, East Antarctica. *The Cryosphere, 17*(2), 1003–1022. https://doi.org/10.5194/tc-17-1003-2023

Luthcke, S. B., Thomas, T. C., Pennington, T. A., Rebold, T. W., Nicholas, J. B., Rowlands, D. D., et al. (2021). ICESat-2 Pointing Calibration and Geolocation Performance. *Earth and Space Science, 8*(3). https://doi.org/10.1029/2020EA001494

MacGregor, J. A., Anandakrishnan, S., Catania, G. A., & Winebrenner, D. P. (2011). The grounding zone of the Ross Ice Shelf, West Antarctica, from ice-penetrating radar. *Journal of Glaciology, 57*(205), 917–928. https://doi.org/10.3189/002214311798043780

Magruder, L., Brunt, K., Neumann, T., Klotz, B., & Alonzo, M. (2021). Passive Ground-Based Optical Techniques for Monitoring the On-Orbit ICESat-2 Altimeter Geolocation and Footprint Diameter. *Earth and Space Science, 8*(10). https://doi.org/10.1029/2020EA001414

Makinson, K., Holland, P. R., Jenkins, A., Nicholls, K. W., & Holland, D. M. (2011). Influence of tides on melting and freezing beneath Filchner-Ronne Ice Shelf, Antarctica. *Geophysical Research Letters, 38*(6). https://doi.org/10.1029/2010GL046462

Makinson, K., King, M. A., Nicholls, K. W., & Hilmar Gudmundsson, G. (2012). Diurnal and semidiurnal tide-induced lateral movement of Ronne Ice Shelf, Antarctica. *Geophysical Research Letters, 39*(10). https://doi.org/10.1029/2012GL051636

Markus, T., Neumann, T., Martino, A., Abdalati, W., Brunt, K., Csatho, B., et al. (2017). The Ice, Cloud, and land Elevation Satellite-2 (ICESat-2): Science requirements, concept, and implementation. *Remote Sensing of Environment, 190*, 260–273. https://doi.org/10.1016/j.rse.2016.12.029

Milillo, P., Rignot, E., Rizzoli, P., Scheuchl, B., Mouginot, J., Bueso-Bello, J., & Prats-Iraola, P. (2019). Heterogeneous retreat and ice melt of Thwaites Glacier, West Antarctica. *Science Advances, 5*(1), eaau3433. https://doi.org/10.1126/sciadv.aau3433

Milillo, P., Rignot, E., Rizzoli, P., Scheuchl, B., Mouginot, J., Bueso-Bello, J. L., et al. (2022). Rapid glacier retreat rates observed in West Antarctica. *Nature Geoscience, 15*(1), 48–53. https://doi.org/10.1038/s41561-021-00877-z

Milillo, P., Rignot, E., Mouginot, J., Scheuchl, B., Morlighem, M., Li, X., & Salzer, J. T. (2017). On the Short-term Grounding Zone Dynamics of Pine Island Glacier, West Antarctica, Observed With COSMO-SkyMed Interferometric Data. *Geophysical Research Letters, 44*(20), 10,436-10,444. https://doi.org/10.1002/2017GL074320

Minchew, B. M., Simons, M., Riel, B., & Milillo, P. (2017). Tidally induced variations in vertical and horizontal motion on Rutford Ice Stream, West Antarctica, inferred from remotely sensed observations. *Journal of Geophysical Research: Earth Surface, 122*(1), 167–190. https://doi.org/10.1002/2016JF003971

Mohajerani, Y., Jeong, S., Scheuchl, B., Velicogna, I., Rignot, E., & Milillo, P. (2021). Automatic delineation of glacier grounding lines in differential interferometric synthetic-aperture radar data using deep learning. *Scientific Reports, 11*(1), 4992. https://doi.org/10.1038/s41598-021-84309-3

Moholdt, G., Padman, L., & Fricker, H. A. (2014). Basal mass budget of Ross and Filchner-Ronne ice shelves, Antarctica, derived from Lagrangian analysis of ICESat altimetry: Ice shelf basal melting from altimetry. *Journal of Geophysical Research: Earth Surface, 119*(11), 2361–2380. https://doi.org/10.1002/2014JF003171

Mosbeux, C., Padman, L., Klein, E., Bromirski, P. D., & Fricker, H. A. (2023). Seasonal variability in Antarctic ice shelf velocities forced by sea surface height variations. *The Cryosphere, 17*(7), 2585–2606. https://doi.org/10.5194/tc-17-2585-2023

Mueller, R. D., Padman, L., Dinniman, M. S., Erofeeva, S. Y., Fricker, H. A., & King, M. A. (2012). Impact of tide-topography interactions on basal melting of Larsen C Ice Shelf, Antarctica. *Journal of Geophysical Research: Oceans, 117*(C5), n/a-n/a. https://doi.org/10.1029/2011JC007263

Naughten, K. A., De Rydt, J., Rosier, S. H. R., Jenkins, A., Holland, P. R., & Ridley, J. K. (2021). Two-timescale response of a large Antarctic ice shelf to climate change. *Nature Communications, 12*(1), 1991. https://doi.org/10.1038/s41467-021-22259-0

Neumann, T. A., Martino, A. J., Markus, T., Bae, S., Bock, M. R., Brenner, A. C., et al. (2019). The Ice, Cloud, and Land Elevation Satellite – 2 mission: A global geolocated photon product derived from the Advanced Topographic Laser Altimeter System. *Remote Sensing of Environment, 233*, 111325. https://doi.org/10.1016/j.rse.2019.111325

Nicholls, K. W., & Østerhus, S. (2004). Interannual variability and ventilation timescales in the ocean cavity beneath Filchner-Ronne Ice Shelf, Antarctica. *Journal of Geophysical Research, 109*(C4), C04014. https://doi.org/10.1029/2003JC002149

Padman, L., Fricker, H. A., Coleman, R., Howard, S., & Erofeeva, L. (2002). A new tide model for the Antarctic ice shelves and seas. *Annals of Glaciology, 34*, 247–254. https://doi.org/10.3189/172756402781817752

Padman, L., Siegfried, M. R., & Fricker, H. A. (2018). Ocean Tide Influences on the Antarctic and Greenland Ice Sheets. *Reviews of Geophysics, 56*(1), 142–184. https://doi.org/10.1002/2016RG000546

Park, J. W., Gourmelen, N., Shepherd, A., Kim, S. W., Vaughan, D. G., & Wingham, D. J. (2013). Sustained retreat of the Pine Island Glacier. *Geophysical Research Letters, 40*(10), 2137–2142. https://doi.org/10.1002/grl.50379

Reeh, N., Mayer, C., Olesen, O. B., Christensen, E. L., & Thomsen, H. H. (2000). Tidal movement of Nioghalvfjerdsfjorden glacier, northeast Greenland: observations and modelling. *Annals of Glaciology, 31*, 111–117. https://doi.org/10.3189/172756400781820408

Reeh, N., Christensen, E. L., Mayer, C., & Olesen, O. B. (2003). Tidal bending of glaciers: a linear viscoelastic approach. *Annals of Glaciology, 37*, 83–89. https://doi.org/10.3189/172756403781815663

Rignot, E., Mouginot, J., & Scheuchl, B. (2011). Antarctic grounding line mapping from differential satellite radar interferometry. *Geophysical Research Letters, 38*(10). https://doi.org/10.1029/2011GL047109

Rignot, E., Mouginot, J., Morlighem, M., Seroussi, H., & Scheuchl, B. (2014). Widespread, rapid grounding line retreat of Pine Island, Thwaites, Smith, and Kohler glaciers, West Antarctica, from 1992 to 2011. *Geophysical Research Letters, 41*(10), 3502–3509. https://doi.org/10.1002/2014GL060140

Rignot, E. (1996). Tidal motion, ice velocity and melt rate of Petermann Gletscher, Greenland, measured from radar interferometry. *Journal of Glaciology, 42*(142), 476–485. https://doi.org/10.3189/S0022143000003464

Rignot, E., Mouginot, J., & Scheuchl, B. (2016). MEaSUREs Antarctic Grounding Line from Differential Satellite Radar Interferometry (Version 2) [Dataset]. NASA National Snow and Ice Data Center Distributed Active Archive Center. https://doi.org/10.5067/IKBWW4RYHF1Q

Rignot, E., Mouginot, J., & Scheuchl, B. (2017). MEaSUREs InSAR-Based Antarctica Ice Velocity Map (Version 2) [Dataset]. NASA National Snow and Ice Data Center Distribute Active Archive Center. https://doi.org/10.5067/D7GK8F5J8M8R

Robel, A. A., Tsai, V. C., Minchew, B., & Simons, M. (2017). Tidal modulation of ice shelf buttressing stresses. *Annals of Glaciology*, 58(74), 12–20. https://doi.org/10.1017/aog.2017.22

Robel, A. A., Wilson, E., & Seroussi, H. (2022). Layered seawater intrusion and melt under grounded ice. *The Cryosphere, 16*(2), 451–469. https://doi.org/10.5194/tc-16-451-2022

Rosier, S. H. R., Gudmundsson, G. H., & Green, J. A. M. (2015). Temporal variations in the flow of a large Antarctic ice stream controlled by tidally induced changes in the subglacial water system. *The Cryosphere, 9*(4), 1649–1661. https://doi.org/10.5194/tc-9-1649-2015

Rosier, S. H. R., & Gudmundsson, G. H. (2016). Tidal controls on the flow of ice streams. *Geophysical Research Letters, 43*(9), 4433–4440. https://doi.org/10.1002/2016GL068220

Rosier, S. H. R., & Gudmundsson, G. H. (2020). Exploring mechanisms responsible for tidal modulation in flow of the Filchner–Ronne Ice Shelf. *The Cryosphere, 14*(1), 17–37. https://doi.org/10.5194/tc-14-17-2020

Ross, N., Bingham, R. G., Corr, H. F. J., Ferraccioli, F., Jordan, T. A., Le Brocq, A., et al. (2012). Steep reverse bed slope at the grounding line of the Weddell Sea sector in West Antarctica. *Nature Geoscience, 5*(6), 393–396. https://doi.org/10.1038/ngeo1468

Sayag, R., & Worster, M. G. (2013). Elastic dynamics and tidal migration of grounding lines modify subglacial lubrication and melting. *Geophysical Research Letters, 40*(22), 5877–5881. https://doi.org/10.1002/2013GL057942

Scambos, T. A., Haran, T. M., Fahnestock, M. A., Painter, T. H., & Bohlander, J. (2007). MODIS-based Mosaic of Antarctica (MOA) data sets: Continent-wide surface morphology and snow grain size. *Remote Sensing of Environment, 111*(2–3), 242–257. https://doi.org/10.1016/j.rse.2006.12.020

Scheick, J., Leong, W. J., Bisson, K., Arendt, A., Bhushan, S., Fair, Z., et al. (2023). icepyx: querying, obtaining, analyzing, and manipulating ICESat-2 datasets (Version v0.6.4_JOSS) [Software]. Zenodo. https://doi.org/10.5281/ZENODO.7729175

Schmeltz, M., Rignot, E., & MacAyeal, D. R. (2001). Ephemeral grounding as a signal of ice-shelf change. *Journal of Glaciology, 47*(156), 71–77. https://doi.org/10.3189/172756501781832502

Schmeltz, M., Rignot, E., & MacAyeal, D. (2002). Tidal flexure along ice-sheet margins: comparison of InSAR with an elastic-plate model. *Annals of Glaciology, 34*, 202–208. https://doi.org/10.3189/172756402781818049

Schmidt, B. E., Washam, P., Davis, P. E. D., Nicholls, K. W., Holland, D. M., Lawrence, J. D., et al. (2023). Heterogeneous melting near the Thwaites Glacier grounding line. *Nature, 614*(7948), 471–478. https://doi.org/10.1038/s41586-022-05691-0

Schoof, C. (2007). Ice sheet grounding line dynamics: Steady states, stability, and hysteresis. *Journal of Geophysical Research, 112*(F3), F03S28. https://doi.org/10.1029/2006JF000664

Schoof, C. (2011). Marine ice sheet dynamics. Part 2. A Stokes flow contact problem. *Journal of Fluid Mechanics, 679*, 122–155. https://doi.org/10.1017/jfm.2011.129

Schutz, B. E., Zwally, H. J., Shuman, C. A., Hancock, D., & DiMarzio, J. P. (2005). Overview of the ICESat Mission. *Geophysical Research Letters, 32*(21), L21S01. https://doi.org/10.1029/2005GL024009

Siegert, M., Ross, N., Corr, H., Kingslake, J., & Hindmarsh, R. (2013). Late Holocene ice-flow reconfiguration in the Weddell Sea sector of West Antarctica. *Quaternary Science Reviews, 78*, 98–107. https://doi.org/10.1016/j.quascirev.2013.08.003

Smith, A. M. (1991). The use of tiltmeters to study the dynamics of Antarctic ice-shelf grounding lines. *Journal of Glaciology, 37*(125), 51–58. https://doi.org/10.3189/S0022143000042799

Smith, B., Fricker, H. A., Gardner, A., Siegfried, M. R., Adusumilli, S., Csathó, B. M., et al. (2021). ATLAS/ICESat-2 L3A Land Ice Height (Version 5) [Dataset]. NASA National Snow and Ice Data Center Distribute Active Archive Center. https://doi.org/10.5067/ATLAS/ATL06.005

Smith, Benjamin, Fricker, H. A., Holschuh, N., Gardner, A. S., Adusumilli, S., Brunt, K. M., et al. (2019). Land ice height-retrieval algorithm for NASA's ICESat-2 photon-counting laser altimeter. *Remote Sensing of Environment, 233*, 111352. https://doi.org/10.1016/j.rse.2019.111352

Stephenson, S. N., Doake, C. S. M., & Horsfall, J. A. C. (1979). Tidal flexure of ice shelves measured by tiltmeter. *Nature, 282*(5738), 496–497. https://doi.org/10.1038/282496a0

Stubblefield, A. G., Spiegelman, M., & Creyts, T. T. (2021). Variational formulation of marine ice-sheet and subglacial-lake grounding-line dynamics. *Journal of Fluid Mechanics, 919*, A23. https://doi.org/10.1017/jfm.2021.394

Sutterley, T. C., Markus, T., Neumann, T. A., van den Broeke, M., van Wessem, J. M., & Ligtenberg, S. R. M. (2019). Antarctic ice shelf thickness change from multimission lidar mapping. *The Cryosphere, 13*(7), 1801–1817. https://doi.org/10.5194/tc-13-1801-2019

Thomas, R. H. (1979). The Dynamics of Marine Ice Sheets. *Journal of Glaciology, 24*(90), 167–177. https://doi.org/10.1017/S0022143000014726

Thompson, J., Simons, M., & Tsai, V. C. (2014). Modeling the elastic transmission of tidal stresses to great distances inland in channelized ice streams. *The Cryosphere, 8*(6), 2007–2029. https://doi.org/10.5194/tc-8-2007-2014

Tsai, V. C., & Gudmundsson, G. H. (2015). An improved model for tidally modulated grounding-line migration. *Journal of Glaciology, 61*(226), 216–222. https://doi.org/10.3189/2015JoG14J152

Vaughan, D. G. (1995). Tidal flexure at ice shelf margins. *Journal of Geophysical Research: Solid Earth, 100*(B4), 6213–6224. https://doi.org/10.1029/94JB02467

Walker, R. T., Parizek, B. R., Alley, R. B., Anandakrishnan, S., Riverman, K. L., & Christianson, K. (2013). Ice-shelf tidal flexure and subglacial pressure variations. *Earth and Planetary Science Letters, 361*, 422–428. https://doi.org/10.1016/j.epsl.2012.11.008

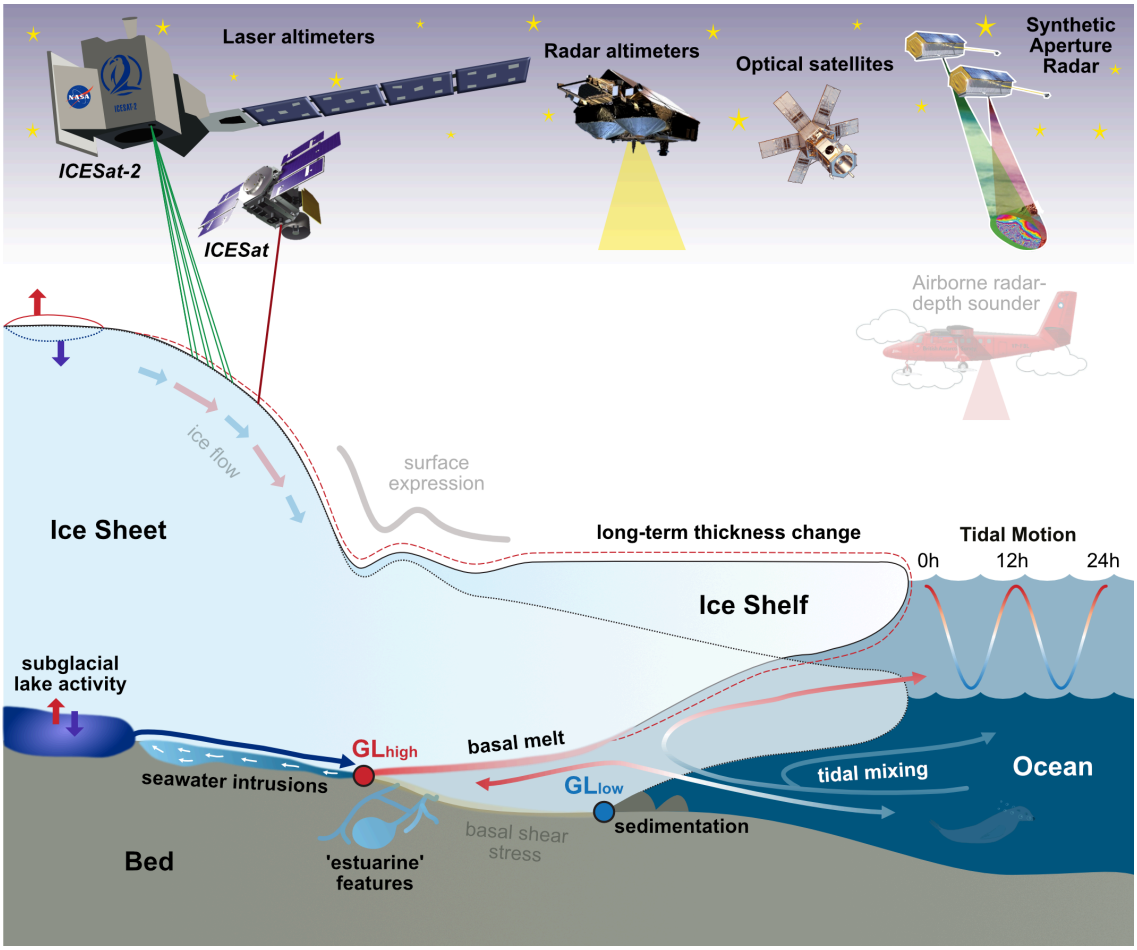
Warburton, K. L. P., Hewitt, D. R., & Neufeld, J. A. (2020). Tidal Grounding-Line Migration Modulated by Subglacial Hydrology. *Geophysical Research Letters, 47*(17). https://doi.org/10.1029/2020GL089088

Wild, C. T., Marsh, O. J., & Rack, W. (2017). Viscosity and elasticity: a model intercomparison of ice-shelf bending in an Antarctic grounding zone. *Journal of Glaciology, 63*(240), 573–580. https://doi.org/10.1017/jog.2017.15

Chapter 3

Coincident lake drainage and grounding line retreat at Engelhardt Subglacial Lake, West Antarctica

In this chapter, I present a 21-year time series of subglacial lake activity at Engelhardt Subglacial Lake in West Antarctica and document the migration of the downstream grounding line over this period. I explore the relationship between lake drainage, GL retreat and subglacial bedforms using a combination of ICESat, ICESat-2 and CryoSat-2 altimetry, RADARSAT-2 and TerraSAR-X DInSAR, and high-resolution digital elevation model data.



The research described in Chapter 3 has been accepted for publication as:

Freer, B. I. D., Marsh, O. J., Hogg, A. E., Fricker, H. A., Siegfried, M. R., Floricioiu, D., Sauthoff, W., Rigby, R., and Wilson, S. F. (2024, *in review*) 'Coincident lake drainage and grounding line retreat at Engelhardt Subglacial Lake, West Antarctica'. *Journal of Geophysical Research: Earth Surface.*

Abstract

Antarctica has an active subglacial hydrological system, with interconnected subglacial lakes fed by subglacial meltwater. Subglacial hydrology can influence basal sliding, inject freshwater into the sub-ice-shelf cavity, and impact sediment transport and deposition which can affect the stability of grounding lines (GLs). We use satellite altimetry data from the ICESat, ICESat-2 and CryoSat-2 missions to document the second recorded drainage of Engelhardt Subglacial Lake (SLE), which began in July 2021 and discharged more than 2.3 km^3 of subglacial water into the Ross Ice Shelf cavity. We use differential synthetic aperture radar interferometry from RADARSAT-2 and TerraSAR-X alongside ICESat-2 repeat-track laser altimetry (RTLA) and REMA digital elevation model strips to detect 2–13 km of GL retreat since the previous drainage event in 2003–06. Combining these satellite observations, we evaluate the mechanism triggering SLE drainage, the cause of the observed GL retreat, and the interplay between subglacial hydrology and GL dynamics. We find that: (i) SLE drainage was initiated by influx from a newly-identified upstream lake; (ii) the observed GL retreat is mainly driven by the continued retreat of Engelhardt Ice Ridge and long-term dynamic thinning that caused a grounded ice plain to reach flotation; and (iii) SLE drainage and GL retreat were largely independent. We also discuss the possible origins and influence of a 27 km grounded promontory found to protrude seaward from the GL. Our observations demonstrate the importance of high-resolution satellite data for improving process-based understanding of dynamic and complex regions around the Antarctic Ice Sheet margins.

Plain Language Summary

Large volumes of water flow beneath the Antarctic Ice Sheet through an interconnected network of rivers and lakes. This water system impacts slipperiness at the base of the ice, affecting how fast it moves. It also delivers freshwater into the ocean, directly contributing to sea-level rise and increasing melt beneath the floating ice shelves. In this study we use satellite data to track the 2021–24 drainage of Engelhardt Subglacial Lake in West Antarctica. This lake is located close to the Ross Ice Shelf grounding line, the point at the edge of the ice sheet where the ice first lifts off the bedrock and starts to float on the ocean. This region of the grounding line has retreated by up to 13 kilometers since the last lake drainage in 2003–06. Here we investigate what caused the drainage, the reasons for the grounding line retreat, and whether the two processes are connected. We also report the growth of a grounded promontory extending 27 kilometers out to sea, which may be evidence of a former ice stream moraine or melt channel. These findings help to improve our limited understanding of the relationship between subglacial hydrology and grounding line dynamics in Antarctica.

3.1. Introduction

The Antarctic Ice Sheet (AIS) stores 57.9 ± 0.9 m of sea-level rise equivalent (Morlighem et al., 2020) and is currently the largest source of uncertainty in future sea-level projections, due to insufficient knowledge of ice sheet processes (IPCC, 2023; Seroussi et al., 2020). AIS dynamics are primarily controlled by the gravitational driving stress, conditions at the ice-bed interface (Paterson, 1994) and the "buttressing" effect of ice shelves (Gudmundsson et al., 2019). Subglacial hydrology can exert a strong influence on basal conditions and can accelerate basal melting which might reduce ice shelf buttressing (Pelle et al., 2023), yet representations of subglacial hydrology are missing from most ice sheet and ice-ocean models (e.g., De Fleurian et al., 2018; S. Sun et al., 2020). This is largely due to the lack of direct observations of the Antarctic subglacial environment, which is difficult to access beneath multiple kilometres of ice (Priscu et al., 2021; Siegfried & Fricker, 2021; Siegfried et al., 2023).

Active subglacial lakes are a key component of Antarctic subglacial hydrology; their fill-and-drain cycles have been shown to impact regional ice velocity (Scambos et al., 2011; Siegfried et al., 2016; Stearns et al., 2008), basal hydrology including bed slipperiness (Carter et al., 2013), nutrient fluxes (Hawkings et al., 2020), sediment transport (Carter et al., 2017; Drews et al., 2017; Siegfried et al., 2023; Simkins et al., 2017) and localised ice shelf melt rates (Marsh et al., 2016). Satellite altimetry provides a window into this behaviour by measuring the signatures of surface uplift and subsidence associated with the respective filling and draining phases (Fricker et al., 2007, 2016; Malczyk et al., 2020; Neckel et al., 2021; Siegfried & Fricker, 2021). Despite recent advances in satellite observation capabilities, we still do not understand many of the processes related to active subglacial lakes (e.g., Stubblefield et al., 2023) and they remain under-sampled in space and time (Siegfried & Fricker, 2021). Key questions remain regarding the triggers and mechanisms of subglacial lake drainage (Siegfried et al., 2023), the timescales for fill-and-drain cycles, and the influence of drainage on grounding zone (GZ) dynamics (Carter et al., 2017; Simkins et al., 2017).

In this study we present the first observations of the 2021–24 drainage of Engelhardt Subglacial Lake (SLE), West Antarctica, using high resolution satellite measurements from Ice, Cloud and land Elevation Satellite-2 (ICESat-2). This event is only the second drainage on record at this lake and provides a rare opportunity to investigate the co-evolution of an actively draining subglacial lake and the downstream grounding line (GL). Leveraging improvements in spatial and temporal sampling of satellite instruments over the past two decades, we compile a 21-year satellite record of ice-sheet surface elevation change associated with the fill-and-drain cycle of SLE, examine the GL evolution before and during the 2021–24 drainage event, and evaluate the interactions between these processes.

3.2. Study Region

Engelhardt Subglacial Lake (SLE) is one in a network of active subglacial lakes beneath Whillans Ice Plain on the Gould Coast, first discovered in the mid-2000s (Fricker et al., 2007). SLE occupies a ~250–350 km^2 region fed by water originating from the upper Kamb and Whillans ice streams (Fig. 3.1a; Carter et al., 2013). Between October 2003 and June 2006, ICESat laser altimetry detected a ~9 m drop in surface elevation at SLE, which was interpreted as a signal of drainage (Fricker et al., 2007). This was the first evidence of SLE drainage in the satellite record, discharging ~2.0 km3 subglacial water across the Ross Ice Shelf (RIS) GL ~10 km downstream. SLE slowly refilled over the next 15 years (Siegfried & Fricker, 2018).

SLE is one of the only active subglacial lakes in Antarctica located within 10 km of the GL (Siegfried & Fricker, 2018). The GL downstream of SLE comprises an east and west embayment separated by a grounded promontory (Fig. 3.1b). In the east embayment the GL has been retreating by 300–500 m yr^{-1} since at least 1963, with the most rapid retreat focused on the GL along Engelhardt Ice Ridge, formerly called Ridge B/C (Bindschadler & Vornberger, 1998; Fricker et al., 2007). It was suggested that the 2003–06 SLE drainage could be linked to the observed GL retreat here, but it remained an open question whether the GL retreat triggered the lake drainage or whether the drainage led to the GL retreat (Fricker & Scambos, 2009). In the west embayment there is greater uncertainty in the GL position, with a small ice plain identified just inland extending to the break-in-slope (Fig. 3.1b; Brunt et al., 2010; Horgan & Anandakrishnan, 2006). ICESat and RADARSAT-2 measurements indicate that this ice plain was grounded until at least 2009 (Brunt et al., 2010; Rignot et al., 2016), and so was likely unaffected by the 2003–06 SLE drainage.

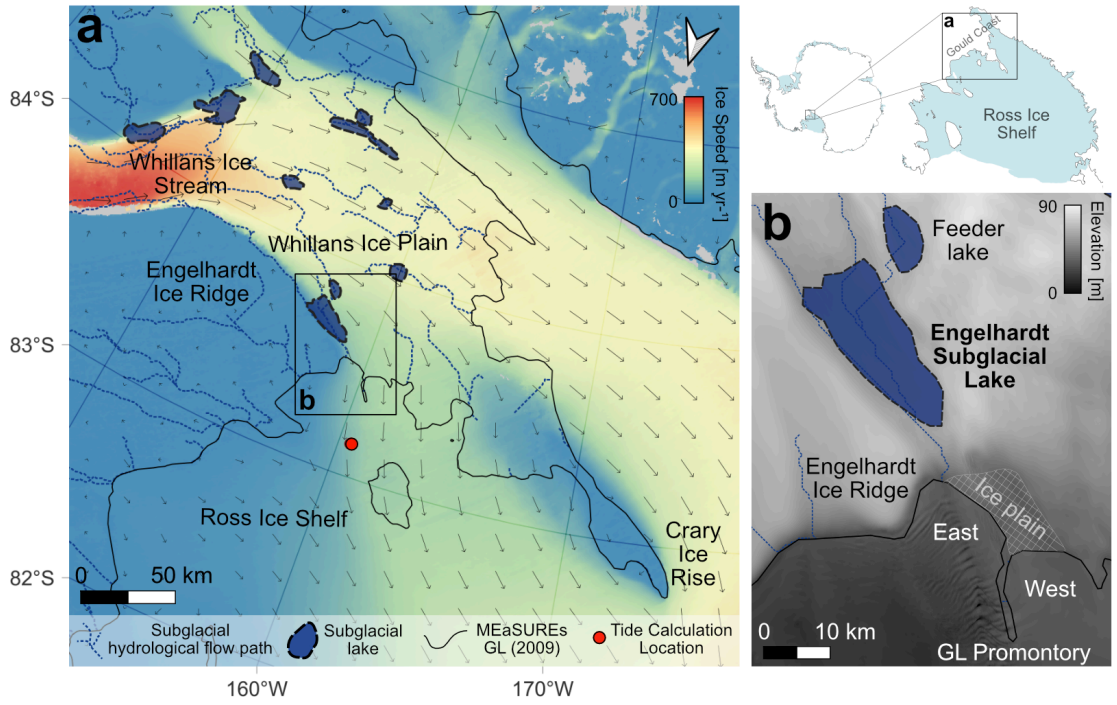


Figure 3.1. Location of Engelhardt Subglacial Lake (SLE) near the Ross Ice Shelf grounding line on the Gould Coast. (a) MEaSUREs ice velocity (Rignot et al., 2017) overlain with the location of known active subglacial lakes (Siegfried & Fricker, 2018), modelled hydrological pathways and the 2009 MEaSUREs GL (Rignot et al., 2016). (b) Zoom of SLE area in (a) showing the estimated subglacial lake boundary on the Reference Elevation Model of Antarctica (REMA) DEM mosaic (Howat et al., 2019). The location of the east and west embayments and GL promontory are labelled, alongside the estimated ice plain area (Brunt et al., 2010).

3.3. Data

Satellite laser altimetry: NASA's ICESat laser altimetry mission operated between February 2003 and October 2009, and carried a 1064 nm laser altimeter that provided high precision (<0.1 m) repeat surface elevation retrievals every ~170 m along-track (Schutz et al., 2005). We used the GLAH06 Level-1B Global Elevation (version 34) product (Zwally et al., 2014), with surface elevations relative to the WGS84 ellipsoid corrected for tides, atmospheric delays, surface characteristics, Gaussian-Centroid offset (Borsa et al., 2014) and saturation (X. Sun et al., 2017).

ICESat-2 launched in 2018. Its photon-counting 532 nm laser altimeter estimates surface elevation along its 1387 reference ground tracks (RGTs), each comprising six beams and repeating every 91 days (Magruder et al., 2021). We used data from: (i) the Level 3A Land Ice Height data product (ATL06 version 6; Smith et al., 2023) from cycles 3–23 (April 2019 – April 2024), which provides mean surface elevation averaged along 40 m ground track (GT) segments spaced 20 m apart; and (ii) the Level 3B Gridded Antarctic Land Ice Height Change product (ATL15 version 4; Smith et al., 2024), which provides 1 km gridded elevation change data, currently available at a quarter-year time step between April 2019 and January 2024 (note the ATL15 coverage period is three months shorter than for ATL06).

***Satellite radar altimetry*:** The European Space Agency's CryoSat-2 mission launched in 2010, carrying a synthetic aperture interferometric (SARIn) radar altimeter. Its SARIn mode provides elevation retrievals every 300 m along-track with an effective spatial resolution of 380–410 m along-track and ~1.7 km across-track (McMillan et al., 2013). We used CryoSat-2 SARIn data over SLE between 2010 and 2021, which we swath-processed at 250 m spatial resolution and averaged at three-monthly intervals using a linear fit method (after Slater et al., 2021, Shepherd et al., 2019, McMillan et al., 2014).

***Synthetic aperture radar (SAR)*:** RADARSAT-2 and TerraSAR-X are side-looking SAR instruments with left-looking capabilities (required to cover the high southern latitudes), launched in 2007. We generated double-difference interferograms (DInSAR) over the SLE region and its GL using RADARSAT-2 data from 2009 and TerraSAR-X data from 2012, 2016 and 2023. Multilooked imagery for both satellites were georeferenced to Bedmap2 surface elevations (Fretwell et al., 2013). Image dates, processing information and sampled tides are provided in Table 3.1.

***Optical imagery*:** We used REMA digital elevation model (DEM) mosaic (version 2) and strip (version 4.1) datasets, created with sub-meter resolution Maxar optical satellite imagery (Howat et al., 2019). The strip DEMs are time-stamped to allow for change detection analysis, but are not registered vertically to satellite altimetry.

Table 3.1. Image processing information and acquisition time for all RADARSAT-2 and TerraSAR-X DInSAR scenes used in this study. The tidal heights for each individual pass were calculated at the location shown in Figure 3.1 [83.161°S, 160.5°W] using the CATS2008 model (Howard et al., 2019), corrected for the inverse barometer effect (IBE) using the daily air pressure values from the National Center for Environmental Prediction and the National Center for Atmospheric Research Reanalysis (NCEP/NCA). The expected vertical height difference for each DInSAR is calculated using the tides from individual passes: *[t2-t1] + [t3-t2]*.

DInSAR Date and *Satellite*	**Spatial Resolution [m] (ground range x azimuth)**	**DEM for geocoding**	**Pass Date/Time**		**Tide height, corrected IBE [m]**	**Expected height difference [m] *[t2-t1] + [t2-t3]***
February 2009 *RADARSAT-2*	12 x 5 *(2 x 6 multilooking)*	Bedmap2 (50 m grid)	t1	2009-02-19 14:31:00	+0.337	-1.79
			t2	2009-03-15 14:31:00	-0.811	
			t3	2009-04-08 14:31:00	-0.171	
September 2012 *TerraSAR-X*	2.5 x 3.3 *(4 x 4 multilooking)*	Bedmap2 (8 m grid)	t1	2012-09-02 14:38:00	-0.349	-0.872
			t2	2012-09-13 14:38:00	-0.507	
			t3	2012-09-24 14:38:00	+0.206	
April 2016 *TerraSAR-X*	2.5 x 3.3 *(4 x 4 multilooking)*	Bedmap2 (8 m grid)	t1	2016-04-08 14:47:00	-0.460	+0.679
			t2	2016-04-19 14:47:00	-0.076	
			t3	2016-04-30 14:47:00	-0.372	
July 2023 *TerraSAR-X*	2.5 x 3.3 *(4 x 4 multilooking)*	Bedmap2 (8 m grid)	t1	2023-06-27 06:31:00	-0.259	+0.166
			t2	2023-07-08 06:31:00	+0.023	
			t3	2023-07-19 06:31:00	+0.139	
October 2023 *TerraSAR-X*	2.5 x 3.3 *(4 x 4 multilooking)*	Bedmap2 (8 m grid)	t1	2023-10-03 06:48:00	-0.608	+0.691
			t2	2023-10-14 06:48:00	-0.359	
			t3	2023-10-25 06:48:00	-0.802	

3.4. Methods

3.4.1. Surface elevation change

We generated a time-series of surface elevation change associated with the fill-and-drain cycle of SLE by combining elevation estimates from three satellite altimeter missions (Fig. 3.2). We selected three ~3 km^2 crossover zones (CZs) at locations over the lake with the highest density of intersecting ICESat and ICESat-2 RGTs. A fourth CZ slightly upstream of the lake contained only ICESat-2 tracks. For each section of ICESat/ICESat-2 track intersecting a CZ we calculated the mean along-track elevation per repeat cycle from the GLAH06 and ATL06 datasets, providing three time-series of elevation change at CZ1–3 from 2003–09 (ICESat) and 2019–24 (ICESat-2), and a time-series at CZ4 for 2019–24 (ICESat-2 only). To extend the record from 2010–20 we calculated a time-series of mean elevation within each CZ from the swath-processed CryoSat-2 data. We used the ICESat-2 ATL15 gridded elevation dataset to determine the spatial extent of drainage and the total ice and (inferred) water volume displacement at quarter-year intervals from 2019–24 (note this does not cover the entire duration of drainage).

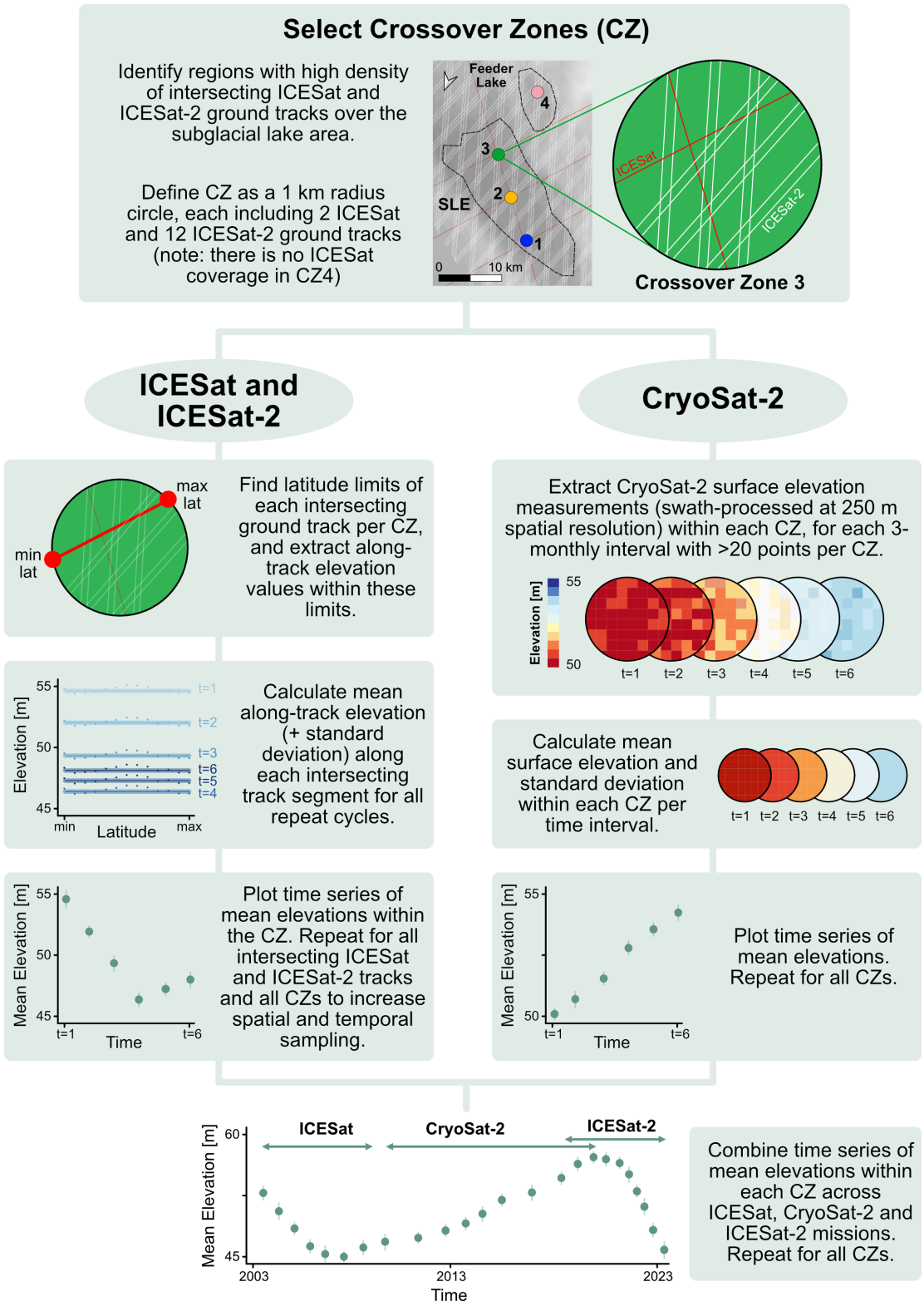


Figure 3.2. Combining satellite laser and radar altimetry elevations. Flowchart of methods used to derive a time-series of mean ice sheet surface elevation values within each crossover zone (CZ1–4) at SLE, using elevation data from ICESat (2003–09) and ICESat-2 (2018–2024) laser altimetry and CryoSat-2 radar altimetry (2010–2021). Note that all elevation values are illustrative.

3.4.2. Subglacial hydrological flow pathways

We used static grids of ice surface elevation from the REMA mosaic (Howat et al., 2019) and ice thickness (from which bed elevation can be inferred; Morlighem et al., 2020) to predict the subglacial water flow routing pathways beneath Whillans Ice Plain based on hydropotential gradients. Hydropotential gradients control where water is driven to flow by gravitational potential (bed elevation) and ice overburden pressure (Shreve, 1972), given by Equation 3.1:

$$\nabla\varphi = \rho \cdot g \cdot \nabla z \cdot \nabla P_w \tag{3.1}$$

where $\nabla\varphi$ is the hydropotential gradient, ρ is the density of water, g is gravitational acceleration, z is bed elevation, and P_w is water pressure. Flow routing pathways were modelled based on the hydropotential surface using the Python package pysheds (Bartos, 2020).

3.4.3. Grounding line change

We located the GL with two independent methods: (i) DInSAR: we traced the landward boundary of the dense fringe belt associated with the vertical tidal motion of the ice (Point F; Rignot et al., 2011) in each RADARSAT-2 and TerraSAR-X double-difference interferogram (dates in Table 3.1); (ii) ICESat-2: we used a repeat track laser altimetry (RTLA) methodology, described in Freer et al. (2023), to provide locations at higher temporal sampling (intra-annual) from 2019–23. This method takes repeat ATL06 elevations along a single ICESat-2 RGT for each repeat cycle and compares to a reference profile taken at the lowest sampled tide to calculate elevation anomalies. From this we obtained the inland limit of tidal flexure (Point F) per repeat cycle, which is the same GL proxy as detected by DInSAR. We repeated this for all RGTs crossing the GL.

3.4.4. Engelhardt Ice Ridge retreat

We assessed the retreat of Engelhardt Ice Ridge along ICESat RGT 172 and ICESat-2 RGT 343 ground track 1R (GT1R) that cross the northern face of the ridge. We extended both time-series between the ICESat and ICESat-2 periods by sampling elevations along each track from all available REMA DEM strips 2012–2022. Where there were small geolocation errors, we manually adjusted the elevation profiles (by up to ±6 m) based on the top ridge surface. We calculated ridge retreat rates across the time-series at the 40-m elevation contour.

3.5. Results

3.5.1. Surface elevation change at SLE

Combined satellite altimetry datasets from the ICESat, ICESat-2 and CryoSat-2 missions yielded a 21-year time-series of surface elevation showing the activity of SLE (Fig. 3.3c). This captured drainage in 2003–06 (Fricker et al., 2007), the 15-year refilling period (Siegfried & Fricker, 2018), and onset of a second drainage event in July 2021.

Between September 2020 and the onset of SLE drainage in July 2021, we observed a ~3 m drop in surface elevations in a small region upstream of SLE (CZ4 in Fig. 3.3c), as surface elevations over SLE continued to rise at a slightly faster rate. Considering its location on the modelled upstream hydrologic flow path (Fig. 3.1b) and correlation to SLE drainage, we interpret this as a signal from a newly-identified upstream 'feeder lake' draining directly into SLE. This upstream lake was not well-sampled by ICESat due to its sparser track spacing (Fig. 3.3a); however, ICESat-2 has denser sampling and the repeat-track surface elevation profiles along RGT 343 GT1R show a sharp fill-and-drain event here immediately preceding SLE drainage (Figs. 3.3, 3.4).

Between July 2021 and January 2024 surface elevations over the SLE area fell by a median value of 10.8 m (interquartile range (IQR): -13.7 to -6.7 m; as calculated from ICESat-2 ATL15; Fig. 3.4), and by more than 15 m in the central lake area (Figs. 3.3b, 3.3c). The rate of surface-lowering accelerated to reach a maximum in July 2023 (Fig. 3.4t), after

which it began to decrease, at first from the upstream end (Figs. 3.4q–t). SAR backscatter images show the development of surface crevasses along the margin of the lake caused by this drainage-induced subsidence (Fig. 3.5a). Based on the subsidence area and total elevation decrease, we estimate that the lake drained at least 2.3 km^3 of subglacial water into the RIS cavity between July 2021 and January 2024. This calculation assumes that total displaced ice volume equals the displaced water volume, which we acknowledge may not always hold due to the effects of viscous ice flow (Sergienko et al., 2007; Stubblefield et al., 2021, 2023). The extended ICESat-2 ATL06 elevation record shows surface subsidence in the downstream part of the SLE continued until at least April 2024 (likely continuing for a couple of months beyond this), leading to a total estimated drainage period of 34–36 months.

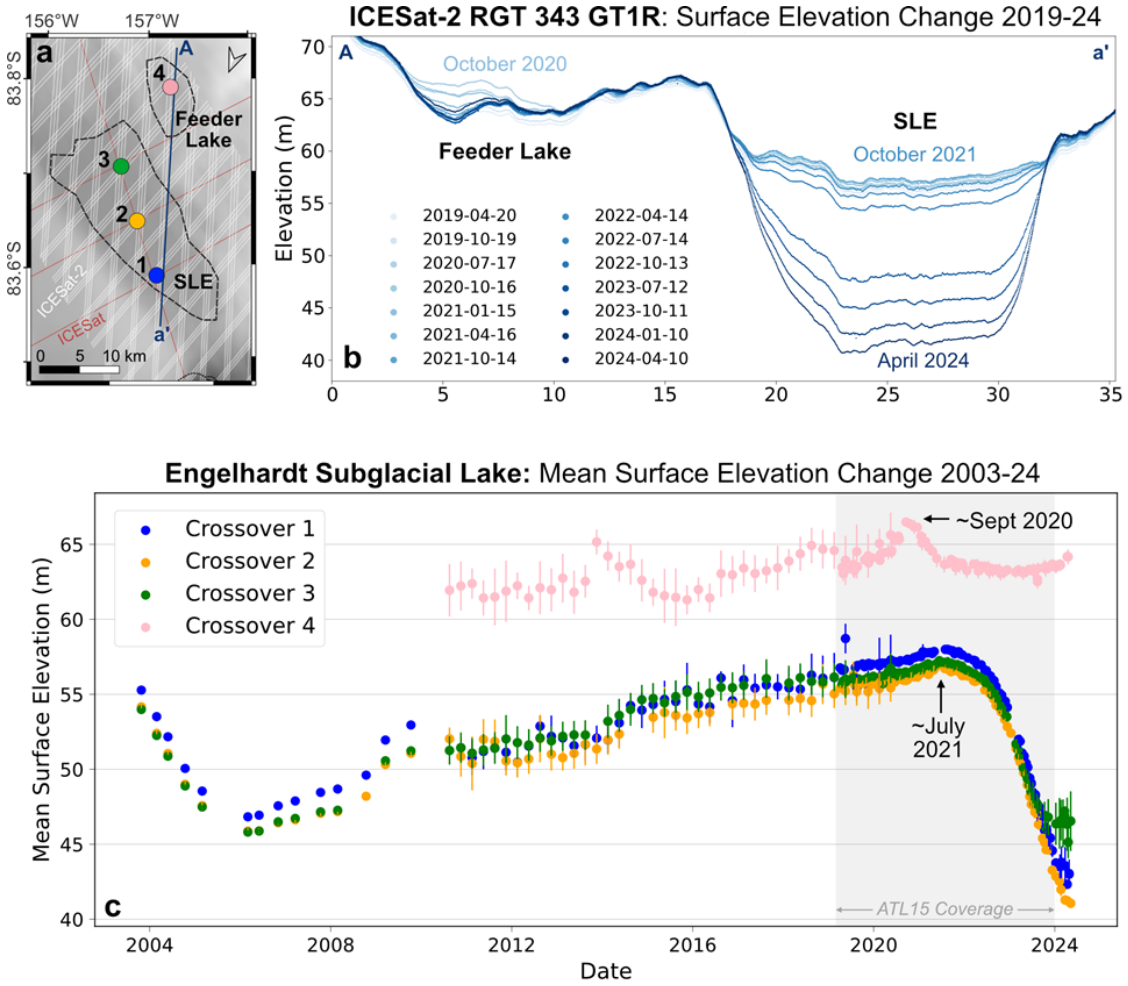


Figure 3.3. Satellite laser and radar altimetry measurements of surface elevation change at SLE, 2003–2024. (a) Location of the four crossover zones (CZ1–4) used to calculate mean elevation change at SLE, and ICESat (red) and ICESat-2 (white) RGTs. (b) Repeat surface elevation profiles along ICESat-2 RGT 343 ground track 1R (GT1R), April 2019 – April 2024; location in (a). (c) 21-year time-series of mean surface elevation at SLE, measured within CZ1–4 by ICESat (2003–09), CryoSat-2 (2010–20) and ICESat-2 (2019–24). Error bars represent one standard deviation of along-track surface elevation measurements within each CZ (note error bars are too small to be visible for some ICESat and ICESat-2 data points). Grey shading shows the ICESat-2 ATL15 coverage period (used in Fig. 3.4).

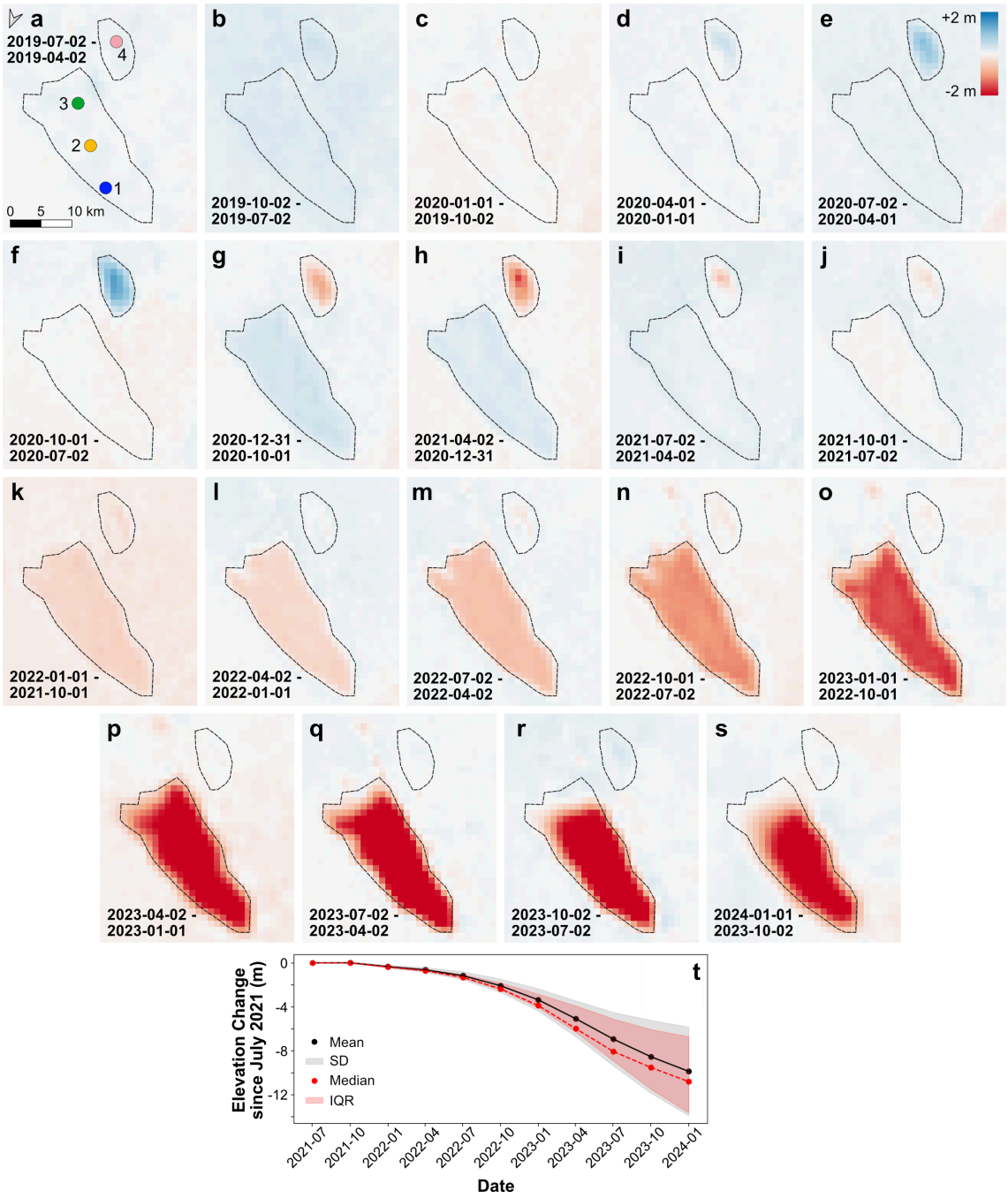


Figure 3.4. Temporal evolution of surface elevation change at SLE, April 2019 – January 2024. (a–s) ATL15 gridded surface elevation change at SLE and its upstream feeder lake between consecutive quarter-year intervals (Smith et al., 2024). Lake boundaries (dashed black lines) were manually delineated based on the observed surface subsidence area, and circles in (a) mark the location of crossover zones 1–4. (q) Mean and median cumulative elevation change within the SLE boundary from the onset of SLE drainage (July 2021 – January 2024).

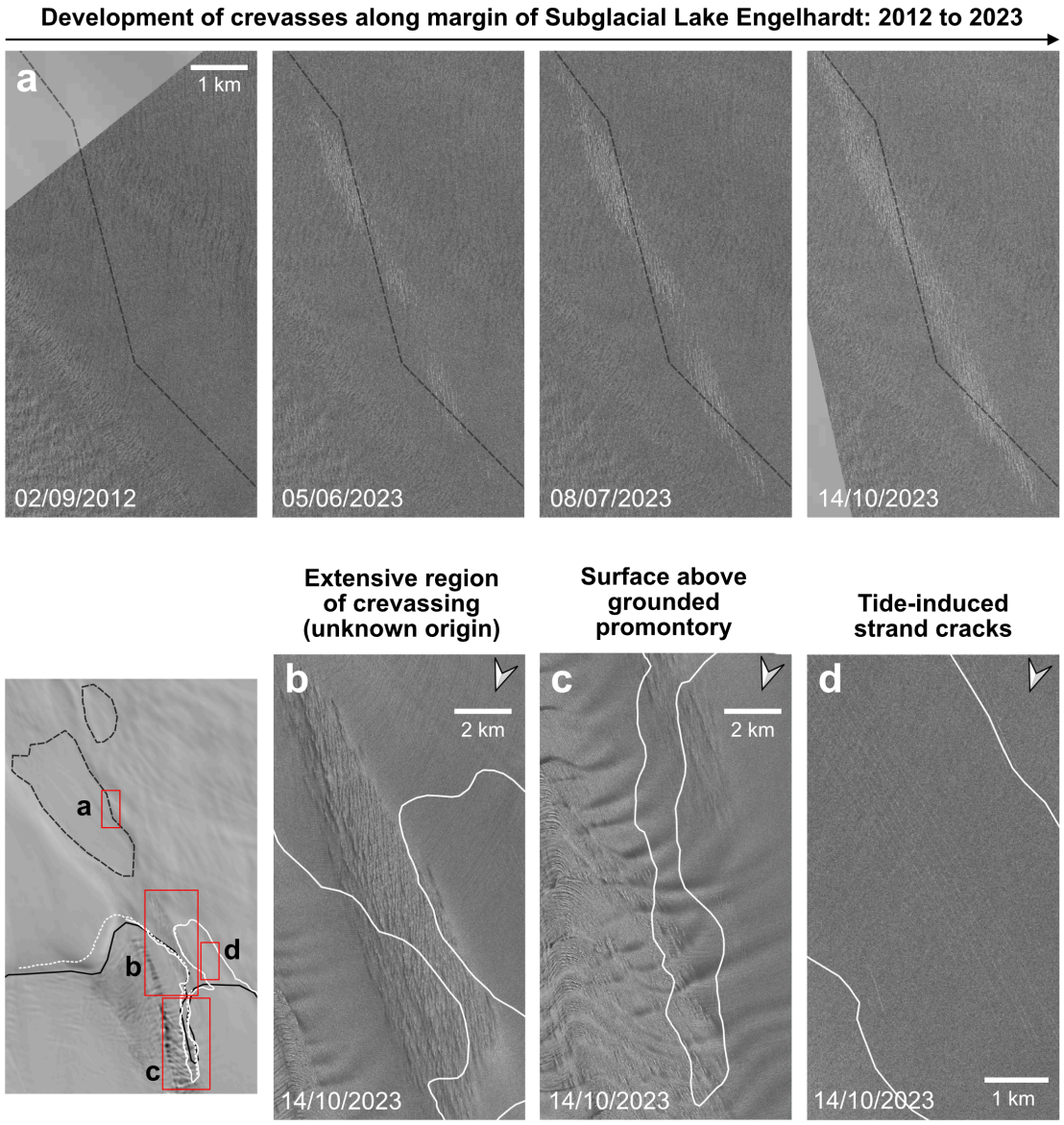


Figure 3.5. SAR imagery showing surface damage and crevassing at SLE and the GZ. (a) Time-series of TerraSAR-X multi-look backscatter images 2012–23 along the SW margin of SLE, showing the development of crevasses caused by drainage-induced surface subsidence (c.f. Fried et al., 2014). (c) Extensive region of crevassing downstream of SLE and at the upstream end of the GZ promontory. (d) Large surface undulations and more complex surface crevassing around the GZ promontory. (e) Tide-induced strand cracks parallel to the newly retreated GL of the west embayment.

3.5.2. *Grounding line retreat*

The SAR, laser altimetry and DEM data revealed extensive GL reconfiguration and surface elevation change across the whole region downstream of SLE between 2009 and 2023. The observed retreat exhibits spatial diversity, with GL retreat and ice thinning observed in the east and west embayments alongside GL advance and ice thickening along the central GL promontory (Fig. 3.6). We describe these regional patterns separately.

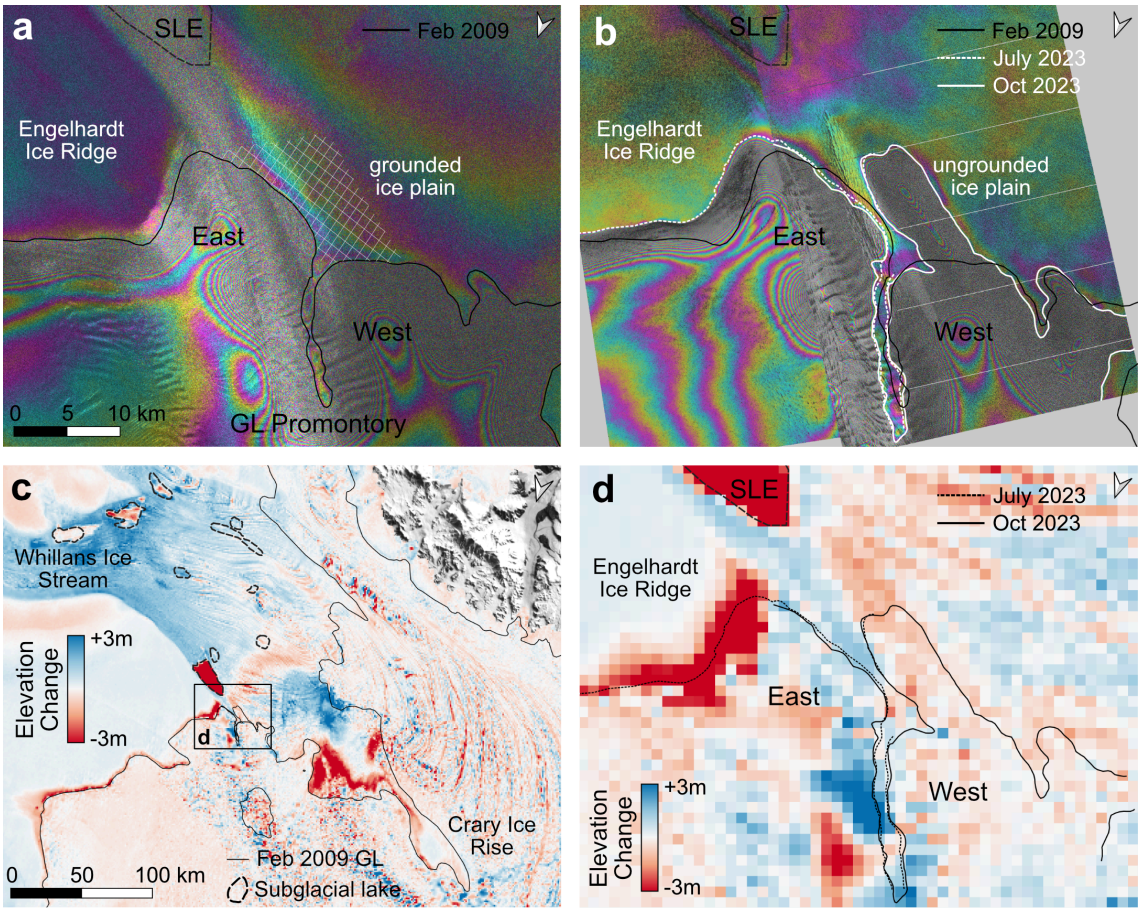


Figure 3.6. GL migration and surface elevation change downstream of SLE, 2009–24. (a) February 2009 RADARSAT-2 DInSAR and derived GL (black line), showing the east and west embayment and central grounded promontory. White hashed area shows the approx. location of the grounded ice plain identified in Brunt et al. (2010). (b) TerraSAR-X DInSAR and derived GLs from July and October 2023 (white dashed and solid lines, respectively). (c) ICESat-2 ATL15 gridded surface elevation change across the wider Gould Coast, 2019–24 (Smith et al., 2024; elevation change uncertainty across this region is shown in Fig. S3.1). (d) Zoom of (c) over the same region as (a–b) showing the 2023 GL positions.

3.5.2.1. East embayment

In the east embayment, comparison of the DInSAR data reveal there was 2–3 km of GL retreat between 2009 and 2023 (Fig. 3.6b). At its most landward position, by 2023 the GL was just ~7 km from SLE. The GL retreat was predominantly focused along Engelhardt Ice Ridge, which coincides with the ongoing longer-term retreat of the steep slope upstream of the GL (Fig. 3.7; Bindschadler & Vornberger, 1998; Fricker et al., 2007; Fricker & Scambos, 2009). SAR repeat sampling is infrequent; however, using the higher frequency sampling from ICESat, ICESat-2 and REMA we were able to estimate the mean rate of retreat of the ridge in between the available DInSAR images, by tracking the migration of the 40-m elevation contour along two intersecting ground tracks (Figs. 3.7e, 3.7f). This showed that the ridge retreated at a constant rate of 0.1–0.2 km yr^{-1} between 2003 and 2024. Notably there was no acceleration or deceleration in ridge retreat following the onset of SLE drainage until a slight observed acceleration in 2024 (Fig. 3.7f). The ridge retreat manifested in a strong (>10 m) thinning signal observed in the ICESat-2 record along this section of the GL between 2019 and 2024 (Fig. 3.6d).

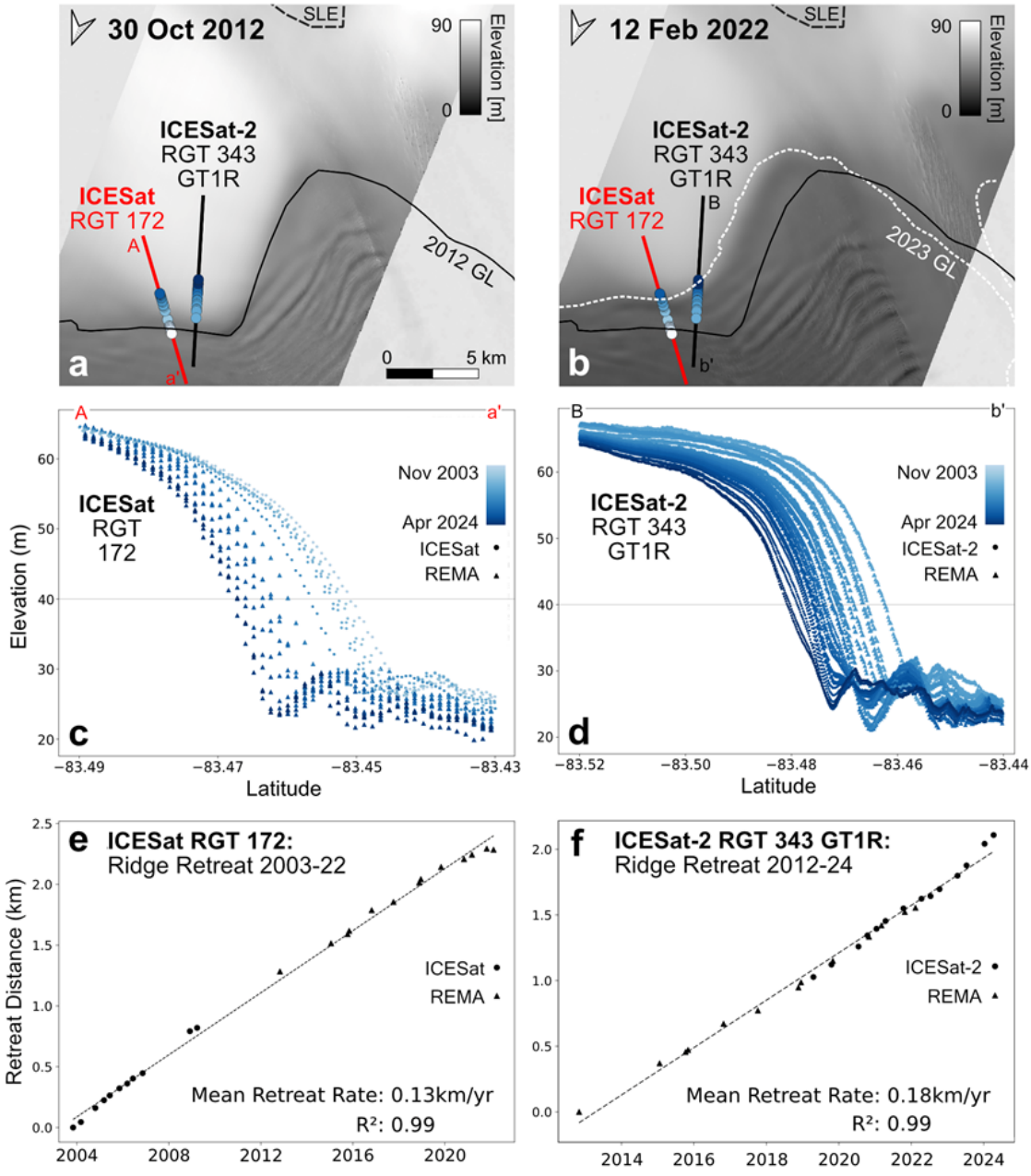


Figure 3.7. Engelhardt Ice Ridge retreat, 2003–24. (a–b) REMA DEM strips from 30 October 2012 and 12 February 2022 (Howat et al., 2019), showing the closest available DInSAR GL positions. Coloured circles mark the location of the ridge at the 40-m elevation contour along ICESat track 172 (red) and ICESat-2 RGT 343 ground track 1R (GT1R) (black) for each of the sampled time stamps in (c–d). (c) Repeat surface elevation profiles along ICESat RGT 172, combining elevations from ICESat November 2003 – March 2009 (circles) and elevations sampled along the same ground track from REMA DEM strips October 2012 – February 2022 (triangles). (d) Repeat surface elevation profiles along ICESat-2 RGT 343 GT1R, combining elevations from ICESat-2 April 2019 – April 2024 (circles) and elevations sampled along the same ground track from REMA DEM strips October 2012 – February 2022 (triangles). (e–f) Ridge retreat distance at the

40-m elevation contour along: (e) ICESat RGT 172, November 2003 – February 2022; and (f) ICESat-2 RGT 343 GT1R, October 2012 – April 2024.

3.5.2.2. West embayment

In the west embayment, the GL retreated by ~13 km between 2009 and 2023 into a region previously identified as a grounded ice plain (Figs. 3.6a, 3.6b; Brunt et al., 2010). We used the SAR and ICESat-2 data to investigate the timing of this ungrounding as well as the thinning rate and tidal flexure of the ungrounded ice plain.

Timeline of ungrounding: Given the sparse SAR coverage this far south and the absence of ICESat-2 data prior to 2019, it is difficult to precisely determine the timing of ice plain ungrounding and GL retreat. However, by combining all available satellite observations during this period we have built a comprehensive timeline to constrain the evolution of the ungrounding from 2009 onwards as well as possible (Fig. 3.8). The first two observations are RADARSAT-2 and TerraSAR-X DInSAR in 2009 and 2012, in which the absence of typical dense fringes over the ice plain in the RADARSAT-2 and TerraSAR-X DInSAR (Figs. 3.8a, 3.8b) indicate that the area was fully grounded. By 2016, a weak tidal flexure signal in the TerraSAR-X DInSAR suggests the ice plain was experiencing ephemeral grounding (Fig. 3.8c; *c.f.* Schmeltz et al., 2001). The next available observations are the first ICESat-2 RTLA measurements from May 2019 onwards, which show consistent evidence of tidal flexure and ungrounding where ground tracks cross the ice plain (Fig. 3.8). Finally, in 2023, extensive fringes in the TerraSAR-X DInSAR images indicate that the whole ice plain was fully afloat (Figs. 3.8e, 3.8f).

Overall, this timeline suggests the main period of GL retreat and subsequent ice plain ungrounding in the west embayment occurred between 2016 and 2019. We can be confident that this is a real signal of GL retreat over this period rather than a product of tidal sampling or aliasing (e.g., Padman et al., 2018), based on the fact that the 2023 DInSAR sampled a lower maximum tidal amplitude and total tide range than in 2009 and 2012 (Table 3.1).

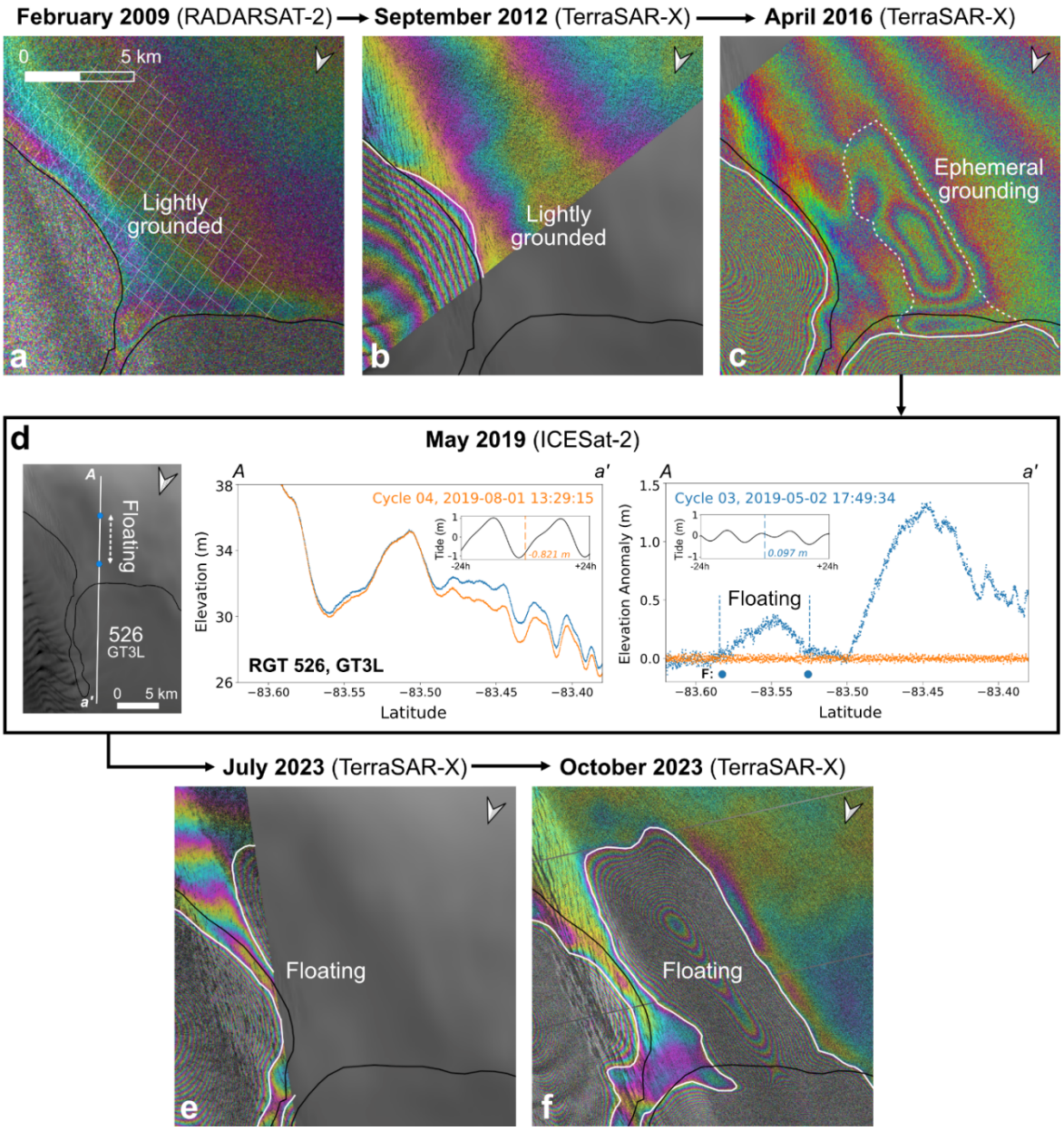


Figure 3.8. Timeline of GL retreat and ice plain ungrounding in the west embayment from a combination of RADARSAT-2 and TerraSAR-X DInSAR and ICESat-2 RTLA. (a) February 2009; (b) September 2012; (c) April 2016 (weak signal of GL retreat marked with dashed white line); (d) May 2019, ICESat-2 repeat elevation and elevation anomalies along RGT 526 GT3L showing tidal flexure (i.e. ungrounding) over the section of the track crossing the ice plain on 2 May 2019; (e) July 2023; (f) October 2023. Black line shows the 2009 GL for comparison between images. The white hashed area in (a) shows the approx. location of the grounded ice plain identified in Brunt et al. (2010). The total expected vertical height difference for each DInSAR image are provided in Table 3.1.

ICESat-2 thinning rates: The gridded ICESat-2 elevation change data shows that the ice in the newly ungrounded ice plain thinned by ~0.5–2 m between 2019 and 2024 (Fig. 3.6d). This region appears to connect to a wider 'crescent' of thinning that extends further inland across Whillans Ice Plain to the western side of the Crary Ice Rise (Fig. 3.6c), standing in contrast to the wider thickening trend of Whillans Ice Stream.

ICESat-2 tidal flexure: The ICESat-2 RTLA results show that there is considerable tidal flexure and tidal GL migration within the newly ungrounded ice plain (Fig. 3.9). This is illustrated along RGT 23 GT2L (Figs. 3.8a–f), where the observed differences in the along-track elevation anomalies between repeat measurements on 26 March, 25 June, and 23 December 2021 reflect the change in extent of tidal flexure and depth of seawater intrusion across the tidal cycle (Fig. 3.9e). The maximum elevation anomaly across the ice plain (+0.8 m) is observed on 25 June, which was sampled immediately after a peak spring tide (Fig. 3.9c). The ice plain was sampled at lower tides on 26 March and 23 December (Fig. 3.9e) and the smaller elevation anomalies on these dates (Figs. 3.9b, 3.9d) indicate less tidal flexure and shallower water depths (Figs. 3.9b, 3.9d). When the RTLA method was applied to all ICESat-2 tracks that cross the ungrounded ice plain (Fig. 3.9g) we observe that the whole region is estuary-like (Horgan et al., 2013), widening and deepening at high tide and possibly re-grounding at low tide. This is further evidenced by the tidal strand cracks visible in the TerraSAR-X backscatter imagery (Fig. 3.5d).

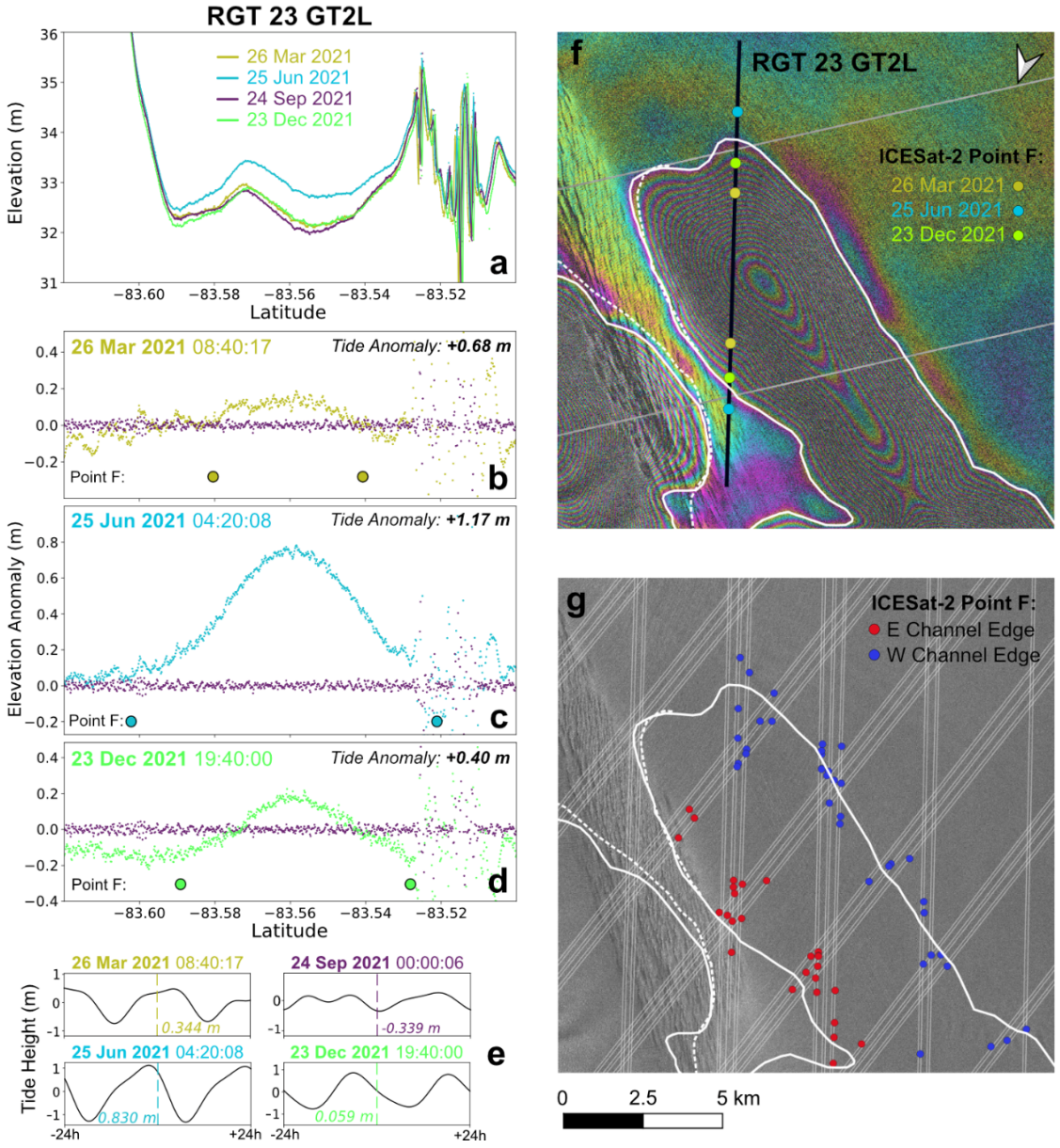


Figure 3.9. ICESat-2 RTLA measurements of tidal flexure and tidal GL migration within the newly ungrounded ice plain at the west embayment. (a) Repeat ATL06 surface elevation profiles along ICESat-2 RGT 23 GT2L from 26 March (gold), 25 June (blue), 24 September (purple) and 23 December (green) 2021 across the newly ungrounded ice plain (location in (f)). (b–d) ATL06 elevation anomalies from 26 March (gold), 25 June (blue) and and 23 December (green) 2021, each calculated against the low tide reference profile of 24 September 2021 (purple). Derived location of Point F (inland limit of tidal flexure) for either side of the channel are shown by the coloured dots along the *x*-axis. (e) Modelled tides 24 h before and after each sampled ICESat-2 overpass, extracted from the Circum-Antarctic Tidal Simulation 2008 (CATS2008_v2023; Howard et al., 2019) using the pyTMD software package (version 2.1.0., Sutterley et al., 2017). (f) Location of derived Point F positions for each date (coloured dots) along ICESat-2 RGT

23 GT2L (solid black) overlain on the October 2023 TerraSAR-X DInSAR. (g) Point F positions along the western (blue) and eastern (red) edge of the newly ungrounded ice plain from all intersecting ICESat-2 RGTs, overlain on the TerraSAR-X multi-look backscatter image from 14 October 2023.

3.5.2.3. Grounded promontory

The DInSAR time-series for the period 2009–23 also show changes in the central grounded promontory that separates the east and west embayments (Fig. 3.10), located in a region of localised ice thickening (Fig. 3.6d). Over this time, this long and narrow feature oriented parallel to ice flow has migrated eastwards by ~1 km and extended ~3 km further seaward. There is evidence of increased surface damage around this feature, with prominent long-wavelength undulations and extensive crevassing (Fig. 3.5c).

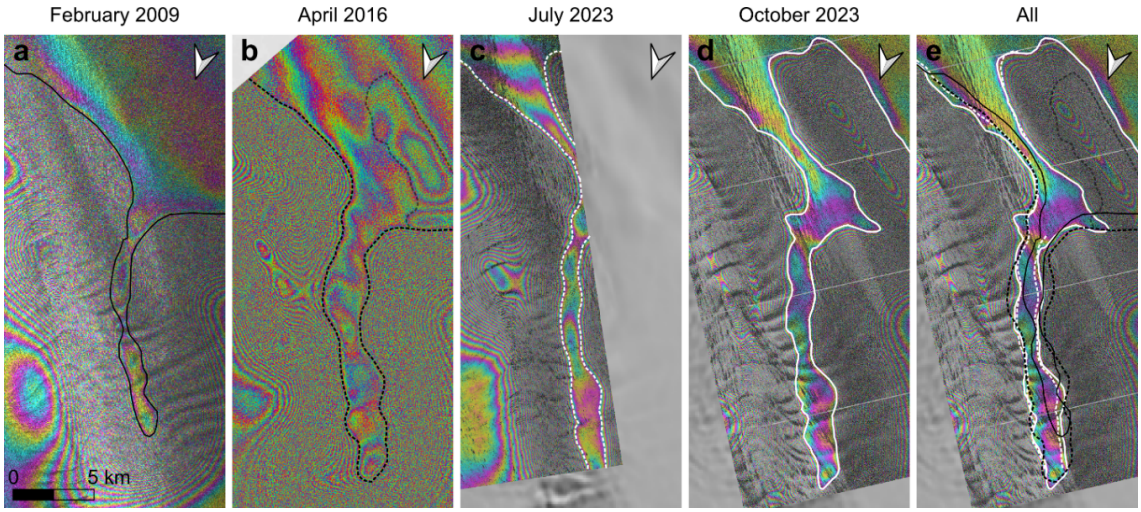


Figure 3.10. DInSAR time-series showing the change in the shape and length of the grounded promontory separating the east and west GL embayments. DInSAR fringes and delineated GL for four epochs: (a) February 2009 (RADARSAT-2); (b) April 2016 (TerraSAR-X); (c) July 2023 (TerraSAR-X); (d) October 2023 (TerraSAR-X). (e) All delineated GL positions overlain on the October 2023 (TerraSAR-X) DInSAR for comparison.

3.6. Discussion

3.6.1. Engelhardt Subglacial Lake (SLE) drainage

The 2021–24 drainage of SLE occurred ~18 years after the last drainage, representing the longest interval observed between successive drainages of the same subglacial lake in Antarctica. We estimate that this event discharged ~2.3 km^3 of subglacial water into the RIS cavity over the 31 months to January 2024. This total drainage volume would have increased as drainage continued until at least April 2024, giving a total estimated drainage period of 34–36 months. The magnitude of surface subsidence over SLE from 2021–24 was at least 5 m greater than was observed during the 2003–06 drainage event (Fig. 3.3c), which discharged an estimated ~2.0 km^3 over a similar total time period of 33 months (Fricker et al., 2007). The higher spatial and temporal density of measurements from ICESat-2 has allowed us to delineate a more accurate lake boundary and track the activity of a newly-identified upstream feeder lake (Figs. 3.3, 3.4).

The onset mechanism suggested for the 2003–06 SLE drainage was the breaching of a weak pressure barrier of ~50 kPa that had kept the downstream end sealed off from the ocean (Fricker et al., 2007). As the lake filled, the rising pressure head reached ~100–200 kPa, breaching the ice seal to initiate drainage. We propose a similar onset mechanism for the 2021–24 drainage, except that the trigger for the seal breach was the pulse of subglacial water discharged from the newly-identified upstream feeder lake in September 2020 (Figs. 3.3, 3.4). This 'cascading drainage' behaviour between interconnected lakes has been observed elsewhere in Antarctica (Fricker et al., 2014; Fricker & Scambos, 2009; Malczyk et al., 2020; Neckel et al., 2021; Siegfried et al., 2023). We note that drainage from the upstream feeder lake may have also initiated the 2003–06 SLE drainage, but we lack observations as it was not well-sampled by ICESat (Fig. 3.3a).

The rate of surface subsidence measured by ICESat-2 accelerated as drainage progressed, reaching a maximum in July 2023 (Figs. 3.3b, 3.3c, 3.4t), likely coinciding with evolution to a more efficient drainage system. Although we define the timing of

drainage onset as when we first detected a decrease in surface elevation over the lake (July 2021), SLE may have begun 'leaking' at slower rates several months beforehand. This has been proposed at subglacial lakes Mercer and Conway (Carter et al., 2013) and was modelled for the 2003–06 SLE drainage (Carter et al., 2017).

The outflow of >2.3 km^3 of freshwater from SLE drainage into the RIS cavity will affect the freshwater budget, local circulation and melt patterns in the cavity (Carter & Fricker, 2012; Gwyther et al., 2023; Hawkings et al., 2020; Nakayama et al., 2021). Basal melt rates at the Gould Coast GL are relatively low (~0.05–1 m yr^{-1}; e.g., MacAyeal, 1984; Holland et al., 2003; Dinniman et al., 2007; Catania et al., 2010), but models indicate that this can increase by a factor of three at subglacial lake drainage outflows (Jenkins, 2011). Therefore, this drainage has the potential to accelerate localised ice thinning and GL retreat (Carter & Fricker, 2012; Pelle et al., 2023).

3.6.2. Revisiting the relationship between SLE drainage and grounding line retreat

Following the 2003–06 drainage of SLE it remained an open question whether GL retreat had triggered the drainage, or whether drainage caused the retreat (Fricker & Scambos, 2009). We revisit this question using the new high-resolution satellite observations made before and during the 2021–24 drainage event, considering the east and west embayments separately.

3.6.2.1. East embayment

The GL retreat along Engelhardt Ice Ridge (Fig. 3.7) in the east embayment continues a longer-term trend that has been observed since at least 1963, suggested to be linked to the deceleration of Whillans Ice Stream (Bindschadler & Vornberger, 1998; Fricker et al., 2007). We find no evidence of acceleration in GL retreat in this area following the onset of SLE drainage in July 2021 (Figs. 3.7e, 3.7f), suggesting that retreat was not directly associated with the drainage. We also consider it unlikely that GL retreat was the primary trigger for the 2021 SLE drainage because the previous drainage event occurred when the GL was much further seaward. Whilst not the primary influence, we cannot rule out the possibility that GL retreat facilitated the onset of drainage by

shortening the bridge of grounded ice between SLE and the RIS cavity, changing the ice surface slope and weakening the hydraulic seal (Hayden & Dow, 2023). This mechanism was proposed for a subglacial lake drainage beneath Crane Glacier in 2004–05 (Scambos et al., 2011).

3.6.2.2. West embayment

The observation of 13 km of GL retreat in the west embayment is a substantial signal for the Gould Coast region. The extent of retreat appears to be controlled by the ice geometry, reaching the landward limit of the relatively thinner ice plain at the break-in-slope (Figs. 3.6a, 3.6b, 3.8, 3.9). Here, as across much of Whillans Ice Plain, the grounded ice sits close to hydrostatic equilibrium with low basal relief, meaning that small amounts of thinning can induce buoyancy-driven GL retreat (Batchelor et al., 2023; Carter et al., 2013; Catania et al., 2012). We suggest that the long-term, localised ice-sheet thinning observed by ICESat-2 inland of the west embayment GL (Fig. 3.6d) has caused the ice plain to unground and the GL to retreat, following the ice plain life cycle of Brunt et al. (2011): from 'lightly grounded' in 2009, to 'ephemerally grounded' in 2016 and fully floating by 2023 (Fig. 3.8). The cause of the localised thinning downstream of SLE, which contrasts the more widespread ice dynamic thickening trend of Whillans Ice Stream (Smith et al., 2020), remains unclear. However, its location within the wider crescent of thinning extending to the southern side of Crary Ice Rise (Fig. 3.6c) suggests it may be linked to larger-scale ice dynamics in the region (e.g., Beem et al., 2014; Siegfried et al., 2016). The ice plain ungrounding may also have been influenced by the complex stick-slip ice dynamics (Weins et al., 2024; Winberry et al., 2009) and possible spatial variations in basal conditions (Christianson et al., 2016); however these interpretations are limited by a lack of ground data (e.g., seismic or GPS) which would be necessary to obtain more detailed insights (e.g., Pratt et al., 2014; Siegfried et al., 2016; Winberry et al., 2014).

Our hypothesis that GL retreat in the west embayment was driven by the ungrounding of an ice plain due to long-term thinning suggests that it was unrelated to the 2021–24 SLE drainage event. This is supported by two key lines of evidence: (i) the timing of the observed GL retreat (2016–19; Fig. 3.8) is uncorrelated with the drainage onset (2021; Fig. 3.3); and (ii) the modelled hydrological pathway (if correct) predicts that

SLE should drain via the east embayment (Fig. 3.1b), where it would exert minimal influence on ice dynamics in the west embayment. However, given the proximity of SLE to the GL it is unlikely that there was no interaction between the two processes. It is possible that SLE drainage accelerated the GL retreat, particularly if ice thinning and GL migration altered the hydropotential gradient (Carter et al., 2013) enough to re-direct the outflow from SLE via the west embayment. This could increase the localised basal melt rate at the GL (Carter & Fricker, 2012; Pelle et al., 2023; Whiteford et al., 2022), which together with tidal flows could drive further thinning and GL retreat (Horgan et al., 2013). It could also change the subglacial conditions–including basal slipperiness–upstream of the GL, influencing ice flow and GL retreat (Sergienko & Haseloff, 2023). Flow-switching of this kind has previously been proposed across Whillans Ice Plain (Carter et al., 2013; Marsh et al., 2016), but it is not possible to unequivocally verify without measurements from the ice shelf cavity.

3.6.2.3. Grounded promontory

The grounded GL promontory separating the east and west embayments is another signature of interaction between subglacial hydrology and the GL. Based on its location, orientation, geometry and surface damage, we suggest that this may be the surface expression of local grounding of the ice on a ridge-like bedform. A CReSIS radar survey over the region (CReSIS, 2014) reveals there is a bump in the bed topography, but without drilling into the substrate we cannot confirm its origin. Since it protrudes seaward by several kilometres, this bed feature is likely to impact localised ocean circulation patterns in the ice shelf cavity. We propose three possible origins of the ridge:

(i) Ice-stream lateral shear-moraine (ISLM): ISLMs are ridges of sediment (predominantly subglacial till) accumulated at ice stream shear margins, enhanced by the presence of subglacial meltwater (Batchelor & Dowdeswell, 2016; Hindmarsh & Stokes, 2008; Stokes & Clark, 2002). The location of the promontory along the Whillans Ice Stream shear margin, which is underlain by deformable till (Kamb, 2001) with a well-established supply of subglacial meltwater, is consistent with an ISLM.

(ii) Esker: Eskers are the depositional evidence of a former subglacial meltwater channel, sometimes formed during subglacial lake outburst floods (Burke et al., 2008). Drews et al. (2017) proposed the first evidence from Antarctica of actively-evolving eskers deposited by subglacial water conduits at the Roi Baudouin Ice Shelf GL. The extensive region of crevassing immediately upstream of the GZ promontory could offer additional evidence for this interpretation (Fig. 3.5b). This surface feature has been observed in satellite imagery as early as 1989 (Bindschadler et al., 1993) and has continued to advect downstream with ice flow. Its origin is unknown, but it could possibly be linked to past GL advancement or evidence of a former subglacial melt channel or collapsed lake. However, we note that eskers have been "notably absent" from the palaeo-record in the Ross Sector (Greenwood et al., 2016).

(iii) Fault-controlled structure: The subglacial ridge may represent the upper footwall of a half-graben, formed by en-echelon faulting during a phase of crustal extension. Several such faults have been identified running parallel beneath the Ross Ice Shelf (e.g., Greischar et al., 1992; Munson & Bentley, 1992), including one that has been proposed to control the expression of Crary Ice Rise (Muto et al., 2013), which suggests it could be plausible for another to exist in this location.

Regardless of origin, the ~3 km lengthening of the promontory between 2009 and 2023 (Fig. 3.10) is most likely the result of localised ice thickening (Fig. 3.6d), which caused the ice to ground on a longer section of the existing bed feature, initiating a positive feedback of enhanced grounding, slow-down and thickening. It is possible that it was also affected by the enhanced sediment erosion, transport and deposition linked to SLE drainage (Carter et al., 2017; Horgan et al., 2013; Livingstone et al., 2019), although the relatively low mean drainage discharge rate (~20 m^3 s^{-1}) indicates any sediment deposition was likely distributed over a substantial area. Depositional features at GLs can provide resistance to flow through lateral drag (Stokes & Clark, 2002) and have been proposed as possible mechanisms for GL stabilisation in the palaeo-record (Alley et al., 2007; Batchelor & Dowdeswell, 2016). Therefore, we suggest that this feature is of interest for future monitoring.

3.6.3. Implications of grounding line retreat

3.6.3.1. Seawater intrusion

The newly ungrounded tidally modulated estuary in the west embayment shows similarities to those observed at the GLs of Amery (Chen et al., 2023) and Totten (Li et al., 2023), and provides a new route for ocean water to flush in and out of the GZ cavity (Horgan et al., 2013). Assuming the ice plain is grounded during low tide, we estimate that the maximum depth of tidal seawater intrusion beneath the ice plain is <1 m at high tide (Fig. 3.9g). These intrusions can reduce basal friction (e.g., Anandakrishnan et al., 2003), affect cavity circulation and enhance basal melt rates (Makinson et al., 2011; Milillo et al., 2019; Robel et al., 2022). Such complex and small-scale ice-ocean interactions have been proposed as a key missing piece in ice sheet models (Rignot, 2023), but are challenging to observe. At SLE this has only been possible as a result of the increased temporal sampling and coverage of ICESat-2, but our ability to fully characterise this behaviour (which would include confirming the flotation state of the ice plain at low tide) would be improved in future by the collection of in situ observations or higher-frequency DInSAR acquisitions (e.g., from COSMO-SkyMed; Brancato et al., 2020; Milillo et al., 2019; Milillo et al., 2017 or other SAR systems and constellations including the future NISAR mission). We note, however, that these signals are extremely complex to interpret as the region is likely subject to bridging stresses and flexural limits imposed by the geometry, incomplete tidal circulation and lags between rising and falling tides (e.g., Freer et al., 2023).

3.6.3.2. Future evolution

Improving projections of future ice loss in Antarctica relies on the better understanding of key processes, including how the GL responds to different forcing mechanisms. Subglacial hydrology upstream of the GL has remained one of the least understood forcings, in part due to a scarcity of observations. The 2021–24 drainage of SLE, as one of the only known active subglacial lake in Antarctica within 10 km of the GL, presented a rare opportunity to study these processes in close proximity, taking advantage of the improvements in spatial and temporal resolution and coverage of satellite datasets since its last drainage two decades ago.

Although the current satellite evidence does not show a direct causal link between lake drainage and GL retreat over this distance, it is possible that a link will develop as the GL continues to retreat towards the lake. If retreat downstream of SLE continues at current rates, the GL in the east embayment could connect with SLE within 40 years, and even sooner in the west embayment. This connection would link SLE with the RIS cavity, affecting local ice and lake dynamics and the overall shape of Whillans Ice Plain. Elsewhere in Antarctica, subglacial lakes have been observed within 40 km of the GL at Whillans and Mercer (Fig. 3.1a), Kamb, MacAyeal, Rutford, Totten and Thwaites (Malczyk et al., 2020; Siegfried & Fricker, 2018) and within 10 km at Pine Island Glacier (Joughin et al., 2016). Together, these ice streams drain 15–20% of the Antarctic ice sheet (Rignot et al., 2019). Understanding if and how their dynamics may be influenced in the future by subglacial hydrology (particularly the fill-and-drain of active subglacial lakes) is an important question, especially in regions subject to rapid GL retreat like Totten, Pine Island and Thwaites (Li et al., 2023; Milillo et al., 2019), where the distance between the GL and subglacial lakes is shortening.

3.7. Summary

We have presented a 21-year record of satellite-derived surface elevation change at Engelhardt Subglacial Lake (SLE) in West Antarctica, which includes the latest drainage event from 2021–24. From July 2021 to April 2024, the ice surface over SLE lowered by up to 15 m, draining more than 2.3 km^3 of subglacial water into the Ross Ice Shelf cavity. Over the same period we have observed significant evolution of the downstream grounding zone (GZ), including 2–3 km of grounding line (GL) retreat along Engelhardt Ice Ridge since 2009, and 13 km of retreat in the west embayment where an ice plain has ungrounded.

Analysis of the satellite observations from the 2021–24 drainage indicates that SLE drainage and GL retreat were largely independent processes: drainage was initiated by the influx of water from a smaller upstream feeder lake; GL retreat in the east embayment was mainly driven by the long-term retreat of Engelhardt Ice Ridge; and GL retreat in the west embayment was due to long-term dynamic ice thinning that caused

the lightly grounded ice plain to reach flotation. However, we acknowledge that there are unobserved mechanisms by which these processes could have influenced each other. For example, the outflow from SLE drainage could increase basal melt in the GZ, thus accelerating thinning and enhancing GL retreat. Additionally, GL retreat would reduce the distance between the lake and the ice shelf, affecting ice surface slope, which could weaken the hydraulic seal sufficiently to facilitate the onset of drainage.

Our observation of an approximately 27 km long and 2 km wide subglacial bedform protruding seaward from the GL poses additional questions about the relationship between subglacial hydrology and the GL. Its identity and exact formation mechanism is not known, but we believe it may be the surface expression of an ice-stream lateral shear-moraine, esker, or a fault-controlled structure. We suggest that its ~3 km lengthening since 2009 may be due to localised ice thickening causing grounding on more of the existing bed feature, possibly enhanced by sediment outflow from SLE drainage.

Overall, our observations highlight the complex interactions between ice dynamics, subglacial hydrology and sediment transport in Antarctic GZs. The new high-resolution satellite data have allowed us to resolve these behaviours much better than in the past, but there are still gaps in our understanding. We suggest that this region is important for examining a variety of dynamic GZ processes – with opportunities for monitoring using a combination of satellite remote sensing (including the upcoming NISAR mission), airborne surveys and drilling campaigns.

Acknowledgments

BF, OM, HF and AH planned the research; BF conducted the data analysis and wrote the manuscript. RR and SW provided the swath-processed CryoSat-2 data. DF provided the TerraSAR-X data; DF and OM processed the DInSAR. WS calculated the hydropotential flow paths. All authors provided insights regarding the interpretation of data and reviewed and edited the manuscript. The authors gratefully acknowledge the National Aeronautics and Space Administration's (NASA) ICESat and ICESat-2 Science Teams and the National Snow and Ice Data Center (NSIDC) for the distribution of the

ICESat and ICESat-2 data; the European Space Agency (ESA) for the acquisition and availability of CryoSat-2 data; and the ESA CryoTempo project (https://cryotempo-eolis.org/) for provision of CryoSat-2 SARIn data. RADARSAT-2 data were collected by the Canadian Space Agency and MDA under guidance of the Polar Space Task Group. We thank Bernd Scheuchl for providing interferograms from 2009. TerraSAR-X data were provided through the science proposal HYD3673.

We thank Howard Conway, Benjamin Hills, Olga Sergienko and two anonymous reviewers for their comments that helped improve the manuscript. Bryony I. D. Freer was supported by Natural Environment Research Council (NERC) Satellite Data in Environmental Science (SENSE) Centre for Doctoral Training (grant no. NE/T00939X/1). Funding is provided to Helen A. Fricker from NASA through funding for the ICESat-2 Science Team (Award: 80NSSC23K0934). M. R. Siegfried and W. Sauthoff were funded by NASA award 80NSSC21K0912. Funding is provided to Anna E. Hogg and Richard Rigby by ESA via the ESA STSE CryoSat+ CryoTop Evolution project and the 4DAntarctica project (ESA-IPL-POE-NB-sp-RPF-2015-951). Funding is provided to Sally F. Wilson by the Panorama Natural Environment Research Council (NERC) Doctoral Training Partnership (DTP), under grant NE/S007458/1. Dana Floricioiu was supported by DLR's Polar Monitor II and Antarctic Ice Sheet CCI (ESA/Contract No. 4000126813/18/I-NB) projects.

Open Research

The ICESat-2 ATL06 L3A Land Ice Height (version 6) data used for measuring surface elevation change and grounding line position 2019–24 are available at the National Snow and Ice Data Center (NSIDC) via https://doi.org/10.5067/ATLAS/ATL06.006 (Smith et al., 2023). The ICESat-2 ATL15 L3B Gridded Antarctic Land Ice Height Change (version 3) data used for measuring surface elevation change 2019–24 are available at NSIDC via https://doi.org/10.5067/ATLAS/ATL15.004 (Smith et al., 2024). The ICESat GLAS/ICESat L1B Global Elevation Data (HDF5) (version 34) data used for measuring surface elevation change 2003–09 are available at NSIDC via https://doi.org/10.5067/ICESAT/GLAS/DATA109 (Zwally et al., 2014). The CryoSat-2

elevation data used for measuring surface elevation change 2010–20 were provided by the ESA CryoTempo-EOLIS project, available at https://cryotempo-eolis.org/point-product/ (Gourmelen et al., 2018). The derived TerraSAR-X interferograms and derived GLs from 2012, 2016 and 2023 are published with the UK Polar Data Centre, available at https://doi.org/10.5285/e1d182b1-6aa6-434e-9390-f7956227cb82 (Marsh & Floriciou et al., 2024). The derived hydrological flow pathways beneath Whillans Ice Stream are published with the UK Polar Data Centre, available at https://doi.org/10.5285/0df5d4e9-2fcd-4420-b403-24d76848a5a5 (Sauthoff & Freer, 2024). The MEaSUREs grounding line product (version 2) used to show the 2009 grounding line position is available at NSIDC via https://doi.org/10.5067/IKBWW4RYHF1Q. The Reference Elevation Model of Antarctica (REMA) digital elevation model (DEM) mosaic (version 2) and strip (version 4.1) products used to measure the retreat of Engelhardt Ice Ridge are available at the Polar Geospatial Center via https://data.pgc.umn.edu/elev/dem/setsm/REMA/ (Howat et al., 2019).

Supplementary Material

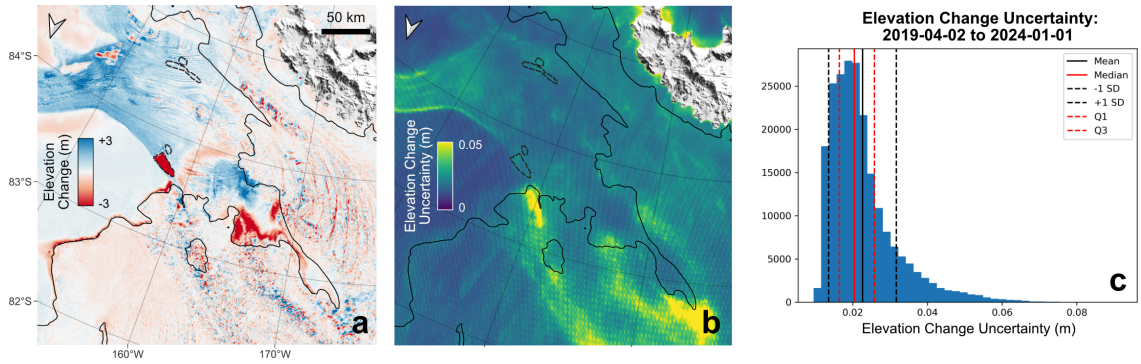


Figure S3.1. ATL15 surface elevation change and elevation change uncertainty across the Gould Coast, 2019 – 2024. (a) ATL15 total elevation change between April 2019 and January 2024. (b) ATL15 elevation change uncertainty over the same time period as in (a). (c) Histogram showing the distribution of elevation change uncertainty values across the entire Gould Coast study area.

References

Alley, R. B., Anandakrishnan, S., Dupont, T. K., Parizek, B. R., & Pollard, D. (2007). Effect of Sedimentation on Ice-Sheet Grounding-Line Stability. *Science, 315(5820)*, 1838–1841. https://doi.org/10.1126/science.1138396

Anandakrishnan, S., Voigt, D. E., Alley, R. B., & King, M. A. (2003). Ice stream D flow speed is strongly modulated by the tide beneath the Ross Ice Shelf. *Geophysical Research Letters, 30(7)*. https://doi.org/10.1029/2002GL016329

Bartos, M. (2020). Pysheds: Simple and fast watershed delineation in python. https://doi.org/ 10.5281/zenodo.3822494

Batchelor, C. L., & Dowdeswell, J. A. (2016). Lateral shear-moraines and lateral marginal-moraines of palaeo-ice streams. *Quaternary Science Reviews, 151*, 1–26. https://doi.org/10.1016/j.quascirev.2016.08.020

Batchelor, C. L., Christie, F. D. W., Ottesen, D., Montelli, A., Evans, J., Dowdeswell, E. K., et al. (2023). Rapid, buoyancy-driven ice-sheet retreat of hundreds of metres per day. *Nature, 617(7959)*, 105–110. https://doi.org/10.1038/s41586-023-05876-1

Beem, L. H., Tulaczyk, S. M., King, M. A., Bougamont, M., Fricker, H. A., & Christoffersen, P. (2014). Variable deceleration of Whillans Ice Stream, West Antarctica. *Journal of Geophysical Research: Earth Surface*, 119(2), 212–224. https://doi.org/10.1002/2013JF002958

Bindschadler, R. (1993). Siple Coast Project research of Crary Ice Rise and the mouths of Ice Streams B and C, West Antarctica: review and new perspectives. *Journal of Glaciology, 39(133)*, 538–552. https://doi.org/10.3189/S0022143000016439

Bindschadler, R., & Vornberger, P. (1998). Changes in the West Antarctic Ice Sheet since 1963 from declassified satellite photography. *Science, 279(5351)*, 689–692. https://doi.org/10.1126/science.279.5351.689

Borsa, A. A., Moholdt, G., Fricker, H. A., & Brunt, K. M. (2014). A range correction for ICESat and its potential impact on ice-sheet mass balance studies. *The Cryosphere*, 8(2), 345–357. https://doi.org/10.5194/tc-8-345-2014

Brancato, V., Rignot, E., Milillo, P., Morlighem, M., Mouginot, J., An, L., et al. (2020). Grounding Line Retreat of Denman Glacier, East Antarctica, Measured With COSMO-SkyMed Radar Interferometry Data. *Geophysical Research Letters*, 47(7). https://doi.org/10.1029/2019GL086291

Brunt, K. M., Fricker, H. A., & Padman, L. (2011). Analysis of ice plains of the Filchner–Ronne Ice Shelf, Antarctica, using ICESat laser altimetry. *Journal of Glaciology*, 57(205), 965–975. https://doi.org/10.3189/002214311798043753

Brunt, K. M., Fricker, H. A., Padman, L., Scambos, T. A., & O'Neel, S. (2010). Mapping the grounding zone of the Ross Ice Shelf, Antarctica, using ICESat laser altimetry. *Annals of Glaciology*, 51(55), 71–79. https://doi.org/10.3189/172756410791392790

Burke, M. J., Woodward, J., Russell, A. J., Fleisher, P. J., & Bailey, P. (2008). Controls on the sedimentary architecture of a single event englacial esker: Skeiðarárjökull, Iceland. *Quaternary Science Reviews*, 27(19–20), 1829–1847. https://doi.org/10.1016/j.quascirev.2008.06.012

Carter, S. P., Fricker, H. A., & Siegfried, M. R. (2017). Antarctic subglacial lakes drain through sediment-floored canals: theory and model testing on real and idealized domains. *The Cryosphere, 11(1)*, 381–405. https://doi.org/10.5194/tc-11-381-2017

Carter, S. P., & Fricker, H. A. (2012). The supply of subglacial meltwater to the grounding line of the Siple Coast, West Antarctica. *Annals of Glaciology, 53(60)*, 267–280. https://doi.org/10.3189/2012AoG60A119

Carter, S. P., Fricker, H. A., & Siegfried, M. R. (2013). Evidence of rapid subglacial water piracy under Whillans Ice Stream, West Antarctica. *Journal of Glaciology, 59(218)*, 1147–1162. https://doi.org/10.3189/2013JoG13J085

Catania, G., Hulbe, C., & Conway, H. (2010). Grounding-line basal melt rates determined using radar-derived internal stratigraphy. *Journal of Glaciology*, 56(197), 545–554. https://doi.org/10.3189/002214310792447842

Catania, G., Hulbe, C., Conway, H., Scambos, T. A., & Raymond, C. F. (2012). Variability in the mass flux of the Ross ice streams, West Antarctica, over the last millennium. *Journal of Glaciology, 58(210)*, 741–752. https://doi.org/10.3189/2012JoG11J219

Chen, H., Rignot, E., Scheuchl, B., & Ehrenfeucht, S. (2023). Grounding Zone of Amery Ice Shelf, Antarctica, From Differential Synthetic-Aperture Radar Interferometry. *Geophysical Research Letters, 50(6)*, e2022GL102430. https://doi.org/10.1029/2022GL102430

Christianson, K., Jacobel, R. W., Horgan, H. J., Alley, R. B., Anandakrishnan, S., Holland, D. M., & DallaSanta, K. J. (2016). Basal conditions at the grounding zone of Whillans Ice Stream, West Antarctica, from ice-penetrating radar. *Journal of Geophysical Research: Earth Surface*, 121(11), 1954–1983. https://doi.org/10.1002/2015JF003806

CReSIS (2024) CReSIS Radar Depth Sounder MCoRDS 4 Data, Lawrence, Kansas, USA. Digital Media. http://data.cresis.ku.edu/.

De Fleurian, B., Werder, M. A., Beyer, S., Brinkerhoff, D. J., Delaney, I., Dow, C. F., et al. (2018). SHMIP The subglacial hydrology model intercomparison Project. *Journal of Glaciology*, 64(248), 897–916. https://doi.org/10.1017/jog.2018.78

Dinniman, M. S., Klinck, J. M., & Smith Jr., W. O. (2007). Influence of sea ice cover and icebergs on circulation and water mass formation in a numerical circulation model of the Ross Sea, Antarctica. *Journal of Geophysical Research: Oceans*, 112(C11). https://doi.org/10.1029/2006JC004036

Drews, R., Pattyn, F., Hewitt, I. J., Ng, F. S. L., Berger, S., Matsuoka, K., et al. (2017). Actively evolving subglacial conduits and eskers initiate ice shelf channels at an Antarctic grounding line. *Nature Communications, 8(1)*, 15228. https://doi.org/10.1038/ncomms15228

Freer, B. I. D., Marsh, O. J., Hogg, A. E., Fricker, H. A., & Padman, L. (2023). Modes of Antarctic tidal grounding line migration revealed by Ice, Cloud, and land Elevation

Satellite-2 (ICESat-2) laser altimetry. *The Cryosphere, 17(9)*, 4079–4101. https://doi.org/10.5194/tc-17-4079-2023

Fretwell, P., Pritchard, H. D., Vaughan, D. G., Bamber, J. L., Barrand, N. E., Bell, R., et al. (2013). Bedmap2: improved ice bed, surface and thickness datasets for Antarctica. *The Cryosphere*, *7(1)*, 375–393. https://doi.org/10.5194/tc-7-375-2013

Fricker, H. A., Siegfried, M. R., Carter, S. P., & Scambos, T. A. (2016). A decade of progress in observing and modelling Antarctic subglacial water systems. *Philosophical Transactions of the Royal Society A: Mathematical, Physical and Engineering Sciences, 374(2059)*, 20140294. https://doi.org/10.1098/rsta.2014.0294

Fricker, H. A. & Scambos, T. (2009). Connected subglacial lake activity on lower Mercer and Whillans Ice Streams, West Antarctica, 2003–2008. *Journal of Glaciology, 55(190)*, 303–315. https://doi.org/10.3189/002214309788608813

Fricker, H. A., Scambos, T., Bindschadler, R., & Padman, L. (2007). An Active Subglacial Water System in West Antarctica Mapped from Space. *Science, 315(5818)*, 1544–1548. https://doi.org/10.1126/science.1136897

Fricker, H. A., Carter, S. P., Bell, R. E., & Scambos, T. (2014). Active lakes of Recovery Ice Stream, East Antarctica: a bedrock-controlled subglacial hydrological system. *Journal of Glaciology, 60(223)*, 1015–1030. https://doi.org/10.3189/2014JoG14J063

Gourmelen, N., Escorihuela, M. J., Shepherd, A., Foresta, L., Muir, A., Garcia-Mondéjar, A., et al. (2018). CryoSat-2 swath interferometric altimetry for mapping ice elevation and elevation change. *Advances in Space Research, 62(6)*, 1226–1242. https://doi.org/10.1016/j.asr.2017.11.014

Greenwood, S. L., Clason, C. C., Helanow, C., & Margold, M. (2016). Theoretical, contemporary observational and palaeo-perspectives on ice sheet hydrology: Processes and products. *Earth-Science Reviews*, 155, 1–27. https://doi.org/10.1016/j.earscirev.2016.01.010

Greischar, L. L., Bentley, C. R., & Whiting, L. R. (1992). An analysis of gravity measurements on the Ross Ice Shelf, Antarctica. In Elliot, D. H. (Ed.) *Contributions to Antarctic Research III, Antarctic Research series* (Vol. 57, pp. 105–155). Washington, DC: American Geophydical Union.

Gudmundsson, G. H., Paolo, F. S., Adusumilli, S., & Fricker, H. A. (2019). Instantaneous Antarctic ice sheet mass loss driven by thinning ice shelves. *Geophysical Research Letters, 46(23)*, 13903–13909. https://doi.org/10.1029/2019GL085027

Gwyther, D. E., Dow, C. F., Jendersie, S., Gourmelen, N., & Galton-Fenzi, B. K. (2023). Subglacial Freshwater Drainage Increases Simulated Basal Melt of the Totten Ice Shelf. Geophysical Research Letters, 50(12), e2023GL103765. https://doi.org/10.1029/2023GL103765

Hawkings, J. R., Skidmore, M. L., Wadham, J. L., Priscu, J. C., Morton, P. L., Hatton, J. E., et al. (2020). Enhanced trace element mobilization by Earth's ice sheets. *Proceedings of the National Academy of Sciences, 117(50)*, 31648–31659. https://doi.org/10.1073/pnas.2014378117

Hayden, A.-M., & Dow, C. F. (2023). Examining the effect of ice dynamic changes on subglacial hydrology through modelling of a synthetic Antarctic glacier. *Journal of Glaciology*, 1–14. https://doi.org/10.1017/jog.2023.65

Hindmarsh, R. C. A., & Stokes, C. R. (2008). Formation mechanisms for ice-stream lateral shear margin moraines. *Earth Surface Processes and Landforms*, 33(4), 610–626. https://doi.org/10.1002/esp.1665

Holland, D. M., Jacobs, S. S., & Jenkins, A. (2003). Modelling the ocean circulation beneath the Ross Ice Shelf. *Antarctic Science*, 15(1), 13–23. https://doi.org/10.1017/S0954102003001019

Horgan, H. J., Alley, R. B., Christianson, K., Jacobel, R. W., Anandakrishnan, S., Muto, A., et al. (2013). Estuaries beneath ice sheets. *Geology*, 41(11), 1159–1162. https://doi.org/10.1130/G34654.1

Horgan, H. J., & Anandakrishnan, S. (2006). Static grounding lines and dynamic ice streams: Evidence from the Siple Coast, West Antarctica. *Geophysical Research Letters, 33(18)*. https://doi.org/10.1029/2006GL027091

Howard, S. L., Padman, L., & Erofeeva, S. Y. (2019). CATS2008: Circum-Antarctic Tidal Simulation version 2008 (Version 1) [Software]. U.S. Antarctic Program (USAP) Data Center. https://doi.org/10.15784/601235

Howat, I. M., Porter, C., Smith, B. E., Noh, M.-J., and Morin, P. (2019) The Reference Elevation Model of Antarctica. *The Cryosphere, 13*, 665–674, https://doi.org/10.5194/tc-13-665-2019

Intergovernmental Panel on Climate Change (IPCC) (Ed.). (2023). Ocean, Cryosphere and Sea Level Change. In Climate Change 2021 – The Physical Science Basis: Working Group I Contribution to the Sixth Assessment Report of the Intergovernmental Panel on Climate Change (pp. 1211–1362). Cambridge: Cambridge University Press. https://doi.org/10.1017/9781009157896.011

Jenkins, A. (2011). Convection-driven melting near the grounding lines of ice shelves and tidewater glaciers. *Journal of Physical Oceanography, 41(12)*, 2279–2294. https://doi.org/10.1175/JPO-D-11-03.1

Joughin, I., Shean, D. E., Smith, B. E., & Dutrieux, P. (2016). Grounding line variability and subglacial lake drainage on Pine Island Glacier, Antarctica. *Geophysical Research Letters*, 43(17), 9093–9102. https://doi.org/10.1002/2016GL070259

Kamb, B. (2001). Basal Zone of the West Antarctic Ice Streams and its Role in Lubrication of Their Rapid Motion. In *The West Antarctic Ice Sheet: Behavior and Environment* (pp. 157–199). American Geophysical Union (AGU). https://doi.org/10.1029/AR077p0157

Li, T., Dawson, G. J., Chuter, S. J., & Bamber, J. L. (2023). Grounding line retreat and tide-modulated ocean channels at Moscow University and Totten Glacier ice shelves, East Antarctica. *The Cryosphere, 17(2)*, 1003–1022. https://doi.org/10.5194/tc-17-1003-2023

Livingstone, S. J., Sole, A. J., Storrar, R. D., Harrison, D., Ross, N., & Bowling, J. (2019). Brief communication: Subglacial lake drainage beneath Isunguata Sermia, West Greenland: geomorphic and ice dynamic effects. *The Cryosphere, 13(10)*, 2789–2796. https://doi.org/10.5194/tc-13-2789-2019

MacAyeal, D. R. (1984). Thermohaline circulation below the Ross Ice Shelf: A consequence of tidally induced vertical mixing and basal melting. *Journal of Geophysical Research: Oceans*, *89(C1)*, 597–606. https://doi.org/10.1029/JC089iC01p00597

Magruder, L., Brunt, K., Neumann, T., Klotz, B., & Alonzo, M. (2021). Passive ground-based optical techniques for monitoring the on-orbit ICESat-2 altimeter geolocation and footprint diameter. *Earth and Space Science, 8(10)*. https://doi.org/10.1029/2020EA001414

Makinson, K., Holland, P. R., Jenkins, A., Nicholls, K. W., & Holland, D. M. (2011). Influence of tides on melting and freezing beneath Filchner-Ronne Ice Shelf, Antarctica. *Geophysical Research Letters, 38(6)*. https://doi.org/10.1029/2010GL046462

Malczyk, G., Gourmelen, N., Goldberg, D., Wuite, J., & Nagler, T. (2020). Repeat Subglacial Lake Drainage and Filling Beneath Thwaites Glacier. *Geophysical Research Letters, 47(23)*, e2020GL089658. https://doi.org/10.1029/2020GL089658

Marsh, O., Floricioiu, D., & Freer, B. (2024). Double-difference TerraSAR-X interferograms and derived grounding lines at the grounding line of the Kamb and

Whillans Ice Streams, West Antarctica, 2012-2023 (Version 1.0) [Dataset]. NERC EDS UK Polar Data Centre. https://doi.org/10.5285/e1d182b1-6aa6-434e-9390-f7956227cb82

Marsh, O. J., Fricker, H. A., Siegfried, M. R., Christianson, K., Nicholls, K. W., Corr, H. F. J., & Catania, G. (2016). High basal melting forming a channel at the grounding line of Ross Ice Shelf, Antarctica. *Geophysical Research Letters, 43(1)*, 250–255. https://doi.org/10.1002/2015GL066612

McMillan, M., Corr, H., Shepherd, A., Ridout, A., Laxon, S., & Cullen, R. (2013). Three-dimensional mapping by CryoSat-2 of subglacial lake volume changes. *Geophysical Research Letters, 40(16)*, 4321–4327. https://doi.org/10.1002/grl.50689

McMillan, M., Shepherd, A., Sundal, A., Briggs, K., Muir, A., Ridout, A., et al. (2014). Increased ice losses from Antarctica detected by CryoSat-2. *Geophysical Research Letters*, *41(11),* 3899–3905. https://doi.org/10.1002/2014GL060111

Milillo, P., Rignot, E., Mouginot, J., Scheuchl, B., Morlighem, M., Li, X., & Salzer, J. T. (2017). On the Short-term Grounding Zone Dynamics of Pine Island Glacier, West Antarctica, Observed With COSMO-SkyMed Interferometric Data: PIG Grounding Line Dynamics. *Geophysical Research Letters*, 44(20), 10,436-10,444. https://doi.org/10.1002/2017GL074320

Milillo, P., Rignot, E., Rizzoli, P., Scheuchl, B., Mouginot, J., Bueso-Bello, J., & Prats-Iraola, P. (2019). Heterogeneous retreat and ice melt of Thwaites Glacier, West Antarctica. *Science Advances*, 5(1), eaau3433. https://doi.org/10.1126/sciadv.aau3433

Morlighem, M., Rignot, E., Binder, T., Blankenship, D., Drews, R., Eagles, G., et al. (2020). Deep glacial troughs and stabilizing ridges unveiled beneath the margins of the Antarctic ice sheet. *Nature Geoscience, 13(2),* 132–137. https://doi.org/10.1038/s41561-019-0510-8

Munson, C. G., & Bentley, C. R. (1992). The crustal structure beneath ice stream C and ridge BC, West Antarctica from seismic refraction and gravity measurements. In Yoshida, Y., Kaminuma, K., & Shiraishi, K. (Eds.) *Recent Progress in Antarctic Earth Science* (pp. 507–514). Tokyo: TERRAPUB.

Muto, A., Christianson, K., Horgan, H. J., Anandakrishnan, S., & Alley, R. B. (2013). Bathymetry and geological structures beneath the Ross Ice Shelf at the mouth of Whillans Ice Stream, West Antarctica, modeled from ground-based gravity measurements. *Journal of Geophysical Research: Solid Earth*, 118(8), 4535–4546. https://doi.org/10.1002/jgrb.50315

Nakayama, Y., Cai, C., & Seroussi, H. (2021). Impact of Subglacial Freshwater Discharge on Pine Island Ice Shelf. *Geophysical Research Letters*, *48(18),* e2021GL093923. https://doi.org/10.1029/2021GL093923

Neckel, N., Franke, S., Helm, V., Drews, R., & Jansen, D. (2021). Evidence of Cascading Subglacial Water Flow at Jutulstraumen Glacier (Antarctica) Derived From Sentinel-1 and ICESat-2 Measurements. *Geophysical Research Letters, 48(20),* e2021GL094472. https://doi.org/10.1029/2021GL094472

Paterson, W. S. B. (1994). *Physics of glaciers* (3rd edition). Oxford: Pergamon.

Pelle, T., Greenbaum, J. S., Dow, C. F., Jenkins, A., & Morlighem, M. (2023). Subglacial discharge accelerates future retreat of Denman and Scott Glaciers, East Antarctica. *Science Advances, 9(43)*, eadi9014. https://doi.org/10.1126/sciadv.adi9014

Pratt, M. J., Winberry, J. P., Wiens, D. A., Anandakrishnan, S., & Alley, R. B. (2014). Seismic and geodetic evidence for grounding-line control of Whillans Ice Stream stick-slip events. *Journal of Geophysical Research: Earth Surface*, 119(2), 333–348. https://doi.org/10.1002/2013JF002842

Priscu, J. C., Kalin, J., Winans, J., Campbell, T., Siegfried, M. R., Skidmore, M., et al. (2021). Scientific access into Mercer Subglacial Lake: scientific objectives, drilling operations and initial observations. *Annals of Glaciology*, *62(85–86),* 340–352. https://doi.org/10.1017/aog.2021.10

Rignot, E. (2023). Observations of grounding zones are the missing key to understand ice melt in Antarctica. *Nature Climate Change, 13(10)*, 1010–1013. https://doi.org/10.1038/s41558-023-01819-w

Rignot, E., Mouginot, J., & Scheuchl, B. (2011). Antarctic grounding line mapping from differential satellite radar interferometry. *Geophysical Research Letters, 38(10)*. https://doi.org/10.1029/2011GL047109

Rignot, E., Mouginot, J., & Scheuchl, B. (2016). MEaSUREs Antarctic Grounding Line from Differential Satellite Radar Interferometry (Version 2) [Dataset]. NASA National Snow and Ice Data Center Distributed Active Archive Center. https://doi.org/10.5067/IKBWW4RYHF1Q

Rignot, E., Mouginot, J., & Scheuchl, B. (2017). MEaSUREs InSAR-Based Antarctica Ice Velocity Map (Version 2) [Dataset]. NASA National Snow and Ice Data Center Distributed Active Archive Center. https://doi.org/10.5067/D7GK8F5J8M8R

Rignot, E., Mouginot, J., Scheuchl, B., van den Broeke, M., van Wessem, M. J., & Morlighem, M. (2019). Four decades of Antarctic Ice Sheet mass balance from 1979–

2017. *Proceedings of the National Academy of Sciences*, 116(4), 1095–1103. https://doi.org/10.1073/pnas.1812883116

Robel, A. A., Wilson, E., & Seroussi, H. (2022). Layered seawater intrusion and melt under grounded ice. *The Cryosphere, 16(2)*, 451–469. https://doi.org/10.5194/tc-16-451-2022

Sauthoff, W., & Freer, B. (2024). Subglacial water flow paths beneath Whillans Ice Plain, West Antarctica (Version 1.0) [Dataset]. NERC EDS UK Polar Data Centre. https://doi.org/10.5285/0df5d4e9-2fcd-4420-b403-24d76848a5a5

Scambos, T. A., Berthier, E., & Shuman, C. A. (2011). The triggering of subglacial lake drainage during rapid glacier drawdown: Crane Glacier, Antarctic Peninsula. *Annals of Glaciology, 52(59)*, 74–82. https://doi.org/10.3189/172756411799096204

Schutz, B. E., Zwally, H. J., Shuman, C. A., Hancock, D., & DiMarzio, J. P. (2005). Overview of the ICESat Mission. *Geophysical Research Letters, 32(21)*, L21S01. https://doi.org/10.1029/2005GL024009

Sergienko, O., & Haseloff, M. (2023). 'Stable' and 'unstable' are not useful descriptions of marine ice sheets in the Earth's climate system. *Journal of Glaciology, 69(277)*, 1483–1499. https://doi.org/10.1017/jog.2023.40

Sergienko, O. V., MacAyeal, D. R., & Bindschadler, R. A. (2007). Causes of sudden, short-term changes in ice-stream surface elevation. *Geophysical Research Letters, 34(22)*. https://doi.org/10.1029/2007GL031775

Seroussi, H., Nowicki, S., Payne, A. J., Goelzer, H., Lipscomb, W. H., Abe-Ouchi, A., et al. (2020). ISMIP6 Antarctica: a multi-model ensemble of the Antarctic ice sheet evolution over the 21st century. *The Cryosphere, 14(9)*, 3033–3070. https://doi.org/10.5194/tc-14-3033-2020

Shreve, R. L. (1972). Movement of water in glaciers. *Journal of Glaciology, 11(62)*, 205–214. https://doi.org/10.3189/S002214300002219X

Siegfried, M. R., & Fricker, H. A. (2021). Illuminating active subglacial lake processes with ICESat-2 laser altimetry. *Geophysical Research Letters, 48(14)*. https://doi.org/10.1029/2020GL091089

Siegfried, M. R., & Fricker, H. A. (2018). Thirteen years of subglacial lake activity in Antarctica from multi-mission satellite altimetry. *Annals of Glaciology, 59(76)*, 42–55. https://doi.org/10.1017/aog.2017.36

Siegfried, M. R., Fricker, H. A., Carter, S. P., & Tulaczyk, S. (2016). Episodic ice velocity fluctuations triggered by a subglacial flood in West Antarctica. *Geophysical Research Letters*, 43(6), 2640–2648. https://doi.org/10.1002/2016GL067758

Simkins, L. M., Anderson, J. B., Greenwood, S. L., Gonnermann, H. M., Prothro, L. O., Halberstadt, A. R. W., et al. (2017). Anatomy of a meltwater drainage system beneath the ancestral East Antarctic ice sheet. *Nature Geoscience, 10(9)*, 691–697. https://doi.org/10.1038/ngeo3012

Shepherd, A., Gilbert, L., Muir, A. S., Konrad, H., McMillan, M., Slater, T., et al. (2019). Trends in Antarctic Ice Sheet Elevation and Mass. *Geophysical Research Letters*, 46(14), 8174–8183. https://doi.org/10.1029/2019GL082182

Shreve, R. L. (1972). Movement of water in glaciers. *Journal of Glaciology*, 11(62), 205–214. https://doi.org/10.3189/S002214300002219X

Slater, T., Shepherd, A., McMillan, M., Leeson, A., Gilbert, L., Muir, A., et al. (2021). Increased variability in Greenland Ice Sheet runoff from satellite observations. *Nature Communications*, 12(1), 6069. https://doi.org/10.1038/s41467-021-26229-4

Smith, B., Fricker, H. A., Gardner, A. S., Medley, B., Nilsson, J., Paolo, F. S., et al. (2020). Pervasive ice sheet mass loss reflects competing ocean and atmosphere processes. *Science*, 368(6496), 1239–1242. https://doi.org/10.1126/science.aaz5845

Smith, B., Adusumilli, S., Csathó, B. M., Felikson, D., Fricker, H. A., Gardner, A., Holschuh, N., Lee, J., Paolo, F. S., Siegfried, M. R., Sutterley, T. and the ICESat-2 Science Team. (2023a). ATLAS/ICESat-2 L3A Land Ice Height (Version 6) [Dataset]. NASA National Snow and Ice Data Center Distributed Active Archive Center. https://doi.org/10.5067/ATLAS/ATL06.006

Smith, B., Jelley, B. P., Dickinson, S., Sutterley, T., Neumann, T., & Harbeck, K. (2024). ATLAS/ICESat-2 L3B Gridded Antarctic and Greenland Height Change (Version 4) [Dataset]. NASA National Snow and Ice Data Center Distributed Active Archive Center. https://doi.org/10.5067/ATLAS/ATL15.004

Stearns, L. A., Smith, B. E., & Hamilton, G. S. (2008). Increased flow speed on a large East Antarctic outlet glacier caused by subglacial floods. *Nature Geoscience, 1(12)*, 827–831. https://doi.org/10.1038/ngeo356

Stokes, C. R., & Clark, C. D. (2002). Ice stream shear margin moraines. *Earth Surface Processes and Landforms, 27(5)*, 547–558. https://doi.org/10.1002/esp.326

Stubblefield, A. G., Meyer, C. R., Siegfried, M. R., Sauthoff, W., & Spiegelman, M. (2023). Reconstructing subglacial lake activity with an altimetry-based inverse method. *Journal of Glaciology*, 1–15. https://doi.org/10.1017/jog.2023.90

Sutterley, T. C., Alley, K., Brunt, K., Howard, S., Padman, L. and Siegfried, M. (2017) pyTMD: Python-based tidal prediction software (Version 2.1.0) [Software]. Zenodo. doi: 10.5281/zenodo.5555395

Sun, S., Pattyn, F., Simon, E. G., Albrecht, T., Cornford, S., Calov, R., et al. (2020). Antarctic ice sheet response to sudden and sustained ice-shelf collapse (ABUMIP). *Journal of Glaciology*, 66(260), 891–904. https://doi.org/10.1017/jog.2020.67

Sun, X., Abshire, J. B., Borsa, A. A., Fricker, H. A., Yi, D., DiMarzio, J. P., et al. (2017). ICESat/GLAS Altimetry Measurements: Received Signal Dynamic Range and Saturation Correction. *IEEE Transactions on Geoscience and Remote Sensing: A Publication of the IEEE Geoscience and Remote Sensing Society, 55(10)*, 5440–5454. https://doi.org/10.1109/TGRS.2017.2702126

Wiens, D. A., Aster, R. C., Nyblade, A. A., Bromirski, P. D., Gerstoft, P., & Stephen, R. A. (2024). Ross Ice Shelf Displacement and Elastic Plate Waves Induced by Whillans Ice Stream Slip Events. *Geophysical Research Letters, 51(7)*, e2023GL108040. https://doi.org/10.1029/2023GL108040

Whiteford, A., Horgan, H. J., Leong, W. J., & Forbes, M. (2022). Melting and refreezing in an ice shelf basal channel at the grounding line of the Kamb Ice Stream, West Antarctica. *Journal of Geophysical Research: Earth Surface, 127(11)*, e2021JF006532. https://doi.org/10.1029/2021JF006532

Winberry, J. P., Anandakrishnan, S., Alley, R. B., Bindschadler, R. A., & King, M. A. (2009). Basal mechanics of ice streams: Insights from the stick-slip motion of Whillans Ice Stream, West Antarctica. *Journal of Geophysical Research: Earth Surface*, 114(F1). https://doi.org/10.1029/2008JF001035

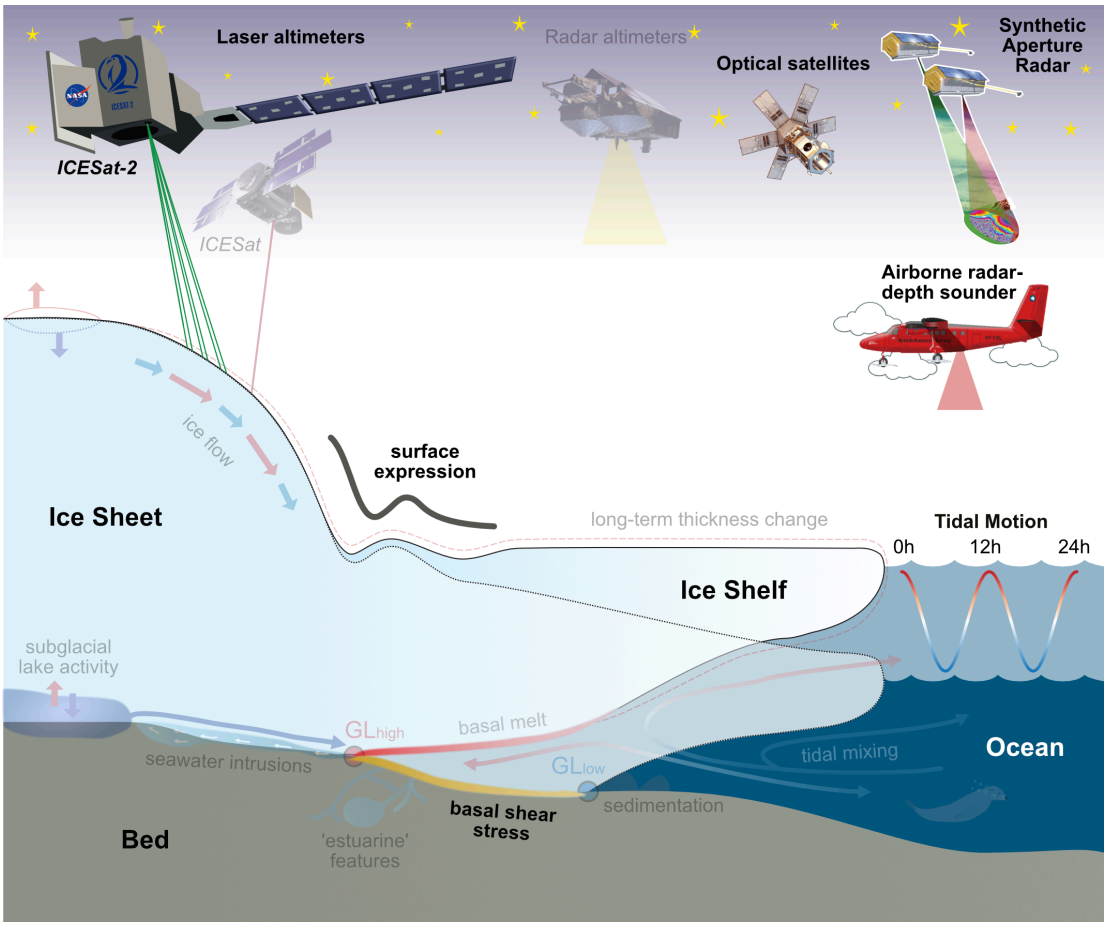
Winberry, J. P., Anandakrishnan, S., Alley, R. B., Wiens, D. A., & Pratt, M. J. (2014). Tidal pacing, skipped slips and the slowdown of Whillans Ice Stream, Antarctica. *Journal of Glaciology*, 60(222), 795–807. https://doi.org/10.3189/2014JoG14J038

Zwally, H. J., Schutz, B., DiMarzio, J. P., & Hancock, D. (2014). GLAS/ICESat L1B Global Elevation Data (HDF5) (Version 34) [Dataset]. NASA National Snow and Ice Data Center Distributed Active Archive Center. https://doi.org/10.5067/ICESAT/GLAS/DATA109

Chapter 4

Surface impression of the basal stress transition at the grounding line of Ross Ice Shelf, Antarctica

In this chapter I map the spatial distribution and shape of the wave-like surface feature associated with the basal stress transition around the entire Ross Ice Shelf grounding zone. To achieve this, I primarily utilise data from a high-resolution digital elevation model and ICESat-2 laser altimetry, alongside airborne radar-depth sounder measurements and TerraSAR-X DInSAR for validation. I examine how satellite observations of these features, combined with mathematical modelling, can improve estimates of grounding line location, glacier characteristics and ice thickness at Antarctic grounding zones.



This chapter has been prepared as a manuscript for submission to the Journal of Glaciology, co-authored with O. J. Marsh, A. T. Bradley, H. A. Fricker and A. E. Hogg.

Abstract

The dynamics of the Antarctic Ice Sheet and its future contribution to sea-level rise are highly dependent on the behaviour of the surrounding ice shelves. A particularly critical region is the grounding zone (GZ), over which the ice transitions from grounded to floating, where basal properties, ocean forcing, and ice dynamics interact. As ice moves across the GZ the sharp change in basal stress can cause a wave-like surface feature (WSF) to form, which allows a smooth transition between relatively steep slopes on the grounded ice and relatively flat floating ice shelf. This can serve as a useful proxy for the grounding line (GL). We use high resolution digital elevation models and ICESat-2 laser altimetry to map WSFs around the Ross Ice Shelf GZ. We then integrate these observations with a viscous beam model to infer the relative strength of basal drag and ice viscosity at each GZ, locate the GL from a single surface height profile and improve estimates of ice thickness and basal slope in the GZ. In addition, ICESat-2 observations showing the temporal evolution of a WSF at a retreating GL provide insights into the interaction between tidal processes and long-term GL retreat, and could help identify regions susceptible to future instabilities. This study highlights the value of integrating high-resolution satellite observations with process models to advance our understanding of ice sheet dynamics in Antarctica.

4.1. Introduction

4.1.1. Background

The Antarctic Ice Sheet (AIS) is a vital indicator of climatic change and a primary driver of sea level rise (IPCC, 2023). Ice sheet dynamics and instabilities are strongly controlled by the dynamics at the grounding line (GL), which marks the boundary between the grounded ice sheet and surrounding floating ice shelves within a wider grounding zone (GZ) (Rignot et al., 2008; Thomas et al., 1979). To improve confidence in projections of future ice sheet evolution and sea level rise we need to better resolve the geometry, bed properties and dynamics of Antarctic GZs over both short and long timescales. This effort is currently hindered by a lack of widespread observations (Rignot, 2023).

Ice dynamics change dramatically as ice moves across the GZ: there is a shift in basal conditions from shear-dominated flow of grounded ice and basal sliding upstream of the GL, to longitudinal stretching on the floating ice shelf (Schoof, 2007). This induces a rapid change in vertical velocity and surface elevation over a short horizontal scale (on the order of a few kilometres) (Schoof, 2011). This change in basal stress regime can lead to surface undulations in the surface immediately downstream of the GL (Barcilon & MacAyeal, 1993; Chugonov & Wilchinsky, 1996; Durand et al., 2009; Lestringant, 1994; Nowicki & Wingham, 2008; Sayag & Worster, 2011, 2013; Schoof, 2011). These undulations comprise a depression, located at the first surface elevation minimum after the primary ice sheet slope, and a seaward bump, located at the first surface elevation maximum after the depression (Fig. 4.1). This feature, termed a "wave-like surface feature" (WSF) by Schoof (2011), has been observed at several Antarctic GZs (e.g., Anandakrishnan et al., 2007; Chartrand & Howat, 2023; Hulbe et al., 2016; Swithinbank, 1955; Vaughan, 1994) and included in schematic representations of the GZ (Fricker et al., 2009; Friedl et al., 2020); however, there has been no systematic assessment of its distribution and dimensions across Antarctica or any attempt to use it to infer conditions at the GL.

Here, we examine the distribution and spatial variability of WSFs around Ross Ice Shelf using high-resolution satellite observations. We then use the viscous beam model of Schoof (2011) to infer potential causes of differences in the WSF profile, and demonstrate that by integrating observations with the model, we can improve estimates of GL position and ice thickness within Antarctic GZs. Finally, we highlight a region where we observe a WSF evolve over time and discuss the implications of our observations for monitoring GL retreat.

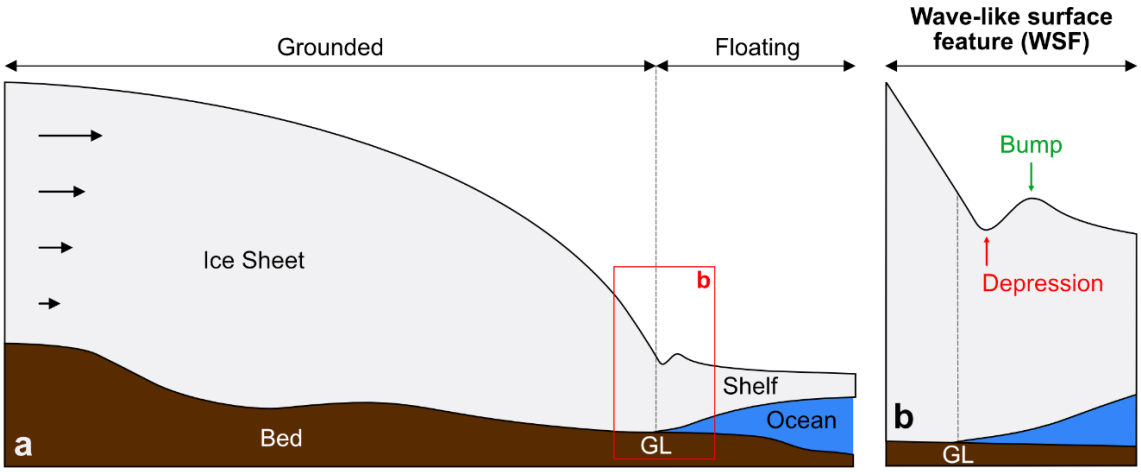


Figure 4.1. Schematic of the wave-like surface feature (WSF) observed at some Antarctic grounding zones.

4.1.2. Motivation for studying WSFs

There are four key reasons why we are interested in improving understanding of WSFs: (i) characterising ice and basal properties; (ii) informing process modelling; (iii) improving estimates of ice thickness and basal melt rates in GZs; (iv) change detection. We elaborate on these below.

(i) Characterising ice and basal properties: Basal drag and ice viscosity are poorly known around Antarctica and difficult to directly measure (Barnes & Gudmundsson, 2022). WSFs may hold valuable information about these properties at Antarctic GZs, including how they vary in space and time. Barcilon & MacAyeal (1993) first proposed that it may be possible to derive some information about basal conditions across different GZs by examining the geometry of these surface features. Schoof (2011) demonstrated that a full Stokes (viscous "beam") model of an ice sheet predicts the formation of a WSF at the GL. This model, which is in one-horizontal dimension, assumes a linear viscous rheology, and neglects any elastic deformation, can be used to describe analytically the wavelength and amplitude of the WSF. In particular, the wavelength of this WSF is a function of the ice thickness, surface velocity, ice viscosity and basal drag coefficient, while the amplitude depends on these as well as velocity

gradient across the GL and the downstream basal melt rate. This theoretical framework therefore provides an opportunity to infer hidden characteristics of the GZ that are otherwise poorly constrained, by analysing spatial and temporal variations in this feature from satellite observations.

(ii) Informing process modelling: We propose that it is possible to use observations of the WSF surface profile combined with the viscous beam model of Schoof (2011) to more accurately locate the GL position associated with the basal stress transition. This is the critical boundary represented in ice sheet models and needs to be precisely located to ensure accurate results (Durand et al., 2009; Gladstone et al., 2012). The most common techniques for locating the GL from satellite observations are to identify either the inland tidal flexure limit (e.g., Fricker & Padman, 2006; Rignot et al., 2011) or the break in surface slope (e.g., Bindschadler et al., 2011). In practice, these derived GL proxies can be offset from the actual location of the basal stress transition point felt by the ice, either due to the effects of tidal GL migration, complex topography or crevassing close to the break in surface slope (Friedl et al., 2020). Many ice sheet models also define the GL position from the flotation criterion alone (Docquier et al., 2011), which is unrealistic due to the deviation of ice from hydrostatic equilibrium within GZs – especially in the presence of WSFs (Chartrand & Howat, 2023).

(iii) Improving estimates of ice thickness and basal melt rates in GZs: The deviation of the ice from hydrostatic equilibrium in the presence of a WSF (Chartrand & Howat, 2023) amplifies errors in satellite-derived estimates of ice thickness and basal melt rate made from surface measurements using the hydrostatic assumption (Chuter & Bamber, 2015; Griggs & Bamber, 2011; Jenkins, 2006; Milillo et al., 2019). This area is often masked out (Paolo et al., 2015; Wilson et al., 2017) or interpolated to ensure a smooth, though not necessarily accurate, transition between floating and grounded ice thickness (e.g., Fretwell et al., 2013; Morlighem et al., 2020). Given that ice sheet models are highly sensitive to ice thickness and basal melt rates close to the GL (Arthern & Williams, 2017; Goldberg et al., 2019), measurement errors in these regions could significantly impact projections of future ice sheet dynamics and sea level.

(iv) Change detection: Monitoring how WSFs may or may not change over time could provide a useful early signal of changes to GZ behaviour or wider ice sheet dynamics – indicating possible unfolding instabilities, such as marine ice sheet instability (Weertman, 1974). Our approach, requiring just one satellite overpass to locate the GL for a single time stamp, may enable observations of GZ behaviour at higher temporal resolution in regions where maintaining coherence between satellite passes for differential synthetic aperture radar interferometry (DInSAR) or repeat-track laser altimetry (RTLA) methods is challenging.

4.1.3. Study Area

We focused our study on the GZ of Ross Ice Shelf (Fig. 4.2), which encompasses a range of different glaciological settings, including topographically confined outlet glaciers flowing into the ice shelf from the Trans-Antarctic Mountains on its western margin, and unconfined ice streams of the Siple Coast to the east (Truffer & Echelmeyer, 2003). We included the GL of all major ice streams and glaciers, as defined in the MEaSUREs Antarctic Boundaries dataset (Mouginot et al., 2017). Along the Siple Coast this included (from south to north): Mercer, Whillans, Kamb, Bindschadler, MacAyeal, Echelmeyer Ice Streams (formerly collectively known as Ice Streams A-F). On the Trans-Antarctic side this included (from south to north) Scott, Amundsen, Liv, Shackleton, Beardmore, Lennox-King, Nimrod, Byrd and Mulock Glaciers.

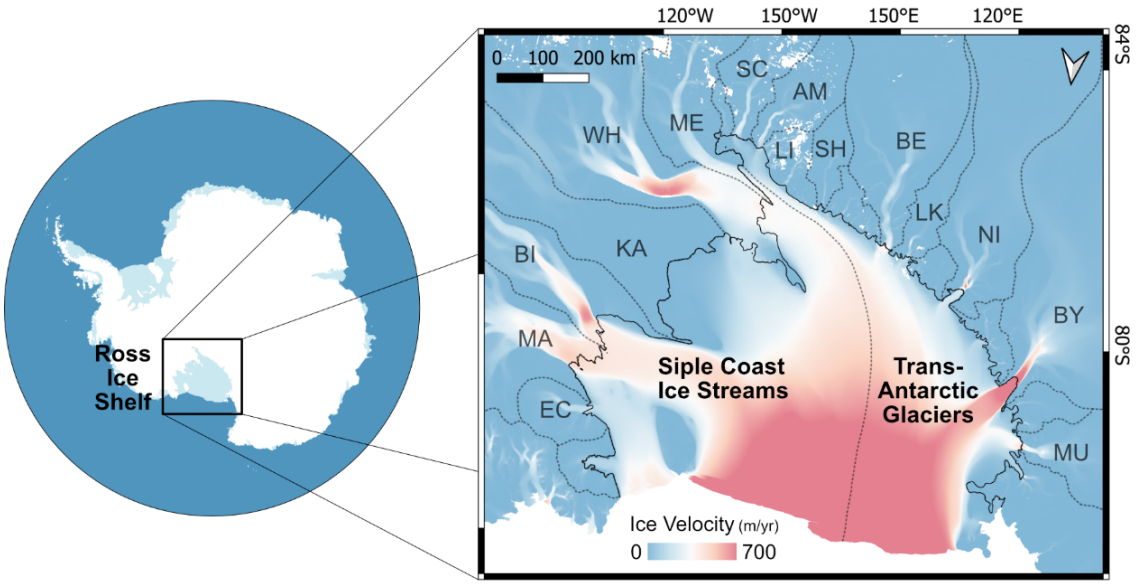


Figure 4.2. Location map of the Ross Ice Shelf ice streams and outlet glaciers examined in this study. We show catchment boundaries of the major Siple Coast ice streams and Trans-Antarctic glaciers (Mouginot et al., 2017). Clockwise from bottom left these include, EC: Echelmeyer, MA: MacAyeal, BI: Bindschadler, KA: Kamb, WH: Whillans, ME: Mercer, SC: Scott, AM: Amundsen, LI: Liv, SH: Shackleton, BE: Beardmore, LK: Lennox-King, NI: Nimrod, BY: Byrd, MU: Mulock.

4.2. Data

4.2.1. REMA Digital Elevation Model

To assess the spatial distribution of WSFs at the Ross Ice Shelf GZ, we used surface elevations from the Reference Elevation Model of Antarctica (REMA) digital elevation model (DEM) mosaic (version 2; Howat et al., 2019). This dataset was created using sub-meter resolution WorldView stereoscopic optical satellite imagery acquired during the austral summer seasons between 2009 and 2021, and registered vertically to the WGS-84 ellipsoid using satellite radar and laser altimetry. Individual DEMs were mosaicked together to create a static dataset that represents the average state of the surface over the data collection period. The resulting DEM has a horizontal resolution of 8 m with absolute vertical uncertainties of <1 m. We converted DEM elevations to height above mean sea level using the Eigen-6C4 geoid (Förste et al., 2014).

4.2.2. *ICESat-2 satellite laser altimetry*

To assess the temporal evolution of WSFs, we used repeat surface elevation measurements from ICESat-2, a photon-counting 532 nm satellite laser altimeter launched by NASA in 2018. ICESat-2 estimates surface elevation along its 1387 reference ground tracks (RGTs; each comprising six individual ground tracks: *GT1L, 1R, 2L, 2R, 3L, 3R*) every 91 days (Magruder et al., 2021). We used data from the Level 3A Land Ice Height data product (ATL06 version 6; Smith et al., 2023) from cycles 3–20 (April 2019 to August 2023), which provides mean surface elevation averaged along 40 m ground track (GT) segments spaced 20 m apart. ICESat-2 surface elevations are referenced to the WGS-84 ellipsoid, which we converted to height above mean sea level using the Eigen-6C4 geoid (Förste et al., 2014).

4.2.3. *MCoRDS airborne radar-depth sounder*

To validate satellite-derived ice thickness estimates, we obtained individual profiles of ice thickness, ice surface and ice bottom elevations across the Kamb and Mulock GZs from two airborne surveys with the Multichannel Coherent Radar Depth Sounder (MCoRDS). At Kamb Ice Stream we used MCoRDS Level 2 ice thickness data from a survey on 27 December 2013 (Wang et al., 2016), collected as part of the Center for Remote Sensing of Ice Sheets (CReSIS) project. At Mulock Glacier we used MCoRDS Level 2 ice thickness data from a survey on 16 December 2017, collected as part of Operation IceBridge (Paden et al., 2010). Uncertainties in MCoRDS ice thickness measurements are estimated to be ±50 m (Medley et al., 2014). All MCoRDS elevations are referenced to the WGS-84 ellipsoid, which we converted to height above mean sea level using the Eigen-6C4 geoid (Förste et al., 2014).

4.2.4. *Ice thickness, velocity and DInSAR GL*

To sample GL ice thickness and velocity at each WSF, we used data from BedMachine Antarctica (version 3; Morlighem, 2022) and the NASA Making Earth System Data Records for Use in Research Environments (MEaSUREs) program (Rignot et al., 2017). Additionally, we compared our derived GL positions to the MEaSUREs GL (Rignot et al., 2016), which marks the inland limit of tidal flexure (Point F) derived using DInSAR with 2009 RADARSAT-2 data.

4.3. Methods

4.3.1. *Measuring WSF geometry*

We determined the amplitude and wavelength of WSFs using an automated algorithm that calculates local maxima and minima along a 1D surface height profile (Fig. 4.3). Ideally, this profile should be oriented perpendicular to the GL and parallel to ice flow to match the geometry represented in an idealised 1D flowline model like the viscous beam model of Schoof (2011). In reality GLs tend to be more sinuous and are rarely aligned perfectly perpendicular to ice flow. To create a set of near-ideal profiles at each glacier and ice stream, we defined a series of lines oriented perpendicular to the MEaSUREs GL at 1 km spacing using the SAGA Cross Profile algorithm (Conrad et al., 2015), and sampled REMA DEM surface heights every 20 m along each one. In regions where the MEaSUREs GL is particularly sinuous, we manually simplified the GL to remove small-scale embayments and headlands while maintaining the general location and orientation with respect to ice flow.

The algorithm (Fig. 4.3) identifies the main peaks and troughs along each smoothed surface height profile (steps 1–3), and classifies the WSF depression at the most landward trough and the WSF bump at the first local peak seaward of the depression (step 5). WSF amplitude is calculated as half of the vertical height difference between the depression and bump, and wavelength is calculated as double the horizontal distance between the depression and bump (steps 6–7). To avoid misclassifying depressions in regions with more complex topography and GL curvature,

we visually checked the WSF classification along each profile and added additional constraints where necessary, for example specifying a threshold surface height above which no depression could be located (step 4). We removed all cross-profiles where no WSF was detected.

To assess the *spatial* distribution of WSFs, we applied our algorithm (Fig. 4.3) to each of the 1 km-spaced REMA surface height profiles around the Ross Ice Shelf GL. To assess the *temporal* evolution of WSFs we applied the same algorithm to repeat ICESat-2 surface height measurements along an individual ICESat-2 ground track (RGT 343 GT1R), which crosses the retreating GL at Engelhardt Ice Ridge on the Kamb Ice Stream (location in Fig. 4.6). This allowed us to calculate a time series of WSF amplitude and wavelength between April 2019 and July 2023. We note that in this study a detailed assessment of WSF evolution is only conducted along a single ICESat-2 ground track, in order to demonstrate its application. This could readily be scaled up to all suitable ground tracks in the future.

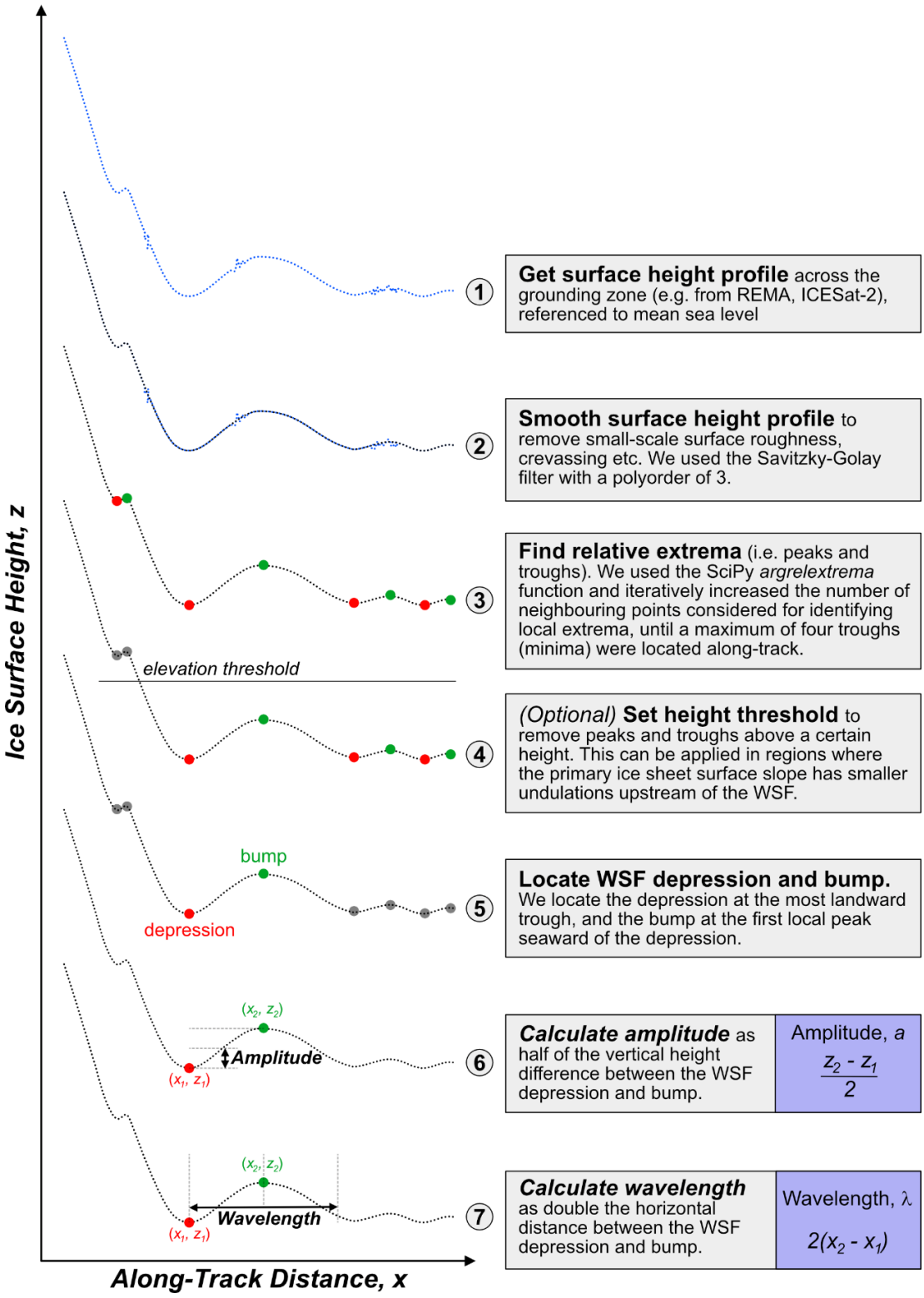


Figure 4.3. Flowchart of the algorithm used to locate the WSF depression and bump, and calculate its amplitude and wavelength, from a single surface height profile across the GZ. This used the SciPy library (Virtanen et al., 2020) and the Savitzky-Golay smoothing filter (Savitzky & Golay, 1964).

4.3.2. Integrating satellite observations with a viscous beam model

4.3.2.1. Viscous beam model description

Ice dynamics change across the GZ due to the basal stress transition: in the grounded ice there is a balance between gravitational driving and drag, while in the ice shelf gravitational driving is balanced by extensional stresses. Mathematically, this gives rise to a boundary layer (Schoof, 2007) in which both of these stresses are important. Within this boundary layer, there is a sublayer (Schoof, 2011), across which the vertical velocity and surface slope transition sharply. The behaviour in this region is akin to a viscous "beam", in which a WSF leads to a continuous transition in surface slope across the GL. Vertical velocities in this region satisfy a "beam-like" equation, i.e. resembling an elastic beam equation (e.g., Holdsworth, 1969), but with vertical displacement that usually enters a beam equation replaced by vertical velocity (Appendix A). Although we use the term 'viscous beam theory' henceforth to describe the behaviour, we stress that this model describes purely viscous behaviour and has no elastic component. The length- and vertical-scale of this region depend on two length scales, which are modulated by basal drag and ice viscosity.

The beam-like equation satisfied by the vertical velocities gives rise to oscillatory features in the vertical velocity profile immediately downstream of the basal stress transition at the GL (at $x = 0$; Fig. 4.4a), from which the shape of the ice surface (Fig. 4.4b) and ice base (Fig. 4.4c) can be determined (Appendix A). The solution to this equation, and the relationship between the vertical velocity and surface profile (Schoof, 2011) allows us to determine the spatial relationship between the location of the GL and the WSF depression in the surface profile, and the deviation of ice thickness from that expected by a hydrostatic equilibrium calculation.

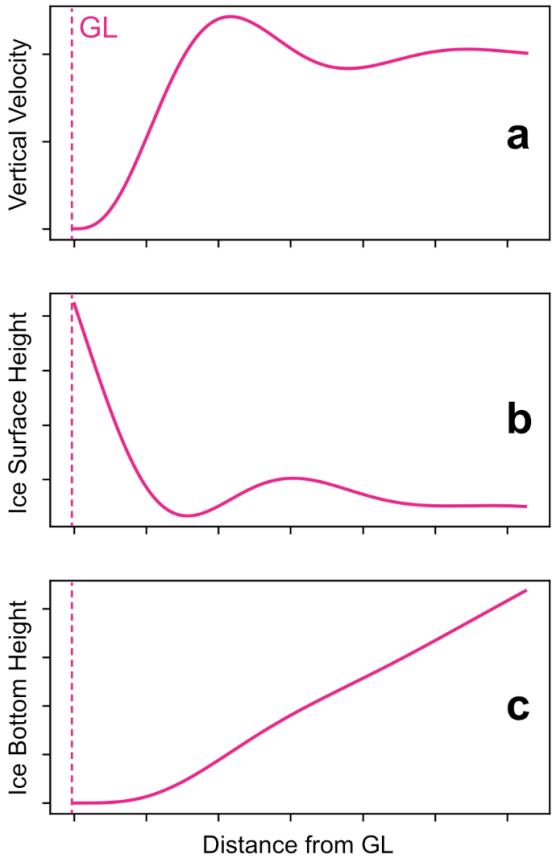


Figure 4.4. The dimensionless, analytical profiles of (a) vertical velocity, (b) ice surface and (c) ice bottom height immediately downstream of the GL (dashed line), from the viscous beam model of Schoof (2011). Predictions of real-world WSF characteristics are recovered by reversing the vertical and horizontal scaling appropriate to the dimensions of each observed WSF.

4.3.2.2. Fitting the viscous beam models to satellite observations

To compare the observed WSF profiles to the modelled profiles, we selected a 'representative' REMA surface profile for each glacier and ice stream (locations in Fig. 4.6). These profiles are chosen to best match the model's conditions, specifically those crossing the GL perpendicularly, parallel to ice flow, and with a clearly defined WSF. Bindschadler Ice Stream has two contrasting flow regimes; to capture these we selected two representative profiles–one from a region where the ice flows relatively quickly, and one where it flows relatively slowly ('Bindschadler-fast' and 'Bindschadler-slow'). We included the ICESat-2 profile from Engelhardt Ice Ridge as an additional representative profile ('Kamb-Engelhardt'), measured along RGT 343 (GT1R) on 17 July 2020.

We integrated our observed representative surface profiles with the model in the following two ways:

1. **Inverting for the relative strength of basal drag and ice viscosity:**

In the viscous beam theory, the basal drag and ice viscosity affect the length scales over which the basal stress transition acts, which in turn affects the wavelength and amplitude of the WSF (Schoof, 2011). This relationship can be described analytically (Appendix B). The theory predicts that the ratio between the drag and viscous terms in the model are proportional to a function of the ice thickness and velocity at the GL, and inversely proportional to the wavelength of the WSF, namely:

$$\frac{C^{\alpha}}{\eta^{\beta}} \propto \frac{{u_{gl}}^{1/5}{h_{gl}}^{3/5}}{\lambda} \tag{4.1}$$

where u_{gl} and h_{gl} are velocity and thickness at the GL, λ is the wavelength of the WSF, C is the basal drag coefficient in a Weertman-type sliding law, η is ice viscosity (assumed to have a linear rheology), and α and β are exponents indicating the relative importance of these two terms.

We applied our observations of WSF wavelength, GL ice thickness (Morlighem, 2022) and GL ice velocity (Rignot et al., 2017) to this theory to infer the relative strength of basal drag and ice viscosity at each GZ.

2. **Fitting the modelled surface profile to satellite observations:**

We fitted the dimensionless surface profile from the viscous beam model (Fig. 4.4b) to each observed representative WSF surface profile. We scaled the modelled profile in the x direction to match the observed WSF wavelength, and in the y direction to fit the slope upstream of the WSF depression (more details on this fitting routine are provided in Appendix A). We used this approach to:

a. Locate the modelled basal stress transition at the GL from the observed WSF dimensions. This is located just under half a wavelength upstream of the depression (Schoof, 2011).
b. Calculate modelled values of ice thickness, h_m, and ice bottom height, R_m, along each profile and compare these with values estimated using hydrostatic equilibrium.

4.3.3. Examine the impact of WSFs on ice thickness estimates in the GZ

We used measurements of ice thickness, ice surface and ice bottom heights from the two MCoRDS airborne surveys across the Mulock and Kamb GZs (Section 3.3) to investigate the impact of WSFs on our estimates of ice thickness obtained by assuming hydrostatic equilibrium. Along each profile we compared the following thickness values (Fig. 4.5):

1. The MCoRDS ice thickness, $\boldsymbol{h}$ (we consider this to be the 'true' ice thickness).
2. The hydrostatic thickness, $\boldsymbol{h_i}$, calculated from the MCoRDS freeboard assuming hydrostatic equilibrium. This was estimated using:

$$h_i = \frac{(z - F_c)\rho_w}{\rho_w - \rho_i} \tag{4.2}$$

where z is the surface height above mean sea level (i.e. freeboard) measured by MCoRDS, ρ_w and ρ_i are the densities of water and meteoric ice, respectively, and F_c is the firn air correction. Therefore, h_i gives the equivalent ice thickness assuming the ice column (including the firn layer) is at meteoric ice density.

3. The estimated ice thickness from the viscous beam model, $\boldsymbol{h_m}$, calculated as the difference between the modelled ice surface and ice bottom heights.

We used density values of ρ_i = 917 kg m^{-3} (standard value for density of meteoric ice; Benn & Evans, 2010) and ρ_w = 1027 kg m^{-3} (mean global seawater density; Griggs & Bamber, 2009). We applied the modelled firn correction provided in the BedMachine dataset (Morlighem, 2022) to convert MCoRDS ice thickness to meteoric ice equivalent, so it could be directly compared with the hydrostatic ice thickness and height values. When applying the firn correction we found that the BedMachine firn correction consistently underestimated the firn layer thickness at Mulock Glacier by ~16 m and overestimated the firn layer thickness at Kamb Ice Stream by ~2.5 m. To account for this, we manually adjusted F_c in each setting (more details given in Supplementary S4.1).

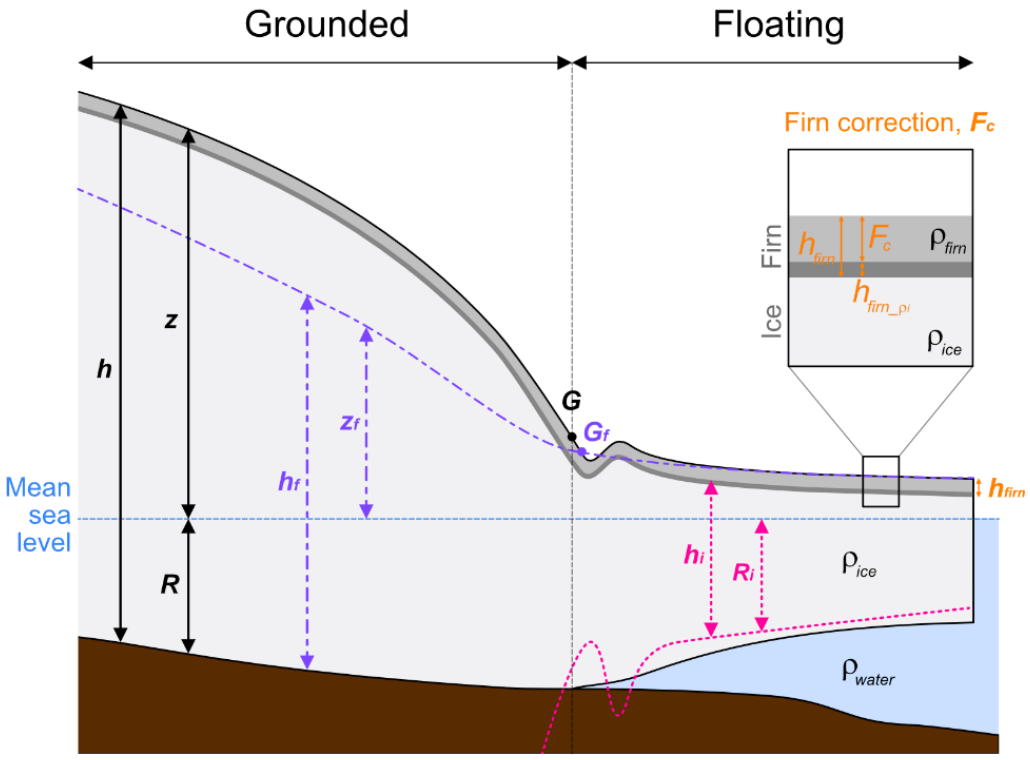


Figure 4.5. Grounding zone schematic, showing the different measurements of ice thickness (*h = measured; h_f = flotation; h_i = hydrostatic; h_{firn} = firn)*, ice surface height (*z = measured; z_f = flotation)* and ice bottom height (*R = measured, R_i = hydrostatic)*, referenced to mean sea level. Point G marks the true GL, and Point G_f marks the floatation GL, located where the h_f first exceeds *h*. The inset panel shows the geometry of the firn correction, F_c, calculated as the difference between the actual thickness of the firn, h_{firn}, and the thickness if the firn was at the density of meteoric ice, $h_{firn\_\rho i}$. The densities of water, ice and firn are denoted by ρ_{water}, ρ_{ice} and ρ_{firn}.

4.4. Results

4.4.1. Spatial variability of WSFs

We identified WSFs at the GZ of seven of the nine Trans-Antarctic glaciers we examined, and three of the six Siple Coast ice streams: Bindschadler, Kamb and Whillans (Fig. 4.6). The mean amplitude and wavelength of WSFs varies for each glacier; amplitudes are generally larger in the Trans-Antarctic side (Figs. 4.6, 4.7; Table 4.1). We found higher amplitude WSFs (>5 m) only at the GZs of the Trans-Antarctic glaciers, Mulock, Nimrod and Scott (Fig. 4.7). The Siple Coast WSFs typically have smaller amplitude, comparable to those at the Beardmore and Byrd Glaciers on the Trans-Antarctic side. There is less variability in WSF wavelengths between the Siple Coast ice streams and Trans-Antarctic glaciers. We discuss details for each region below:

Trans-Antarctic: The most prominent WSF is on Mulock Glacier, with a mean amplitude of 14.3 ± 5.7 m and wavelength of 3.4 ± 0.8 km. Here the WSF extends along almost the entire length of the GL (Fig. 4.6). The next largest WSF is at Nimrod Glacier, which has a mean amplitude of ~10 m and wavelength of ~5 km but is much more discontinuous along the GL. We note that the Nimrod GZ is located ~7 km downstream of a large (~75 m-deep) surface over-deepening, which complicates the interpretation of the WSF. The smallest WSFs were observed on Byrd Glacier (mean amplitude of 1.3 ± 0.6 m and wavelength of 3.7 ± 1.3 km) and Beardmore Glacier (mean amplitude of 1.6 ± 0.8 m and wavelength of 2.8 ± 0.6 km). No WSFs were identified on the Lennox-King or Amundsen Glaciers.

Siple Coast: There is a WSF across ~70% of the GL of Kamb Ice Stream and the slow-flowing northern part of Bindschadler Ice Stream (Fig. 4.6) with amplitudes mostly ranging between 1 and 2 m (exceeding 4 m in a few places), and wavelengths between 1 and 4 km. A >6 m-deep depression was identified along a ~20 km section of the Kamb GZ (marked in Fig. 4.6), which corresponds to the location of a previously identified large subglacial melt channel (Whiteford et al., 2022). Part of the melt channel is superimposed on the WSF here and so we omitted all profiles crossing this section to avoid overestimating mean amplitudes. Along the Whillans GZ, we observed

discontinuous WSFs across both the fast-flowing and slower sections. The mean amplitude of these features are typically smaller than along Kamb Ice Stream, at ~1 m (up to a maximum of ~2.5 m), but with much greater range of measured wavelengths from 1 to 7 km. We identified no WSFs on Echelmeyer, MacAyeal or Mercer ice streams or on most of the fast-flowing section of Bindschadler Ice Stream.

Overall, we found no direct relationship between the amplitude or wavelength of WSFs observed at each GZ with the measured ice thickness, velocity or velocity gradient at the GL (Fig. S4.2).

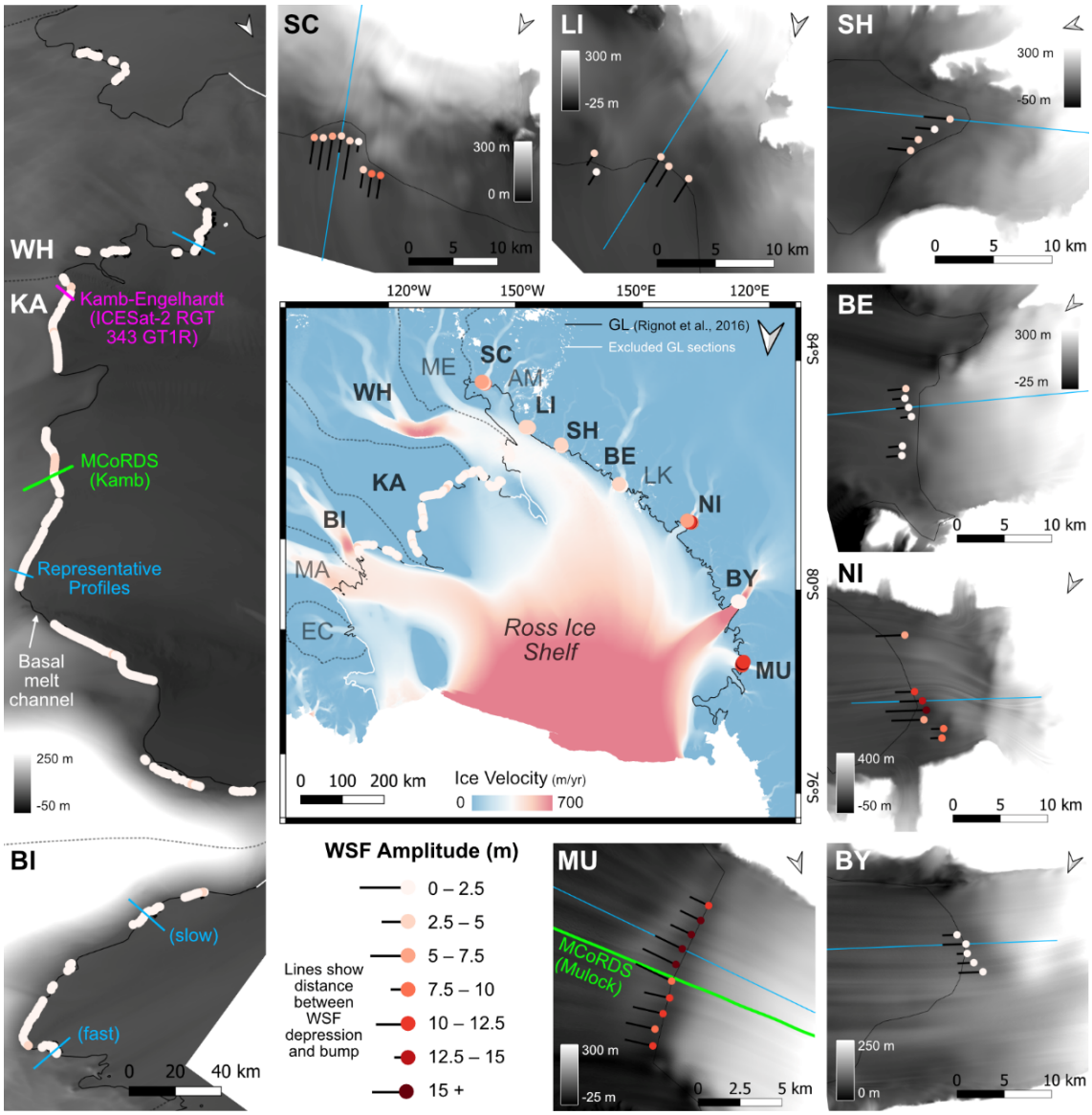


Figure 4.6. Location, amplitude, and wavelength of WSFs around Ross Ice Shelf, observed from the REMA DEM. The central panel shows the location of glaciers and ice streams included in this study, marked in bold where WSFs have been identified (clockwise from bottom left, EC: Echelmeyer, MA: MacAyeal, BI: Bindschadler, KA: Kamb, WH: Whillans, ME: Mercer, SC: Scott, AM: Amundsen, LI: Liv, SH: Shackleton, BE: Beardmore, LK: Lennox-King, NI: Nimrod, BY: Byrd, MU: Mulock). Outer panels show the location of WSFs at each GZ, with the WSF depression (circles) coloured by amplitude. Black lines depict the distance between the WSF depression and bump (i.e., half the WSF wavelength).

Table 4.1. Amplitude and wavelength (mean and standard deviation, SD) of the observed WSFs at each Ross Ice Shelf GZ in this study.

	Glacier/Ice Stream	WSF Amplitude (m)		WSF Wavelength (km)	
		Mean	SD	Mean	SD
Trans-Antarctic	Beardmore	1.58	0.79	2.83	0.56
	Byrd	1.27	0.61	3.65	1.27
	Liv	2.91	1.05	3.41	1.36
	Mulock	14.3	5.73	3.37	0.75
	Nimrod	10.5	4.04	5.02	2.31
	Scott	5.39	2.57	4.99	1.64
	Shackleton	3.18	0.71	3.57	0.76
Siple Coast	Bindschadler	1.01	0.78	2.12	1.10
	Kamb	1.32	0.82	1.71	0.53
	Whillans	0.70	0.34	3.54	1.28

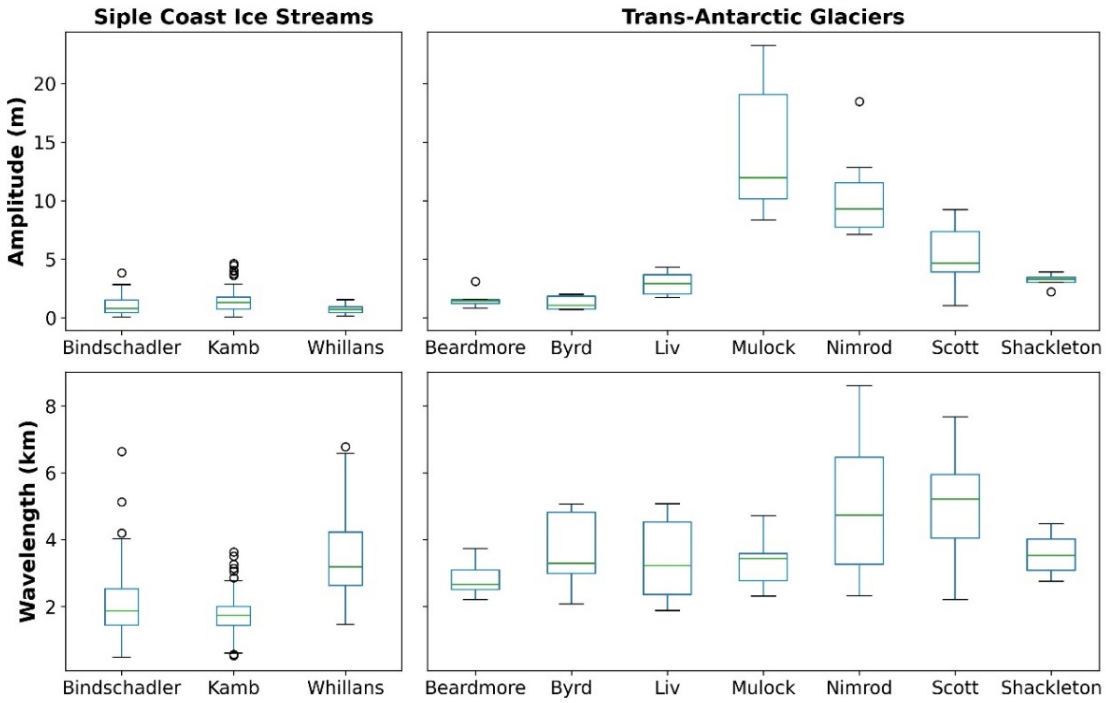


Figure 4.7. Boxplot showing the amplitude and wavelength of the WSFs on the Trans-Antarctic glaciers and Siple Coast ice streams.

4.4.2. *Inferring ice viscosity and basal drag*

We calculated the ratio between basal drag and ice viscosity as a function of WSF wavelength, GL ice thickness and GL ice velocity, as predicted by the viscous beam model (Fig. 4.8; Schoof, 2011). We superimposed locations of Ross Ice Shelf glaciers and ice streams, based on the satellite-derived values from each representative profile. This graph can be interpreted in two ways: if all of these glaciers had the same viscosity it indicates the relative strength of basal drag, with glaciers located towards the top left (more purple) having higher drag. Alternatively, if all of these glaciers had the same basal drag coefficient, it becomes an indicator of ice viscosity, with glaciers towards the bottom right (more yellow) having higher viscosity.

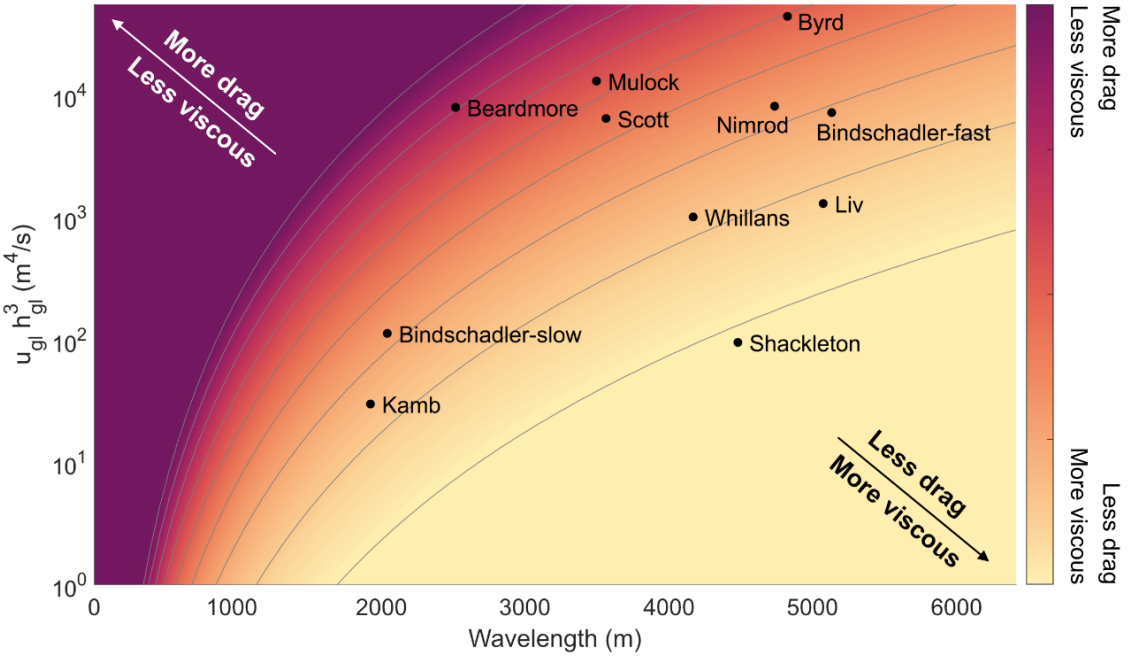


Figure 4.8. The ratio between the basal drag and ice viscosity (Equation 4.1, Appendix B) as a function of WSF wavelength, λ, GL ice velocity, u_{gl}, and GL ice thickness, h_{gl}. Also shown are locations of individual Ross Ice Shelf glaciers and ice streams determined from satellite-derived values along their representative profiles. Grey lines show contours of consistent drag-to-viscosity ratio.

This graph indicates that Beardmore, Mulock and Byrd Glaciers have the highest drag-to-viscosity ratios, suggesting they have either relatively high drag or relatively low ice viscosity compared to other glaciers and ice streams (or a combination of the two). This is despite Byrd Glacier having a WSF wavelength approx. 2.5 times longer than at Beardmore Glacier. Shackleton Glacier has the lowest drag-to-viscosity ratio, suggesting that it experiences very low basal drag, or has highly viscous ice. There are similarly low ratios at Liv Glacier, and Whillans and Kamb Ice Streams. The WSF at Bindschadler-fast has almost double the wavelength than at Bindschadler-slow, yet these settings have very similar drag-to-viscosity ratios. Likewise, Kamb Ice Stream has a much smaller WSF wavelength and slower ice flow than Whillans Ice Stream, yet the drag-to-viscosity ratios are similar in both settings.

4.4.3. Locating the GL

For each representative profile, we compared the location of the GL predicted by the viscous beam model to the location of the InSAR-derived GL (Rignot et al., 2016) (Fig. 4.9). The InSAR GL should indicate Point F, the inland limit of tidal flexure, whereas our modelled GL should indicate the location of the basal stress transition. The modelled and InSAR GL positions match to within a few hundred metres at Beardmore, Scott and Shackleton Glaciers and Kamb-Engelhardt and Whillans Ice Streams. For all other settings the modelled GL is located further upstream than the InSAR GL – within 1 km at Bindschadler (fast) and Kamb Ice Streams, within 2 km at Bindschadler (slow), Byrd and Mulock Glaciers, and almost 3 km upstream at Liv and Nimrod Glaciers. We note that the modelled surface profile underestimated the observed WSF amplitude by up to 5 m at Nimrod and Scott Glaciers (Figs. 4.9i, 4.9j), and at Mulock Glacier the measured amplitude is more than double the magnitude predicted by the viscous beam model (Fig. 4.9h).

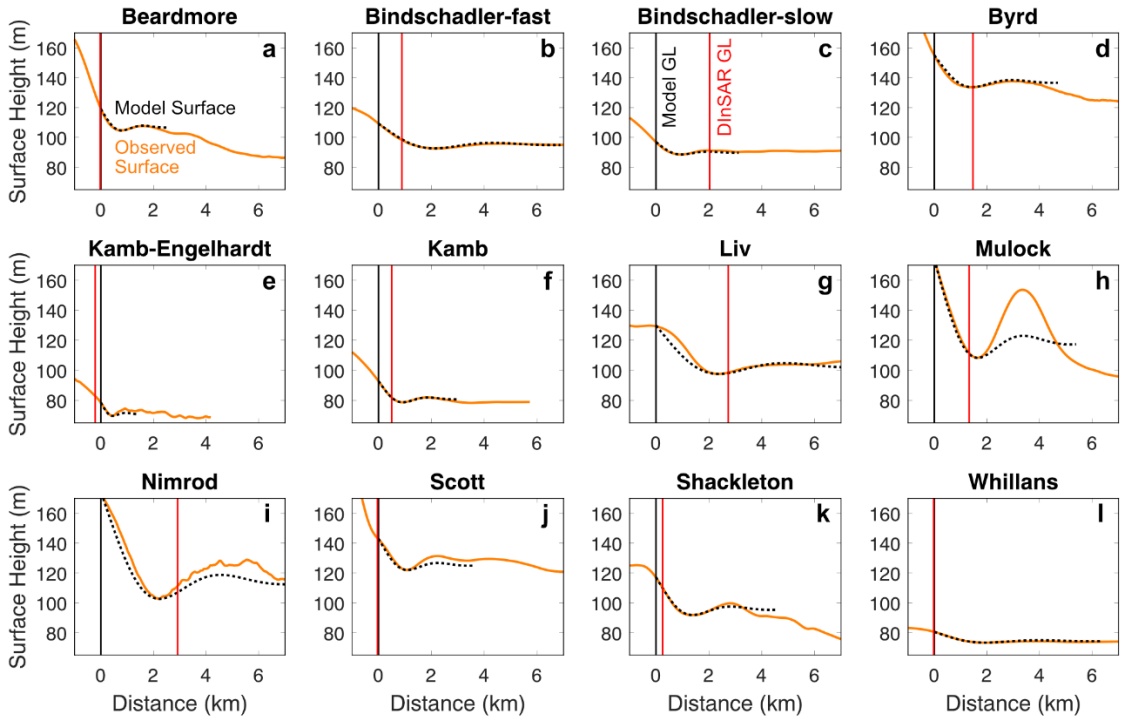


Figure 4.9. Observed and modelled WSF surface profiles and GL positions for each Ross Ice Shelf glacier. Each panel shows the observed surface height along each representative profile (orange) and the fitted surface profile from the viscous beam model (dashed black line; Schoof, 2011). Vertical lines show the GL position predicted by the viscous beam model (black), always at $x=0$ at the basal stress transition point, and the DInSAR GL (red), which marks the inland limit of tidal flexure (Rignot et al., 2016).

4.4.4. Impact of WSF on GZ ice thickness estimates

We examined how the presence of WSFs can affect calculations of GZ ice thickness using the hydrostatic assumption and show how this can be improved by combining satellite observations with the viscous beam model.

If we consider a theoretical ice surface and basal profile across a WSF from the viscous beam model (Schoof, 2011), we would expect the hydrostatic thickness to be significantly overestimated close to the modelled GL (upstream of the WSF depression), underestimated over the depression, and slightly overestimated over the WSF bump (Fig. 4.10). We tested this at the Kamb and Mulock GZs by comparing ice thickness, ice surface and ice bottom heights across each WSF measured by MCoRDS surveys (Paden

et al., 2010; Wang et al., 2016) to the same values: (i) calculated from the measured surface assuming hydrostatic equilibrium; and (ii) derived from the viscous beam model (Schoof, 2011) (Figs., 4.11, 4.12). We find significant differences between the modelled ice thickness and that obtained by using hydrostatic equilibrium in both locations.

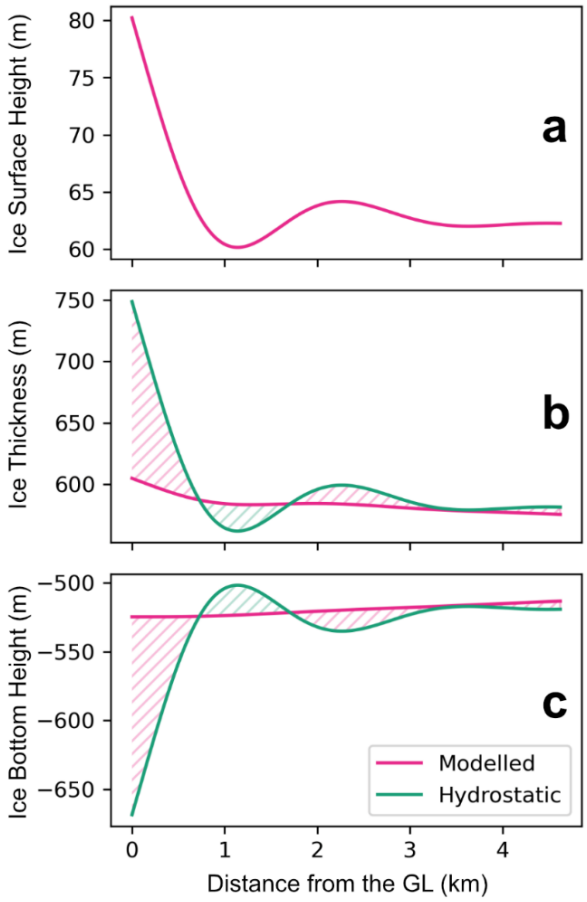


Figure 4.10. Modelled and hydrostatic ice surface, thickness and bottom height across the GZ for a modelled WSF surface profile. (a) The modelled WSF surface profile (Schoof, 2011), scaled to the dimensions of the Kamb WSF. (b) Modelled (pink) and hydrostatic (green) ice thickness along the same profile. (c) Modelled and hydrostatic ice bottom height along the same profile. Pink hashed areas indicate where the use of hydrostatic equilibrium overestimates ice thickness and ice bottom depth, and green hashed areas indicate where it underestimates ice thickness and ice bottom depth.

Ice thickness errors using the hydrostatic assumption: Across the Mulock GZ the hydrostatic ice thickness, h_i, gives an overestimate of ice thickness, h (Paden et al., 2010), by >400 m (~40%) inland of the WSF depression, an underestimate of ice thickness by ~100 m (~10%) at the depression itself, and an overestimate of ice thickness by up to ~150 m (~15%) over the WSF bump (Fig. 4.11b). Across the Kamb GZ, which has a much smaller WSF, the hydrostatic ice thickness, h_i, gives an overestimate of ice thickness, h (Wang et al., 2016), by >50 m (~8%) inland of the WSF depression, an underestimate of ice thickness by up to 40 m (~6%) at the depression itself and an overestimate of ice thickness by up to 10 m (~2%) over the peak of the bump (Fig. 4.12b). At both Mulock Glacier and Kamb Ice Stream, the overestimate of hydrostatic ice thickness over the WSF bump translated to an overestimate of the hydrostatic ice bottom depth, R_i, and steeper basal ice slopes in the vicinity of the GL (Figs. 4.11c, 4.12c). In both settings, these errors in ice thickness and ice base profile broadly match the modelled pattern of hydrostatic thickness deviation over the WSF (Fig. 4.10).

Improvements in ice thickness estimates using viscous beam model: Across the Mulock and Kamb WSFs, the viscous beam model predicts values of ice thickness and ice bottom height, h_m and R_m, that are much closer to the values measured by MCoRDS than those estimated using hydrostatic equilibrium (Fig. 4.11b, 4.11c, 4.12b, 4.12c). Across the Mulock WSF, h_m is within ~2% of the MCoRDS ice thickness (Fig. 4.11b), and across the Kamb WSF, h_m is within ~1% (Fig. 4.12b). In both cases this translates to a much gentler and more realistic predicted basal slope (Figs. 4.11c, 4.12c).

GL estimates using viscous beam model: At Mulock Glacier, the viscous beam model predicts the basal stress transition is located >2 km upstream of the DInSAR GL, which represents the inland limit of tidal flexure. At Kamb Ice Stream, the modelled GL is located ~ 1 km upstream of the DInSAR GL, which is shown by the inland limit of the dense fringes in the TerraSAR-X interferogram (Fig. 4.12d). The larger wavelength DInSAR fringes that extend ~1 km inland may indicate some ungrounding or tidal flexure as far inland as the modelled GL.

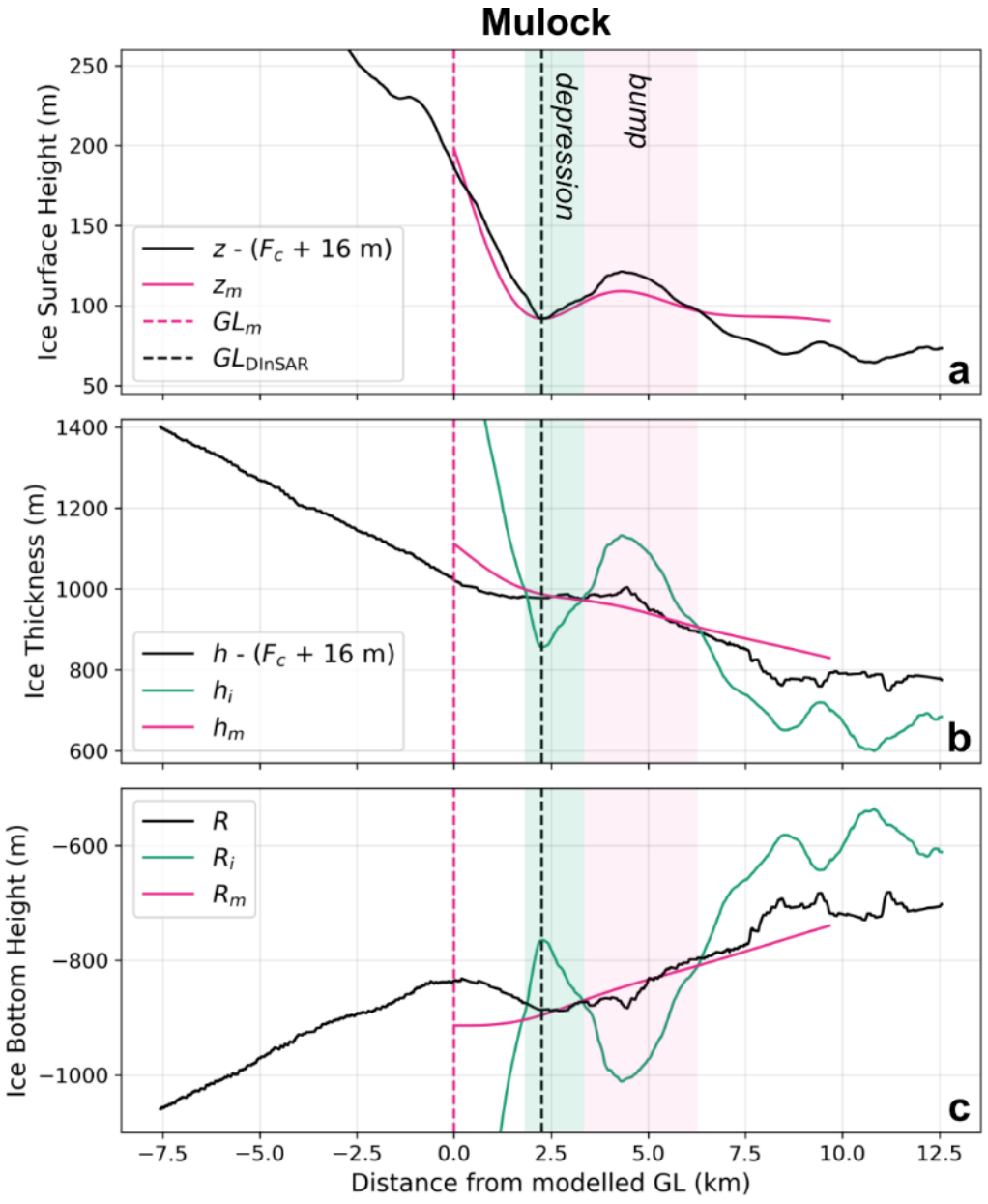


Figure 4.11. Measured, hydrostatic and modelled ice surface height, ice thickness and ice bottom height across the Mulock WSF (location in Fig. 4.6). (a) Ice surface height measured by MCoRDS, z (black; Paden et al., 2010), and derived from the viscous beam model, z_m (pink). (b) Ice thickness measured by MCoRDS, h (black), calculated from the MCoRDS surface using the hydrostatic assumption, h_i (green), and derived from the viscous beam model, h_m (pink). (c) Ice bottom height measured by MCoRDS, R (black); calculated using the hydrostatic assumption, R_i (green); and derived from the viscous beam model, R_m (pink).

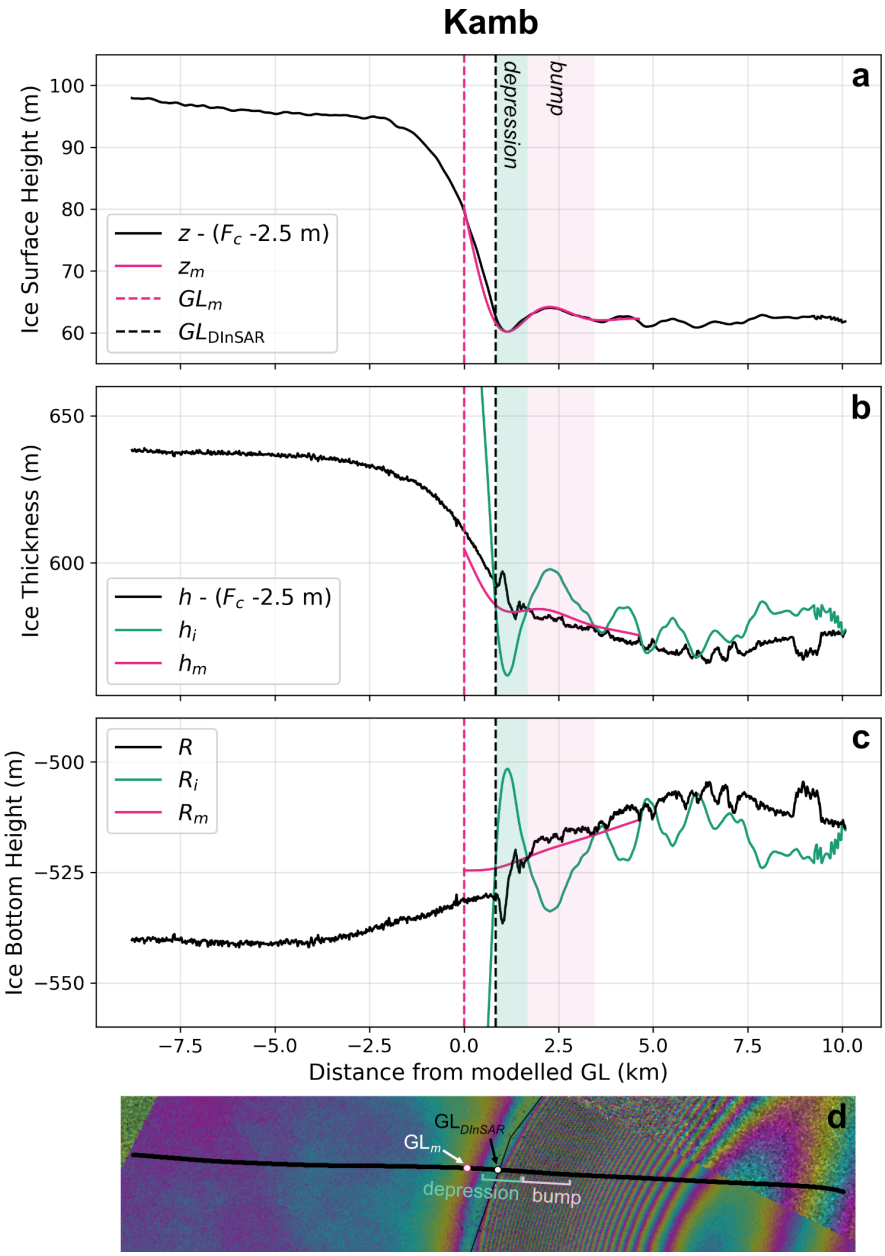


Figure 4.12. Measured, hydrostatic and modelled ice surface height, ice thickness and ice bottom height across the Kamb WSF (location in Fig. 4.6). (a) Ice surface height measured by MCoRDS, z (black; Wang et al., 2016) and derived from the viscous beam model, z_m (pink). (b) Ice thickness measured by MCoRDS, h (black), calculated using the hydrostatic assumption, h_i (green), and derived from the viscous beam model, h_m (pink). (c) Ice bottom height measured by MCoRDS, R (black); calculated using the hydrostatic assumption, R_i (green); and derived from the viscous beam model, R_m (pink). (d) TerraSAR-X InSAR fringes show the location of MCoRDS profile (thick black line) across the Kamb GZ (same distance along-track as in panels a-c), and the location of the modelled and DInSAR GLs and the WSF depression and bump. Individual TerraSAR-X scenes were acquired at: (i) 2017-02-27 T14:38:59; (ii) 2017-03-10 T14:38:59; and (iii) 2017-03-21 T14:38:59.

4.4.5. Temporal evolution of WSFs

ICESat-2 repeat surface height profiles across the GZ at Engelhardt Ice Ridge, measured along RGT 343 (GT1R), show that in April 2019 there was a prominent WSF at the base of the ridge with an amplitude of ~4.8 m (Fig. 4.13b) and wavelength of >1.7 km (Fig. 4.13c). The depression and bump are marked at D1 and B1 in Fig. 4.13a. Between 2019 and 2023 the ridge retreated by an average of ~0.17 km yr^{-1} (Fig. 4.13; Chapter 3/Freer et al., 2024). Over the same period, we observed no change in the along-track position of the WSF depression and bump nor in the WSF wavelength, but the depression became progressively shallower, with the amplitude decreasing to <1 m by October 2021. By April 2022, we observed that, where the ridge had retreated a new WSF depression had started to form ~0.8 km further inland, at position D2 in Fig. 4.13a, whilst the original depression (D1) had almost completely infilled or rebounded (Fig. 4.13a). This marks a sudden shift in the WSF position between D1/B1 and D2/B2. The newly formed WSF had an amplitude of ~0.35 m and wavelength of 0.7 km in April 2022. From April 2022 onwards the new depression began to deepen, increasing its amplitude to ~2.2 m and wavelength to ~0.9 km by July 2023.

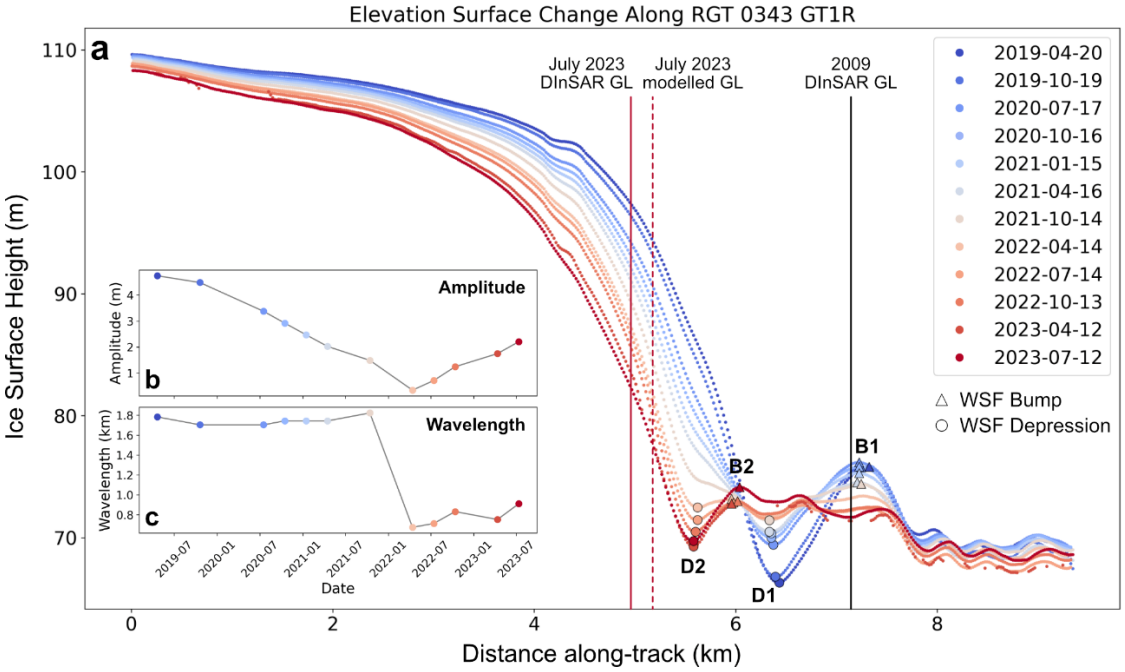


Figure 4.13. Change in surface height over the WSF at Engelhardt Ice Ridge between 2019 and 2023 from repeat ICESat-2 measurements along RGT 343 GT1R (location in Fig. 4.6). Coloured circles mark the location of the WSF depression minima at each ICESat-2 repeat (between two stable positions D1 and D2) and coloured triangles mark the WSF bump maxima. Vertical lines show the DInSAR GL positions from 2009 (Rignot et al., 2016) and July 2023 (Chapter 3; Freer et al., 2024) and the GL position predicted by the viscous beam model using the July 2023 ICESat-2 surface profile. (b) Time series of the WSF amplitude between 2019 and 2023. (c) Time series of the WSF wavelength between 2019 and 2023.

4.5. Discussion

4.5.1. Spatial variability of WSFs

We have shown that WSFs are common at the GZ of many of the major tributaries of Ross Ice Shelf. They are observed at seven of the nine largest Trans-Antarctic glaciers and three Siple Coast ice streams. They are notably absent or below the limit of detection at the GZs of the faster-flowing Siple Coast ice streams, as well as at the Amundsen and Lennox-King Glaciers (Fig. 4.6). Where WSFs do exist, they can be discontinuous and vary in size considerably, both between and within GZs (Fig. 4.7). Where they are absent or discontinuous, it suggests that either conditions in these regions are not conducive to

WSF formation, they are too small for detection, or their surface signature is disrupted by other ice dynamic processes such as crevassing. Here we discuss possible explanations for this variability.

WSFs form due to the relaxation of the ice in response to the sharp transition in basal traction across the GL (Schoof, 2011). Therefore, we would expect a more pronounced surface response where this transition is sharper, focusing deformation in a narrower zone (Hulbe et al., 2016). The sharpest transition from high drag (no slip) to no drag (free slip) would typically be expected in settings with hard bedrock and narrow GZs (i.e., steep surface and bed slopes and minimal tidal GL migration). These are characteristics associated with the Trans-Antarctic glaciers, and could explain why we see the largest amplitude WSFs (>5 m) there (Fig. 4.7). In contrast, over the faster ice streams of the Siple Coast, where ice flow is driven by deformation within or sliding over soft, deformable subglacial till (Alley et al., 1986, 1987; Blankenship et al., 1986; Kamb, 2001; Tulaczyk et al., 2000), the magnitude of change in basal traction across the GL is much smaller (Hindmarsh, 1993). The sharpness of the transition is expected to be further dampened in the presence of ice plains (e.g., Whillans et al., 2001), where tidal GL migration causes the change in vertical velocity across the GZ to be distributed over a wider area varying rapidly during daily cycles (Chapter 2; Brancato et al., 2020; Chen et al., 2023; Ciraci et al., 2023; Freer et al., 2023; Kim et al., 2024; Milillo et al., 2017, 2019, 2022; Rignot et al., 2024; Zhong et al., 2023).

These factors could explain the absence of observed WSFs at the GZ of Echelmeyer, MacAyeal, Bindschadler and Mercer Ice Streams, as well as large parts of Whillans Ice Stream (Fig. 4.6). The formation of WSFs at these GZs may also be disrupted by the sinuous path, flow-parallel orientation, and frequent migration of the GLs at these ice streams (Truffer & Echelmeyer, 2003). In particular, WSF formation at Whillans Ice Stream could be affected by the complex tidally-modulated stick-slip ice dynamics there (Bindschadler et al., 2003a, b). The absence or discontinuity of WSFs at certain Trans-Antarctic glaciers is also likely to be influenced by additional two-dimensional factors not accounted for in the one-horizontal dimension viscous beam theory, specifically the lateral stresses due to the topographical confinement of the ice, the more undulating bed

topography, and the sinuosity of the GL in relation to ice flow direction (Horgan & Anandakrishnan, 2006; Mayer & Huybrechts, 1999; Rabus & Lang, 2002; Wild et al., 2017). Additionally, we do not see WSFs where the GL is oriented close to parallel to ice flow, as is most clear at the Mercer GZ (Fig. 4.6).

Without more data it is not possible to uniquely determine which parameters influence the spatial variability in the WSF profile, but we have inferred the ratio of basal drag to ice viscosity in each setting by integrating our satellite observations of WSF wavelength, GL ice thickness and GL ice velocity with the viscous beam model of Schoof (2011) (Fig. 4.8). This shows that the highest drag-to-viscosity ratios are predicted for the larger Trans-Antarctic glaciers and lower ratios are predicted for all Siple Coast ice streams. This is reasonable, as we would expect there to be higher drag at the Trans-Antarctic glaciers flowing over hard bedrock compared to the till-deformation driven ice stream flow at the Siple Coast (Truffer & Echelmeyer, 2003; Arthern et al., 2015). Exceptions to this pattern are the smaller Liv and Shackleton Glaciers, which have a much lower drag-to-viscosity ratios than the other Trans-Antarctic glaciers. In these settings, relative ice viscosity (primarily controlled by ice temperature and stress) may exert a more important control on WSF geometry given that these glaciers are in the southern part of Ross Ice Shelf, fed by cold ice from the East Antarctic Plateau. Alternatively, basal drag may be reduced by other factors, such as the suspected ice plain at the Liv GZ.

As well as improving our understanding of the spatial variability of WSFs, these results demonstrate that it is possible to learn something about basal and internal ice properties by simply examining the geometry of WSFs. It is not possible to explicitly quantify basal drag or ice viscosity using this method, however, as there are too many free parameters and we are limited by uncertainties in measurements of ice thickness, effects of 2D geometry and poor knowledge of velocity gradient. We have shown that glaciers with very different WSF wavelengths can have very similar inferred drag-to-viscosity ratios (e.g., Kamb and Whillans Ice Streams), and conversely glaciers with very similar WSF wavelengths can have very different inferred drag-to-viscosity ratios (e.g., Byrd and Shackleton Glaciers).

4.5.2. Improving estimates of GL location and ice thickness using a viscous beam model

The shape of the dimensionless analytical profile from the viscous beam model (Schoof, 2011; Fig. 4.4b) is independent from any of the physical parameters described above, which means that our lack of knowledge of these parameters does not preclude using this profile to estimate GL location and ice thickness. We have shown that fitting this profile to satellite observations provides an independent method to locate the GL and significantly improves estimates of ice thickness across the GZ.

4.5.2.1. An independent method to locate the GL

The viscous beam model locates the GL that best represents the basal stress transition, approx. half a wavelength upstream of the WSF depression (Fig. 4.6; Schoof, 2011). This applies regardless of the fitting parameters and requires only a single surface height profile to locate the GL, in contrast to the minimum of two required for any tidal measurement (e.g., Brunt et al., 2011; Fricker & Padman, 2006). While some static or break-in-slope methods also require only a single surface profile (e.g., Bindschadler et al., 2011), the distance between the observed break-in-slope and the true GL is poorly defined and varies considerably around Antarctica, influenced by factors such as ice thickness, velocity, rheology and basal friction (Bamber & Bentley, 1994; Brunt et al., 2010; Dawson & Bamber, 2017; Depoorter et al., 2013; Fricker & Padman, 2006; Rignot et al., 2011).

In contrast, the distance between the WSF depression and GL is well-defined in the viscous beam model (Schoof, 2011), which means that the modelled GL should directly indicate the location of the sharp basal stress transition (Fig. 4.9) – a crucial boundary condition for ice sheet models (Schoof, 2007). GLs are known to migrate with ocean tides (Chapter 2), and in regions experiencing tidal GL migration, this basal stress boundary should be located at the most inland limit of GL migration at high tide. It is at this point where the rapid reduction in vertical velocity induces the relaxation of the ice surface to form the shape of the WSF across the GZ (Schoof, 2011). Any InSAR-derived GL proxy (e.g., Rignot et al., 2016) may not detect the most upstream GL position or basal stress boundary if it doesn't sample the highest tidal states (Freer et al., 2023). The

modelled GL therefore has the key advantage of identifying the most upstream GL position (and the most important GL position for ice sheet models) independent of tidal sampling. This could be particularly useful for quantifying the full extent of tidal GL migration in areas where the highest tidal states have not been sampled by satellites and can explain some of the offset between the modelled- and InSAR-derived GLs at some Ross Ice Shelf glaciers (Fig. 4.9).

4.5.2.2. Improving estimates of ice thickness in the GZ

Satellite-derived ice thickness estimates within GZs are subject to large uncertainties due to the breakdown of hydrostatic equilibrium (Chuter & Bamber, 2015; Griggs & Bamber, 2011; Kim et al., 2024). Our results show that that uncertainties in hydrostatic thickness are amplified in the presence of WSFs. Specifically, thickness tends to be overestimated at the GL and across the WSF bump, and underestimated across the WSF depression (Figs. 4.10–4.12). By mapping the spatial distribution of WSFs, as we have done for Ross Ice Shelf (Fig. 4.6), we can identify locations in Antarctica where satellite-derived estimates of ice thickness (e.g., Fretwell et al., 2013; Morlighem et al., 2020) and basal melt rates are likely to be most erroneous.

The most accurate and reliable way to measure ice thickness is using radar depth sounders (e.g., Paden et al., 2010), but this is restricted by poor geographic coverage around Antarctica. We have shown that it is possible to improve upon hydrostatic estimates of ice thickness in GZs with WSFs by fitting the dimensionless, analytical viscous beam model to satellite observations. Across the Mulock GZ, we found that using the viscous beam model reduces thickness errors from ~10% to ~2% at the WSF depression and from ~15% to ~2% at the WSF bump (Fig. 4.11). Across the Kamb WSF, using the viscous beam model reduces thickness errors to <1 % (Fig. 4.12). The slightly higher uncertainty at Mulock Glacier may be attributed to the relatively poor fit of the modelled surface height profile (Fig. 4.11a), which we suggest could be influenced by factors not included in the simple 1D viscous beam model, such as bed topography, upstream topographic confinement, or non-zero basal melt rates. This approach only requires a single height profile over the GL, for which we have complete coverage around the AIS from high-resolution DEMs and satellite altimetry (e.g., Howat et al.,

2019; Smith et al., 2019). Therefore, this could be applied to all GZs with WSFs to provide ice thickness estimates much closer to the measured values from radar-depth sounding but with significantly increased geographical coverage.

Reducing errors in estimates of ice thickness and ice basal profiles in Antarctic GZs has a number of important implications. Firstly, the estimated ice thickness at the GL is one of the dominant uncertainties in our calculations of ice sheet discharge (Rignot et al., 2008). Improving estimates of ice thickness with this method could, therefore, improve ice discharge estimates at GZs with prominent WSFs. Secondly, satellite-derived ice shelf basal melt rates are typically calculated using measurements of ice thickness, surface height and velocity (Dutrieux et al., 2013; Shean et al., 2019). While only affecting a narrow region on the ice-sheet scale, it is within GZs that basal melt rates are generally highest (Rignot & Jacobs, 2002; Holland et al., 2008) and ice sheet models are most sensitive to changes in thickness and basal melt (Arthern & Williams, 2017; Goldberg et al., 2019). Therefore, improving thickness estimates should improve estimates of basal melt rate in GZs with WSFs. Moreover, the use of the viscous beam model considerably reduces errors in the estimated basal slope (Fig. 4.11c, 4.12c). This is important because recent studies have identified basal slope as a key control over sub-ice shelf melt rates (Anselin et al., 2024; Begemen et al., 2022; Schmidt et al., 2023).

Finally, overestimation of ice thickness and ice bottom depth can cause GLs derived using the flotation criterion (e.g., Goldberg et al., 2009) to be located too far seaward. This is because the flotation criterion would assume the thicker ice is grounded, thus misplacing the GL. Many ice sheet models use a flotation GL (Docquier et al., 2011), which may therefore have considerable errors at GZs with WSFs. By providing a more accurate representation of the ice thickness and bottom depth, the viscous beam model helps to ensure that the GL is correctly located, reflecting the true grounding conditions. This refinement is crucial for accurate ice sheet modelling, as an incorrect GL position can lead to errors in predicting ice flow dynamics and, consequently, projections of future changes in ice sheet mass and sea level rise (e.g., Robel et al., 2022).

4.5.3. Temporal evolution of WSFs

While we have mainly focused on the spatial distribution of WSFs, we have also shown evidence that WSF geometry can evolve over time. Repeat ICESat-2 surface height profiles along RGT 343 (GT1R) revealed that the WSF depression at the base of the Engelhardt Ice Ridge on the Kamb Ice Stream shallowed, migrated inland and deepened again over the period April 2019 to July 2023 (Fig. 4.13). We cannot use the viscous beam model (Schoof, 2011) to attribute the observed changes in WSF amplitude and wavelength to a specific change in ice thickness, basal melt rate, ice velocity or velocity gradient – the theoretical causes of WSF change – because the GL position itself is not constant. Instead, we suggest that the observed temporal evolution of the WSF reflects the viscous response of the ice surface to the retreat of the basal stress transition point as the GL retreated. The GL at Engelhardt Ice Ridge has been retreating since at least 1963 (Bindschadler & Vornberger, 1998; Fricker et al., 2007), and DInSAR measurements show there was ~2 km of GL retreat along ICESat-2 ground track 343 (GT1R) between 2009 and 2023 (Chapter 3; Freer et al., 2024). The modelled GL position from July 2023 predicts the basal stress transition was located ~500 m upstream of the WSF depression, within 200 m of the July 2023 DInSAR GL (Fig. 4.13a).

In Chapter 3 (Freer et al., 2024), we inferred that this GL retreated at a constant rate between 2003 and 2023, based on the observation that the ridge itself retreated at a constant rate of ~0.17 km yr^{-1} over this period. If the basal stress transition – theoretically always located approx. half a wavelength upstream of the WSF depression (Schoof, 2011) – migrated steadily inland, we would expect a similarly steady inland migration of the WSF. Instead, as the ridge retreated we observed the WSF depression (D1 in Fig. 4.13) gradually become shallower until a new depression (D2) with a smaller wavelength formed ~0.8 km further inland, which then gradually deepened over time (Fig. 4.13). The sudden shift of the depression position between October 2021 and April 2022 could, therefore, imply that the shift in the dominant position of the basal stress transition GL was more sudden.

One possible explanation is that the original basal stress transition GL was originally located just upstream of D1, and that retreat was initiated as seawater was

able to intrude to a secondary stable GL position inland of D2 – at first only during the rarest of high tides, and then more regularly across the tide cycle. This could have operated as a "threshold" mode of tidal GL migration (see Chapter 2; Freer et al., 2023), whereby the GL oscillates between two stable positions (inland of D1 and D2) depending on the tide and modulated by the shape of the bed. As water started to reach the inland GL position at the majority of tides, the ice would respond viscously to the more frequent ungrounding (as unable to support the overlying steep slope), causing the ridge to retreat and a new WSF depression to form at D2. It would be difficult to confirm this theory by measuring the extent and mode of tidal migration using ICESat-2 RTLA (Chapter 2; Freer et al., 2023), because the amplitude of the tidal signal would be obscured by the much larger long-term elevation change signal from the ridge retreat and WSF evolution.

Additionally, the timing of the shift in WSF position closely follows the onset of drainage of the upstream Subglacial Lake Engelhardt (Chapter 3; Freer et al., 2024), which returns to the question of whether the lake drainage and GL retreat are related. Outflow from the lake drainage could have increased localised basal melt rates (e.g., Marsh et al., 2016), triggering the sudden shift in WSF depression position, but this is difficult to confirm with satellite data alone.

We caution that similar signals of WSF temporal evolution could be misinterpreted when detected in ice sheet elevation change maps (e.g., from gridded CryoSat-2 or ICESat-2 data). A 5–10 m deepening of the WSF depression over a period of several months would present as an anomalously high region of ice thinning (e.g., Fig. 3.5d in Chapter 3), which could be misinterpreted, for example, as a region of anomalously high basal melt rate at the GL or – depending on its location – as a signal of subglacial lake drainage.

Regardless, these findings suggest that observing changes in the amplitude, wavelength and location of WSFs around Antarctica could provide early indications of GL advance or retreat that may not be observable by other methods (e.g., due to infrequency of coherent InSAR, low tidal signal etc.). This would be an exciting avenue

for future study and could take advantage of the unprecedented repeat-track capabilities of ICESat-2 altimetry.

4.5.4. Limitations of our approach

It is important to emphasise that the methodologies outlined above, whether employing the viscous beam model to derive basal drag and ice viscosity or to improve estimates of GL position and GZ ice thickness, rely on the fact that the surface feature we are measuring is in fact a WSF caused by the change in basal stress and vertical velocity at the GL. We recognise that WSFs are not present at all GZs (Fig. 4.6) and can be discontinuous or challenging to define, with their formation potentially obscured by other factors such as topographic confinement or bed topography. Moreover, the effectiveness of this method may be compromised in regions where the viscous beam model fails to fit the amplitude or upstream surface slope of the observed WSF, as we found at Mulock, Nimrod and Liv Glaciers (Fig. 4.9). These limitations introduce additional uncertainties in our estimates of basal drag, ice viscosity, GL position and ice thickness, potentially accounting for some of the deviations from measured values (e.g., the DInSAR GL or MCoRDS ice thickness). Further uncertainties in derived thickness may arise from the applied firn corrections, which are sparsely measured and validated within Antarctic GZs (Van den Broeke et al., 2008).

Other WSF-like features at the GZ could originate from different processes, in which case assumptions based on the viscous beam model break down. For example, a prominent (>20 m deep) surface depression along ~20 km of the Kamb GZ (location in Fig. 4.6), which could be misidentified as a high-amplitude WSF, is in fact the surface signature of a large subglacial melt channel (Whiteford et al., 2022). Basal crevassing has also been proposed as a potential cause for similar surface undulations (e.g., Child et al., 2021), but these tend to be located further downstream from the GL than we would expect for a WSF, and have been ruled out as a cause of the Kamb WSF by low-frequency radar imaging (Hulbe and Catania, 2010; MacGregor et al., 2011). Additionally, surface troughs can form along shear margins (Alley et al., 2019), which might be misidentified as WSFs, although these tend to exhibit slightly different morphologies, with a sharper depression and absence of the seaward bump. Upstream of the GL, undulating

subglacial topography can produce surface bumps that are difficult to distinguish from the depression and bump associated with WSFs (Brunt et al., 2010). We found this to be most common at the Trans-Antarctic glaciers, which have steeper and more variable subglacial topography. Notably, a large depression upstream of the Nimrod GL – likely originating from a bedrock over-deepening caused by ice funnelling through a narrow topographic passage – could be misclassified as a WSF but is situated too far upstream of the GL. These examples underscore the importance of considering the wider glaciological setting when interpreting WSFs, and particularly their location with respect to the GL. In settings where the origin of WSF-like features is uncertain, caution must therefore be exercised when applying the methods described in this paper that use the viscous beam model to estimate ice or basal properties, GL location and ice thickness.

4.6. Summary

We have mapped the spatial distribution and size variation of wave-like surface features (WSFs) around the grounding zone (GZ) of Ross Ice Shelf, Antarctica, using high-resolution digital elevation models and ICESat-2 laser altimetry. WSFs form at the GZ as a result of the basal stress transition between the grounded ice sheet and floating ice shelf, and are resolved in full Stokes models of ice sheets which incorporate the grounding line (GL). We identified WSFs at seven Trans-Antarctic outlet glaciers and three Siple Coast ice streams, with the largest amplitude (>14 m) observed at Mulock Glacier and the most extensive WSF at the Kamb Ice Stream (observed along ~70% of the GZ).

We have shown that the viscous beam model of Schoof (2011), which describes the shape of the WSF in a boundary layer at the GZ, can be used to infer the relative strength of basal drag and ice viscosity. We have developed a novel method to locate the GL from a surface height profile across the GZ, integrating satellite observations of WSF geometry with the dimensionless, analytical surface profile from the viscous beam model. This requires only a single surface height profile to locate the basal stress transition, overcoming the limitations of many tidal GL proxies, and thus could be applied at all GZs where we observe WSFs. This method also improves estimates of ice thickness and basal slope across the GZ compared to estimates based on the hydrostatic

assumption, validated against ice thickness measurements from two airborne radar depth-sounder surveys across the Kamb Ice Stream and Mulock Glacier GZs (Paden et al., 2010; Wang et al., 2016). Given that ice sheet models are very sensitive to these GZ conditions (Arthern & Williams, 2017), improving our measurement estimates using this approach could help to reduce uncertainty in projections of future ice sheet evolution and sea level rise.

Finally, we documented the temporal evolution of a WSF at the retreating GL of Engelhardt Ice Ridge using repeat ICESat-2 measurements, which provides higher-resolution time series of GL retreat and novel insights into the interactions between tidal processes and long-term GL retreat. We propose this approach could be applied across Antarctica to identify early signs of GL retreat and regions that are potentially susceptible to future instability.

Acknowledgements

I would like to thank the members of my 2023 ICESat-2 Hackweek project group, Danielle Grau, Maria Lozano and Anna Puggaard, who together contributed to initial method development and early ideas for this study. We acknowledge the use of data products from CReSIS generated with support from the University of Kansas, NASA Operation IceBridge grant NNX16AH54G, NSF grants ACI-1443054, OPP-1739003, and IIS-1838230, Lilly Endowment Incorporated, and Indiana METACyt Initiative.

Bryony I. D. Freer was supported by Natural Environment Research Council (NERC) Satellite Data in Environmental Science (SENSE) Centre for Doctoral Training (grant no. NE/T00939X/1). Alexander T. Bradley is supported by the PROTECT project, which received funding from the European Union's Horizon 2020 research and innovation program under grant agreement no. 869304. Funding is provided to Helen A. Fricker from NASA through funding for the ICESat-2 Science Team (Award: 80NSSC23K0934). Funding is provided to Anna E. Hogg by ESA via the ESA STSE CryoSat+ CryoTop Evolution project and the 4DAntarctica project (ESA-IPL-POE-NB-sp-RPF-2015-951).

Appendix A

The viscous beam model of Schoof (2011) predicts the existence of an extensional stress boundary layer around the grounding zone (GZ). Within this, a sublayer (the 'WSF sublayer') emerges, in which the surface and basal elevations adjust to avoid a sharp discontinuity in slope across the grounding line (GL). In the WSF sublayer, the vertical velocity V satisfies a 'beam-like' equation (Schoof, 2011):

$$-\frac{\eta h^3}{3} V'''' = \rho_i \Delta s + \rho_w (1 - \rho_i/\rho_w) g \Delta l \tag{4.A1}$$

Where η is the ice viscosity (assumed constant in the framework of a Newtonian rheology), h is hydrostatic ice thickness at the GL, ρ_i and ρ_w are the densities of ice and water respectively, Δs and Δl are the deviations of the surface and base from their hydrostatic position and ' denotes a derivate with respect to the horizontal coordinate (the viscous beam model is a one-horizontal dimension model).

Schoof (2011) showed that, within the GZ, equation 4.A1 has an analytical solution:

$$V = A_1 \left(1 + \frac{\cos\left(\frac{3\pi}{5} + A_2 \sin\left(\frac{2\pi}{5}\right) x\right) e^{-A_2 \cos\left(\frac{2\pi}{5}\right) x} - \cos\left(\frac{\pi}{5}\right) e^{-A_2 x}}{2 \sin\left(\frac{2\pi}{5}\right) \sin\left(\frac{\pi}{5}\right)} \right) \tag{4.A2}$$

Here, the shape of the profile is constant but the amplitude and wavelength scale with A_1 and A_2, and x is a dimensionless along-WSF sublayer coordinate. Given the solution (4.A2), the dimensionless shape of the ice base (L) and surface (S) can be determined from Schoof (2011):

$$L = A_3 \int_0^x V \, dx \tag{4.A3}$$

$$S = \left(1 - \frac{\rho_w}{\rho_i}\right) L - V'''' \tag{4.A4}$$

where A_3 is a constant that determines adjustment to the slope of the base and surface caused by thinning of the ice shelf once it is in hydrostatic equilibrium. Example profiles of V, L and S are shown in Figure 4.4.

Appendix A

In this study, we co-located the dimensionless surface profile with the satellite observations of WSFs using the coordinates of the depression point (x_1, z_1; illustrated in Fig. 4.3). The wavelength is scaled through A_2 so that the location of the downstream bump in the model profile matches the location of the observed bump (x_2). The amplitude is scaled through A_1 so that the slope of the surface upstream of the depression (z_0) also matches the observations. A_3 alters the slope of the ice shelf downstream of the bump.

Appendix B

From (4.A2)–(4.A4), the dimensionless wavelength λ/l of oscillations in the surface profile is a function only of A_2, where:

$$A_2 = \left(\frac{3}{rU^{(0)}\left(H^{(0)}\right)^3}\right)^{\frac{1}{5}} \tag{4.B1}$$

Here λ is the dimensional wavelength of the WSF, l is the lengthscale of the WSF sublayer (see below) and r is $\frac{\rho_i}{\rho_w}$. In addition, $H^{(0)}$ is the dimensionless GL ice thickness and $U^{(0)}$ is the dimensionless GL velocity, which is linearly related to the observed GL velocity u_{gl} by (Schoof, 2011):

$$u_{gl} = U^{(0)}\left(\frac{\rho_i g a^2 L_s}{C}\right)^{\frac{1}{3}} \tag{4.B2}$$

with g the gravitational acceleration, a the accumulation rate (assumed spatially constant), C is the basal drag coefficient (assumed to relate basal velocity to basal shear stress with a Weertman-type sliding law and spatially constant), and L_s is the lengthscale of the ice sheet. $H^{(0)}$ is the dimensionless GL ice thickness, which is linearly related to the GL ice thickness by:

$$h_{gl} = H^{(0)}\left(\frac{CaL_s^2}{\rho g}\right)^{\frac{1}{3}} \tag{4.B3}$$

More specifically, the dimensionless wavelength is $\lambda/l = X_p(A_2) - X_t(A_2)$ where X_p and X_t are, respectively, the locations of the first positive peak and trough of a function which is itself a function only of A_2X, with X a dimensionless co-ordinate within the WSF sublayer. As such, $A_2X_p - A_2X_t$ is equal to a constant k, which can be determined numerically and thus,

$$\frac{\lambda}{l} = \frac{k}{A_2} \tag{4.B4}$$

The lengthscale of the WSF sublayer is (Schoof, 2011):

$$L = \frac{1}{L_s}\left(C\left(\frac{aL}{\eta^2 \rho g}\right)^{\frac{1}{3}}\right)^{\frac{12}{25}} \quad (4.B5)$$

Combining (4.B1)–(4.B5), and re-arranging terms to isolate those involving the basal friction and viscosity, we obtain the following relationship between the observed WSF wavelength λ, GL thickness h_{gl}, and GL velocity u_{gl}:

$$\lambda = k\frac{r^{1/5}(\rho g)^{46/75}\eta^{24/25}}{C^{46/75}a^{37/75}L^{47/75}}{u_{gl}}^{1/5}{h_{gl}}^{3/5} \quad (4.B6)$$

Assuming that the accumulation rate, ice density, and lengthscale are constant and known, equation (4.B6) can be re-arranged into an expression relating the ratio of viscosity and basal drag:

$$\frac{C^{\alpha}}{\eta^{\beta}} = K\frac{{u_{gl}}^{1/5}{h_{gl}}^{3/5}}{\lambda} \quad (4.B7)$$

where $K = k\frac{r^{1/5}(\rho g)^{46/75}}{a^{37/75}L_s^{47/75}}$ is a constant that is assumed known, and $\alpha = \frac{46}{75}, \beta = \frac{24}{25}$.

Thus, the satellite observations of WSF wavelength, GL thickness, and GL velocity can be used to infer details of the relative strength of basal drag and ice viscosity at each glacier or ice stream. Where the right-hand side of (4.B7) is relatively large, basal drag is relatively larger than viscosity. Conversely, where the right-hand side of (4.B7) is relatively small, basal drag is relatively smaller than viscosity.

We applied this procedure to each of the Ross Ice Shelf glaciers and ice streams in this study using the measured WSF wavelength, GL ice thickness and velocity from the individual representative profiles.

Supplementary Material

S4.1 Adjustment of the Firn Correction (Supplementary Text)

In this study we have used the BedMachine firn correction to give an idea of the spatial variance across the GL, but have applied an adjustment given the residual height mismatch compared to the MCoRDS surface heights – explained in more detail below.

In BedMachine, ice thickness over the grounded ice is calculated using either mass conservation (in fast-flowing regions) or streamline diffusion (in slow-flowing regions). Over the floating ice shelves, ice thickness is estimated by applying hydrostatic equilibrium to REMA surface heights with a calibrated firn air content correction. This correction is simulated by the firn densification model from Ligtenberg et al. (2011) that has been forced at the surface by RACMO2.3p2 (van Wessem et al., 2018), giving us the difference between the actual depth of the firn layer and the depth of the firn if it were at the density of meteoric ice. Notably, it has then been recalibrated using radar data to minimise the misfit between hydrostatic and measured ice thickness, specifically forcing a smooth transition between grounded and floating ice thickness over the first 3 km downstream of the GL (Morlighem et al., 2020). All BedMachine heights are referenced to the Eigen-6C4 geoid (Förste et al., 2014).

Mulock Glacier

Along the Mulock Glacier GZ profile we found that BedMachine surface heights are consistently lower than the measured MCoRDS surface height (Paden et al., 2010) corrected for the firn column height (i.e. comparing z_B with $z - F_c$; Fig. S4.1a). We have not corrected for tides or dynamic ocean topography (DOT) so these could theoretically be a source of error; but for this to be true we would expect the difference solely to occur seaward of the GL (i.e. only over floating ice affected by tides/dynamic ocean topography). As the discrepancy occurs along the entire surface height profile, we propose that it is most likely due to an underestimation of the firn column height. To address this we have added 16 m to the firn correction parameter, F_c, along the whole track (Fig. S4.1a). This is used to adjust the measured MCoRDS surface height, z, to reference the top of the firn layer were it at the density of meteoric ice (i.e. the same

surface as referenced in BedMachine and by calculations of hydrostatic and flotation thickness).

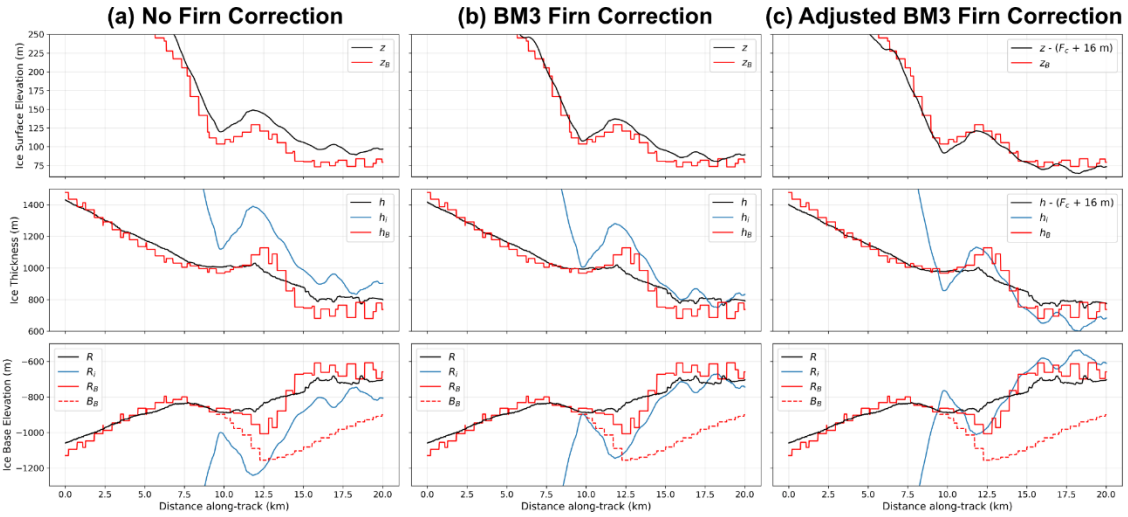


Figure S4.1a. Ice surface, thickness and base elevation profiles across the Mulock Glacier WSF from MCoRDS (Paden et al., 2010), BedMachine (Morlighem, 2022) and calculated using the hydrostatic assumption, using different firn corrections. (a) No firn correction; (b) BedMachine firn correction; (e) adjusted firn correction (BedMachine firn correction +16 m).

Kamb Ice Stream

Along the Kamb profile we found that BedMachine surface heights are consistently higher than the measured MCoRDS surface heights (Wang et al., 2016) corrected for the firn column height. To address this, we have adjusted the firn correction used in the analysis of ice thickness across the GL (BedMachine firn correction – 2.5 m) (Fig. S4.1b).

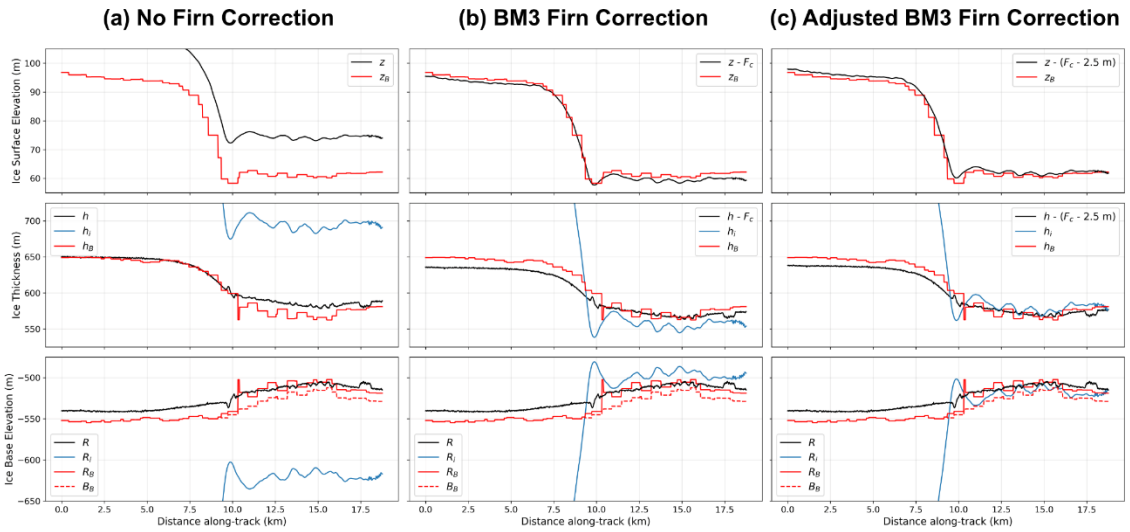


Figure S4.1b. Ice surface, thickness and base elevation profiles across the Kamb WSF from MCoRDS (Wang et al., 2016), BedMachine (Morlighem, 2022) and calculated using the hydrostatic assumption, using different firn corrections. (a) No firn correction; (b) BedMachine firn correction; (e) adjusted firn correction (BedMachine firn correction -2.5 m).

S4.2. Amplitude vs. Wavelength of Ross Ice Shelf WSFs (Supplementary Figure)

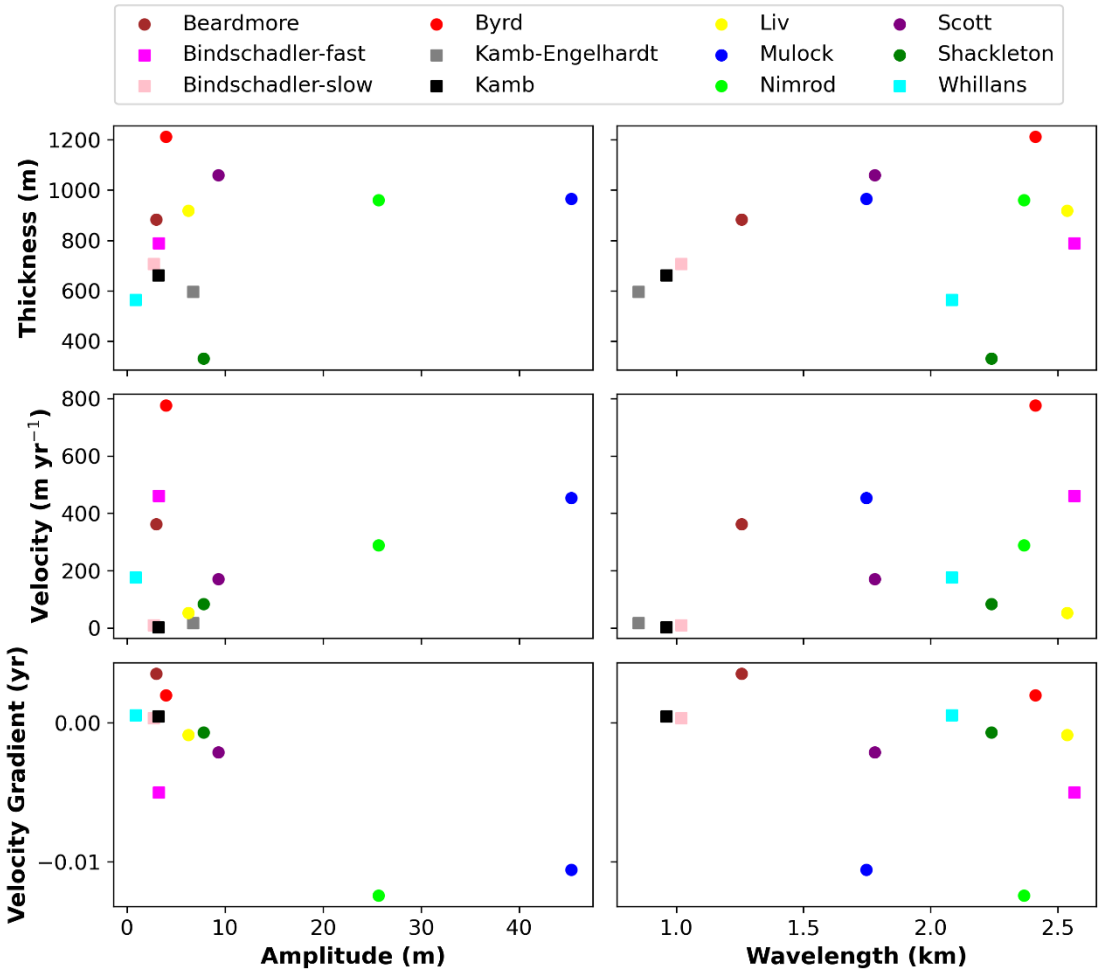


Figure 4.S2. Relationship between amplitude and wavelength of the WSFs of the representative profile from each glacier and the ice thickness, velocity, and velocity gradient at the intersection with their respective grounding line. Square markers are used for Siple Coast ice streams, circles for Trans-Antarctic glaciers.

References

Alley, K. E., Scambos, T. A., Alley, R. B., & Holschuh, N. (2019). Troughs developed in ice-stream shear margins precondition ice shelves for ocean-driven breakup. *Science Advances*, 5(10), eaax2215. https://doi.org/10.1126/sciadv.aax2215

Alley, R. B., Blankenship, D. D., Bentley, C. R., & Rooney, S. T. (1986). Deformation of till beneath ice stream B, West Antarctica. *Nature*, 322(6074), 57–59. https://doi.org/10.1038/322057a0

Alley, R. B., Blankenship, D. D., Bentley, C. R., & Rooney, S. T. (1987). Till beneath ice stream B: 3. Till deformation: Evidence and implications. *Journal of Geophysical Research: Solid Earth*, 92(B9), 8921–8929. https://doi.org/10.1029/JB092iB09p08921

Anandakrishnan, S., Catania, G. A., Alley, R. B., & Horgan, H. J. (2007). Discovery of Till Deposition at the Grounding Line of Whillans Ice Stream. *Science*, 315(5820), 1835–1838. https://doi.org/10.1126/science.1138393

Anselin, J., Holland, P. R., Jenkins, A., & Taylor, J. R. (2024). Ice base slope effects on the turbulent ice shelf-ocean boundary current. *Journal of Physical Oceanography*. https://doi.org/10.1175/JPO-D-23-0256.1

Arthern, R. J., & Williams, C. R. (2017). The sensitivity of West Antarctica to the submarine melting feedback. *Geophysical Research Letters*, 44(5), 2352–2359. https://doi.org/10.1002/2017GL072514

Arthern, R. J., Hindmarsh, R. C. A., & Williams, C. R. (2015). Flow speed within the Antarctic ice sheet and its controls inferred from satellite observations. *Journal of Geophysical Research: Earth Surface*, 120(7), 1171–1188. https://doi.org/10.1002/2014JF003239

Bamber, J., & Bentley, C. (1994). A comparison of satellite-altimetry and ice-thickness measurements of the Ross Ice Shelf, Antarctica. *Annals of Glaciology*, 20, 357–364. https://doi.org/10.3189/1994AoG20-1-357-364

Barcilon, V., & MacAyeal, D. R. (1993). Steady flow of a viscous ice stream across a no-slip/free-slip transition at the bed. *Journal of Glaciology*, 39(131), 167–185. https://doi.org/10.3189/S0022143000015811

Barnes, J. M., & Gudmundsson, G. H. (2022). The predictive power of ice sheet models and the regional sensitivity of ice loss to basal sliding parameterisations: a case study of Pine Island and Thwaites glaciers, West Antarctica. *The Cryosphere*, 16(10), 4291–4304. https://doi.org/10.5194/tc-16-4291-2022

Begeman, C. B., Asay-Davis, X., & Van Roekel, L. (2022). Ice-shelf ocean boundary layer dynamics from large-eddy simulations. *The Cryosphere*, 16(1), 277–295. https://doi.org/10.5194/tc-16-277-2022

Benn, D., & Evans, D. J. A. (2010). Glaciers and Glaciation, 2nd edition (2nd ed.). London: Routledge. https://doi.org/10.4324/9780203785010

Bindschadler, R., Choi, H., Wichlacz, A., Bingham, R., Bohlander, J., Brunt, K., et al. (2011). Getting around Antarctica: new high-resolution mappings of the grounded and freely-floating boundaries of the Antarctic ice sheet created for the International Polar Year. *The Cryosphere*, 5(3), 569–588. https://doi.org/10.5194/tc-5-569-2011

Bindschadler, R. A., King, M. A., Alley, R. B., Anandakrishnan, S., & Padman, L. (2003). Tidally controlled stick-slip discharge of a West Antarctic ice. *Science* (New York, N.Y.), 301(5636), 1087–1089. https://doi.org/10.1126/science.1087231

Bindschadler, R. A., Vornberger, P. L., King, M. A., & Padman, L. (2003). Tidally driven stick–slip motion in the mouth of Whillans Ice Stream, Antarctica. *Annals of Glaciology*, 36, 263–272. https://doi.org/10.3189/172756403781816284

Bindschadler, Robert, & Vornberger, P. (1998). Changes in the West Antarctic Ice Sheet Since 1963 from Declassified Satellite Photography. *Science*, 279(5351), 689–692. https://doi.org/10.1126/science.279.5351.689

Blankenship, D. D., Bentley, C. R., Rooney, S. T., & Alley, R. B. (1986). Seismic measurements reveal a saturated porous layer beneath an active Antarctic ice stream. *Nature*, 322(6074), 54–57. https://doi.org/10.1038/322054a0

Brancato, V., Rignot, E., Milillo, P., Morlighem, M., Mouginot, J., An, L., et al. (2020). Grounding Line Retreat of Denman Glacier, East Antarctica, Measured With COSMO-SkyMed Radar Interferometry Data. *Geophysical Research Letters*, 47(7). https://doi.org/10.1029/2019GL086291

van den Broeke, M. R., Berg, W. J. van de, & Meijgaard, E. van. (2008). Firn depth correction along the Antarctic grounding line. *Antarctic Science*, 20(5), 513–517. https://doi.org/10.1017/S095410200800148X

Brunt, K. M., Fricker, H. A., Padman, L., Scambos, T. A., & O'Neel, S. (2010). Mapping the grounding zone of the Ross Ice Shelf, Antarctica, using ICESat laser altimetry. *Annals of Glaciology*, 51(55), 71–79. https://doi.org/10.3189/172756410791392790

Brunt, K. M., Fricker, H. A., & Padman, L. (2011). Analysis of ice plains of the Filchner–Ronne Ice Shelf, Antarctica, using ICESat laser altimetry. *Journal of Glaciology*, 57(205), 965–975. https://doi.org/10.3189/002214311798043753

Chartrand, A. M., & Howat, I. M. (2023). A comparison of contemporaneous airborne altimetry and ice-thickness measurements of Antarctic ice shelves. *Journal of Glaciology*, 1–14. https://doi.org/10.1017/jog.2023.49

Chen, H., Rignot, E., Scheuchl, B., & Ehrenfeucht, S. (2023). Grounding Zone of Amery Ice Shelf, Antarctica, From Differential Synthetic-Aperture Radar Interferometry. *Geophysical Research Letters*, 50(6), e2022GL102430. https://doi.org/10.1029/2022GL102430

Child, S. F., Stearns, L. A., van der Veen, C. J., & Elósegui, P. (2021). Basal Crevasse Formation on Byrd Glacier, East Antarctica, as Proxy for Past Subglacial Flooding Events. *Geophysical Research Letters*, 48(15), e2020GL090978. https://doi.org/10.1029/2020GL090978

Chugunov, V. A., & Wilchinsky, A. V. (1996). Modelling of a marine glacier and ice-sheet-ice-shelf transition zone based on asymptotic analysis. *Annals of Glaciology*, 23, 59–67. https://doi.org/10.3189/S0260305500013264

Chuter, S. J., & Bamber, J. L. (2015). Antarctic ice shelf thickness from CryoSat-2 radar altimetry. *Geophysical Research Letters*, 42(24), 10,721-10,729. https://doi.org/10.1002/2015GL066515

Ciracì, E., Rignot, E., Scheuchl, B., Tolpekin, V., Wollersheim, M., An, L., et al. (2023). Melt rates in the kilometer-size grounding zone of Petermann Glacier, Greenland, before and during a retreat. *Proceedings of the National Academy of Sciences*, 120(20), e2220924120. https://doi.org/10.1073/pnas.2220924120

Conrad, O., Bechtel, B., Bock, M., Dietrich, H., Fischer, E., Gerlitz, L., et al. (2015). System for Automated Geoscientific Analyses (SAGA) v. 2.1.4. *Geoscientific Model Development*, 8(7), 1991–2007. https://doi.org/10.5194/gmd-8-1991-2015

Dawson, G. J., & Bamber, J. L. (2017). Antarctic Grounding Line Mapping From CryoSat-2 Radar Altimetry. *Geophysical Research Letters*, 44(23), 11,886-11,893. https://doi.org/10.1002/2017GL075589

Depoorter, M. A., Bamber, J. L., Griggs, J. A., Lenaerts, J. T. M., Ligtenberg, S. R. M., van den Broeke, M. R., & Moholdt, G. (2013). Calving fluxes and basal melt rates of Antarctic ice shelves. *Nature*, 502(7469), 89–92. https://doi.org/10.1038/nature12567

Docquier, D., Perichon, L., & Pattyn, F. (2011). Representing Grounding Line Dynamics in Numerical Ice Sheet Models: Recent Advances and Outlook. *Surveys in Geophysics*, 32(4–5), 417–435. https://doi.org/10.1007/s10712-011-9133-3

Durand, G., Gagliardini, O., de Fleurian, B., Zwinger, T., & Le Meur, E. (2009). Marine ice sheet dynamics: Hysteresis and neutral equilibrium. *Journal of Geophysical Research*, 114(F3), F03009. https://doi.org/10.1029/2008JF001170

Dutrieux, P., Vaughan, D. G., Corr, H. F. J., Jenkins, A., Holland, P. R., Joughin, I., & Fleming, A. H. (2013). Pine Island glacier ice shelf melt distributed at kilometre scales. *The Cryosphere*, 7(5), 1543–1555. https://doi.org/10.5194/tc-7-1543-2013

Förste, C., Bruinsma, S. L., Abrikosov, O., Lemoine, J.-M., Marty, J. C., Flechtner, F., et al. (2014). EIGEN-6C4 The latest combined global gravity field model including GOCE data up to degree and order 2190 of GFZ Potsdam and GRGS Toulouse [Dataset]. GZF Data Services. https://doi.org/10.5880/ICGEM.2015.1

Freer, B. I. D., Marsh, O. J., Hogg, A. E., Fricker, H. A., & Padman, L. (2023). Modes of Antarctic tidal grounding line migration revealed by Ice, Cloud, and land Elevation Satellite-2 (ICESat-2) laser altimetry. *The Cryosphere*, 17(9), 4079–4101. https://doi.org/10.5194/tc-17-4079-2023

Freer, B. I. D., Marsh, O. J., Hogg, A. E., Fricker, H. A., Siegfried, M. R., Floricioiu, D., Sauthoff, W., Rigby, R., and Wilson, S. F. (2024, *in review*) Synchronous lake drainage and grounding line retreat at Engelhardt Subglacial Lake, West Antarctica. *Journal of Geophysical Research: Earth Surface.*

Fretwell, P., Pritchard, H. D., Vaughan, D. G., Bamber, J. L., Barrand, N. E., Bell, R., et al. (2013). Bedmap2: improved ice bed, surface and thickness datasets for Antarctica. *The Cryosphere*, 7(1), 375–393. https://doi.org/10.5194/tc-7-375-2013

Fricker, H. A., & Padman, L. (2006). Ice shelf grounding zone structure from ICESat laser altimetry. *Geophysical Research Letters*, 33(15), L15502. https://doi.org/10.1029/2006GL026907

Fricker, H. A., Scambos, T., Bindschadler, R., & Padman, L. (2007). An Active Subglacial Water System in West Antarctica Mapped from Space. *Science*, 315(5818), 1544–1548. https://doi.org/10.1126/science.1136897

Fricker, H. A., Coleman, R., Padman, L., Scambos, T. A., Bohlander, J., & Brunt, K. M. (2009). Mapping the grounding zone of the Amery Ice Shelf, East Antarctica using InSAR, MODIS and ICESat. *Antarctic Science*, 21(5), 515–532. https://doi.org/10.1017/S095410200999023X

Friedl, P., Weiser, F., Fluhrer, A., & Braun, M. H. (2020). Remote sensing of glacier and ice sheet grounding lines: A review. *Earth-Science Reviews*, 201, 102948. https://doi.org/10.1016/j.earscirev.2019.102948

Gladstone, R. M., Payne, A. J., & Cornford, S. L. (2012). Resolution requirements for grounding-line modelling: sensitivity to basal drag and ice-shelf buttressing. *Annals of Glaciology*, 53(60), 97–105. https://doi.org/10.3189/2012AoG60A148

Goldberg, D., Holland, D. M., & Schoof, C. (2009). Grounding line movement and ice shelf buttressing in marine ice sheets. *Journal of Geophysical Research: Earth Surface*, 114(F4), 2008JF001227. https://doi.org/10.1029/2008JF001227

Goldberg, D. N., Gourmelen, N., Kimura, S., Millan, R., & Snow, K. (2019). How Accurately Should We Model Ice Shelf Melt Rates? *Geophysical Research Letters*, 46(1), 189–199. https://doi.org/10.1029/2018GL080383

Griggs, J. A., & Bamber, J. L. (2009). Ice shelf thickness over Larsen C, Antarctica, derived from satellite altimetry. *Geophysical Research Letters*, 36(19), 2009GL039527. https://doi.org/10.1029/2009GL039527

Griggs, J. A., & Bamber, J. L. (2011). Antarctic ice-shelf thickness from satellite radar altimetry. *Journal of Glaciology*, 57(203), 485–498. https://doi.org/10.3189/002214311796905659

Hindmarsh, R. C. A. (1993). Qualitative Dynamics of Marine Ice Sheets. In W. R. Peltier (Ed.), *Ice in the Climate System* (pp. 67–99). Berlin, Heidelberg: Springer Berlin Heidelberg. https://doi.org/10.1007/978-3-642-85016-5_5

Holdsworth, G. (1969). Flexure of a Floating Ice Tongue. *Journal of Glaciology*, 8(54), 385–397. https://doi.org/10.3189/S0022143000026976

Holland, P. R., Jenkins, A., & Holland, D. M. (2008). The Response of Ice Shelf Basal Melting to Variations in Ocean Temperature. *Journal of Climate*, 21(11), 2558–2572. https://doi.org/10.1175/2007JCLI1909.1

Horgan, H. J., & Anandakrishnan, S. (2006). Static grounding lines and dynamic ice streams: Evidence from the Siple Coast, West Antarctica. *Geophysical Research Letters, 33(18)*. https://doi.org/10.1029/2006GL027091

Howat, I. M., Porter, C., Smith, B. E., Noh, M.-J., and Morin, P. (2019) The Reference Elevation Model of Antarctica. *The Cryosphere*, 13, 665–674, https://doi.org/10.5194/tc-13-665-2019

Hulbe, C. L., Klinger, M., Masterson, M., Catania, G., Cruikshank, K., & Bugni, A. (2016). Tidal bending and strand cracks at the Kamb Ice Stream grounding line, West Antarctica. *Journal of Glaciology*, 62(235), 816–824. https://doi.org/10.1017/jog.2016.74

Hulbe, C. L. & Catania, G. (2010). Ice-penetrating radar data across Siple Coast grounding lines (Version 1) [Dataset]. NASA National Snow and Ice Data Center Distributed Active Archive Center. doi:10.7265/N5M043BH.

Intergovernmental Panel on Climate Change (IPCC) (Ed.). (2023). Ocean, Cryosphere and Sea Level Change. In Climate Change 2021 – The Physical Science Basis: Working Group I Contribution to the Sixth Assessment Report of the Intergovernmental Panel on Climate Change (pp. 1211–1362). Cambridge: Cambridge University Press. https://doi.org/10.1017/9781009157896.011

Jenkins, A., Corr, H. F. J., Nicholls, K. W., Stewart, C. L., & Doake, C. S. M. (2006). Interactions between ice and ocean observed with phase-sensitive radar near an Antarctic ice-shelf grounding line. *Journal of Glaciology*, 52(178), 325–346. https://doi.org/10.3189/172756506781828502

Kamb, B. (2001). Basal Zone of the West Antarctic Ice Streams and its Role in Lubrication of Their Rapid Motion. In *The West Antarctic Ice Sheet: Behavior and Environment* (pp. 157–199). American Geophysical Union (AGU). https://doi.org/10.1029/AR077p0157

Kim, J. H., Rignot, E., Holland, D., & Holland, D. (2024). Seawater Intrusion at the Grounding Line of Jakobshavn Isbræ, Greenland, From Terrestrial Radar Interferometry. *Geophysical Research Letters*, 51(6), e2023GL106181. https://doi.org/10.1029/2023GL106181

Lestringant, R. (1994). A two-dimensional finite-element study of flow in the transition zone between an ice sheet and an ice shelf. *Annals of Glaciology*, 20, 67–72. https://doi.org/10.3189/1994AoG20-1-67-72

MacGregor, J. A., Anandakrishnan, S., Catania, G. A., & Winebrenner, D. P. (2011). The grounding zone of the Ross Ice Shelf, West Antarctica, from ice-penetrating radar. *Journal of Glaciology*, 57(205), 917–928. https://doi.org/10.3189/002214311798043780

Magruder, L., Brunt, K., Neumann, T., Klotz, B., & Alonzo, M. (2021). Passive Ground-Based Optical Techniques for Monitoring the On-Orbit ICESat-2 Altimeter Geolocation and Footprint Diameter. *Earth and Space Science*, 8(10). https://doi.org/10.1029/2020EA001414

Marsh, O. J., Fricker, H. A., Siegfried, M. R., Christianson, K., Nicholls, K. W., Corr, H. F. J., & Catania, G. (2016). High basal melting forming a channel at the grounding line of Ross Ice Shelf, Antarctica. *Geophysical Research Letters*, 43(1), 250–255. https://doi.org/10.1002/2015GL066612

Mayer, C., & Huybrechts, P. (1999). Ice-dynamic conditions across the grounding zone, Ekströmisen, East Antarctica. *Journal of Glaciology*, 45(150), 384–393. https://doi.org/10.3189/S002214300000188X

Milillo, P., Rignot, E., Rizzoli, P., Scheuchl, B., Mouginot, J., Bueso-Bello, J., & Prats-Iraola, P. (2019). Heterogeneous retreat and ice melt of Thwaites Glacier, West Antarctica. *Science Advances*, 5(1), eaau3433. https://doi.org/10.1126/sciadv.aau3433

Milillo, P., Rignot, E., Rizzoli, P., Scheuchl, B., Mouginot, J., Bueso-Bello, J. L., et al. (2022). Rapid glacier retreat rates observed in West Antarctica. *Nature Geoscience*, 15(1), 48–53. https://doi.org/10.1038/s41561-021-00877-z

Milillo, P., Rignot, E., Mouginot, J., Scheuchl, B., Morlighem, M., Li, X., & Salzer, J. T. (2017). On the Short-term Grounding Zone Dynamics of Pine Island Glacier, West Antarctica, Observed With COSMO-SkyMed Interferometric Data: PIG Grounding Line Dynamics. *Geophysical Research Letters*, 44(20), 10,436-10,444. https://doi.org/10.1002/2017GL074320

Morlighem, M. (2022). MEaSUREs BedMachine Antarctica (Version 3) [Dataset]. NASA National Snow and Ice Data Center Distributed Active Archive Center. https://doi.org/10.5067/FPSU0V1MWUB6.

Morlighem, M., Rignot, E., Binder, T., Blankenship, D., Drews, R., Eagles, G., et al. (2020). Deep glacial troughs and stabilizing ridges unveiled beneath the margins of the Antarctic ice sheet. *Nature Geoscience*, 13(2), 132–137. https://doi.org/10.1038/s41561-019-0510-8

Mouginot, J., Scheuchl, B. & Rignot, E. (2017). MEaSURES Antarctic Boundaries for IPY 2007-2009 from Satellite Radar (Version 2) [Dataset]. NASA National Snow and Ice Data Center Distributed Active Archive Center. https://doi.org/10.5067/AXE4121732AD

Nowicki, S. M. J., & Wingham, D. J. (2008). Conditions for a steady ice sheet–ice shelf junction. *Earth and Planetary Science Letters*, 265(1), 246–255. https://doi.org/10.1016/j.epsl.2007.10.018

Paden, J., Li, J., Leuschen, C., Rodriguez-Morales, F., & Hale, R. (2010) IceBridge MCoRDS L2 Ice Thickness (Version 1) [Dataset]. NASA National Snow and Ice Data Center Distributed Active Archive Center. https://doi.org/10.5067/GDQ0CUCVTE2Q.

Paolo, F. S., Fricker, H. A., & Padman, L. (2015). Volume loss from Antarctic ice shelves is accelerating. *Science*, 348(6232), 327–331. https://doi.org/10.1126/science.aaa0940

Rabus, B. T., & Lang, O. (2002). On the representation of ice-shelf grounding zones in SAR interferograms. *Journal of Glaciology*, 48(162), 345–356. https://doi.org/10.3189/172756502781831197

Rignot, E., Mouginot, J., & Scheuchl, B. (2011). Antarctic grounding line mapping from differential satellite radar interferometry. *Geophysical Research Letters, 38(10)*. https://doi.org/10.1029/2011GL047109

Rignot, E. (2023). Observations of grounding zones are the missing key to understand ice melt in Antarctica. *Nature Climate Change*, 13(10), 1010–1013. https://doi.org/10.1038/s41558-023-01819-w

Rignot, E., & Jacobs, S. S. (2002). Rapid Bottom Melting Widespread near Antarctic Ice Sheet Grounding Lines. *Science*, 296(5575), 2020–2023. https://doi.org/10.1126/science.1070942

Rignot, E., Bamber, J. L., van den Broeke, M. R., Davis, C., Li, Y., van de Berg, W. J., & van Meijgaard, E. (2008). Recent Antarctic ice mass loss from radar interferometry and regional climate modelling. *Nature Geoscience*, 1(2), 106–110. https://doi.org/10.1038/ngeo102

Rignot, E., Mouginot, J., & Scheuchl, B. (2016). MEaSUREs Antarctic Grounding Line from Differential Satellite Radar Interferometry (Version 2) [Dataset]. NASA National Snow and Ice Data Center Distributed Active Archive Center. https://doi.org/10.5067/IKBWW4RYHF1Q

Rignot, E., Mouginot, J., & Scheuchl, B. (2017). MEaSUREs InSAR-Based Antarctica Ice Velocity Map (Version 2) [Dataset]. NASA National Snow and Ice Data Center Distributed Active Archive Center. https://doi.org/10.5067/D7GK8F5J8M8R

Rignot, E., Ciracì, E., Scheuchl, B., Tolpekin, V., Wollersheim, M., & Dow, C. (2024). Widespread seawater intrusions beneath the grounded ice of Thwaites Glacier, West Antarctica. *Proceedings of the National Academy of Sciences*, 121(22), e2404766121. https://doi.org/10.1073/pnas.2404766121

Robel, A. A., Pegler, S. S., Catania, G., Felikson, D., & Simkins, L. M. (2022). Ambiguous stability of glaciers at bed peaks. *Journal of Glaciology*, 68(272), 1177–1184. https://doi.org/10.1017/jog.2022.31

Savitzky, Abraham., & Golay, M. J. E. (1964). Smoothing and Differentiation of Data by Simplified Least Squares Procedures. *Analytical Chemistry*, 36(8), 1627–1639. https://doi.org/10.1021/ac60214a047

Sayag, R., & Worster, M. G. (2011). Elastic response of a grounded ice sheet coupled to a floating ice shelf. *Physical Review E*, 84(3), 036111. https://doi.org/10.1103/PhysRevE.84.036111

Sayag, R., & Worster, M. G. (2013). Elastic dynamics and tidal migration of grounding lines modify subglacial lubrication and melting. *Geophysical Research Letters*, 40(22), 5877–5881. https://doi.org/10.1002/2013GL057942

Schmidt, B. E., Washam, P., Davis, P. E. D., Nicholls, K. W., Holland, D. M., Lawrence, J. D., et al. (2023). Heterogeneous melting near the Thwaites Glacier grounding line. *Nature*, 614(7948), 471–478. https://doi.org/10.1038/s41586-022-05691-0

Schoof, C. (2007). Ice sheet grounding line dynamics: Steady states, stability, and hysteresis. *Journal of Geophysical Research*, 112(F3), F03S28. https://doi.org/10.1029/2006JF000664

Schoof, C. (2011). Marine ice sheet dynamics. Part 2. A Stokes flow contact problem. *Journal of Fluid Mechanics*, 679, 122–155. https://doi.org/10.1017/jfm.2011.129

Shean, D. E., Joughin, I. R., Dutrieux, P., Smith, B. E., & Berthier, E. (2019). Ice shelf basal melt rates from a high-resolution digital elevation model (DEM) record for Pine Island Glacier, Antarctica. *The Cryosphere*, 13(10), 2633–2656. https://doi.org/10.5194/tc-13-2633-2019

Smith, B., Adusumilli, S., Csathó, B. M., Felikson, D., Fricker, H. A., Gardner, A., Holschuh, N., Lee, J., Paolo, F. S., Siegfried, M. R., Sutterley, T. and the ICESat-2 Science Team. (2023a). ATLAS/ICESat-2 L3A Land Ice Height (Version 6) [Dataset]. NASA National Snow and Ice Data Center Distributed Active Archive Center. https://doi.org/10.5067/ATLAS/ATL06.006

Smith, Benjamin, Fricker, H. A., Holschuh, N., Gardner, A. S., Adusumilli, S., Brunt, K. M., et al. (2019). Land ice height-retrieval algorithm for NASA's ICESat-2 photon-counting laser altimeter. *Remote Sensing of Environment*, 233, 111352. https://doi.org/10.1016/j.rse.2019.111352

Swithinbank, C. (1955). Ice Shelves. *The Geographical Journal*, 121(1), 64–76. https://doi.org/10.2307/1791807

Thomas, R. H. (1979). The Dynamics of Marine Ice Sheets. *Journal of Glaciology*, 24(90), 167–177. https://doi.org/10.1017/S0022143000014726

Truffer, M., & Echelmeyer, K. A. (2003). Of isbræ and ice streams. *Annals of Glaciology*, 36, 66–72. https://doi.org/10.3189/172756403781816347

Tulaczyk, S., Kamb, W. B., & Engelhardt, H. F. (2000). Basal mechanics of Ice Stream B, west Antarctica: 1. Till mechanics. *Journal of Geophysical Research: Solid Earth*, 105(B1), 463–481. https://doi.org/10.1029/1999JB900329

Vaughan, D. G. (1994). Investigating tidal flexure on an ice shelf using kinematic GPS. *Annals of Glaciology*, 20, 372–376. https://doi.org/10.3189/1994AoG20-1-372-376

Virtanen, P., Gommers, R., Oliphant, T. E., Haberland, M., Reddy, T., Cournapeau, D., et al. (2020). SciPy 1.0: fundamental algorithms for scientific computing in Python. *Nature Methods*, 17(3), 261–272. https://doi.org/10.1038/s41592-019-0686-2

Wang, Z., Gogineni, S., Rodriguez-Morales, F., Yan, J.-B., Paden, J., Leuschen, C., et al. (2016). Multichannel Wideband Synthetic Aperture Radar for Ice Sheet Remote Sensing: Development and the First Deployment in Antarctica. *IEEE Journal of Selected Topics in Applied Earth Observations and Remote Sensing*, 9(3), 980–993. https://doi.org/10.1109/JSTARS.2015.2403611

Weertman, J. (1974). Stability of the Junction of an Ice Sheet and an Ice Shelf. *Journal of Glaciology*, 13(67), 3–11. https://doi.org/10.1017/S0022143000023327

Whillans, I. M., Bentley, C. R., & Van Der Veen, C. J. (2001). Ice Streams B and C. In *The West Antarctic Ice Sheet: Behavior and Environment* (pp. 257–281). American Geophysical Union (AGU). https://doi.org/10.1029/AR077p0257

Whiteford, A., Horgan, H. J., Leong, W. J., & Forbes, M. (2022). Melting and Refreezing in an Ice Shelf Basal Channel at the Grounding Line of the Kamb Ice Stream, West Antarctica. *Journal of Geophysical Research: Earth Surface*, 127(11), e2021JF006532. https://doi.org/10.1029/2021JF006532

Wild, C. T., Marsh, O. J., & Rack, W. (2017). Viscosity and elasticity: a model intercomparison of ice-shelf bending in an Antarctic grounding zone. *Journal of Glaciology*, 63(240), 573–580. https://doi.org/10.1017/jog.2017.15

Wilson, N., Straneo, F., & Heimbach, P. (2017). Satellite-derived submarine melt rates and mass balance (2011–2015) for Greenland's largest remaining ice tongues. *The Cryosphere*, 11(6), 2773–2782. https://doi.org/10.5194/tc-11-2773-2017

Zhong, M., Simons, M., Minchew, B., & Zhu, L. (2023). Inferring Tide-Induced Ephemeral Grounding in an Ice-Shelf-Stream System: Rutford Ice Stream, West Antarctica. *Journal of Geophysical Research: Earth Surface*, 128(2), e2022JF006789. https://doi.org/10.1029/2022JF006789

Chapter 5

Synthesis and Conclusions

This thesis aimed to enhance our understanding of the patterns and drivers of grounding line (GL) migration in Antarctica and our ability to monitor this region over a range of timescales. I have achieved this aim using data from NASA's ICESat-2 satellite laser altimetry mission, along with other laser and radar altimetry, DInSAR, high-resolution digital elevation models and radar-depth sounding datasets (Figure 5.1).

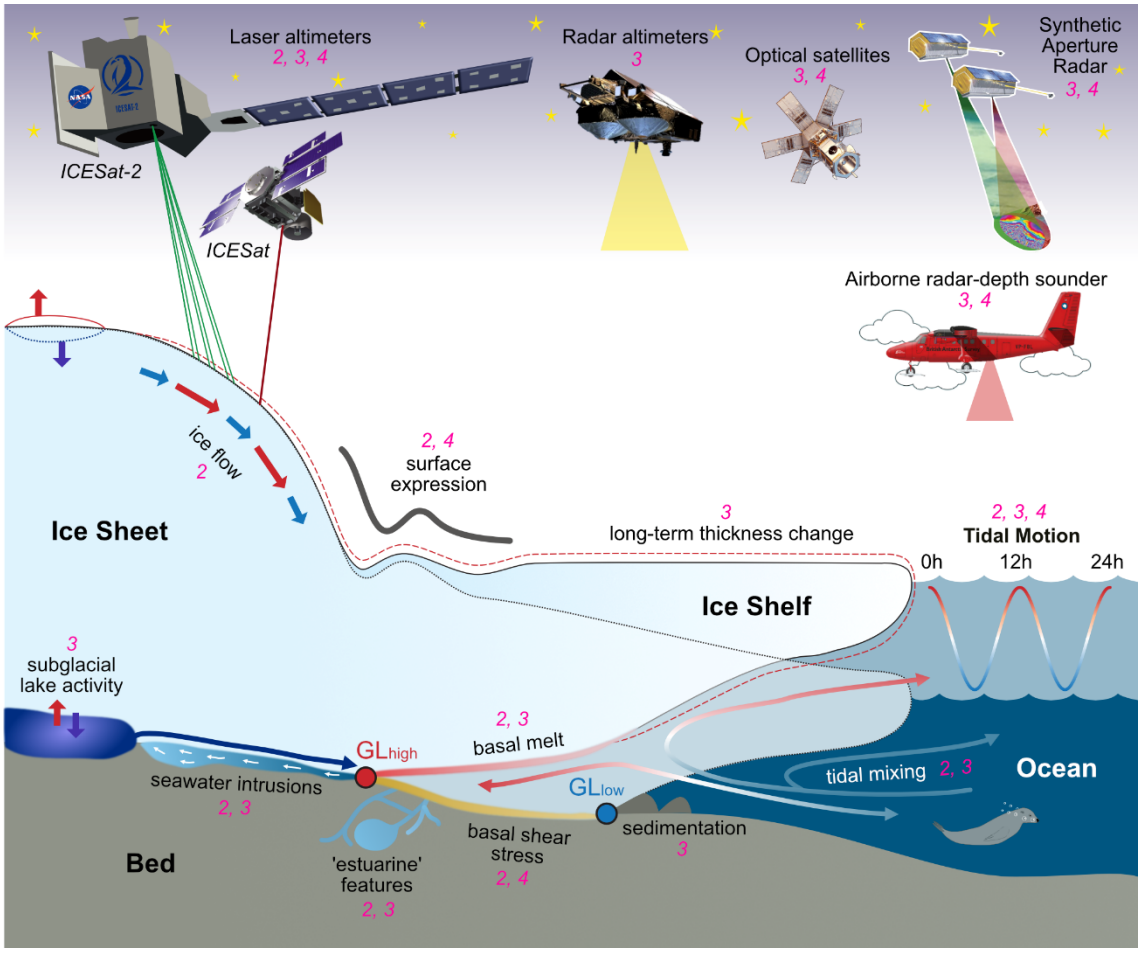


Figure 5.1 (copy of Figure 1.7). Schematic depicting the key grounding zone processes and satellite missions used in this thesis. Pink numbers indicate which Chapter(s) each process has been addressed in throughout the thesis.

Firstly, I developed a new method to measure short-term tidal GL migration at a higher relative temporal resolution than previously possible using ICESat-2 (Chapter 2). Applying this method at two Antarctic ice plains revealed new insights into tidal grounding zone (GZ) behaviour on hourly to daily timescales (Chapters 2 & 3). Next, I examined the interactions between subglacial hydrology and the GZ on monthly to decadal timescales by analysing the response of the GL to the fill-and-drain activity of Engelhardt Subglacial Lake over the past 20 years (Chapter 3). Finally, I conducted the first widespread assessment of the wave-like surface feature associated with the long-term position of the basal stress transition around the GZ of the Ross Ice Shelf, and showed that, by combining these observations with a viscous beam model, it is possible to improve estimates of GL location and ice thickness in these sensitive regions (Chapter 4).

In this synthesis chapter I demonstrate how the original aims and objectives of this thesis have been achieved. I summarise the key scientific findings, highlighting connections between the results of each chapter, and discuss potential future research avenues that have emerged from this work.

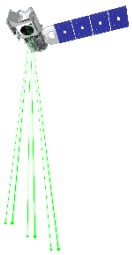
5.1. Summary and synthesis of principle findings

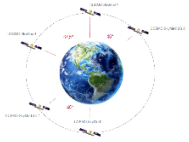
5.1.1. A new method to detect tidal GL migration with ICESat-2 (Chapter 2)

I developed a new method to measure short-term, tidal GL migration using ICESat-2 repeat-track laser altimetry (RTLA). This is the first study that has used ICESat-2 to measure tidal GL migration in Antarctica. The method locates Point F – the inland limit of tidal ice shelf flexure – from pairs of repeat measurements of surface elevation along any given ICESat-2 ground track that crosses the GL, using the lowest-sampled tide as a reference profile. This allows us to locate multiple positions of Point F along each ground track as it migrates with the tide, which enables a closer investigation of tidal processes acting in the GZ and seawater intrusions occurring over hourly to daily timescales.

This new ICESat-2 RTLA method complements DInSAR-based techniques for measuring tidal GL migration (e.g., Brancato et al., 2020; Chen et al., 2023; Ciracì et al., 2023; Milillo et al., 2017, 2019, 2022; Rignot, 2024), adding to the suite of tools that we can use to understand tidal GZ behaviour around the Antarctic Ice Sheet. It is particularly effective at identifying ice plains and characterising the tidal behaviour within these regions, as I have shown at the Bungenstockrücken ice plain (Chapter 2) and the newly ungrounded ice plain downstream of Engelhardt Subglacial Lake (Chapter 3). As with any remote-sensing method, however, it is subject to certain limitations and the most useful insights are to be made when combined with other satellite, airborne or in-situ measurements. Table 5.1 summarises the key advantages and limitations of the new ICESat-2 RTLA approach compared to DInSAR for measuring tidal GL migration, informed by the findings of this thesis.

Table 5.1. Advantages and limitations of ICESat-2 RTLA and DInSAR (and specifically short-repeat DInSAR) for monitoring tidal grounding zone processes.

Method	Advantages	Limitations
ICESat-2 RTLA 	Only includes vertical component of displacement Requires minimum of 2 repeat-tracks to identify Point F High along-track resolution (0.7 m) Coverage extends further south (<88 °S) Can detect ice plains that are difficult to capture from InSAR Computationally efficient	Provides information only in discrete locations along predefined tracks with a set orientation (may not be optimal in relation to GZ shape) Data loss in presence of clouds and blowing snow Surface roughness (e.g., crevassing) introduces noise 91-day repeat cycle leads to loss of coherence for RTLA in dynamic GZs or regions of long-term thickness change

DInSAR e.g., Sentinel-1, TerraSAR-X 	Continuous spatial coverage High spatial resolution (~ 30 m) Unaffected by clouds	The derived flexure pattern is a combination of multiple separate tidal states (greater ambiguity) Contributions from topography and horizontal movement may not be fully removed, introducing some ambiguity for interpretation. Requires a minimum of 3 SAR images with sufficiently short temporal baseline to ensure sufficient coherence (limited availability) Loss of coherence in dynamic GZs Large data volumes Sentinel-1 has large pole hole (no coverage south of ~78°S) and TerraSAR-X has to be tasked to observe the southernmost locations.
Short-repeat DInSAR e.g., COSMO-SkyMed (CSK), ICEYE 	Shorter interferometric baseline (up to sub-daily) makes it possible to maintain coherence over dynamic GZs (e.g., Rignot et al., 2024) Unprecedented spatial resolution (range resolution of 0.75 m for ICEYE and 2.1 m for CSK)	Commercial, paid-for data products limits its widespread use Large data volumes Even CSK can lose coherence on very dynamic regions (e.g., margins of Thwaites; Milillo et al., 2019)

A key point to emphasise is that the effective high temporal resolution of tidal GL migration measurements using ICESat-2 RTLA is only achievable in relatively stable GZs where the magnitude of the tidal signal is greater than any other cause of surface elevation change. In these regions, such as the Bungenstockrücken ice plain, we can confidently use repeat ICESat-2 measurements with a temporal baseline of as much as 3 years to locate Point F with respect to the tidal cycle. In more dynamic settings subject to long-term thinning, GL retreat or rapid advection of elevation gradients or crevasses, the ICESat-2 RTLA method can still be applied but may require sub-dividing the time-series into shorter subsections for defining the choice of reference profile (*detailed further in Section 5.1.5*). However, in settings where the long-term thinning rate is particularly high – such as Engelhardt Ice Ridge GL, where we observed over 10 m of thinning between 2019 and 2023 (Chapters 3 & 4; Figs. 3.5, 3.6, 4.13) – the ICESat-2 RTLA method cannot be used because the tidal signal is completely obscured. In this case, only ground-based GNSS measurements are likely to fully capture the variability in GL position.

5.1.2. The GL migrates by up to 15 km with the tide at two Antarctic ice plains (Chapters 2 & 3)

The new ICESat-2 RTLA methodology is particularly effective at identifying ice plains, which can be difficult using other methods (Fricker et al., 2009). Ice plains are regions of low surface slope near the GZ where the ice is close to hydrostatic equilibrium (Alley et al., 1989; Brunt et al., 2010, 2011; Corr et al., 2001). In Chapters 2 and 3 I applied this technique to two different ice plains, one on the Ronne Ice Shelf and one on the Ross Ice Shelf, and demonstrated its effectiveness at characterising tidal GZ behaviours within these regions.

I identified up to 15 km of tidal GL migration at the Bungenstockrücken ice plain on the Ronne Ice Shelf, mapping its 1300 km^2 zone of ephemeral grounding for the first time. At the time of publication, this was the largest distance of tidal GL migration observed anywhere in Antarctica (Chapter 2; Freer et al., 2023). Two studies have since revealed tidal GL migration distances of a similar order of magnitude at the Amery Ice Shelf (Chen et al., 2023) and Thwaites Glacier (Rignot et al., 2024). I subsequently

observed up to 13 km of tidal GL migration across the newly identified ice plain downstream of Engelhardt Subglacial Lake (Chapter 3; Freer et al., 2024). These observations contribute to a growing body of evidence that Antarctic GLs can migrate across the tide cycle by much larger distances than anticipated by hydrostatic equilibrium (Milillo et al., 2019; Rignot, 2023), and support the notion that there are 'estuaries' at the margins of the ice sheet (Horgan et al., 2013).

The implications of this are twofold. Firstly, it may affect our calculations of long-term GL migration based on sparsely sampled, individual GL measurements through time (e.g., Rignot et al., 2014) if they have been collected at different points in the tide cycle. Secondly, it shows that vigorous tidal seawater intrusions are reaching further beneath the ice sheet than previously thought, creating significant zones of vulnerability of the glaciers to direct ocean melt (Rignot, 2023). Model simulations predict that these kinds of seawater intrusions could double the estimated contribution of AIS to future sea-level rise (Parizek et al., 2013; Robel et al., 2022; Seroussi & Morlighem, 2018), yet tidal GL migration and melt is not included in most ice sheet models (Burgard et al., 2022). This is currently limited by a lack of direct evidence of the extent and spatial occurrence of these intrusions, and calls into question the use of fixed or slowly-moving GL boundary in ice sheet models (Milillo et al., 2019). The new ICESat-2 RTLA method presented in Chapter 2 offers a new way to address this across Antarctica into the future.

5.1.3. Four modes of tidal GL migration revealed with ICESat-2 (Chapter 2)

Using the ICESat-2 RTLA methodology I identified four distinct modes of tidal GL migration at the Bungenstockrücken ice plain: *linear, asymmetric, threshold* and *hysteresis* (Figs. 2.6, 5.2). This is the first time that we have had observations with high enough temporal resolution across the tide cycle to determine specific tidal GL migration modes, which can provide observational validation for numerical models of tidal ice flexure and GL migration.

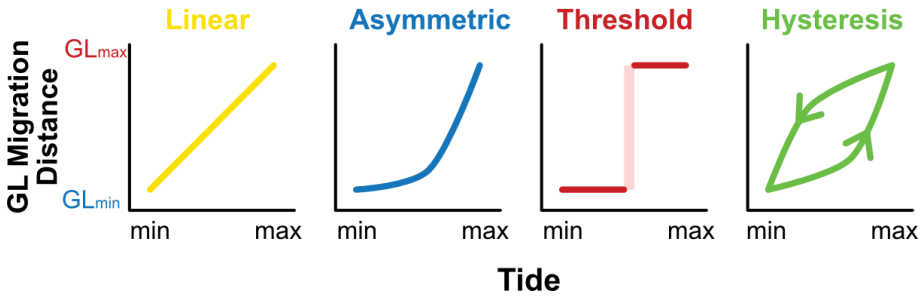


Figure 5.2. Schematic of the four modes of tidal GL migration identified from ICESat-2 RTLA measurements at the Bungenstockrücken ice plain (Chapter 2; Freer et al., 2023).

The classic view of tidal GL migration is that the GL position migrates in proportion to tidal forcing (i.e. in a *linear* migration mode, e.g., Sayag & Worster, 2013). Some recent modelling studies have predicted that tidal GL migration should be asymmetric, migrating further inland during high tides compared to its downstream migration during low tides (e.g., Tsai & Gudmundsson, 2015; Warburton et al., 2020; Zhong et al., 2023). The ICESat-2 data at Bungenstockrücken ice plain (Chapter 2) provide the first observational evidence of asymmetric tidal GL migration in Antarctica. Additionally, I presented the first evidence of the newly-defined threshold and hysteresis modes of tidal GL migration, which can be used to understand tidal GZ processes elsewhere in Antarctica. For example, the recent observations of seawater intrusions out of phase with the tide at Amery Ice Shelf (Chen et al., 2023) and Thwaites Glacier (Rignot et al., 2024) may provide further evidence of hysteresis mode of tidal GL migration, related to the entrapment of water within bedrock cavities (as proposed in Chapter 2: Fig. 2.7 and Rignot et al., 2024) or resistance to flow through subglacial

sediments during the falling tide phase (Warburton et al., 2020). Furthermore, I used the idea of a threshold mode of tidal GL migration to explain the observed temporal evolution of the wave-like surface feature (WSF) at the retreating GL of Engelhardt Ice Ridge (Chapter 4).

Given that the mechanism of migration varies spatially, obtaining reliable observations of the spatial distribution of these GL migration modes around Antarctica is needed to inform the parameterisation of GL processes in larger ice sheet modelling studies (e.g., Mosbeux et al., 2023). It could also be useful to inform understanding of the formation of the corrugation ridges or ribs observed in the palaeo sediment record, thought to be the sequential imprints of tidal GL migration during a rapid periods of GL retreat (e.g., Batchelor et al., 2023; Graham et al., 2022). I have successfully demonstrated how ICESat-2 RTLA, alongside the newly-classified migration modes, can be used to achieve this.

5.1.4. A 21-year record of subglacial lake activity at Engelhardt Subglacial Lake (Chapter 3)

In 2023 I discovered a second drainage of Engelhardt Subglacial Lake (SLE) on the Gould Coast, West Antarctica. I used ICESat-2 altimetry to document this drainage, which occurred between July 2021 and at least April 2024, discharging an estimated ~2.3 km^3 of subglacial water into the Ross Ice Shelf cavity. By extending this record with CryoSat-2 radar altimetry and ICESat laser altimetry (Fig. 3.2) I compiled a 21-year time series of the fill-and-drain activity of SLE (Fig. 3.3), building on previous assessments (Fricker et al., 2007; Siegfried & Fricker, 2018). This captured the drainage in 2003–06, the subsequent 15-year refilling period, and the onset of the second drainage in 2021. This is the longest observed interval between successive drainages of the same subglacial lake in Antarctica. Moreover, the higher spatial and temporal density of ICESat-2 measurements enabled the delineation of a more accurate lake boundary and the identification of a newly-identified upstream feeder lake (Figs. 3.3, 3.4). This upstream lake drained sharply between September 2020 and July 2021, most likely discharging water directly into SLE, which we propose was the trigger for the onset of drainage at SLE.

5.1.5. 13 km of GL retreat and the ungrounding of an ice plain downstream of Engelhardt Subglacial Lake (Chapter 3)

I presented evidence of significant long-term GL migration downstream of SLE using a combination of ICESat-2 laser altimetry, TerraSAR-X DInSAR and REMA digital elevation model strips. This revealed that the GL along the Engelhardt Ice Ridge retreated by 2–3 km between 2009 and 2023, continuing a pattern of retreat observed here since at least 1963 (Bindschadler & Vornberger, 1998; Fricker et al., 2007). The GL in the west embayment retreated by ~13 km over the same period into a region previously identified as a grounded ice plain (Brunt et al., 2010), which had thinned by ~0.5–2 m between 2019 and 2024 (Fig. 3.6). The first evidence of this ice plain ungrounding and GL retreat was observed using the new ICESat-2 RTLA approach (Chapter 2), which I had to adapt to separate the signals of tidal flexure from long-term thinning (Figs. 3.8, 3.9). This was achieved by subdividing the ICESat-2 time series into shorter periods to keep the temporal baseline within one year between each repeat cycle and the reference cycle (Fig. 5.3).

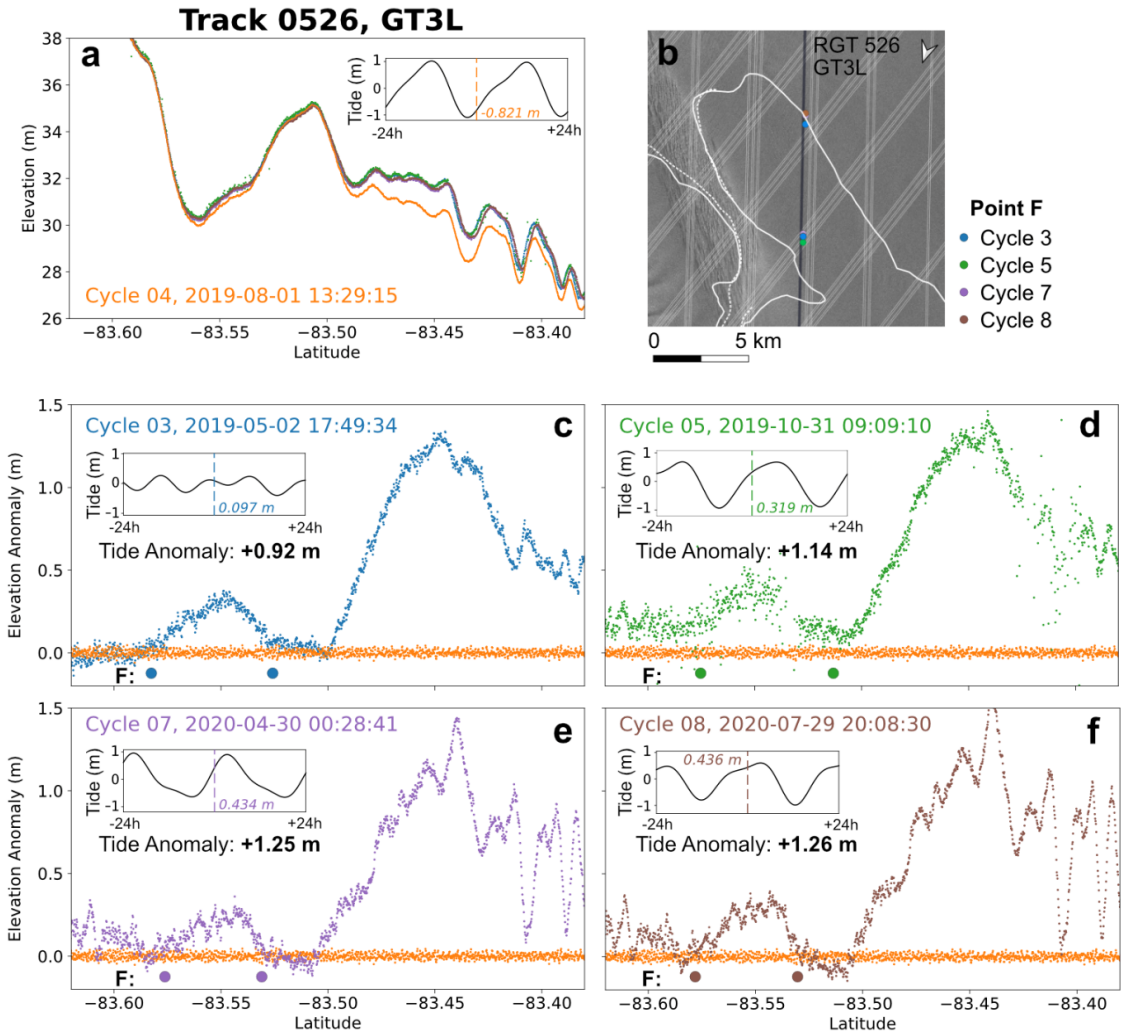


Figure 5.3. Evidence from the ICESat-2 record of tidal flexure (i.e., ungrounding) across the ice plain downstream of SLE from at least May 2019 onwards. (a) ICESat-2 ATL06 repeat elevation profiles along RGT 526 GT3L for cycles 3, 4, 5, 7 and 8. Cycle 4 was sampled at the lowest tide, so is used as the reference elevation profile for calculating anomalies in (c–f). Inset plot shows the CATS2008 modelled tide height during the period 24 h before and after cycle 4 was sampled (Howard et al., 2019). (b) Location of ICESat-2 RGT 526 GT3L across the newly ungrounded section of the West Embayment, downstream of Engelhardt Subglacial Lake, with the TerraSAR-X derived GLs from July and October 2023 (dashed and solid white lines) and the ICESat-2-derived Point F positions (coloured circles). (c–f) ICESat-2 ATL06 elevation anomalies along RGT 526 GT3L for cycles 3, 5, 7 and 8, calculated against the reference profile from the low tide surface elevation profile (cycle 4). Derived Point F positions are shown with coloured circles along the *x*-axis.

Having used ICESat-2 RTLA to confirm that there was consistent tidal flexure and ungrounding within the ice plain from at least 2019 onwards (Fig. 5.3), I was able to task a series of TerraSAR-X acquisitions between June and October 2023 to get a more complete picture of the newly ungrounded ice plain (Fig. 3.8; 5.4). I note here that SLE is further south than most regular DInSAR coverage, and so has only been imaged during specific campaigns. By compiling all available satellite observations over the ice plain from ICESat-2 (2019–2023) and DInSAR (at specific time stamps in 2009, 2012, 2016 and 2023; Fig. 3.8), I inferred that long-term thinning (Fig. 3.6d) caused the ice plain to unground between 2009 and 2023 following the ice plain life cycle of Brunt et al. (2011). A gradual reduction in ephemeral grounding over time due to ice thinning has been observed before (Schmeltz et al., 2001), but this is the first time we have actively observed the transition of the same ice plain through these distinct life-cycle stages, from 'lightly grounded' (Fig. 5.4a, d), to 'ephemeral grounding' (Fig. 5.4b, e) to 'relict ice plain' (i.e. fully floating; Fig. 5.4c, f). ICESat-2 RTLA results show this region experiences tidal GL migration (Fig. 3.9), with the floating region widening and deepening at higher tides, but it remains an open question whether the ice plain re-grounds at low tide. Determining this would require improved temporal sampling of the surface during low tidal states, either from DInSAR (Zhong et al., 2023) or ICESat-2.

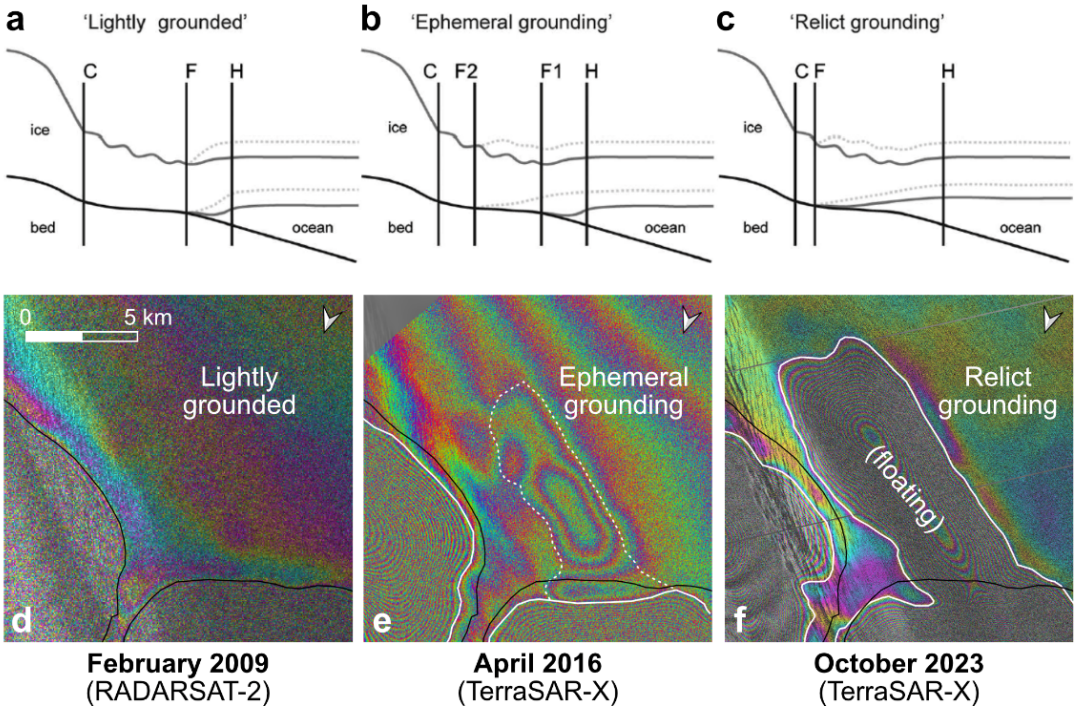


Figure 5.4. The schematic life cycle of an ice plain at low and high (dashed line) tide (reproduced from Brunt et al., 2011) compared to DInSAR observation showing a similar evolution of the ice plain downstream of Engelhardt Subglacial Lake. (a) An ice plain where the regions between Points F and C (the coupling line/first break-in-slope, I_b) is 'lightly grounded; (b) an ice plain experiencing 'ephemeral grounding', where Point F migrates between positions F1 and F2 depending on the tide; (c) a 'relict' ice plain, where the ice downstream of Point F has recently become fully floating but the surface has not yet fully conformed to flotation. (d) RADARSAT-2 DInSAR from February 2009 (solid black line = Point F shown by solid black line); (e) TerraSAR-X DInSAR from April 2016 showing signals of ephemeral grounding (solid white line = Point F1; dashed line = Point F2); (f) TerraSAR-X DInSAR from October 2023 (solid white line = Point F). Information about DInSAR processing is given in Table 3.1.

5.1.6. Revisiting the interaction between subglacial lake drainage and GL migration (Chapters 3 & 4)

Direct observations of subglacial hydrology close to the GZ are extremely rare (Siegfried & Fricker, 2021; Siegfried et al., 2023). Therefore, the 2021–24 drainage of Engelhardt Subglacial Lake (SLE) – one of the only active subglacial lakes in Antarctica located within 10 km of the GL (Siegfried & Fricker, 2018) – provided a unique opportunity to examine the interactions between subglacial hydrology and GL migration. Following its last drainage in 2003–06, it remained an open question whether GL retreat had triggered the drainage or vice versa (Fricker & Scambos, 2009). The new high-resolution satellite observations made over SLE and its downstream GL before and during the 2021–24 drainage event allowed us to revisit this question, and led us to conclude that the lake drainage and GL retreat were largely independent processes. GL retreat in the east embayment was primarily driven by the long-term retreat of Engelhardt Ice Ridge (Bindschadler & Vornberger, 1998; Fricker et al., 2007). In contrast, GL retreat in the west embayment resulted from long-term dynamic ice thinning that caused the lightly grounded ice plain to reach flotation. This ungrounding occurred between 2016 and 2019, at least two years before the onset of SLE drainage.

Later in the thesis, I re-examined the temporal evolution of the wave-like surface feature (WSF) at the base of the retreating Engelhardt Ice Ridge in further detail, and identified a sudden shift in its position and wavelength between October 2021 and April 2022 (Chapter 4; Fig. 4.13). Given that this occurred shortly after the onset of SLE drainage in July 2021, it once more raised the question of whether the GL retreat here was affected by SLE drainage, perhaps via a sudden change in in basal melt or basal friction. However, there is still not enough evidence from the satellite record alone to confirm this.

5.1.7. Evidence of subglacial bed form detected from satellite imagery (Chapter 3)

Using the 2009–2023 DInSAR time series over the GZ downstream of SLE, I observed a migration and lengthening of the central grounded promontory that separates the east and west embayments (Chapter 3; Fig. 3.10). This feature is located in a region of localised ice thickening (Fig. 3.6d), and I interpreted this as a signal that the ice here has become more grounded over time on a ridge-like subglacial bed feature – possibly an ice-stream lateral shear moraine (ISLM), esker, or a fault-controlled structure. If any of these interpretations are correct, it would represent the first satellite-derived evidence of such subglacial bed features in Antarctica. However, we cannot confirm its origin without drilling into the substrate. An airborne radar survey over this feature indicates the presence of a bump in the bed topography, but this interpretation is compromised by the high radar attenuation caused by the extensive surface crevassing along this part of the profile (Fig. 5.5; CReSIS, 2024).

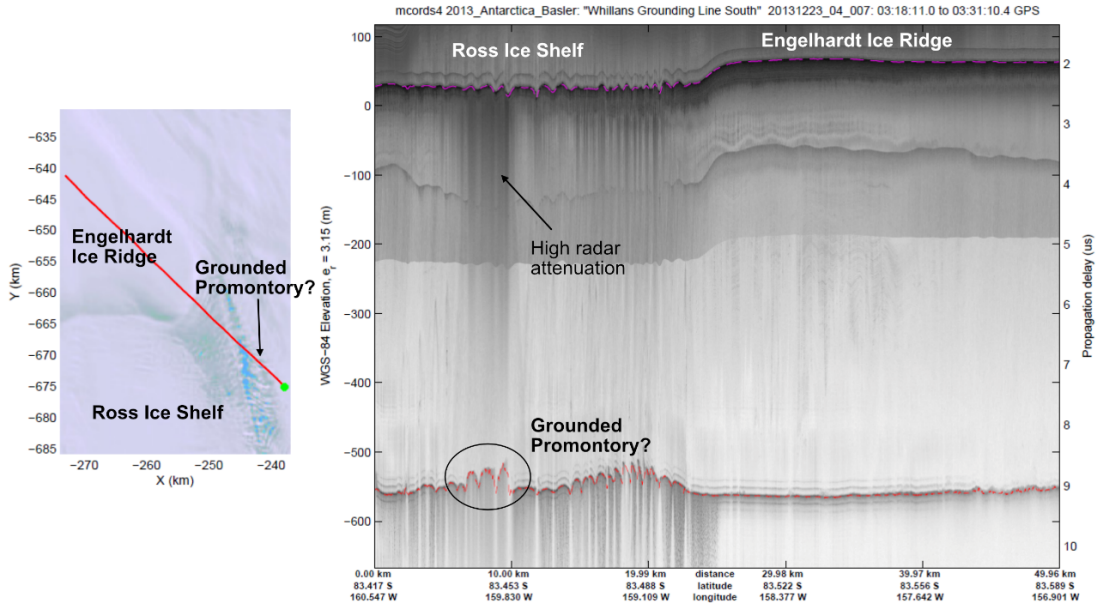


Figure 5.5. Airborne radar-depth sounding profile across the Engelhardt Ice Ridge (CReSIS, 2024), showing possible evidence of a subglacial bed ridge at the location of the grounded promontory observed in the DInSAR record. Pink and red dashed lines mark the automatic picks of the surface and bed elevations from the radar profiles.

5.1.8. First large-scale study of wave-like surface features at Antarctic GZs (Chapter 4)

Wave-like surface features (WSFs) form at the GL as a result of the basal stress transition between the grounded ice sheet and floating ice shelf (Schoof, 2011). They have been resolved in Full Stokes ice sheet models of the GL yet remain largely undocumented in the observational record around the Antarctic Ice Sheet. I observed WSFs in many of the satellite altimetry and DEM observations in Chapters 2 and 3, both at the Bungenstockrücken ice plain (Figs. 2.2c–e, 2.4b, d, 2.7d) and downstream of SLE (Figs. 3.6c, d). I subsequently conducted the first large-scale study of these features in Antarctica, recording WSF location, amplitude, and wavelength around the entire Ross Ice Shelf GL (Chapter 4).

Using surface elevations from the REMA digital elevation model and ICESat-2, this revealed that WSFs exist at seven Trans-Antarctic outlet glaciers and three Siple Coast ice streams. The most prominent WSF was observed at the GL of the Mulock Glacier, with a mean amplitude of 14.3 ± 5.7 m and wavelength of 3.4 ± 0.8 km, and the most continuous WSF is found at the Kamb Ice Stream, where it extends along ~70% of the GL. There was a notable absence of WSFs along the fast-flowing trunks of the Siple Coast ice streams, where we suggested the smoother basal stress transition between the streaming ice and ice shelf may have limited WSF formation (Hindmarsh, 1993; Whillans et al., 2001). The discontinuous WSFs at certain Trans-Antarctic glaciers are likely to be largely influenced by additional 2D factors, specifically the lateral stresses due to the topographical confinement of the ice, the more undulating bed topography, and the sinuosity of the GL in relation to ice flow direction (Horgan and Anandakrishnan, 2006; Mayer and Huybrechts, 1999; Rabus and Lang, 2002; Wild et al., 2017).

5.1.9. Inferring basal drag and ice viscosity from the geometry of wave-like surface features in Antarctic GZs (Chapter 4)

Basal drag and ice viscosity are poorly known around Antarctica and difficult to directly measure (Barnes & Gudmundsson, 2022). I presented a new integrated modelling and observational approach, that combines satellite observations of WSFs with the viscous "beam" model of Schoof (2011) to calculate the ratio of basal drag to ice viscosity across different Ross Ice Shelf glaciers and ice streams (Chapter 4; Fig. 4.8). The results predicted the highest drag to viscosity ratios for the larger Trans-Antarctic glaciers, where the most prominent WSFs are observed, while lower ratios are predicted for all Siple Coast ice streams (Fig. 4.8). These predictions align with our expectations: higher drag is anticipated at the Trans-Antarctic glaciers that flow over hard bedrock, compared to the till-deformation driven flow of the Siple Coast ice streams (Truffer & Echelmeyer, 2003; Arthern et al., 2015).

Whilst it was not possible to precisely quantify values of basal drag and ice viscosity, this proof-of-concept study successfully bridges the gap between high-level theoretical modelling and satellite observations, demonstrating that such an integrated approach can yield valuable insights into ice sheet and GZ properties that are otherwise poorly constrained.

5.1.10. An independent method to locate the GL that best represents the basal stress transition (Chapter 4)

The location of basal stress transition at the GL between grounded and floating ice is a critical boundary condition for large-scale ice sheet models (Durand et al., 2009; Gladstone et al., 2012; Schoof, 2007). Current approaches for determining the GL from satellite observations – using either hydrostatic, tidal or surface slope techniques (Sect. 1.2) – often fail to accurately locate this stress boundary due to the effects of tidal GL migration, complex surface or basal topography, or crevassing near the break-in-slope (Friedl et al., 2020).

I presented a novel approach to locate the basal stress transition by combining satellite observations of wave-like surface features (WSFs) with the dimensionless surface profile from a viscous beam model (Schoof, 2011). The modelled GL, located consistently ~half a wavelength upstream of the WSF depression (Fig. 4.6), should correspond to the upstream limit of tidal GL migration, where the rapid reduction in vertical velocity induces the viscous relaxation of the ice surface, forming a WSF (Schoof, 2011). When applied to different GZs of the Ross Ice Shelf (Fig. 4.9), the modelled GL was mostly located upstream and within 2 km of the DInSAR GL. Any deviations are likely to arise from the flexure-derived DInSAR GL sampling Point F at non-maximum tides. These findings align with observations at the Bungenstockrücken ice plain (Chapter 2), where Point F was found to consistently migrate as far inland as the WSF break-in-slope at high tide (Fig. 2.4).

This method could feasibly be applied at any GZ in Antarctica with a WSF. As it requires just a single elevation profile and is independent from any other physical parameters, it overcomes the limitations of many other GZ proxies, such as the loss of DInSAR or ICESat-2 RTLA coherence over very dynamic GZs.

5.1.11. Improving ice thickness estimates in Antarctic GZs (Chapter 4)

Satellite-derived estimates of ice thickness and basal melt rate within Antarctic GZs are highly uncertain – especially where WSFs are present – due to the deviation of the ice from hydrostatic equilibrium (Chartrand & Howat, 2023; Chuter & Bamber, 2015; Griggs & Bamber, 2011; Jenkins et al., 2006; Kim et al., 2024; Milillo et al., 2019). Consequently, these regions are often masked out (e.g., Griggs & Bamber, 2011; Paolo et al., 2015; Wilson et al., 2017) or interpolated across (e.g., Fretwell et al., 2013; Morlighem et al., 2020). In Chapter 4, I demonstrated with examples from the Mulock and Kamb GZs that integrating a viscous beam model (Schoof, 2011) with satellite observations of WSFs can reduce errors in hydrostatic ice thickness estimates to within 2% (Figs. 4.11, 4.12), validated against airborne RDS measurements (Paden et al., 2010; Wang et al., 2016).

By mapping the location of WSFs around the Ross Ice Shelf (Fig. 4.6) I have identified regions where satellite-derived estimates of ice thickness and basal melt are likely to be most erroneous, and therefore where this method should be best applied to make improvements. This is critical, given that limited knowledge of ice thickness leads to large uncertainties both ice discharge estimates, which affects assessments of ice sheet mass balance (e.g., Otosaka et al., 2023), and ice-sheet model projections of future ice sheet dynamics and sea level rise (Arthern & Williams, 2017; Goldberg et al., 2019).

5.2. Uncertainty Evaluation

Here I discuss the key sources of uncertainty associated with the datasets and methods used in this thesis, the extent to which these uncertainties affect the results, the strategies employed to mitigate them, and suggestions for deeper uncertainty analyses in future work. I focus primarily on uncertainties in the ICESat-2 datasets and methodologies, but also discuss uncertainties related to deriving GL positions from DInSAR and measuring GL retreat and WSF dimensions using the REMA digital elevation model.

5.2.1. ICESat-2 Datasets and Methods

The primary ICESat-2 datasets used in this work are the L3A along-track land ice height product (ATL06) and the L3B gridded land ice height change product (ATL15). These datasets have been used in various analyses throughout this work:

- **ATL06:** Used in the development of the RTLA methodology (Chapter 2), which is subsequently used to measure tidal GL migration at two Antarctic GZs (Chapters 2 & 3). It is also used to measure the surface height change during SLE drainage (Chapter 3), and the long-term GL retreat and WSF evolution at Engelhardt Ice Ridge (Chapters 3 & 4).
- **ATL15:** Used to assess long-term surface elevation change across the Gould Coast region from 2019–24 and to delineate the boundary and drainage rates during the 2021–24 SLE lake drainage event (Chapter 3).

5.2.1.1. ATL06 Dataset

The ICESat-2 ATLAS land ice elevation products are subject to errors from various sources including: (1) background noise; (2) sampling errors; (3) complex topography; (4) misidentified photon events; (5) first-photon bias (FPB; inherent to photon-counting detectors); (6) vertical geolocation errors; (7) atmospheric forward scattering; and (8) subsurface scattering (Smith et al., 2022). During the ATL06 processing, errors from 1 and 2 (above) are treated as random and are quantified in the product's error estimates; 3 and 4 can be addressed with consistency checks; 5 and 6 are corrected during the ATL06 processing; and 7 and 8 remain unquantified (this remains a future avenue of research). Uncertainty information is provided in the ATL06 data product as:

(i) *ATL06_quality_summary*, a flag indicating the quality of each data segment (0 = high quality, 1 = potential issues e.g. from cloud cover, background photon clustering or blowing snow).
(ii) *h_li_sigma*, the propagated sampling and FPB error.
(iii) *sigma_geo_h*, the vertical geolocation error.

In this work, only segments flagged as high quality (*ATL06_quality_summary = 0*) were used, ensuring the use of only the most reliable data. Additionally, segments without valid across-track-slope measurements or where the minimum segment difference exceeded 1 m were excluded. The magnitude of errors *h_li_sigma* and *sigma_geo_h* were generally found to be less than 1 cm, occasionally increasing to up to 5 cm along certain ground tracks in more complex topography.

5.2.1.2. ATL06 Methods: RTLA

The ATL06 errors described above, which were found to constitute < 1% of the observed tidal flexure signal, were not directly accounted for in the RTLA methodology (Chapter 2). However, these errors were largely averaged out when the B-spline was fitted to each elevation profile (Section 2.3.2.2.). The RTLA methodology itself introduces additional uncertainties in the final derived Point F positions, which are used to assess

tidal GL migration. These uncertainties will arise predominantly from the spline fitting process and the automated method for locating Point F using the 2nd derivative of the elevation anomaly. While these uncertainties have not been explicitly accounted for in this work (due to the difficulty of quantifying them in a statistical way), three key areas could benefit from deeper uncertainty analysis in future:

- **B-spline Approximation:** The error information provided in the ATL06 data is retained throughout all RTLA processing steps, allowing for the possibility of propagating these uncertainties through the spline fitting process. This would provide an estimate of the uncertainty of the spline itself. Additionally, weighting the B-spline based on the error estimates of individual data points could minimise the impact of less reliable points, leading to a more accurate final spline.
- **Locating Point F:** To assess the impact of spline fitting on derived Point F positions for each repeat pass, a sensitivity analysis could be conducted using Monte Carlo simulations or bootstrap approaches. These methods would simulate a range of possible spline fits, within the error bounds of the original data and using a range of smoothing parameters, and feed them into the automated algorithm that identifies the peak of the 2nd derivative. This analysis would help quantify the horizontal uncertainty in the resulting Point F position per sampled tide, improving confidence in the subsequent classification of tidal migration modes.
- **Classifying Tidal GL Migration Modes:** The classification of tidal migration modes (Chapter 2) was done visually, using a non-automated approach. As a result, the associated uncertainty has not been quantified statistically. This is partly due to the limited number of derived Point F positions along each ground track during the ICESat-2 acquisition period (typically fewer than 10) that can be used to classify the different modes. As more data becomes available, it will be possible to more robustly assess the uncertainty associated with each mode classification, especially if the aforementioned assessment of Point F horizontal uncertainty is accounted for.

5.2.1.3. ATL06 Methods: Crossover Zone Analysis

To quantify uncertainties in the surface elevation time series at Engelhardt Subglacial Lake (SLE; Chapter 3), I calculated the standard deviation of elevation values within each crossover zone (CZ) were calculated for each of the ICESat GLAH06, CryoSat-2, and ICESat-2 ATL06 datasets (Figs. 3.2 and 3.3). The standard deviations were generally small relative to the magnitude of surface elevation change signal caused by the fill-and-drain of the SLE (typically <0.5 m for most ICESat and ICESat-2 data, and <2 m for most CryoSat-2 data). These uncertainties were presented with all reported surface elevation change values cited in Chapter 3.

Furthermore, prior to generating the elevation change time-series', I tested for significant variations in elevation change rates within each ~3 km3 CZ. No statistically significant variation was found, indicating that using a CZ of this size was appropriate for capturing the lake drainage signal. However, to address this more robustly in future (particularly over more topographically varied regions), it should be possible to correct the elevations within each CZ onto a flat plane using a DEM surface such as REMA (Howat et al., 2019). Additionally, comparing CryoSat-2 and ICESat-2 surface elevations within each CZ during overlapping time periods help cross-validate the datasets (e.g. MacMillan et al., 2013). The differences between measured elevations could reveal insights into the additional penetration of CryoSat-2 radar through the snowpack.

5.2.1.4. ATL15 Dataset

Errors from lower-level ICESat-2 products (ATL03 and ATL06) are propagated to higher-level products (ATL11 and ATL15). When data is gridded in the ATL15 product, additional uncertainties arise from the spatial resolution of the ICESat-2 ground tracks (which varies with latitude, becoming denser further south), the temporal sampling of these tracks, and the grid resolution (1 km).

In ATL15, the uncertainty in gridded height differences per pixel is provided by the *delta_h_sigma* variable (Smith et al., 2024). For the Gould Coast study region, the median uncertainty in the total elevation change between April 2019 and January 2024 was ~0.02

m, with the highest uncertainties reaching ~0.06 m. The spatial distribution of these uncertainties (Fig. S3.1) shows a concentration in floating ice shelf areas, particularly downstream of the SLE GZ. This is likely due to the challenges in accurately correcting for vertical tidal motion in these regions during the gridding process (Smith et al., 2024).

5.2.1.5. ATL15 Methods: Calculating Subglacial Lake Drainage Rate

Given that the uncertainties in ATL15 represent a very small percentage of the total elevation change observed during SLE drainage (several metres), they were not directly incorporated into the uncertainty calculations presented in Chapter 3. However, the spatial uncertainty of the measured cumulative surface elevation change (Fig. 3.4) was quantified by calculating both the standard deviation and interquartile range of elevation change values across all ATL15 pixels within the SLE lake boundary during the drainage period (Fig. 3.4t).

To enhance the uncertainty assessment using ATL15 data, a cross-validation with CryoSat-2 data could be conducted. This would require a consideration of the different scattering responses of the radar vs laser altimeters. Additionally, the measured rates of surface elevation change from ATL15 during subglacial lake drainage could be validated over shorter time periods against surface deformation observed by DInSAR, assuming overlapping temporal coverage is available. If DInSAR data were available for the entire lake area, it could provide an additional measure of the lake volume drainage rate.

5.2.2. Deriving DInSAR Grounding Lines

The primary sources of error in the DInSAR data used to derive GL positions (Chapter 3) include the following:

- **Geolocation Errors:** These errors can occur when there are discrepancies between the surface heights at the time of DInSAR acquisition and those in the reference DEM, in this case, BedMap2 (Fretwell et al., 2013). The sensitivity of these errors depends on the satellite's look angle. For TerraSAR-X, with a look angle of approx. 45°, a 1 m elevation difference relative to the

reference DEM would translate to a 1 m horizontal geolocation offset. Even when considering above-average long-term elevation changes near the Whillans Ice Plain GZ, the impact on the derived GL positions is minimal, thus exerting a negligible effect on the assessment of long-term GL migration.

- **Tidally-Induced Horizontal Velocity Variations:** These cannot be separated from vertical movement, and may incorrectly suggest flotation in some regions because of short-term velocity change. However, the magnitude of this error will have minimal impact on the derived GLs from the 2023 DInSAR images where the GL retreat signal was very clear. Quantifying this could help to infer the flotation state of the 2016 DInSAR, where the flotation signal was weaker (Fig. 3.8c).

These process uncertainties are challenging to quantify, which limits our ability to statistically propagate these errors into the resulting GL position estimates. Previous studies deriving DInSAR GLs have (somewhat arbitrarily) cited a constant ±100 m horizontal error in GL position as a general estimate (e.g. Rignot et al., 2011). If we took this same approach, these errors would still represent <5% of the total GL retreat distance observed at SLE, thus exerting minimal impact on the final results.

5.2.3. Measuring Grounding Line Retreat and WSF Dimensions with the REMA Digital Elevation Model

The REMA DEM has been undergone extensive quality control to remove erroneous surface signals caused by clouds and shadows in the optical imagery, rough terrain and crevassing (Howat et al., 2019). The residual elevation errors, after registration with altimetry data, mostly less than 1 m on along the Gould/Siple Coast (Chapters 3 & 4) and slightly higher (up to 3 m) along the Trans-Antarctic margin (Chapter 4) due to the rougher topography (Figure 5.6). However, relative (point-to-point) errors in the DEM are on the order of decimetres. A more detailed discussion of these uncertainties can be found in Howat et al. (2019).

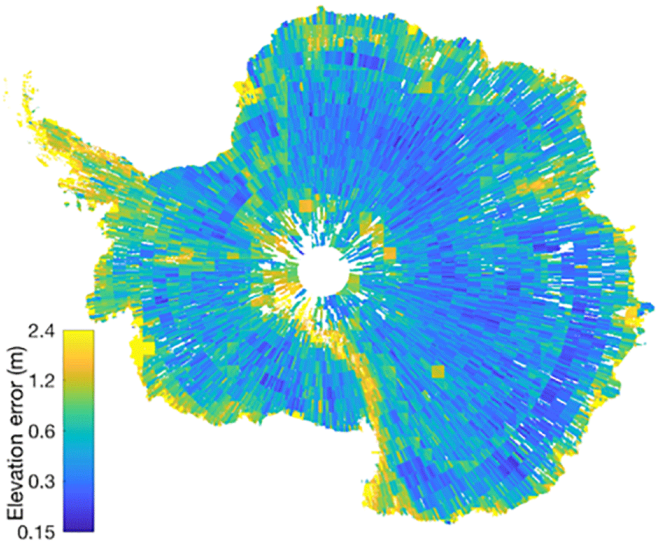


Figure 5.6. REMA elevation error, obtained from the root mean square of the differences in elevation between the DEM and altimetry data following registration, or the differences among co-registered DEMs in the case of alignment. Note the logarithmic colour scale. Figure reproduced from Howat et al., (2019).

These uncertainties were not directly quantified when assessing WSF dimensions (Chapter 4). A more comprehensive uncertainty analysis could be conducted in future using Monte Carlo simulations or bootstrap analysis. Such approaches could simulate a range of elevation profiles within the REMA uncertainty bounds, allowing a sensitivity test on the resulting calculation of WSF wavelength and amplitude.

For assessing the retreat rate of Engelhardt Ridge using time-stamped REMA DEM strips alongside repeat ICESat and ICESat-2 profiles (Chapter 3), manual co-registration was required. Unlike the DEM mosaic (used in Chapter 4), the timestamped strip DEMs are not vertically registered to satellite altimetry, leading to greater uncertainty in absolute elevations. To overcome this, each elevation profile sampled from a strip DEM was manually adjusted to align with the closest ICESat-2 elevation profile at the top of the ridge. While this approach likely introduced some additional uncertainty in the horizontal position of the ridge (used to estimate GL retreat rates), this has not been explicitly quantified. Nonetheless, this uncertainty is not expected to have significantly impacted the derived ridge retreat rates.

5.3. Recommendations for future work

Several future research avenues have emerged from this thesis. Firstly, I consider the how we could scale-up our assessments of both the spatial extent and modes of tidal GL migration around Antarctica, using a combination of satellite datasets. Additionally, I propose a continent-wide assessment of the spatial and temporal distribution of wave-like surface features at Antarctic GZs and explore how this could be used to inform basal sliding parameterisations in ice sheet models. Next, I suggest some *in situ* measurement campaigns that could complement and validate satellite measurements of the GZ. Finally, I look to future satellite missions and explore how these could contribute to advances in our understanding of GZ processes.

5.3.1. Antarctic-wide assessment of the spatial extent of tidal GL migration

I demonstrated that ICESat-2 RTLA can be used to measure tidal GL migration (Chapter 2). Having successfully implemented this technique at the Bungenstockrücken and SLE ice plains, a valuable next step would be to scale up this analysis across Antarctica. The ultimate goal would be to derive a comprehensive ice-sheet-wide dataset of the extent of tidal GL migration. Such a dataset could be used to: (i) enhance confidence in long-term records of GL migration, (ii) deepen our understanding of the magnitude and significance of tidal seawater intrusions around Antarctica, and (iii) inform ice sheet model projections that currently do not include these critical processes.

I envisage that any future pan-Antarctic dataset of tidal GL migration would need to be compiled using a combination of satellite datasets, and integrated with airborne radar data (e.g., RINGS Action Group, 2022). The ICESat-2 RTLA method developed in this thesis would be pivotal to achieve this, particularly for measuring the southernmost ice shelves and regions with ice plains. In more dynamic regions like Thwaites Glacier, the only method currently capable of resolving tidal GL migration is short-repeat DInSAR using data from the ICEYE and COSMO-SkyMed constellations (Brancato et al., 2020; Chen et al., 2023; Milillo et al., 2019, 2022; Rignot et al., 2024). This data is not currently open-access, hindering ice-sheet wide application, and is limited by its sampling of the lowest tides (Zhong et al., 2023).

A crucial first step would be to compare observations of tidal GL migration from short-repeat DInSAR vs. ICESat-2 RTLA, to ensure compatibility of data between satellite sources. This comparison would be most suitable in a region where the tidal signal can be isolated from long-term changes, such as Bungenstockrücken ice plain. However, this approach is contingent on the ability to task and acquire short-repeat DInSAR over the selected region.

Efficient processing and analysis of the vast quantities of satellite and airborne data required for this endeavour could benefit from the application of Artificial Intelligence (AI) methods. For example, scaling up the automated ICESat-2 RTLA approach could leverage syntactic pattern recognition techniques, using inputs of modelled tide height (e.g., Howard et al., 2019) and repeat ICESat-2 surface measurements. Recurrent or convolutional neural networks (LeCun et al., 2015) could be used to distinguish short-term tide-forced fluctuations of ice shelf height from longer-term surface elevation trends, a key challenge identified in Chapters 3 and 4.

5.3.2. Antarctic-wide assessment of tidal GL migration modes

ICESat-2 RTLA is currently the only satellite method capable of identifying specific *modes* of migration, as detailed in Chapter 2. This is difficult to achieve with other methods, including short-repeat DInSAR, due to the ambiguity associated with combining three or four sampled tides within each DInSAR scene. It would therefore be a promising avenue for future research to scale up our classification of tidal GL migration modes across all Antarctic ice shelves with valid ICESat-2 measurements. Scaling this up continent-wide, or at least on all ice shelves where there are valid ICESat-2 measurements, would be a useful avenue of future research. Such an effort would enhance our understanding of the spatial variability of tidal GL behaviour, and could also inform model parameterisations (e.g., Mosbeux et al., 2023).

Since the analysis presented in Chapter 2 (Freer et al., 2023), an additional two years of ICESat-2 observations have been acquired. Incorporating a longer time period of observations could significantly improve our confidence in the classification of different migration modes, particularly by increasing the range of tidal states sampled.

Ideally, this would include observations of both the lowest and highest tides, as well as a range of rising and falling tide phases (e.g., Zhong et al., 2023).

It is likely that there are other tidal migration modes or behaviours that remain unobserved. At Bungenstockrücken the hysteresis mode was observed over the semi-diurnal tide cycle (hours to days). However, more recent studies suggest the possibility of longer timescales of asymmetric intrusions and extrusions, potentially related to the longer spring-neap tide cycles or subglacial hydrology (Chen et al., 2023; Rignot et al., 2024). Further ICESat-2 observations could investigate these phenomena in greater detail, potentially leading to the identification and definition of new modes of tidal GL migration.

5.3.3. Antarctic-wide assessment of wave-like surface features in GZs

The spatial distribution and temporal evolution of wave-like surface features (WSFs) across Antarctic GZs remain largely undocumented. The research presented in Chapter 4 offered the first comprehensive assessment of these features around the Ross Ice Shelf. Expanding this analysis to the entire Antarctic Ice Sheet would be a valuable next step. The REMA DEM mosaic (Howat et al., 2019) provides complete surface elevation coverage of the whole ice sheet including the ice shelves, facilitating a circum-Antarctic assessment of the spatial distribution and geometry of WSFs using the same methodology. Then, by applying viscous beam theory (Schoof, 2011) to these observations (Chapter 4), we could improve estimates of GL position, ice thickness and basal slope within all Antarctic GZs where WSFs are present. Developing the Schoof (2011) model further into two dimensions would be extremely valuable and improve its application to satellite observations. To measure the temporal evolution of WSFs continent-wide, we could apply the methods of Chapter 4 either to time-stamped REMA DEM strips or repeat measurements along ICESat/ICESat-2 ground tracks crossing the GL at appropriate orientations (e.g., Fig. 4.13). This could provide early-warnings of GL retreat in regions where it is difficult to locate the GL at regular intervals with other techniques.

5.3.4. Deriving further basal information from observations of wave-like surface features

The exact mechanism of contact and sliding between the ice and the underlying material is not known from observational data, and so ice sheet models use a wide range of sliding laws that express basal drag in terms of the basal velocity and/or effective pressure (Barnes & Gudmundsson, 2022). The Weertman (1957) sliding law is widely used in modelling, and is a power law of the form

$$v_b = C\tau_b^m \tag{5.1}$$

where τ_b is the basal drag, C is a sliding parameter, v_b is the basal velocity and m is the sliding exponent.

Alternatively, Coulomb's law of solid friction is a sliding law that depends instead on effective pressure, taking the form

$$\tau_b = \mu_k N \tag{5.2}$$

where μ_k is a coefficient of friction and N is the effective pressure.

Marine Ice Sheet Model Intercomparison Project (MISMIP) experiments close to the GL using the Full Stokes Elmer/Ice model (Pattyn et al., 2012) indicate the use of different sliding laws significantly affects the pattern of vertical velocity across the GL (Fig. 5.7a–c) as well as the dimensions of the WSF (Fig. 5.7d) (Carlos Martín, 2024, *personal communication*). This supports the conclusion that vertical velocity and WSF dimensions are highly sensitive to basal drag and the way it is imposed. It may therefore be possible to use satellite observations of WSFs alongside more advanced 3-D ice sheet models to better quantify basal drag or inform the choice of basal sliding laws used at the GL (Brondex et al., 2017).

Additionally, basal drag can vary in space and time due to local interactions between the ice, subglacial water, bedrock and sediment (Cuffey & Paterson, 2010). Therefore, looking at the temporal evolution of WSFs using the approach described in Chapter 4 (e.g., Fig. 4.13) may give insights into how basal drag evolves over time and what this might mean for changes in subglacial water or sediment supply in the GZ. This

could help to derive a set of improved, physically based parameterisations for basal drag at Antarctic GZs that evolve with space and time), which could be tested in forecast ice-sheet models such as Elmer/Ice (Gagliardini et al., 2013).

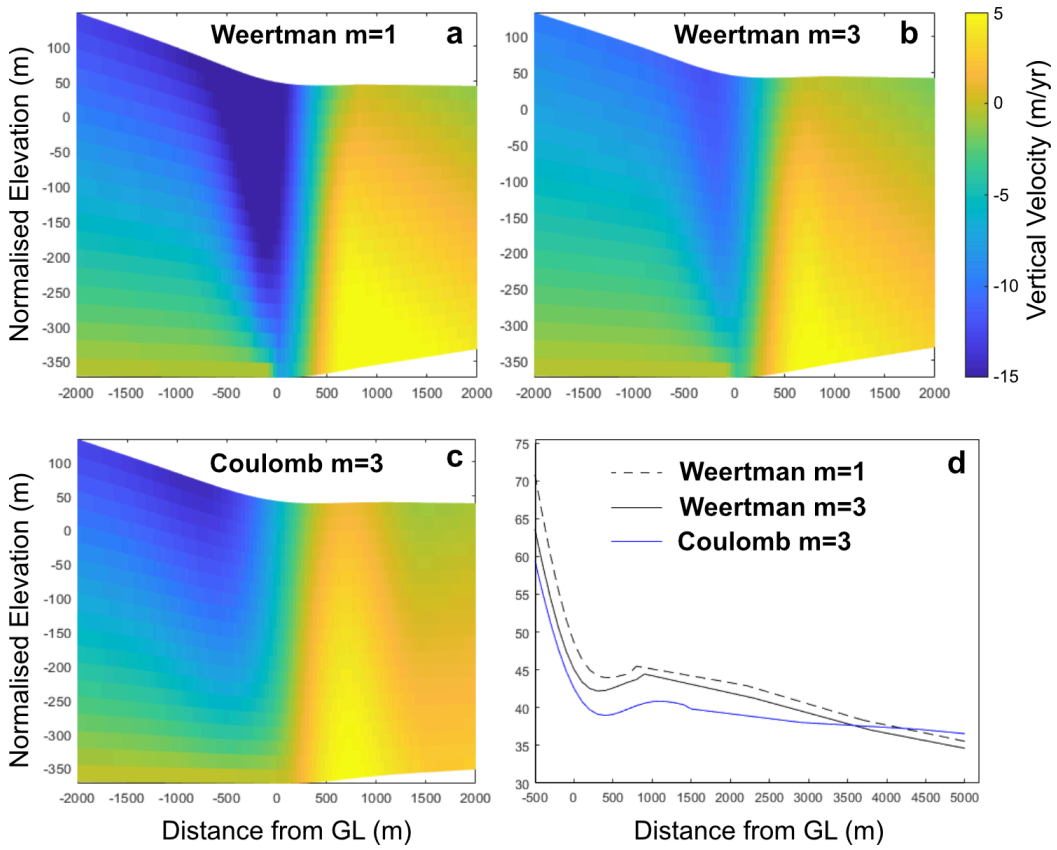


Figure 5.7. Effect of basal sliding law on vertical velocity near the GL and WSF surface profile (re-run of MISMIP experiment 1a4; Pattyn et al., 2012). (a–c) Vertical velocity across the GL using: (a) Weertman sliding law with exponent 1 (Equation 5.1); (b) Weertman sliding law with exponent 3 (Equation 5.1); (c) Coulomb sliding law with exponent 3 (Equation 5.2). (d) Surface elevation profiles showing the WSF profile for each sliding law in (a–c). Figure produced by Carlos Martín (2024; personal communication).

5.3.5. In situ measurements to validate and complement satellite datasets

Satellite observations can now give us more widespread observations of where tidal GL migration is occurring in Antarctica. Nevertheless, more continuous, in-situ observations are required to understand the properties of these seawater intrusions and their impact on basal melt rate, basal shear stress and sedimentation within GZs. These variables are crucial for parameterising the (currently absent) tidal processes in ice sheet models (Bradley & Hewitt, 2024; Robel et al., 2022). Targeted and comprehensive ground-based surveys in GZs subject to extreme tidal variability would be valuable to better understand the processes occurring within and beneath the ice in GZs on tidal timescales.

This kind of observational campaign should take place in a stable region where the tidal GL migration signal can be readily isolated from other sources of long-term elevation change. Measurements should be taken for a minimum duration of one full spring-neap tide cycle (14 days). Some suggestions for measurements include:

- **Terrestrial radar interferometry and GNSS** to continuously measure signals of ice shelf flexure and ice surface velocity, and for comparison with less-frequent satellite-derived measurements from DInSAR and ICESat-2 (Drews et al., 2017, 2021). Terrestrial InSAR has been recently employed at the GL of Jackobshavn Isbræ in Greenland, detecting kilometre-scale tidal seawater intrusions up to 10–20 cm in height (Kim et al., 2024).
- **Radar depth sounding**, either airborne or ground-based, to detect evidence of seawater intrusions upstream of the GL by measuring bed reflectivity or detecting the existence of subglacial channels (e.g., Corr, 2021; Drews et al., 2017; MacGregor et al., 2011). Radar can also be used to measure ice thickness and precise GL location, which could be used to validate the estimates from satellite measurements (as we demonstrated at the Mulock and Kamb GZs in Chapter 4).
- **Autonomous phase-sensitive Radio Echo Sounders (ApRES)** to continuously measure precise changes in ice thickness and englacial strain that are used to calculate basal melt rates across the tide cycle (e.g., Vaňková et al., 2020).

Deploying a network of ApRES instruments along a transect crossing the GZ could yield insights into the impact of tidal GL migration on basal melt rates. If there is a WSF in the GZ, this could also be used to measure changes in vertical velocity with depth as ice moves across the basal stress transition.

- **Swath-radar, seismic, and magneto-telluric (MT)** measurements to identify any changes in basal melt, basal sediment distribution, and subglacial saltwater-freshwater dynamics, both across the GZ and throughout the tide cycle (e.g., Gustafson et al., 2022).
- **Firn layer depth** measurements to reduce uncertainties in calculations of ice shelf thickness from surface elevations, as discussed in Chapter 4. Firn cores are rarely drilled at the GL and the spatial distribution of the firn depth correction at GZs around Antarctica is especially poorly known (van den Broeke et al., 2008).

To fully understand the magnitude and routes of ocean heat reaching the GL, these measurements in the GZ should be accompanied by observations further seaward within the ice shelf cavity (Fig. 5.8; Rignot, 2023). The bathymetry of many Antarctic ice shelf cavities, as well as large portions of the continental shelf, remains largely unknown (Dorschel et al., 2022), and we have sparse direct measurements of ocean currents and basal melt rates. These observations would require a combination of instruments deployed from ships or drilled through boreholes, including autonomous underwater vehicles (e.g., Davis et al., 2023; Schmidt et al., 2023).

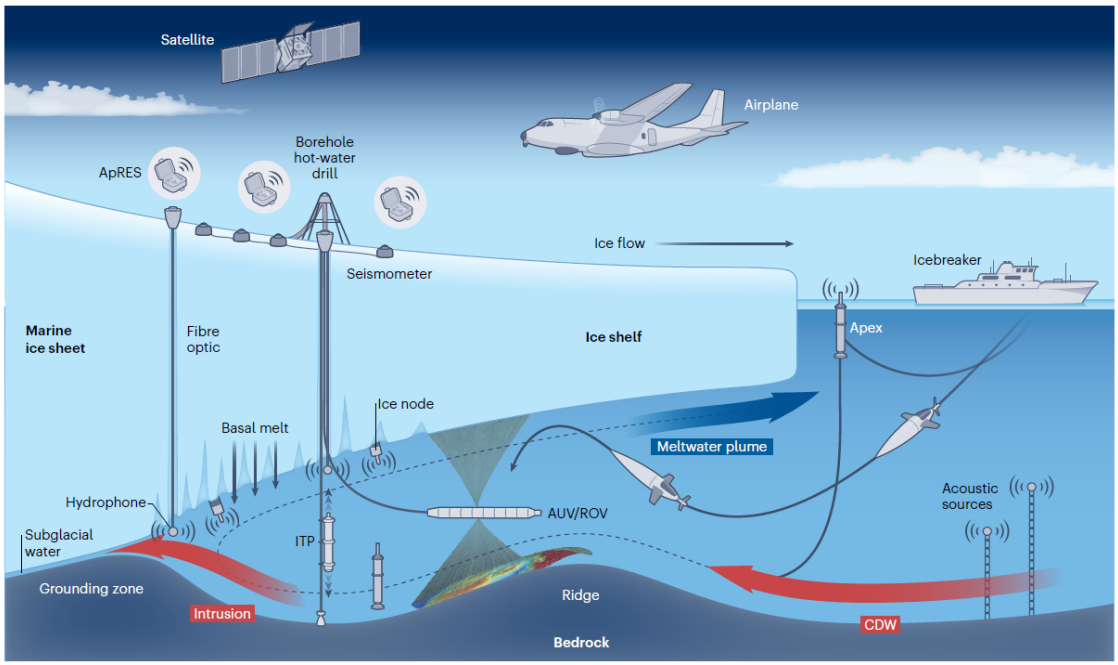


Figure 5.8. Suggested observations of ice-shelf cavities required to understand ice melt in Antarctica. Figure reproduced from Rignot (2023).

5.3.6. Looking forward to upcoming satellite missions

It is critical that we and continue to develop and launch satellite missions capable of monitoring the Polar Regions, as they provide our only means to acquire continent-wide observations of ice sheet change. In particular, monitoring ice sheet elevation change and GL migration is important to identify emerging instabilities as we approach potential tipping points, such as the initiation of marine ice sheet instability in the Amundsen Sea Embayment (Reed et al., 2024; Rosier et al., 2021). Such instabilities are major sources of uncertainty in future sea level rise predictions (Fig. 1.8; IPCC, 2023). Therefore, it is important to look to future missions and consider their instrument and orbit design at an early stage to maximise the quality and quantity of observations of these critical ice sheet processes.

To improve future observations of tidal GZ processes in particular, a key factor will be how satellites can sample the full tidal range around Antarctica, especially during

low tides (Zhong et al., 2023), and at what resolution and frequency. Satellite constellations like ICEYE and COSMO-SkyMed are already rapidly improving our capabilities for this (Rignot et al., 2024), but are limited by the cost-restrictions and lack of open-access data. Publicly-funded space agency satellite missions currently in development that will advance our capabilities for measuring Antarctic GL migration include:

- **NISAR**: A dual-frequency (L-/S-band) SAR satellite due to be launched by NASA and the Indian Space Research Organisation in 2024 (Kellogg et al., 2020). This will provide high-resolution DInSAR over the ice sheet margins.
- **CRISTAL**: A dual-frequency (Ka-/Ku-band) radar altimeter due to be launched by ESA in 2028 (Kern et al., 2020). CRISTAL will have fully-focused SAR capabilities, significantly improving along-track resolution and the ability to resolve smaller-scale and steeper ice sheet topography – critical in GZs.
- **Sentinel-1C, -1D and Next Generation (NG)**: An ESA programme to ensure the continuity of C-band SAR monitoring beyond 2030. Two more C-band SAR satellites (Sentinel-1C and -1D) are planned to join and eventually replace Sentinel-1A. This will reduce satellite repeat time from 12 days to 6 days (or shorter), improving InSAR coherence, though coverage will still be limited to north of ~78°S. Sentinel-1 NG aims to further improve the spatial resolution and reduce revisit times to < 4 days.
- **Earth Dynamics Geodetic Explorer (EDGE)**, currently in the early development stage as a Phase A concept study for NASA's new Earth System Explorers Program. EDGE will use a swath-mapping laser altimeter with 40 beams arranged in 5 x 120 m wide "mini-swaths" to quantify ice sheet surface topography and short-term elevation change at high spatial resolution (EDGE Team, 2024).

Looking further ahead, emerging satellite technologies currently used primarily in the defence sector could greatly improve our observational capabilities over Antarctic GZs. One promising example is High-Altitude Platform Stations (HAPS) like the Airbus Zephyr. These are solar-powered unmanned aerial vehicles capable of maintaining a fixed position at altitudes of 20–50 km for days to weeks. If deployed over an Antarctic GZ – such as a region of extensive tidal GL migration or during another subglacial lake drainage near the GL – these systems could provide continuous observations of ice sheet elevation with very high spatial and temporal resolution and immediate data downlink. This capability has the potential to revolutionise our understanding of GZ processes, addressing many of the observational gaps highlighted in this thesis.

5.4. Concluding Remarks

It has been suggested that *"observations of grounding zones are the missing key to understand ice melt in Antarctica"* (Rignot, 2023). Ice sheet models have struggled to adequately reproduce historical ice sheet and sea level change (Aschwanden et al., 2021) and the lack of representation of GZ melt driven by tidal processes and subglacial hydrology could be a key missing piece of the puzzle (Bradley & Hewitt, 2024). This thesis has made substantial contributions to improving our understanding of GZ processes across a range of timescales, both through methodological advances and new observations in key Antarctic GZs.

The ICESat-2 RTLA method (Chapter 2) offers a new tool for mapping the extent and modes of tidal GL migration around Antarctica. Observations at the Ronne and Ross Ice Shelves (Chapters 2 and 3) add to the growing body of evidence suggesting that the influence of tides on Antarctic ice sheet dynamics is much larger than originally thought (Brancato et al., 2020; Chen et al., 2023; Freer et al., 2023; Milillo et al., 2017, 2019, 2022; Rignot et al., 2024; Zhong et al., 2023). Notably, the role of seawater intrusions upstream of GLs remains a key uncertainty for projecting future ice sheet mass loss (Bradley & Hewitt, 2024; Robel et al., 2022; Warburton et al., 2020). Observations of a major subglacial lake drainage event close to the GZ allowed us to address critical questions

about the interactions between subglacial hydrology and GZ behaviour (Chapter 3). Furthermore, the integration of observations and numerical modelling to examine the previously undocumented wave-like surface features around the Ross Ice Shelf GZ (Chapter 4) has improved estimates of basal properties, GL position, and ice thickness—properties that remain highly uncertain in many parts of Antarctica.

Despite these advancements, we still lack satellite observations with adequate spatial and temporal resolution to fully characterise GL migration around Antarctica and separate its signal from long-term change. A comprehensive campaign combining satellite observations, airborne remote sensing, and in-situ surveys of the ice and the ocean will be essential to fully understand these GZ processes and incorporate them accurately into ice sheet and climate models (Rignot, 2023). This coordinated effort will be crucial for improving our projections of future ice sheet behaviour and global sea level rise.

References

Alley, R. B., Blankenship, D. D., Rooney, S. T., & Bentley, C. R. (1989). Sedimentation beneath ice shelves — the view from ice stream B. *Marine Geology*, *85*(2–4), 101–120. https://doi.org/10.1016/0025-3227(89)90150-3

Arthern, R. J., & Williams, C. R. (2017). The sensitivity of West Antarctica to the submarine melting feedback. *Geophysical Research Letters*, *44*(5), 2352–2359. https://doi.org/10.1002/2017GL072514

Arthern, R. J., Hindmarsh, R. C. A., & Williams, C. R. (2015). Flow speed within the Antarctic ice sheet and its controls inferred from satellite observations. *Journal of Geophysical Research: Earth Surface*, *120*(7), 1171–1188. https://doi.org/10.1002/2014JF003239

Aschwanden, A., Bartholomaus, T. C., Brinkerhoff, D. J., & Truffer, M. (2021). Brief communication: A roadmap towards credible projections of ice sheet contribution to sea level. *The Cryosphere*, *15*(12), 5705–5715. https://doi.org/10.5194/tc-15-5705-2021

Barnes, J. M., & Gudmundsson, G. H. (2022). The predictive power of ice sheet models and the regional sensitivity of ice loss to basal sliding parameterisations: a case study

of Pine Island and Thwaites glaciers, West Antarctica. *The Cryosphere*, *16*(10), 4291–4304. https://doi.org/10.5194/tc-16-4291-2022

Batchelor, C. L., Christie, F. D. W., Ottesen, D., Montelli, A., Evans, J., Dowdeswell, E. K., et al. (2023). Rapid, buoyancy-driven ice-sheet retreat of hundreds of metres per day. *Nature*, *617*(7959), 105–110. https://doi.org/10.1038/s41586-023-05876-1

Bindschadler, R., & Vornberger, P. (1998). Changes in the West Antarctic Ice Sheet Since 1963 from Declassified Satellite Photography. *Science*, *279*(5351), 689–692. https://doi.org/10.1126/science.279.5351.689

Brancato, V., Rignot, E., Milillo, P., Morlighem, M., Mouginot, J., An, L., et al. (2020). Grounding Line Retreat of Denman Glacier, East Antarctica, Measured With COSMO-SkyMed Radar Interferometry Data. *Geophysical Research Letters*, *47*(7). https://doi.org/10.1029/2019GL086291

van den Broeke, M. R., Berg, W. J. van de, & Meijgaard, E. van. (2008). Firn depth correction along the Antarctic grounding line. *Antarctic Science*, *20*(5), 513–517. https://doi.org/10.1017/S095410200800148X

Bradley, A. T. & Hewitt, I. J. (2024) Tipping point in ice-sheet grounding-zone melting due to ocean water intrusion. *Nature Geoscience*. https://doi.org/10.1038/s41561-024-01465-7

Brondex, J., Gagliardini, O., Gillet-Chaulet, F., & Durand, G. (2017). Sensitivity of grounding line dynamics to the choice of the friction law. *Journal of Glaciology*, *63*(241), 854–866. https://doi.org/10.1017/jog.2017.51

Brunt, K. M., Fricker, H. A., Padman, L., Scambos, T. A., & O'Neel, S. (2010). Mapping the grounding zone of the Ross Ice Shelf, Antarctica, using ICESat laser altimetry. *Annals of Glaciology*, *51*(55), 71–79. https://doi.org/10.3189/172756410791392790

Brunt, K. M., Fricker, H. A., & Padman, L. (2011). Analysis of ice plains of the Filchner–Ronne Ice Shelf, Antarctica, using ICESat laser altimetry. *Journal of Glaciology*, *57*(205), 965–975. https://doi.org/10.3189/002214311798043753

Burgard, C., Jourdain, N. C., Reese, R., Jenkins, A., & Mathiot, P. (2022). An assessment of basal melt parameterisations for Antarctic ice shelves. *The Cryosphere*, *16*(12), 4931–4975. https://doi.org/10.5194/tc-16-4931-2022

Chartrand, A. M., & Howat, I. M. (2023). A comparison of contemporaneous airborne altimetry and ice-thickness measurements of Antarctic ice shelves. *Journal of Glaciology*, 1–14. https://doi.org/10.1017/jog.2023.49

Chen, H., Rignot, E., Scheuchl, B., & Ehrenfeucht, S. (2023). Grounding Zone of Amery Ice Shelf, Antarctica, From Differential Synthetic-Aperture Radar Interferometry. *Geophysical Research Letters*, *50*(6), e2022GL102430. https://doi.org/10.1029/2022GL102430

Chuter, S. J., & Bamber, J. L. (2015). Antarctic ice shelf thickness from CryoSat-2 radar altimetry. *Geophysical Research Letters*, *42*(24), 10,721-10,729. https://doi.org/10.1002/2015GL066515

Ciracì, E., Rignot, E., Scheuchl, B., Tolpekin, V., Wollersheim, M., An, L., et al. (2023). Melt rates in the kilometer-size grounding zone of Petermann Glacier, Greenland, before and during a retreat. *Proceedings of the National Academy of Sciences*, *120*(20), e2220924120. https://doi.org/10.1073/pnas.2220924120

Corr, H. (2021). Processed airborne radio-echo sounding data from the GRADES-IMAGE survey covering the Evans and Rutford Ice Streams, and ice rises in the Ronne Ice Shelf, West Antarctica (2006/2007) (Version 1.0) [Dataset]. NERC EDS UK Polar Data Centre. https://doi.org/10.5285/C7EA5697-87E3-4529-A0DD-089A2ED638FB

Corr, H. F. J., Doake, C. S. M., Jenkins, A., & Vaughan, D. G. (2001). Investigations of an "ice plain" in the mouth of Pine Island Glacier, Antarctica. *Journal of Glaciology*, *47*(156), 51–57. https://doi.org/10.3189/172756501781832395

CReSIS (2024) MCoRDS 2013 Data [Dataset]. Lawrence, Kansas, USA. Digital Media. http://data.cresis.ku.edu/.

Cuffey, K., & Paterson, W. S. B. (2010). *The physics of glaciers* (4th Edition). Burlington, MA: Butterworth-Heinemann/Elsevier.

Davis, P. E. D., Nicholls, K. W., Holland, D. M., Schmidt, B. E., Washam, P., Riverman, K. L., et al. (2023). Suppressed basal melting in the eastern Thwaites Glacier grounding zone. *Nature, 614*(7948), 479–485. https://doi.org/10.1038/s41586-022-05586-0

Dorschel, B., Hehemann, L., Viquerat, S., Warnke, F., Dreutter, S., Tenberge, Y. S., et al. (2022). The International Bathymetric Chart of the Southern Ocean Version 2. *Scientific Data*, *9*(1), 275. https://doi.org/10.1038/s41597-022-01366-7

Drews, R., Pattyn, F., Hewitt, I. J., Ng, F. S. L., Berger, S., Matsuoka, K., et al. (2017). Actively evolving subglacial conduits and eskers initiate ice shelf channels at an Antarctic grounding line. *Nature Communications*, *8*(1), 15228. https://doi.org/10.1038/ncomms15228

Drews, R., Wild, C. T., Marsh, O. J., Rack, W., Ehlers, T. A., Neckel, N., & Helm, V. (2021). Grounding-Zone Flow Variability of Priestley Glacier, Antarctica, in a Diurnal

Tidal Regime. *Geophysical Research Letters*, *48*(20), e2021GL093853. https://doi.org/10.1029/2021GL093853

Durand, G., Gagliardini, O., de Fleurian, B., Zwinger, T., & Le Meur, E. (2009). Marine ice sheet dynamics: Hysteresis and neutral equilibrium. *Journal of Geophysical Research*, *114*(F3), F03009. https://doi.org/10.1029/2008JF001170

EDGE Team (2024) *Earth Dynamics Geodetic Explorer Webpage*. Available at: https://edge.ucsd.edu/

Freer, B. I. D., Marsh, O. J., Hogg, A. E., Fricker, H. A., & Padman, L. (2023). Modes of Antarctic tidal grounding line migration revealed by Ice, Cloud, and land Elevation Satellite-2 (ICESat-2) laser altimetry. *The Cryosphere*, *17*(9), 4079–4101. https://doi.org/10.5194/tc-17-4079-2023

Fretwell, P., Pritchard, H. D., Vaughan, D. G., Bamber, J. L., Barrand, N. E., Bell, R., et al. (2013). Bedmap2: improved ice bed, surface and thickness datasets for Antarctica. *The Cryosphere*, *7*(1), 375–393. https://doi.org/10.5194/tc-7-375-2013

Fricker, H. A., & Scambos, T. (2009). Connected subglacial lake activity on lower Mercer and Whillans Ice Streams, West Antarctica, 2003–2008. *Journal of Glaciology*, *55*(190), 303–315. https://doi.org/10.3189/002214309788608813

Fricker, H. A., Scambos, T., Bindschadler, R., & Padman, L. (2007). An Active Subglacial Water System in West Antarctica Mapped from Space. *Science*, *315*(5818), 1544–1548. https://doi.org/10.1126/science.1136897

Fricker, H. A., Coleman, R., Padman, L., Scambos, T. A., Bohlander, J., & Brunt, K. M. (2009). Mapping the grounding zone of the Amery Ice Shelf, East Antarctica using InSAR, MODIS and ICESat. *Antarctic Science*, *21*(5), 515–532. https://doi.org/10.1017/S095410200999023X

Friedl, P., Weiser, F., Fluhrer, A., & Braun, M. H. (2020). Remote sensing of glacier and ice sheet grounding lines: A review. *Earth-Science Reviews*, *201*, 102948. https://doi.org/10.1016/j.earscirev.2019.102948

Gagliardini, O., Zwinger, T., Gillet-Chaulet, F., Durand, G., Favier, L., De Fleurian, B., et al. (2013). Capabilities and performance of Elmer/Ice, a new-generation ice sheet model. *Geoscientific Model Development*, *6*(4), 1299–1318. https://doi.org/10.5194/gmd-6-1299-2013

Gladstone, R. M., Payne, A. J., & Cornford, S. L. (2012). Resolution requirements for grounding-line modelling: sensitivity to basal drag and ice-shelf buttressing. *Annals of Glaciology*, *53*(60), 97–105. https://doi.org/10.3189/2012AoG60A148

Goldberg, D. N., Gourmelen, N., Kimura, S., Millan, R., & Snow, K. (2019). How Accurately Should We Model Ice Shelf Melt Rates? *Geophysical Research Letters*, *46*(1), 189–199. https://doi.org/10.1029/2018GL080383

Graham, A. G. C., Wåhlin, A., Hogan, K. A., Nitsche, F. O., Heywood, K. J., Totten, R. L., et al. (2022). Rapid retreat of Thwaites Glacier in the pre-satellite era. *Nature Geoscience*, *15*, 706–713. https://doi.org/10.1038/s41561-022-01019-9

Griggs, J. A., & Bamber, J. L. (2011). Antarctic ice-shelf thickness from satellite radar altimetry. *Journal of Glaciology*, *57*(203), 485–498. https://doi.org/10.3189/002214311796905659

Gustafson, C. D., Key, K., Siegfried, M. R., Winberry, J. P., Fricker, H. A., Venturelli, R. A., & Michaud, A. B. (2022). A dynamic saline groundwater system mapped beneath an Antarctic ice stream. *Science*, *376*(6593), 640–644. https://doi.org/10.1126/science.abm3301

Hindmarsh, R. C. A. (1993). Qualitative Dynamics of Marine Ice Sheets. In W. R. Peltier (Ed.), *Ice in the Climate System* (pp. 67–99). Berlin, Heidelberg: Springer Berlin Heidelberg. https://doi.org/10.1007/978-3-642-85016-5_5

Horgan, H. J., & Anandakrishnan, S. (2006). Static grounding lines and dynamic ice streams: Evidence from the Siple Coast, West Antarctica. *Geophysical Research Letters*, *33*(18). https://doi.org/10.1029/2006GL027091

Horgan, H. J., Alley, R. B., Christianson, K., Jacobel, R. W., Anandakrishnan, S., Muto, A., et al. (2013). Estuaries beneath ice sheets. *Geology*, *41*(11), 1159–1162. https://doi.org/10.1130/G34654.1

Howard, S. L., Padman, L., & Erofeeva, S. Y. (2019). CATS2008: Circum-Antarctic Tidal Simulation version 2008 (Version 1) [Data set]. U.S. Antarctic Program (USAP) Data Center. https://doi.org/10.15784/601235

Howat, I. M., Porter, C., Smith, B. E., Noh, M.-J., and Morin, P. (2019) The Reference Elevation Model of Antarctica. *The Cryosphere*, 13, 665–674, https://doi.org/10.5194/tc-13-665-2019

Intergovernmental Panel on Climate Change (IPCC) (2023a). Ocean, Cryosphere and Sea Level Change. In *Climate Change 2021 – The Physical Science Basis: Working Group I Contribution to the Sixth Assessment Report of the Intergovernmental Panel on Climate Change* (pp. 1211–1362). Cambridge: Cambridge University Press. https://doi.org/10.1017/9781009157896.011

Jenkins, A., Corr, H. F. J., Nicholls, K. W., Stewart, C. L., & Doake, C. S. M. (2006). Interactions between ice and ocean observed with phase-sensitive radar near an Antarctic ice-shelf grounding line. *Journal of Glaciology*, *52*(178), 325–346. https://doi.org/10.3189/172756506781828502

Kellogg, K., Hoffman, P., Standley, S., Shaffer, S., Rosen, P., Edelstein, W., et al. (2020). NASA-ISRO Synthetic Aperture Radar (NISAR) Mission. In *2020 IEEE Aerospace Conference* (pp. 1–21). Big Sky, MT, USA: IEEE. https://doi.org/10.1109/AERO47225.2020.9172638

Kern, M., Cullen, R., Berruti, B., Bouffard, J., Casal, T., Drinkwater, M. R., et al. (2020). The Copernicus Polar Ice and Snow Topography Altimeter (CRISTAL) high-priority candidate mission. *The Cryosphere*, *14*(7), 2235–2251. https://doi.org/10.5194/tc-14-2235-2020

Kim, J. H., Rignot, E., Holland, D., & Holland, D. (2024). Seawater Intrusion at the Grounding Line of Jakobshavn Isbræ, Greenland, From Terrestrial Radar Interferometry. *Geophysical Research Letters*, *51*(6), e2023GL106181. https://doi.org/10.1029/2023GL106181

LeCun, Y., Bengio, Y., & Hinton, G. (2015). Deep learning. *Nature*, *521*(7553), 436–444. https://doi.org/10.1038/nature14539

MacGregor, J. A., Anandakrishnan, S., Catania, G. A., & Winebrenner, D. P. (2011). The grounding zone of the Ross Ice Shelf, West Antarctica, from ice-penetrating radar. *Journal of Glaciology*, *57*(205), 917–928. https://doi.org/10.3189/002214311798043780

Mayer, C., & Huybrechts, P. (1999). Ice-dynamic conditions across the grounding zone, Ekströmisen, East Antarctica. *Journal of Glaciology*, *45*(150), 384–393. https://doi.org/10.3189/S002214300000188X

McMillan, M., Corr, H., Shepherd, A., Ridout, A., Laxon, S., & Cullen, R. (2013). Three-dimensional mapping by CryoSat-2 of subglacial lake volume changes. *Geophysical Research Letters, 40(16)*, 4321–4327. https://doi.org/10.1002/grl.50689

Milillo, P., Rignot, E., Rizzoli, P., Scheuchl, B., Mouginot, J., Bueso-Bello, J., & Prats-Iraola, P. (2019). Heterogeneous retreat and ice melt of Thwaites Glacier, West Antarctica. *Science Advances*, *5*(1), eaau3433. https://doi.org/10.1126/sciadv.aau3433

Milillo, P., Rignot, E., Rizzoli, P., Scheuchl, B., Mouginot, J., Bueso-Bello, J. L., et al. (2022). Rapid glacier retreat rates observed in West Antarctica. *Nature Geoscience*, *15*(1), 48–53. https://doi.org/10.1038/s41561-021-00877-z

Milillo, P., Rignot, E., Mouginot, J., Scheuchl, B., Morlighem, M., Li, X., & Salzer, J. T. (2017). On the Short-term Grounding Zone Dynamics of Pine Island Glacier, West Antarctica, Observed With COSMO-SkyMed Interferometric Data. *Geophysical Research Letters*, *44*(20), 10,436-10,444. https://doi.org/10.1002/2017GL074320

Morlighem, M., Rignot, E., Binder, T., Blankenship, D., Drews, R., Eagles, G., et al. (2020). Deep glacial troughs and stabilizing ridges unveiled beneath the margins of the Antarctic ice sheet. *Nature Geoscience*, *13*(2), 132–137. https://doi.org/10.1038/s41561-019-0510-8

Mosbeux, C., Padman, L., Klein, E., Bromirski, P. D., & Fricker, H. A. (2023). Seasonal variability in Antarctic ice shelf velocities forced by sea surface height variations. *The Cryosphere*, *17*(7), 2585–2606. https://doi.org/10.5194/tc-17-2585-2023

Otosaka, I. N., Shepherd, A., Ivins, E. R., Schlegel, N.-J., Amory, C., van den Broeke, M. R., et al. (2023). Mass balance of the Greenland and Antarctic ice sheets from 1992 to 2020. *Earth System Science Data*, *15*(4), 1597–1616. https://doi.org/10.5194/essd-15-1597-2023

Paden, J., Li, J., Leuschen, C., Rodriguez-Morales, F., & Hale, R. (2010) IceBridge MCoRDS L2 Ice Thickness (Version 1) [Dataset]. NASA National Snow and Ice Data Center Distributed Active Archive Center. https://doi.org/10.5067/GDQ0CUCVTE2Q.

Paolo, F. S., Fricker, H. A., & Padman, L. (2015). Volume loss from Antarctic ice shelves is accelerating. *Science*, *348*(6232), 327–331. https://doi.org/10.1126/science.aaa0940

Parizek, B. R., Christianson, K., Anandakrishnan, S., Alley, R. B., Walker, R. T., Edwards, R. A., et al. (2013). Dynamic (in)stability of Thwaites Glacier, West Antarctica. *Journal of Geophysical Research: Earth Surface*, *118*(2), 638–655. https://doi.org/10.1002/jgrf.20044

Pattyn, F., Schoof, C., Perichon, L., Hindmarsh, R. C. A., Bueler, E., de Fleurian, B., et al. (2012). Results of the Marine Ice Sheet Model Intercomparison Project, MISMIP. *The Cryosphere*, *6*(3), 573–588. https://doi.org/10.5194/tc-6-573-2012

Rabus, B. T., & Lang, O. (2002). On the representation of ice-shelf grounding zones in SAR interferograms. *Journal of Glaciology*, *48*(162), 345–356. https://doi.org/10.3189/172756502781831197

Reed, B., Green, J. A. M., Jenkins, A., & Gudmundsson, G. H. (2024). Recent irreversible retreat phase of Pine Island Glacier. *Nature Climate Change*, *14*(1), 75–81. https://doi.org/10.1038/s41558-023-01887-y

Rignot, E., Mouginot, J., Morlighem, M., Seroussi, H., & Scheuchl, B. (2014). Widespread, rapid grounding line retreat of Pine Island, Thwaites, Smith, and Kohler glaciers, West Antarctica, from 1992 to 2011. *Geophysical Research Letters*, *41*(10), 3502–3509. https://doi.org/10.1002/2014GL060140

Rignot, E., Mouginot, J., & Scheuchl, B. (2011). Antarctic grounding line mapping from differential satellite radar interferometry. *Geophysical Research Letters, 38(10)*. https://doi.org/10.1029/2011GL047109

Rignot, E. (2023). Observations of grounding zones are the missing key to understand ice melt in Antarctica. *Nature Climate Change*, *13*(10), 1010–1013. https://doi.org/10.1038/s41558-023-01819-w

RINGS Action Group. (2022). *RINGS White Paper: Collaborative international effort to map all Antarctic ice-sheet margins*. Scientific Committee on Antarctic Research. https://doi.org/10.5281/zenodo.6638327

Robel, A. A., Wilson, E., & Seroussi, H. (2022). Layered seawater intrusion and melt under grounded ice. *The Cryosphere*, *16*(2), 451–469. https://doi.org/10.5194/tc-16-451-2022

Rosier, S. H. R., Reese, R., Donges, J. F., De Rydt, J., Gudmundsson, G. H., & Winkelmann, R. (2021). The tipping points and early warning indicators for Pine Island Glacier, West Antarctica. *The Cryosphere, 15*(3), 1501–1516. https://doi.org/10.5194/tc-15-1501-2021

Sayag, R., & Worster, M. G. (2013). Elastic dynamics and tidal migration of grounding lines modify subglacial lubrication and melting. *Geophysical Research Letters*, *40*(22), 5877–5881. https://doi.org/10.1002/2013GL057942

Schmeltz, M., Rignot, E., & MacAyeal, D. R. (2001). Ephemeral grounding as a signal of ice-shelf change. *Journal of Glaciology*, *47*(156), 71–77. https://doi.org/10.3189/172756501781832502

Schmidt, B. E., Washam, P., Davis, P. E. D., Nicholls, K. W., Holland, D. M., Lawrence, J. D., et al. (2023). Heterogeneous melting near the Thwaites Glacier grounding line. *Nature*, *614*(7948), 471–478. https://doi.org/10.1038/s41586-022-05691-0

Schoof, C. (2007). Ice sheet grounding line dynamics: Steady states, stability, and hysteresis. *Journal of Geophysical Research*, *112*(F3), F03S28. https://doi.org/10.1029/2006JF000664

Schoof, C. (2011). Marine ice sheet dynamics. Part 2. A Stokes flow contact problem. *Journal of Fluid Mechanics*, *679*, 122–155. https://doi.org/10.1017/jfm.2011.129

Seroussi, H., & Morlighem, M. (2018). Representation of basal melting at the grounding line in ice flow models. *The Cryosphere*, *12*(10), 3085–3096. https://doi.org/10.5194/tc-12-3085-2018

Siegfried, M. R., & Fricker, H. A. (2021). Illuminating Active Subglacial Lake Processes With ICESat-2 Laser Altimetry. *Geophysical Research Letters*, *48*(14). https://doi.org/10.1029/2020GL091089

Siegfried, Matthew R., & Fricker, H. A. (2018). Thirteen years of subglacial lake activity in Antarctica from multi-mission satellite altimetry. *Annals of Glaciology*, *59*(76pt1), 42–55. https://doi.org/10.1017/aog.2017.36

Siegfried, M.R., Venturelli, R. A., Patterson, M. O., Arnuk, W., Campbell, T. D., Gustafson, C. D., et al. (2023). The life and death of a subglacial lake in West Antarctica. *Geology*, *51*(5), 434–438. https://doi.org/10.1130/G50995.1

Smith, B., Hancock, D., Harbeck, K., Roberts, L., Neumann, T., Brunt, K. , Fricker, H. A., Gardner, A., Siegfried, M., Adusumilli, S., Csatho, B., Holschuh, N., Nilsson, J., Paolo, F., & Felikson, D. (2022). Ice, Cloud, and Land Elevation Satellite (ICESat-2) Project Algorithm Theoretical Basis Document (ATBD) for Land Ice Along-Track Height Product (ATL06), Version 6. ICESat-2 Project, DOI: 10.5067/VWOKQDYJ7ODB.

Smith, B. & ICESat-2 Science Development Team (2024) Ice, Cloud, and Land Elevation Satellite (ICESat-2) Algorithm Theoretical Basis Document (ATBD) for Land Ice DEM and Land Ice Height Change (ATL14 and 15), Release 4. ICESat-2 Project.

Truffer, M., & Echelmeyer, K. A. (2003). Of isbræ and ice streams. *Annals of Glaciology*, *36*, 66–72. https://doi.org/10.3189/172756403781816347

Tsai, V. C., & Gudmundsson, G. H. (2015). An improved model for tidally modulated grounding-line migration. *Journal of Glaciology*, *61*(226), 216–222. https://doi.org/10.3189/2015JoG14J152

Vaňková, I., Nicholls, K. W., Corr, H. F. J., Makinson, K., & Brennan, P. V. (2020). Observations of Tidal Melt and Vertical Strain at the Filchner-Ronne Ice Shelf, Antarctica. *Journal of Geophysical Research: Earth Surface*, *125*(1). https://doi.org/10.1029/2019JF005280

Wang, Z., Gogineni, S., Rodriguez-Morales, F., Yan, J.-B., Paden, J., Leuschen, C., et al. (2016). Multichannel Wideband Synthetic Aperture Radar for Ice Sheet Remote Sensing: Development and the First Deployment in Antarctica. *IEEE Journal of Selected Topics in Applied Earth Observations and Remote Sensing*, *9*(3), 980–993. https://doi.org/10.1109/JSTARS.2015.2403611

Warburton, K. L. P., Hewitt, D. R., & Neufeld, J. A. (2020). Tidal Grounding-Line Migration Modulated by Subglacial Hydrology. *Geophysical Research Letters*, *47*(17). https://doi.org/10.1029/2020GL089088

Weertman, J. (1957). On the Sliding of Glaciers. *Journal of Glaciology*, *3*(21), 33–38. https://doi.org/10.3189/S0022143000024709

Whillans, I. M., Bentley, C. R., & Van Der Veen, C. J. (2001). Ice Streams B and C. In *The West Antarctic Ice Sheet: Behavior and Environment* (pp. 257–281). American Geophysical Union (AGU). https://doi.org/10.1029/AR077p0257

Wild, C. T., Marsh, O. J., & Rack, W. (2017). Viscosity and elasticity: a model intercomparison of ice-shelf bending in an Antarctic grounding zone. *Journal of Glaciology*, *63*(240), 573–580. https://doi.org/10.1017/jog.2017.15

Wilson, N., Straneo, F., & Heimbach, P. (2017). Satellite-derived submarine melt rates and mass balance (2011–2015) for Greenland's largest remaining ice tongues. *The Cryosphere*, *11*(6), 2773–2782. https://doi.org/10.5194/tc-11-2773-2017

Zhong, M., Simons, M., Minchew, B., & Zhu, L. (2023). Inferring Tide-Induced Ephemeral Grounding in an Ice-Shelf-Stream System: Rutford Ice Stream, West Antarctica. *Journal of Geophysical Research: Earth Surface*, *128*(2), e2022JF006789. https://doi.org/10.1029/2022JF006789